ANL-GenIV-142

Generation IV Nuclear Energy System Initiative

RCCS Studies and NSTF Preparation Air-Cooled Option

Nuclear Engineering Division

About Argonne National Laboratory
Argonne is a U.S. Department of Energy laboratory managed by UChicago Argonne, LLC under contract DE-AC02-06CH11357. The Laboratory's main facility is outside Chicago, at 9700 South Cass Avenue, Argonne, Illinois 60439. For information about Argonne and its pioneering science and technology programs, see www.anl.gov.

DOCUMENT AVAILABILITY

Online Access: U.S. Department of Energy (DOE) reports produced after 1991 and a growing number of pre-1991 documents are available free via DOE's SciTech Connect (http://www.osti.gov/scitech/)

Reports not in digital format may be purchased by the public from the National Technical Information Service (NTIS):
U.S. Department of Commerce National
Technical Information Service 5301
Shawnee Rd
Alexandra, VA 22312
www.ntis.gov
Phone: (800) 553-NTIS (6847) or (703) 605-6000
Fax: (703) 605-6900
Email: **orders@ntis.gov**

Reports not in digital format are available to DOE and DOE contractors from the Office of Scientific and Technical Information (OSTI):
U.S. Department of Energy
Office of Scientific and Technical Information
P.O. Box 62
Oak Ridge, TN 37831-0062
www.osti.gov
Phone: (865) 576-8401
Fax: (865) 576-5728
Email: **reports@osti.gov**

Disclaimer
This report was prepared as an account of work sponsored by an agency of the United States Government. Neither the United States Government nor any agency thereof, nor UChicago Argonne, LLC, nor any of their employees or officers, makes any warranty, express or implied, or assumes any legal liability or responsibility for the accuracy, completeness, or usefulness of any information, apparatus, product, or process disclosed, or represents that its use would not infringe privately owned rights. Reference herein to any specific commercial product, process, or service by trade name, trademark, manufacturer, or otherwise, does not necessarily constitute or imply its endorsement, recommendation, or favoring by the United States Government or any agency thereof. The views and opinions of document authors expressed herein do not necessarily state or reflect those of the United States Government or any agency thereof, Argonne National Laboratory, or UChicago Argonne, LLC.

ANL-GenIV-142

Generation IV Nuclear Energy System Initiative

RCCS Studies and NSTF Preparation
Air-Cooled Option

---

by
S. Lomperski, W. D. Pointer, C. P. Tzanos, T. Y. C. Wei, C. M. Crooks, and O. A. Rodriguez

Nuclear Engineering Division, Argonne National Laboratory

September 2010

Executive Summary

The Very High Temperature Reactor (VHTR) Reactor Cavity Cooling System (RCCS) is a safety-grade system that operates for both normal and accident conditions. During the various accident scenarios where a total loss of active forced cooling in the core occurs, either under pressurized or depressurized conditions, shutdown decay heat removal is passively carried out through the RCCS. Core after-heat is passively conducted and radiated in-vessel through the core elements and downcomer and the riser gaps to the vessel wall. It is then passively transferred to the ex-vessel reactor cavity heat removal system, which is the RCCS. In the air-cooled RCCS design option, the ultimate passive heat sink is the atmosphere. Cold atmospheric air is suctioned into the inlet side of the RCCS, heated up by the removal of the core residual heat from the vessel wall, rises through the hot side of the RCCS and is ultimately discharged from the chimneys back to the atmosphere. Experiment data to validate the codes for confirming RCCS performance will be obtained through the conduct of large-scale integral experiments at the Argonne National Laboratory (ANL) Natural Convection Shutdown Heat Removal Test Facility (NSTF). In preparation for the NSTF tests, RCCS studies in FY10 were focused on the GA-MHTGR air-cooled RCCS to confirm the scaling basis for the experiments and to provide instrumentation support. Study elements are;

(a) the RELAP5 ultimate air heat sink system analyses,
(b) the STARCCM+ air plenums computational fluid dynamics (CFD) analyses, and
(c) the cavity Laser Doppler Velocimetry (LDV) instrumentation feasibility.

In summary:

(a) A full reactor-scale model of the GA-MHTGR air-cooled RCCS has been prepared with RELAP5. A half-scale model has also been prepared to verify the FY06 Argonne scaling study. In addition, a model of the planned NSTF experiment initial configuration is in place. The full-scale model was used as a baseline to test the response of the system to varying heat fluxes and confirm the scaling laws. Cases at 10-kW/m^2, 5-kW/m^2, and 2.5-kW/m^2 full-scale heat fluxes were run. The heat flux of 5.0kW/m^2 represents the reference reactor case of medium heat flux. The high heat flux case corresponds to the system model with l0-kW/m^2. The heat flux of 2.5-kW/m^2 is the low heat flux case. It should be emphasized that these are uniform heat fluxes applied at the reactor vessel outer surface over the heated height. The half-scale system shows qualitative agreement with the scaling analysis in terms of general system phenomena behavior, but quantitative non-dimensionalized analyses will be performed in the future to confirm this. The NSTF experiment configuration model was used to conduct cases at three internal power generation levels. These power levels produce the three proportionally full-scaled heat fluxes previously used. A number of experiment cross section configurations are under discussion but they mainly involve varying the separation distance between the heated surface of the box and the hot risers. The test cavity box depth will be of variable design. There may be experiment configurations where the array of hot riser ducts is offset by a yet-to-be-determined angle to simulate corners of the cavity. This model will be the starting basis for modified RELAP5 models as the experiment matrix is defined.

(b) RANS-based simulations of natural convection and radiation heat transport have been completed using the CFD code STARCCM+. At this stage, the CFD analyses are intended to be used to guide the development of an experimental geometry and test plan for experiments

related to the air-cooled GA-MHTGR RCCS designs. Based on the CAD model describing the full GA-MHTGR RCCS air-side geometry an explicit geometry model was developed. A series of Computational Fluid Dynamics simulations of the GA-MHTGR RCCS system have been completed as a baseline for the development and scaling of the multidimensional aspects of the NSTF experiment. The initial baseline RCCS simulation uses a constant uniform heat flux on the risers rather than a more realistic radiation heat source distribution. The use of the simplified boundary condition enables the initial simulations of the air-cooled full scale reactor RCCS system and its NSTF analog to more easily be used for model development and mesh optimization. A uniform 1.24 kW/m2 heat flux is applied to all the risers, which is consistent with a loss of flow accident in which the risers expel all of the heat from the reactor vessel, (10.0 kW/m2), out off the system. A symmetry boundary condition is applied at the symmetry plane so that the model effectively represents the full system. The temperature distribution in the upper components of the RCCS system with detailed distributions of the hot side components was obtained. Since the heat flux in each riser tube is identical, the temperature distributions in these components are very uniform. However the velocity fields provide some insight into likely regions of thermal stripping or stratification when a more realistic non-uniform heat load distribution is applied. For example, strong recirculation zones form downstream of each of the 90-degree bends in the co-axial ducts. Such flow structures can result in the formation of stagnation points which lead to thermal stresses in adjacent solid materials. However, in this case, these flow features also result in significant turbulence generation, where high turbulent kinetic energies can be observed near the center of each recirculation region.

As with the GA-MHTGR RCCS model, the NSTF experiment-scale STAR-CCM+ CFD model was developed of the proposed experiment geometry. Although based on the experimental geometry currently under discussion, the computational model considers a simplified geometry which neglects the building structure and assumes that adequate ventilation is available to feed coolant to the inlet of the natural convection driven facility. The riser duct heat flux boundary condition and solver settings are the same as those used in the GA-MHTGR model. The predicted temperature profile in the heated region is quite similar to the profile seen in the GA-MHTGR case. As in that case, uniform heating of the RCCS ducts should be expected and the temperature distribution in the RCCS risers as well as the horizontal and vertical duct segments is very uniform. However the single horizontal inlet configuration results in the formation of a strong recirculation zone in the inlet plenum which may affect the duct flow distribution and stability. Steady state velocity profiles and the good convergence behavior of the simulation suggest that the flow field in the risers is fairly stable, but more detailed unsteady analyses are needed to address stability. Similarly a large recirculation zone forms in the upper plenum as a consequence of the offset position of the risers. This recirculation pattern persists through the horizontal segment of the outlet duct and may interfere with the formation of the recirculation patterns seen downstream of each elbow in the RCCS model. Building upon this foundational work, the mesh and modeling strategy will be used in future simulations to evaluate the more complex case in which the radiation heat source is applied/and or calculated as part of the simulation.

(c) A characterization of local gas velocities within the cavity is desired for comparison with CFD code simulations. An evaluation of instrumentation alternatives identified Laser Doppler Velocimetry (LDV) as the most feasible candidate in view of the facility's high operating temperature and the expectation of rather low flow velocities within the cavity. But

LDV cannot function without suspended particles. Maintaining adequate levels of particle "seeding" is difficult in a closed system such as the RCCS and so a feasibility study was conducted to ascertain whether this technique could successfully measure velocity within the cavity. Candidate seeding materials have been tested in a 1.8 x 0.5 x 0.5 m glass enclosure. Based on this feasibility study, it is probable that LDV can be made to function well enough to obtain a number of velocity measurements though it is not yet clear how much effort will be required to obtain an acceptably extensive cavity velocity map. For steady state tests that run tens of hours, it may be acceptable if, say, ten minutes of data collection are required at each location. One could then map dozens of locations over the course of hours. For transient tests, one may only be able to track velocity at a single location during the course of the test. It is likely that trial and error iterations with the actual facility will be necessary for the final selection of a seeding material and injection mode and to arrive at acceptable data rates and seeding intervals.

Table of Contents

Executive Summary ii
Nomenclature ix
1.0 Introduction 1
1.1 GA-MHTGR RCCS Design 2
1.2 NSTF RCCS Experiment Scaling 2
1.2.1 Top-down Scaling 6
1.2.2 Loop Steady State 6
1.2.3 Loop Transient 10
1.2.4 Cavity Steady State 13
1.3 Top-Down Scaling Laws 15
1.3.1 Baseline Scaling 16
1.3.2 Time Number Scaling 19
1.3.3 Alternate Time Number Scaling 20
1.3.4 Stanton Numbering Scaling 21
1.4 Bottom-Up Scaling 24
1.5 Study Approach 25
References 30
2.0 Air Heat Sink System Analyses 31
2.1 RCCS Design View Factors 32
2.1.1 Reactor-Scale Geometry 32
2.1.2 Experiment Geometry 47
2.2 RELAP5 Modeling 52
2.2.1 Full-Scale Model 55
2.2.2 Half-Scale Model 58
2.2.3 Experiment Model 58
2.3 GA Results 61
2.4 RELAP5 Results 63
2.4.1 Full-Scale Model Results 64
2.4.2 Half-Scale Model Results 72
2.4.3 Experiment Model Results 76
2.5 Conclusions 93
References 95
3.0 Air-Cooled RCCS CFD Analysis 96
3.1 Motivation and Objective 96
3.2 RCCS System Model Geometry 96
3.3 Methodology 96
3.4 Fixed Heat Flux RCCS Model and Simulation Results 107
3.5 NSTF Experiment Model 119
3.6 Summary and Planned Future Work 125
4.0 Cavity Velocity Measurement Feasibility Tests 126
4.1 Background 126
4.2 Laser Doppler Velocimetry 126

4.3 LDV in Similar Applications 127
4.4 Experiment Configuration 128
4.5 Test Results 128
4.6 Discussion 132
References 133

List of Figures

1.1 Overall System View of the GA-MHTGR RCCS 3
1.2 View of Ex-Cavity RCCS Outer Cold Duct/Inner Hot Duct Run 4
1.3 Cavity Isometric View of Reactor Vessel and RCCS.....5
1.4 Cavity Plane View of Reactor Vessel and RCCS 6
2.1 Cavity Cross Section-Group of 10 33
2.2 View Factors-Group of 10 35
2.3 Cavity Cross Section-Group of 1 Location.....37
2.4 Cavity Cross Section-Group of 3 Location.....38
2.5 Cavity Cross Section-Group of 4A Location.....42
2.6 Cavity Cross Section-Group of 4B Location 43
2.7 Cavity Cross Section-Group of 5 Location.....45
2.8 Experiment Cross Section-Group of 2 Location.....47
2.9 Two Group Raw and Normalized View Factors with Experiment Cavity Depth (22' Height) 49
2.10 Two Group Raw and Normalized View Factors with Experimental Cavity Depth (9999' Height) 49
2.11 Experiment View Factors with Riser Ducts (2.2' Height).....50
2.12 Experiment View Factors with Riser Ducts (22' Height).....50
2.13 Experiment View Factors with Riser Ducts (44' Height).....51
2.14 Flow Channel Modeling Groups.....54
2.15 Full-Scale Model Cavity and Duct Network 56
2.16 Experiment System Model Cavity and Duct Network 60
2.17 GA Results for RCCS Heat Load 61
2.18 GA Results for Vessel Temperature 62
2.19 Full Scale/Medium Flux Riser Duct Air Total Mass Flow.....65
2.20 Full Scale/Medium Flux Hot Network Air Mass Flow 66
2.21 Full Scale/Medium Flux Riser Duct Air Velocity 66
2.22 Full Scale/Medium Flux Hot Network Air Velocity 67
2.23 Full Scale/Medium Flux RPV Temperature 67
2.24 Full Scale/Medium Flux Cavity Back Liner Temperature 68
2.25 Full Scale/Medium Flux Riser Duct Temperature.....69
2.26 Half Scale/Medium Flux Riser Duct Air Total Mass Flow 73
2.27 Half Scale/Medium Flux Riser Duct Air Velocity 73
2.28 Half Scale/Medium Flux RPV Temperature.....74
2.29 Half Scale/Medium Flux Cavity Back Liner Temperature.....74
2.30 Half Scale/Medium Flux Air System Temperature Profile 75
2.31 Experiment/Medium Flux (4") Chimney Air Total Mass Flow 78
2.32 Experiment/Medium Flux (4") Riser Duct Air Flow.....79
2.33 Experiment/Medium Flux (4") Inner Riser Duct Temperatures.....80
2.34 Experiment/Medium Flux (4") Outer Riser Duct Temperatures 81
2.35 Experiment/Medium Flux (4") RPV Temperature 82
2.36 Experiment/Medium Flux (4") Back Liner Temperature 82
2.37 Experiment/medium Flux (4") Chimney Air Temperatures.....83
2.38 Experiment/Medium Flux (45") Chimney Air Total Mass Flow 87

2.39 Experiment/Medium Flux (45”) Riser Duct Air Flow....88
2.40 Experiment/Medium Flux (45”) Inner Riser Duct Temperatures....89
2.41 Experiment/Medium Flux (45”) Outer Riser Duct Temperatures....90
2.42 Experiment/Medium Flux (45”) RPV Temperature....91
2.43 Experiment/Medium Flux (45”) Back Liner Temperature....91
2.44 Experiment/Medium Flux (45”) Chimney Air Temperatures....92
3.1 Complete RCCS Model....97
3.2 Full RCCS Side Cut Away View....98
3.3 Vertical Dimensions of Cross-Cut Symmetric Half of RCCS (inches)....99
3.4 Vertical Dimensions of Face-On Symmetric Half of RCCS (inches)....100
3.5 Riser Dimension (inches)....101
3.6 Downcomer Dimensions (inches)....101
3.7 Riser and Downcomer Cross-Section Drawing Showing Plenum and Co-axial Duct Location....102
3.8 Upper Hot Plenum Dimensions (inches)....102
3.9 Upper Cold Plenum Dimensions (inches)....103
3.10 Lower Cold Plenum Dimensions (inches)....103
3.11 Detail View Showing Intersection of Lower Cold Plenum with Downcomer and Riser....104
3.12 Co-axial Duct Dimensions (inches)....104
3.13 Co-axial Header Dimensions (inches)....105
3.14 Inlet and Outlet Manifold Dimensions (inches)....105
3.15 Chimney Dimensions (inches)....106
3.16 Mesh Representation of Plane at Center of Risers....108
3.17 Temperature Profile in Risers....108
3.18 Velocity Profile in Risers....109
3.19 Temperature Distribution in RCCS Risers....110
3.20 Temperature Distribution in RCCS Upper System Components....110
3.21 Temperature Distribution in Hot Plenum....111
3.22 Temperature Distribution in Hot Duct from Hot Plenum to Hot Header....111
3.23 Temperature Distribution in Vertical Hot Header from Hot Duct to Outlet Manifold....112
3.24 Velocity Vector Field in RCCS Upper System Components, including Hot and Cold Plena and Co-axial Ducts and Headers....112
3.25 Velocity Vector Field at Mid-plane of Cold Plenum, including Flow from Hot Plenum through Hot Ducts....113
3.26 Velocity Vector Field at Mid-plane of Hot Plenum, including Downflow in Downcomers....113
3.27 Velocity Vector Field in the Co-axial Duct from the Upper Plena to the Vertical Header....114
3.28 Velocity Vector Field in the Vertical Co-axial Header between the Co-axial Duct and the Outlet Manifold....114
3.29 Turbulent Kinetic Energy Distribution in the RCCS Upper System Components....115
3.30 Turbulent Kinetic Energy distribution at the Mid-plane of the Hot Plenum....115

3.31 Turbulent Kinetic Energy Distribution at Mid-plane of Co-axial Duct from Upper Plena to Vertical Header 116
3.32 Turbulent Kinetic Energy Distribution in Vertical Co-axial Header between Co-axial Duct and Outlet Manifold 116
3.33 Streamlines Showing the Path of Air from 5 Different RCCS Riser Tubes 117
3.34 Temperature Along Selected Streamline, which Travels through the RCCS Three Times 118
3.35 Vertical Dimension of the NSTF Air-cooled RCCS Experiment Model 119
3.36 Temperature Distribution Showing Temperature Increase in Riser Section 120
3.37 Temperature Distribution at the Top of the Risers 121
3.38 Temperature Distribution at the Mid-plane of the Horizontal Outlet Ducts 121
3.39 Temperature Distribution at the Mid-plane of the Vertical Ducts Showing the Plume Exiting the Test Section 122
3.40 Velocity Magnitude at the Mid-plane of the Lower Plenum and Inlet Nozzle 122
3.41 Velocity Magnitude in the Riser Section of the NSTF Test Section 123
3.42 Velocity Magnitude at the Top of the Heated Riser Region 123
3.43 Velocity Magnitude at the Mid-plane of the Horizontal Ducts 124
3.44 Vertical Velocity Vector Component at the Mid-plane of the Horizontal Ducts 124
3.45 Velocity Magnitude at the Mid-plane of the Vertical Ducts 125
4.1 Particles Moving Across an Interference Pattern of Light and Dark Fringes (top left) Generate Oscillating Levels of Reflected Light, “Doppler Bursts”, that are Captured by a Detector 126
4.2 The Major Components of the TSI Laser Doppler Velocimetry System 127
4.3 Active LDV Transceivers Oriented for Measurements in Lower Region of Glass Enclosure 129
4.4 Laser Beams Crossing to Form Measurement Volume 129
4.5 Maximum Data Rate for Candidate Seeding Materials 130
4.6 Normalized Count Rate for a) Propylene Glycol, b) Mineral Oil, c) Stick Incense, and d) Coil Incense, and e) Titanium Dioxide 131

List of Tables

1.1 Non-dimensional Variables 8
1.2 Scaling Ratios 18
2.1 View Factors-Group of 10 Azimuthal Distribution 33
2.2 View Areas-Group of 10 35
2.3 View Factors-Group of 1 37
2.4 View Areas-Group of 1 38
2.5 View Factors-Group of 3 40
2.6 View Areas-Group of 3 40
2.7 Vie Factors-Group of 4A 41

2.8 View Areas-Group of 4A 41
2.9 View Factors-Group of 4B 44
2.10 View Areas-Group of 4B.....44
2.11 View Factors-Group of 5.....46
2.12 View Areas-Group of 5 46
2.13 Two Group Experiment View Factors-4” Separation 51
2.14 Two Group Experiment View Areas-4” Separation.....52
2.15 Two Group Experiment View Factors-45” Separation 52
2.16 Two Group Experiment View Areas-45” Separation.....52
2.17 GA Results for Depressurized Conduction Cooldown.....62
2.18 Summary of Cases 64
2.19 Summary of Full Scale/Half Scale Case Results.....70
2.20 Summary of Experiment Scale Results 77

Nomenclature

ANL	Argonne National Laboratory
BOP	Balance-of-Plant
CAD	Computer Aided Design
CFD	Computational Fluid Dynamics
DLOFC	Depressurized Loss of Forced Cooling
HTGR	High Temperature Gas Cooled Reactor
LDV	Laser Doppler Velocimetry
NGNP	Next Generation Nuclear Plant
NSTF	Natural Convection Shutdown Heat Removal Test Facility
PBMR	Pebble Bed Modular Reactor
RANS	Reynolds Averaged Navier Stokes Equations
RCCS	Reactor Cavity Cooling System
RPV	Reactor Pressure Vessel
RVACS	Reactor Vessel Auxiliary Cooling System
VHTR	Very High Temperature Reactor
V&V	Verification and Validation

A = flow area
A_α = flow area in the annulus
A_{in} = flow area of the pipe feeding the tank
A_{out} = flow area of pipe leading out of the tank
C_p = fluid specific heat
D = hydraulic diameter
D_{Ip} = diameter of inner tube
E = enthalpy
E_r = reference enthalpy

f = friction factor
g = acceleration of gravity
H = height
h_a = heat transfer coefficient in the annulus
h_I = heat transfer coefficient in the inner tube
K = loss coefficient
k = conductivity
L = length
L_a = vertical length of the hot leg above the heated section
L_c = vertical length of the cold leg before it enters the heated section
L_h = length of heated section
P_e = perimeter of the ellipsoidal tube
δp_f = frictional pressure drop
P_I = perimeter of the inner tube
p_{in} = pressure at the top of a tank
δp_ℓ = other pressure losses
p_{out} = pressure at the top of the hot leg (exit of return line)
Δp = $p_{in} - p_{out}$
ΔP = dimensionless pressure = $\dfrac{\Delta p}{\rho_o U_r^2}$
R = radius
T_c = temperature of the cold wall
T_e = temperature of water in the annulus
T_I = temperature of water in the inner tube
T_h = reactor vessel temperature
T_{se} = temperature of the ellipsoidal tube
T_{sI} = temperature of the inner tube
T_o = reference temperature
T_{out} = water temperature at the outlet of the heated section of the RCCS
t = time
U = velocity
$u^* = \dfrac{\mu}{\rho H}$ = reference velocity in air-cavity
V = velocity component in the horizontal direction (Y)
W = velocity component in the vertical direction (Z)
X_m = jet ceiling height
x = vapor quality
Y, Z = Cartesian coordinates

Greek Symbols

α = void fraction
α^* = thermal diffusivity
β = volumetric coefficient of thermal expansion
δ = structure thickness
ε = emissivity
μ = dynamic viscosity
θ = non-dimensional temperature
θ_I = non-dimensional temperature of water in the inner tube
θ_{sI} = non-dimensional temperature of inner tube (structure)
θ_{se} = non-dimensional temperature of water in the annulus between the RCCS tubes
ρ = water density
ρ_c = water density in the cold leg before it enters the heated section
σ = Stefan-Boltzmann constant
σ_s = surface tension
τ = non-dimensional transport time
τ^* = non-dimensional conduction time

Subscripts

b = boiling
bv = boiling vertical section
c = cold
d = down
g = vapor
h = hot
I = inner
j = jet
ℓ = liquid
m = mean
o = outer
out = tank outlet
p = pipe
r = reference value
s = structure
out = tank outlet
t = tank
TP = two-phase
x = exit
w = water

Similarity Groups

$B_i = \dfrac{h\delta}{k}$, Biot number

$N_c = \dfrac{A_c h_{cav}}{A_o \rho C_p U_o}$, Cavity convective number

$N_r = \dfrac{A_{rad} \varepsilon \sigma T_o^4}{U_o A_o \rho_o C_p \left(T_r - T_o\right)}$, Cavity radiation number

$F_r = \dfrac{U_r^2}{g L_r}$, Froude number

$F_j = \dfrac{U_j^2 \rho_j}{\left(\rho_a - \rho_j\right) g D_j}$, jet densimetric Froude number

$F = \dfrac{f \ell}{d} + K$, Friction number

$N_o = K_i \left[1 + x^{3/2} \left(\Delta\rho / \rho_g\right)\right] \left(\dfrac{A_o}{A_i}\right)^2$, Orifice number

$\mathrm{Pr} = \dfrac{C_p \mu}{k}$, Prandtl number

$R\alpha = \dfrac{C_p \rho^2 g \beta \left(T_h - T_c\right) H^3}{\mu k}$, Rayleigh number

$Ri = \dfrac{g \beta \left(T_r - T_o\right) L_r}{U_r^2}$, Richardson number

$St_I = \dfrac{4 h_I L_r}{\rho C_p U_r D_{ip}}$, Stanton number (riser duct)

$N_t = \dfrac{T_r - T_o}{T_o}$, Temperature ratio number

$T^* = \dfrac{\alpha}{\delta^2} \dfrac{L_r}{U_r}$, Time Ratio number

1.0 Introduction

The Reactor Cavity Cooling System (RCCS) is a system which is important to the passive safety case being incorporated in the overall safety strategy for the NGNP. The RCCS will be one of the new safety systems specifically designed for the next generation of nuclear power plants being developed under the auspices of the DOE GENIV program. In particular, it is being developed and being incorporated into the proposed reactor and plant designs for the Very High Temperature Reactor (VHTR). The VHTR is a helium gas-cooled nuclear plant with a thermal-spectrum reactor. The RCCS forms a passive heat sink external to the reactor, and is located within the reactor cavity/silo surrounding the metal vessel. During emergency accident conditions when all a/c power is lost, natural convection of the RCCS coolant removes the heat radiated or naturally convected from the metal vessel wall to the inner boundary of the RCCS facing the vessel. This will be a First-of-A-Kind (FOAK) passive safety system for core decay heat removal when the FOAK VHTR is built.

The air-cooled version of the RCCS for the VHTR is very similar to the RVACS that has been proposed for the General Electric PRISM ALMR design. The Natural Convection Shutdown Heat Removal Test Facility (NSTF) at ANL was built to provide a full scale simulation of the air-side of the PRISM RVACS system, and to provide experimental support for the design and analysis of this system. In FY05, work was performed to demonstrate that the NSTF facility can be used to generate experimental data to validate CFD and systems codes for the analysis of an air-cooled RCCS for the VHTR and to support the design and safety analysis of this RCCS type [1.1-1.3]. More specifically, the objectives were to: (a) develop the scaling relations to be used in modifying the existing NSTF facility into a scaled model of the VHTR air-cooled RCCS; and (b) provide a summary of the NSTF modifications needed to conduct scaled simulations of the RCCS. The main conclusion of the FY05 study was that these air-cooling NSTF simulations will generate experimental data suitable for code validation and RCCS design validation and optimization. In FY05, the air-cooled RCCS design of the GA GT-MHR was used as the planning basis.

However, there exists another design option for the VHTR air-cooled RCCS and this is one which was designed for the GA-MHTGR. In FY10, the objective for the effort is to update the NSTF feasibility study conducted in FY05 but to focus on the GA-MHTGR RCCS instead of the GT-MHR RCCS. The objectives of the FY10 work are to reconfirm that the NSTF facility can be used to generate experimental data to validate CFD and systems codes for the analysis of the air-cooled RCCS for the VHTR. More specifically, the objectives are to: (a) update the scaling relations to be used in modifying the existing NSTF facility into a scaled model of the GA-MHTGR air-cooled RCCS; and (b) provide a basis for analytical NSTF modifications needed to conduct scaled experimental simulations of this RCCS. These simulations will generate experimental data for code validation and RCCS design validation and optimization.

In summary, a scaling evaluation of an air-cooled RCCS system was performed based on available information on the RCCS design of the GA-MHTGR. The evaluation

updates the basis that the air-cooled RCCS can be simulated at the ANL NSTF facility at a prototypic scale in the lateral direction and about half scale in the vertical direction. From the non-dimensional analyses it is clear that all similarity conditions cannot be satisfied. Since, by necessity, the scaling is based on a number of approximations, and because no analytical information is available on the performance of a reference air-cooled RCCS, the scaling laws presented here need to be "validated" by analysis of the steady state and transient performance of a reference air-cooled RCCS design. At this time while no specific information is available on the prototype air-cooled RCCS, some analyses with the STAR-CCM+ and RELAP5 GA-MHTGR models have been performed and provide some information on the magnitude of distortions imposed by the similarity conditions that are not satisfied. When more information becomes available, this study will be repeated with the prototype RCCS design to confirm these initial conclusions.

1.1 GA-MHTGR RCCS Design

In the GA-MHTGR design, the reactor vessel is housed in a cavity located next to the Power Conversion Unit Cavity (PCU). The overview of the entire RCCS system from the chimneys to the hot riser tubes/cold down–comers surrounding the vessel inside the cavity is shown in Figure 1.1. There are two sets of four chimneys. Each set of four chimneys is arranged in two alternating groups of a hot discharge outlet chimney and a cold inlet suction chimney side-by-side. The alternating groups share a common manifold and the two sets of four chimneys are connected in such a way that no single fault can disable the entire system. The mid-plane symmetry divides the RCCS in half, each with one set of four chimneys and the hot/cold run of ducting through the reactor building to the reactor cavity. Figure 1.2 shows the hot side metal ducting contained within the cold concrete run of the building which forms the cold channel. The bend and turn down into the reactor cavity with the reactor vessel can also be seen. Within the cavity, Figure 1.3 shows an isometric of the reactor vessel surrounded by the hot riser ducts. The upper cold plenum can be seen feeding the cold down-comers all the way to the bottom cold plenum. The cold air is turned and rises upward through the hot risers removing the reactor vessel wall heat to the upper hot plenum. The upper hot plenum can be seen surrounding the vessel upper head. A plane cross section view of the reactor cavity is show in Figure 1.4. The reactor vessel is shown surrounded by the distributed hot risers. Three reactor supports are displayed and the primary cross-vessel is also shown. The down-comer channels form the outer cavity wall.

1.2 NSTF RCCS Experiment Scaling

In summary, a scaling evaluation of an air-cooled RCCS system was performed based on available information on the RCCS design of the GA-MHTGR. Section 1.1 on the top-down scaling approach presents the non-dimensional conservation equations describing the response of the air-based RCCS during steady-state and transient operations. These equations are used to develop scaling laws that define a scaling of the NSTF that minimizes distortions between scaled experiments and prototype operation. Section 1.3 presents the bottom-up scaling approach. The focus here is on specific selected phenomena and the similarity descriptions thereof.

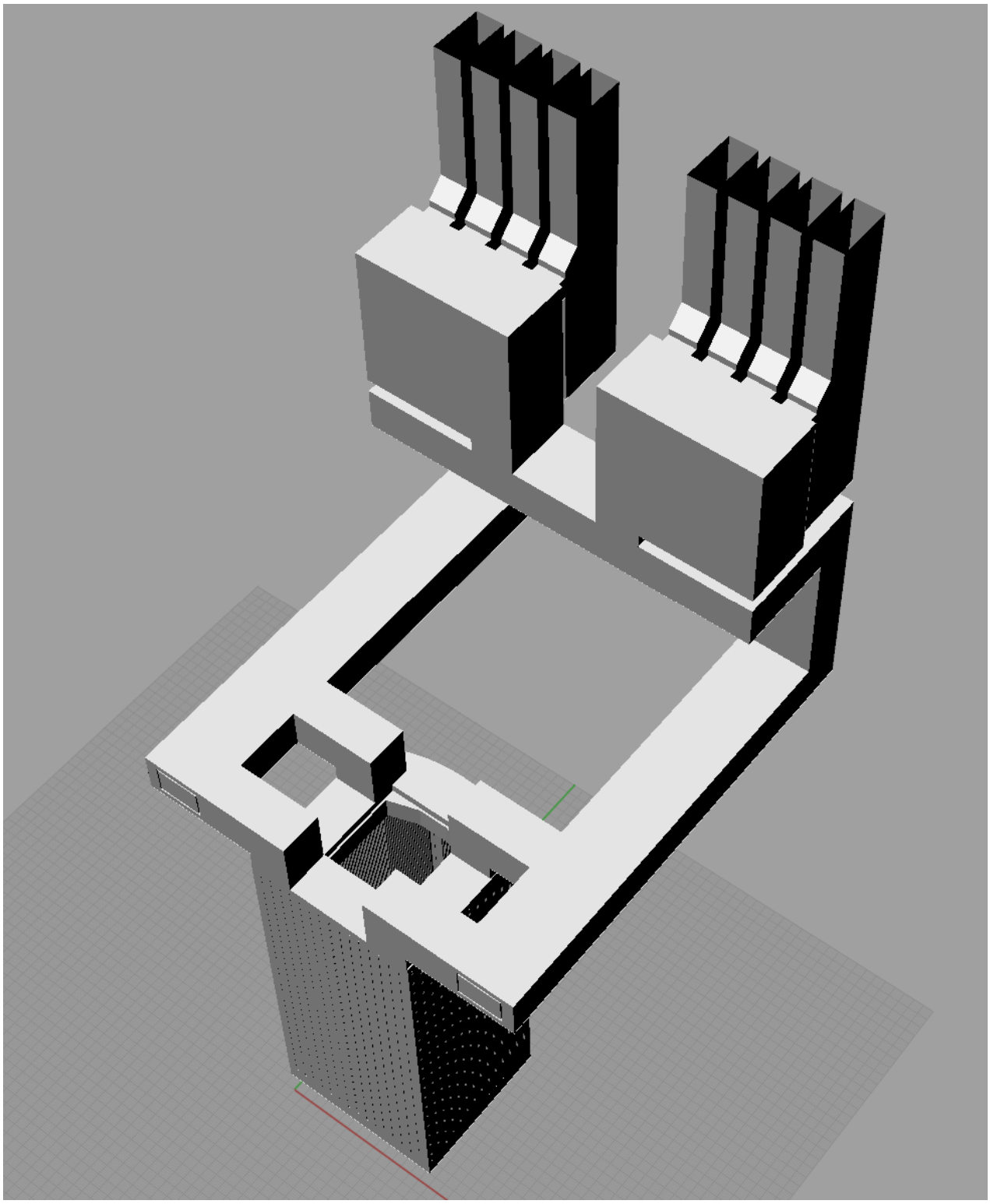

Figure 1.1. Overall System View of the GA-MHTGR RCCS

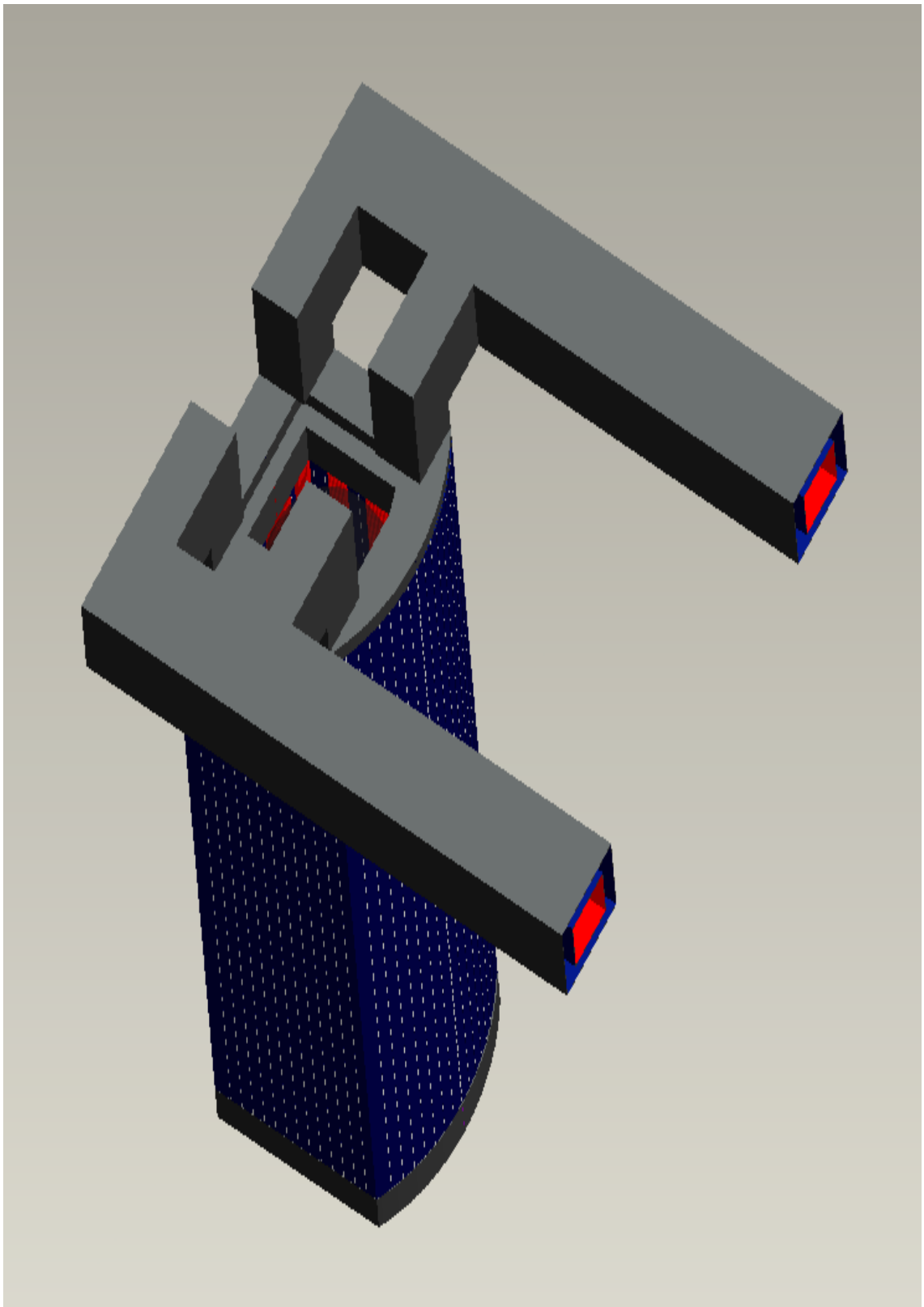

Figure 1.2 View of Ex-Cavity RCCS Outer Cold Duct/Inner Hot Duct Run

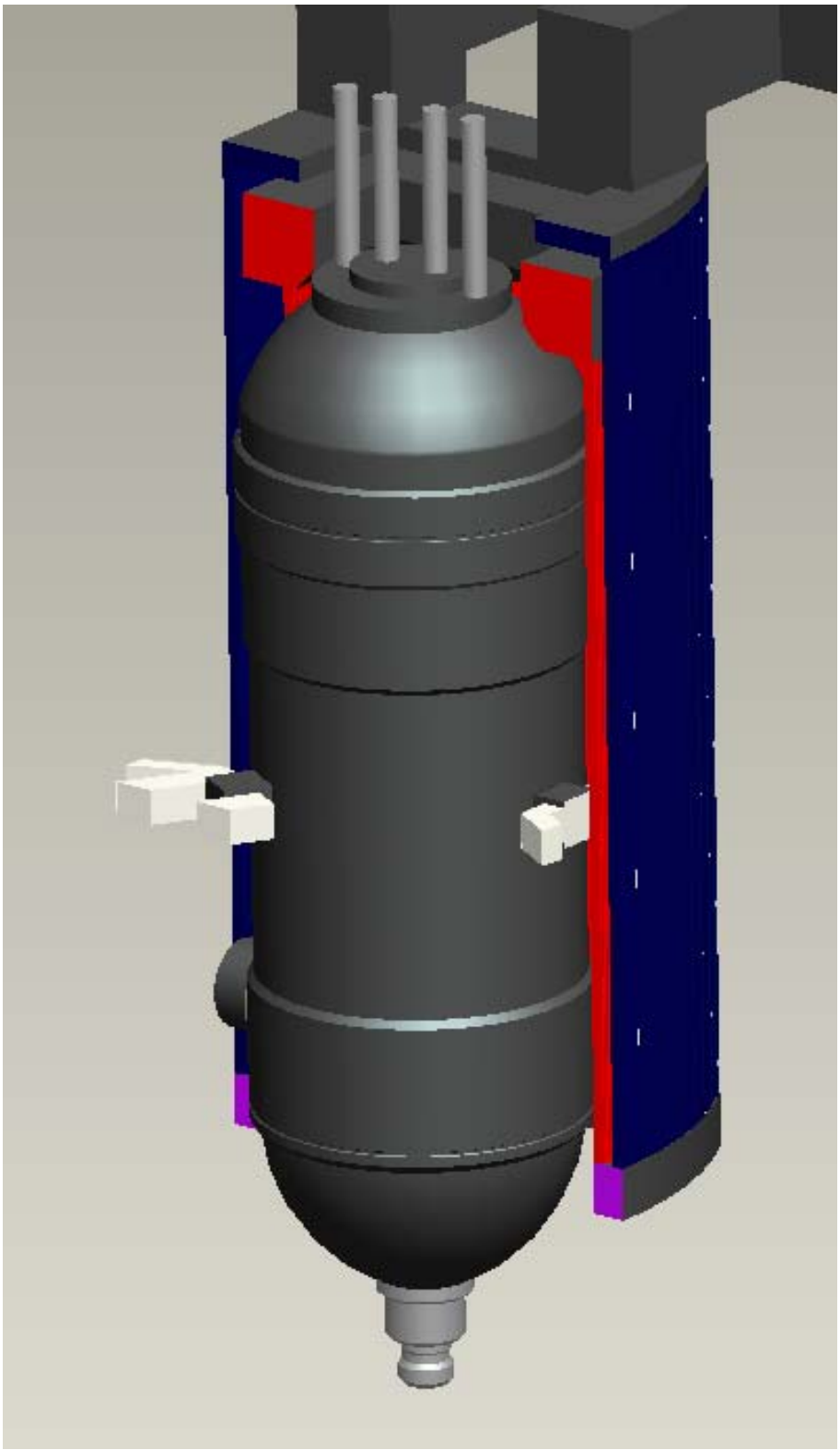

Figure 1.3. Cavity Isometric View of Reactor Vessel and RCCS

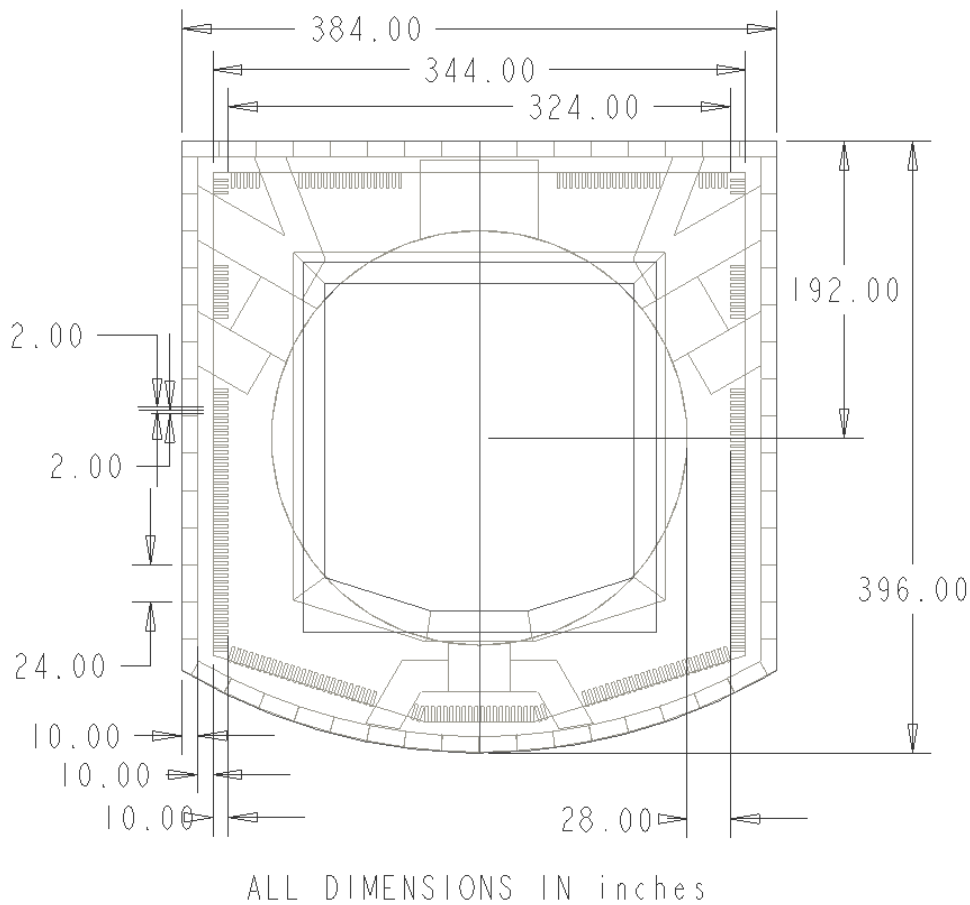

Figure 1.4. Cavity Plane View of Reactor Vessel and RCCS

1.2.1 Top-down Scaling

In this section, simplified one-dimensional conservation equations for mass, energy and momentum are presented for the RCCS loop, and these equation are properly non-dimensionalized to determine the non-dimensional groups that govern the similarity between the prototype RCCS and scaled models of the prototype. For the reactor cavity, the assumption is made that the arrangement of the RCCS riser ducts in the cavity is such that the cavity can be approximated by a simple two-dimensional rectangular cavity with vertical hot and cold walls. For the derivation of scaling ratios, the cavity is represented as a radiating wall (reactor vessel) and a convective boundary condition on the outer surface of the RCCS air riser ducts. This is work based on the scaling evaluation presented in [1.4] for the water-cooled RCCS design option.

1.2.2 Loop Steady State

The integral momentum equation in the air loop/circuit side of the RCCS can be written

$$p_{in} + \rho_c g L_a + \int_0^{L_h} \left(\rho g dL\right)_d = p_{out} + \int_0^{L_h} \left(\rho g dL\right)_u + \rho_h g L_a + \delta p_f + \delta p_\ell \tag{1}$$

The integral on the left side of Eq. (1) is the gravitational head of the cold leg in the heated section, and the integral on the right side is the gravitational head of the hot leg in the same section. The frictional pressure drop in the i th section is

$$\delta p_{f,i} = \frac{1}{2D_i} f_i \rho_l U_i^2 L_i \tag{2}$$

The form pressure losses in the i th section of the loop are

$$\delta p_{\ell,i} = \frac{1}{2} K_i \rho_i U_i^2 \tag{3}$$

where K_i is the pressure loss coefficient in the i th section.

In the sections where the density varies with the temperature, the Boussinesq approximation gives

$$\rho = \rho_o \left[1 - \beta\left(T - T_o\right)\right] \tag{4}$$

where

ρ_o = reference density
β = volumetric coefficient of thermal expansion
T_o = reference temperature

The conservation equations describing the RCCS system are non-dimensionalized using non-dimensional variables as summarized in Table 1.1. A non-dimensional temperature θ is defined in terms of a characteristic temperature rise, $T_r - T_o$, as

$$\theta = \frac{T - T_o}{T_r - T_o} \tag{5}$$

Then, Eq. (4) gives

$$\rho = \rho_o - \rho_o \beta \theta \left(T_r - T_o\right) \tag{6}$$

For $p_{in} = p_{out}$, substitution of Eqs. (6), (2) and (3) into Eq. (1) yields.

Table 1.1 Non-dimensional Variables

z = Z/H	Vertical Distance
y = Y/H	Horizontal Distance
$\ell = L / L_r$	Length
$d = D / L_r$	Diameter
$u = U / U$	Velocity (1-D Flow)
$\Delta P = \Delta p \big/ \left(\rho U_r^2\right)$	Pressure Drop
$V = V / u^*$	Horizontal Velocity in Cavity
$W = W / u^*$	Vertical Velocity in Cavity
$\theta = \left(T - T_o\right) \big/ \left(T_r - T_o\right)$	Temperature
$\tau = U_r t / L_r$	Transport Time
$\tau^* = t\alpha^* / \delta^2$	Conduction Time
$\rho_\ell^* = \rho_\ell / \rho$	Fluid Density

$$-\rho_o g\beta\left(T_r - T_o\right)\theta_c L_a - \rho_o g\beta\left(T_r - T_o\right)\int_0^{L_h}\left(\theta dL\right)_d$$
$$= -\rho_o g\beta\left(T_r - T_o\right)\int_0^{L_h}\left(\theta dL\right)_u - \rho_o g\beta\left(T_r - T_o\right)\theta_a L_a + \frac{1}{2}\sum_i \frac{f_i \rho_i U_i^2 L_i}{D_i} + \frac{1}{2}\sum_i K_i \rho_i U_i^2 \qquad (7)$$

Using a characteristic velocity U_r and a characteristic length L_r, and noting that the Richardson number Ri is

$$Ri = \frac{g\beta\left(T_r - T_o\right)L_r}{U_r^2} \qquad (8)$$

then division of Eq. (7) by $\rho_0 U_r^2$ gives

$$Ri\left[-\int_0^{\ell_h}\left(\theta d\ell\right)_d + \int_0^{\ell_h}\left(\theta d\ell\right)_u + \ell_a\left(\theta_a - \theta_c\right)\right] - \frac{1}{2\rho_0}\left[\sum_i \frac{f_i \rho_i u_i^2 \ell_i}{d_i} + \sum_i K_i \rho_i u_i^2\right] = 0.0 \qquad (9)$$

where

$$\ell_a = \frac{L_a}{L_r}, \quad d_i = \frac{D_i}{L_r}, \quad u_i = \frac{U_i}{U_r}$$

The continuity equation at the i th section of the loop can be written as

$$U_i A_i = A_o U_o$$

where A_0 is a reference flow area and U_o is the velocity at this flow area. The non-dimensional continuity equation is

$$u_i = \frac{A_o}{A_i} u_o$$

and Eq. (9) becomes

$$Ri\left[\ell_a\left(\theta_a - \theta_c\right) - \int_0^{\ell_h}\left(\theta d\ell\right)_d + \int_0^{\ell_h}\left(\theta d\ell\right)_u\right] - \frac{u_o^2}{2}\left[\sum_i\left(\frac{f_i \ell_i}{d_i} + K_i\right)\left(\frac{A_o}{A_i}\right)^2\right] = 0.0 \qquad (10)$$

The energy equation for the fluid in the air riser duct is

$$\frac{\pi}{4} D_{Ip}^2 U \rho C_p \frac{\partial T_I}{\partial Z} = \pi D_{Ip} h_I \left(T_{sI} - T_I\right)$$

or

$$U \rho C_p \frac{\partial T_i}{\partial Z} = \frac{4h_I}{D_{Ip}}\left(T_{sI} - T_I\right) \qquad (11)$$

For

$$U = U_r u, \quad Z = L_r z, \quad u = u_o \frac{A_o}{A}$$

the non-dimensional energy equation is

$$u_o \frac{A_o}{A}\frac{\partial \theta_I}{\partial z} = \frac{4h_I L_r}{\rho C_p U_r D_{Ip}}\left(\theta_{sI} - \theta_I\right)$$

or

$$u_o \frac{A_o}{A}\frac{\partial \theta_I}{\partial z} = St_I\left(\theta_{sI} - \theta_I\right) \qquad (12)$$

and

$$St_I = \frac{4h_I L_r}{\rho C_p U_r D_{Ip}} \qquad (13)$$

is the modified Stanton number for the riser duct.

1.2.3 Loop Transient

In the event that the RCCS has to change operating point in the natural circulation mode, the system will operate in a transient mode for a length of time. In this section, analytical equations are presented for system operation in the transient mode of operation.

The integrated momentum equation in the i th section, where the flow is incompressible, is

$$\rho \frac{dU_i}{dt} L_i = \Delta p_i - g \int_0^{L_i} \rho dL - \frac{1}{2D_i} f_i \rho_i U_i^2 L_i \tag{14}$$

With the Boussinesq approximation in the gravitational term, the above equation gives

$$\rho \frac{dU_i L_i}{dt} = \Delta p_i - g \rho_o L_i + \rho_0 g \beta \left(T_r - T_o \right) \int_0^{L_i} \theta dL - \frac{1}{2D_i} \rho f_i U_i^2 L_i \tag{15}$$

For a non-dimensional time τ defined as

$$\tau = \frac{U_r t}{L_r} \tag{16}$$

Eq. (15) is written as

$$\rho U_r^2 l_i \frac{du_i}{d\tau} = \Delta p_i - g \rho_0 \ell_i L_r + \rho_0 g \beta \left(T_r - T_o \right) L_r \int_0^{l_i} \theta dL - \frac{1}{2} \frac{\rho}{D_i} f_i U_r^2 u_i^2 L_i$$

and for $\rho \approx \rho_0$

$$l_i \frac{du_i}{d\tau} = \Delta P_i - \frac{g L_r}{U_r^2} \ell_i + Ri \int_0^{\ell_i} \theta dl - \frac{1}{2} \frac{f_i u_i^2 L_i}{D_i} \tag{17}$$

From the non-dimensional continuity equation

$$u_i = \frac{A_0}{A_i} u_0$$

the integral momentum equation in the i th section becomes

$$\ell_i \frac{A_0}{A_i}\frac{du_0}{d\tau} = \Delta P_i - \frac{gL_r}{U_r^2}\ell_i + Ri\int_0^{\ell_i}\theta d\ell - \frac{u_0^2 f_i L_i}{2D_i}\left(\frac{A_0}{A_i}\right)^2 \tag{18}$$

Summation of the above integral momentum equation over all the sections of the loop where the fluid is incompressible (liquid water), and accounting of the other pressure losses (expansions, contractions, bends) gives the overall integral momentum equation as

$$\frac{du_0}{d\tau}\sum_i \ell_i \frac{A_0}{A_i} = R_i \sum_i \int_0^{\ell_i}\theta d\ell - \frac{u_0^2}{2}\sum_i\left(\frac{f_i L_i}{D_i} + K_i\right)\left(\frac{A_0}{A_i}\right)^2 \tag{19}$$

The energy equation for the fluid in the riser duct is

$$\frac{\pi}{4}D_{Ip}^2 \rho C_p \frac{\partial T_I}{\partial t} + \frac{\pi}{4}D_{Ip}^2 \rho U C_p \frac{\partial T_I}{\partial Z} = \pi D_{Ip} h_I \left(T_{sI} - T_I\right) \tag{20}$$

The non-dimensional form of this equation is

$$\frac{\partial \theta_I}{\partial \tau} + u_o \frac{A_o}{A}\frac{\partial \theta_I}{\partial z} = \frac{4h_I L_r}{\rho C_p U_r D_{Ip}}\left(\theta_{sI} - \theta_I\right)$$

or

$$\frac{\partial \theta_I}{\partial \tau} + u_o \frac{A_o}{A}\frac{\partial \theta_I}{\partial z} = St_I\left(\theta_{sI} - \theta_I\right) \tag{21}$$

The energy equation for the solid structure in the i th section is

$$\frac{\partial T_s}{\partial t} = \frac{k}{\rho C_p}\frac{\partial^2 T_s}{\partial Z^2} = \alpha_i^* \frac{\partial^2 T_s}{\partial Z^2} \tag{22}$$

For

$$\tau^* = t\frac{\alpha^*}{\delta_i^2} \tag{23}$$

Equation (22) gives

$$\frac{\alpha_i^*}{\delta_i^2}\left(T_r - T_0\right)\frac{\partial \theta_s}{\partial \tau^*} = \alpha_i^* \frac{T_r - T_0}{L_r^2}\frac{\partial^2 \theta_s}{\partial z^2}$$

or

$$\frac{\partial \theta_s}{\partial \tau *} = \frac{\delta_i^2}{L_r^2} \frac{\partial^2 \theta}{\partial z^2} \tag{24}$$

For

$$\tau = t \frac{U_r}{L_r}$$

Equation (23) gives

$$\tau * = \tau \frac{L_r}{U_r} \frac{\alpha_i^*}{\delta_i^2}$$

and Eq. (24) becomes

$$\frac{\partial \theta_s}{\partial \tau} = \left(\frac{\alpha_i^*}{\delta_i^2} \frac{L_r}{U_r} \right) \frac{\delta_i^2}{L_r^2} \frac{\partial^2 \theta_s}{\partial z^2} \tag{25}$$

For the inner and outer pipes of the RCCS, Eq. (25) is written, respectively, as

$$\frac{\partial \theta_{sI}}{\partial \tau} = \left(\frac{\alpha_I^*}{\delta_I^2} \frac{L_r}{U_r} \right) \frac{\delta_I^2}{L_r^2} \frac{\partial^2 \theta_{sI}}{\partial z^2} \tag{26}$$

The boundary conditions between the solid and fluid in the ducts of the RCCS are

$$\left. \frac{\partial \theta_{sI}}{\partial r} \right/_{r_1} = \frac{h_I \delta_I}{k_{s,I}} \left(\theta_{sI,I} - \theta_I \right) \tag{27}$$

Where $r = R/\delta$ (non-dimensional radius).

Taking into consideration the radiative heat transfer from the reactor vessel to the outer wall of the riser duct, the boundary condition at the outer surface of the duct can be written as

$$A_k k_{se} \frac{\partial T_{se}}{\partial R} = A_c h_c \left(T_h - T_{se,o} \right) + A_r \varepsilon \sigma \left(T_h^4 - T_{se,o}^4 \right)$$

or

$$\frac{\partial \theta_{se}}{\partial r} = \frac{A_c h_c \delta_e}{A_k k_{se}} \left(\theta_h - \theta_{se,o} \right) + \frac{\delta_e A_r \varepsilon \sigma T_0^4}{A_k k_{se} \left(T_r - T_o \right)} \left\{ \left[\theta_h \left(\frac{T_r}{T_0} - 1 \right) + 1 \right]^4 - \left[\theta_{se,o} \left(\frac{T_r}{T_0} - 1 \right) + 1 \right]^4 \right\} \quad (28)$$

Where A_k, A_c and A_r are equivalent areas, and $T_{se,o}$ is the temperature of the outer surface of the riser duct.

1.2.4 Cavity Steady State

In a rectangular two-dimensional cavity with one vertical wall heated, the other vertical wall cooled, and the two horizontal walls insulated, the conservation equations for mass, momentum and energy can be written as:

$$\frac{\partial W}{\partial Z} + \frac{\partial V}{\partial Y} = 0 \quad (29)$$

$$\rho \left(W \frac{\partial W}{\partial Z} + V \frac{\partial W}{\partial Y} \right) = -\frac{\partial P}{\partial Z} - \bar{\rho}_o g \left[1 - \beta \left(T - \bar{T}_o \right) \right] + \mu \left(\frac{\partial^2 W}{\partial Z^2} + \frac{\partial^2 W}{\partial Y^2} \right) \quad (30)$$

$$\rho \left(W \frac{\partial V}{\partial Z} + V \frac{\partial V}{\partial Y} \right) = -\frac{\partial P}{\partial Y} + \mu \left(\frac{\partial^2 V}{\partial Z^2} + \frac{\partial^2 V}{\partial Y^2} \right) \quad (31)$$

$$\rho C_p \left(W \frac{\partial T}{\partial Z} + V \frac{\partial T}{\partial Y} \right) = k \left(\frac{\partial^2 T}{\partial Z^2} + \frac{\partial^2 T}{\partial Y^2} \right) \quad (32)$$

where

P = pressure
W = velocity component in the vertical direction (Z)
V = velocity component in the horizontal direction (Y)
$\bar{\rho}$ = density at the reference temperature $\bar{T}$

and the Boussinesq approximation for the temperature dependence of density has been used in the buoyancy term of Eq. (30).

For

$$z = \frac{Z}{H}, \qquad y = \frac{Y}{H} \quad (33a)$$

$$w = \frac{W}{u*}, \quad v = \frac{V}{u*}, \quad u* = \frac{\mu}{\rho H} \tag{33b}$$

$$p = \frac{P + \rho_o g Z}{\rho u*^2}, \quad \theta = \frac{T - \overline{T}_0}{T_h - T_c} \tag{33c}$$

Eqs. (29) to (32) become

$$\frac{\partial w}{\partial z} + \frac{\partial v}{\partial y} = 0 \tag{34}$$

$$w\frac{\partial w}{\partial z} + v\frac{\partial w}{\partial y} = -\frac{\partial p}{\partial z} + \frac{R\alpha}{\Pr}\theta + \frac{\partial^2 w}{\partial z^2} + \frac{\partial^2 v}{\partial y^2} \tag{35}$$

$$w\frac{\partial v}{\partial z} + v\frac{\partial v}{\partial y} = -\frac{\partial p}{\partial y} + \frac{\partial^2 v}{\partial z^2} + \frac{\partial^2 v}{\partial y^2} \tag{36}$$

$$w\frac{\partial \theta}{\partial z} + v\frac{\partial \theta}{\partial y} = \frac{1}{\Pr}\left(\frac{\partial^2 \theta}{\partial z^2} + \frac{\partial^2 \theta}{\partial y^2}\right) \tag{37}$$

where

$R\alpha$ = $\dfrac{C_p \rho^2 g \beta (T_h - T_c) H^3}{\mu k}$ = Rayleigh number

$\Pr$ = $\dfrac{C_p \mu}{k}$ = Prandtl number

T_h = temperature of the hot wall

T_c = temperature of the cold wall

$\overline{T}$ = $0.5\ (T_h + T_c)$

The heat, $Q(t)$, transferred from the reactor vessel to the RCCS at time t can be roughly approximated by

$$Q(t) = A_c h_{cav}\left(T_h - T_{se,o}\right) + A_{rad}\varepsilon\sigma\left(T_h^4 - T_{se,o}^4\right) \tag{38}$$

where: A_c and A_{rad} are equivalent areas of heat transfer by convection and radiation; h_{cav} is the heat transfer coefficient for heat transfer in the reactor cavity by convection; and T_h is an average temperature of the reactor vessel. At steady state

$$Q(o) = A_o U_o \rho_o C_p \left(T_r - T_o\right)$$

where T_r and T_o are the inlet and outlet temperatures at the heated section of the RCCS. Equation (38) can be non-dimensionalized as

$$\frac{Q(o) f(t)}{U_o A_o \rho_o C_p \left(T_r - T_o\right)} = f(t) = \frac{A_c h_{cav}}{A_o \rho_o C_p U_o}\left(\theta_h - \theta_{se,o}\right) + \frac{A_{rad} \varepsilon \sigma T_o^4}{U_o A_o \rho_o C_p \left(T_r - T_o\right)}$$

$$\left\{\left[\theta_h\left(\frac{T_r}{T_o} - 1\right) + 1\right]^4 - \left[\theta_{se,o}\left(\frac{T_r}{T_o} - 1\right) + 1\right]^4\right\} \tag{39}$$

where $Q(t)$ has been written as

$$Q(t) = Q(o) f(t) \tag{40}$$

Equation (39) introduces the non-dimensional groups

$$\frac{A_c h_{cav}}{A_o \rho C_p U_o}, \ \frac{A_{rad} \varepsilon \sigma T_o^4}{U_o A_o \rho_o C_p \left(T_r - T_o\right)}, \text{ and } \frac{T_r - T_o}{T_o} \tag{41}$$

which are here denoted as the "cavity convective number", Nc, the "cavity radiation" number, Nr, and the "temperature ratio" number, Nt, respectively.

1.3 Top-Down Scaling Laws

In this section, the non dimensional groups derived in the previous sections are used to determine approximate similarity relations between the prototype and its simulation at NSTF. For the scaled NSTF model of the RCCS to be similar to the prototype RCCS, the ratio of the value of a similarity group at NSTF conditions to the value of the same group at prototype conditions must be equal to one. In the analysis that follows, the subscript R denotes the ratio of the value of a parameter in the model to the value of the same parameter in the prototype. Thus

$$\psi_R = \frac{\psi(model)}{\psi(prototype)} = \frac{\psi_m}{\psi_p} \tag{42}$$

At NSTF the same materials will be used as in the prototype. Therefore, $\psi_R = 1.0$ for any material property ψ (strictly only at the same temperature).

1.3.1 Baseline Scaling

After the geometric similarity condition is decided, the similarity condition for the friction number

$$\left[\sum_i F_i\left(\frac{A_o}{A_i}\right)^2\right]_R = \left[\sum_i\left(\frac{f_i L_i}{D_i}+K_i\right)\left(\frac{A_o}{A_i}\right)^2\right]_R = 1.0 \tag{43}$$

can be easily satisfied by using appropriate orifices.

Taking the heated section as the reference section, at steady state conditions, the temperature rise, ΔT_o, along the heated section is

$$\Delta T_o = \frac{\dot{Q}}{U_o A_o \rho_o C_p} = T_r - T_o \tag{44}$$

Where T_r and T_o are the temperatures at the inlet and exit of the heated section. From the above definition of the reference section

$$L_r = L_h \quad , \; U_r = U_o$$

Insertion of the above expression for ΔT_o into the steady state integral momentum equation gives

$$U_o = \left\{\frac{g\beta\dot{Q}}{A_o\rho_o C_\rho}\left[\frac{L_c + \frac{1}{2}L_h}{\frac{1}{2}\sum_i \frac{f_i L_i}{D_i}\left(\frac{A_o}{A_i}\right)^2 + \frac{1}{2}\sum_i K_i\left(\frac{A_o}{A_i}\right)^2}\right]\right\}^{1/3} \tag{45}$$

If

$$\left[\sum_i F_i\left(\frac{A_O}{A_i}\right)^2\right]_R = 1.0$$

then

$$U_{OR} = \left\{\frac{\dot{Q}_R}{A_{OR}}\left(L_c + \tfrac{1}{2}L_h\right)_R\right\}^{1/3} \tag{46}$$

From Eq. (44)

$$\Delta T_{oR} = \frac{\dot{Q}_R}{U_{oR} A_{oR}} \tag{47}$$

and the Richardson number ratio becomes

$$Ri_R = \frac{\dot{Q}_R L_{hR}}{U_{oR}^3 A_{oR}} \tag{48}$$

Use of Eq. (46) gives

$$Ri_R = \frac{L_{hR}}{\left(L_c + \frac{1}{2} L_h\right)_R} \tag{49}$$

From the geometric similarity (same in all directions)

$$\ell_R = L_{hR} = L_{cR}$$

and the similarity condition from the Richardson number gives

$$Ri_R = \frac{\ell_R}{\ell_R} = 1$$

Thus, with the U_o and ΔT_o scaling given by Eqs. (46) and (47) the similarity requirement $Ri_R = 1$ is automatically satisfied. This setting of the Richardson number plus other choices gives the scaling laws in Table 2.

Table 1.2 gives the different scaling ratios as a function of the height scaling ratio ℓ_R and their numerical values for $\ell_R = 0.5$. The scaling ratio T_{oR} and the geometric scaling ratios in the lateral direction (D_R, A_{oR}, δ_{iR}, δ_{yR}) have also been set equal to one.

The driver of the table is

$$q''_R = \frac{1}{\sqrt{\ell_R}}$$

From Eq. (54)

$$q''_r = \frac{\dot{Q}_R}{\delta_{yR} \ell_R}$$

Table 1.2 Scaling Ratios

Scaling Ratios	**Values for** $\ell_R = 0.5$
$(N_{Fr})_R = 1$	1
$\delta_{iR} = 1$	1
$U_{oR} = \sqrt{\ell_R}$	0.707
$T_R^* = \sqrt{\ell_R}$	0.707
$(Ri)_R = 1$	1
$\Delta T_{oR} = 1$	1
$T_{oR} = 1$	1
$D_R = \delta_{yR} = 1$	1
$A_{oR} = 1$	1
$q_R'' = \ell_R^{-0.5}$	1.414
$(Nd)_R = \ell_R^{-0.5}$	1.414
$(\mathrm{Re})_R = \sqrt{\ell_R}$	0.707
$h_R = \ell_R^{0.4}$	0.758
$St_R = \ell_R^{0.9}$	0.536
$(Nr)_R = \sqrt{\ell_R}$	0.707
$(Nt)_R = 1$	1
$(Bi)_R = h_R = \ell_R^{0.4}$	0.758

and for δ_{yR} = 1.0, this gives

$$\dot{Q}_R = \sqrt{\ell_R}$$

For A_{oR} = 1.0, Eq. (44) gives

$$\Delta T_{oR} = \frac{\dot{Q}_R}{U_{oR}\, A_{oR}} = 1$$

Since $U_{oR} = \sqrt{\ell_R}$ from $Ri_R = 1.0$ in Eq. (48),

It is interesting to note that the similarity condition for the Froude number also requires

$$U_{oR} = \sqrt{\ell_R} \tag{50}$$

For $\delta_{iR} = 1$ and $U_{oR} = \sqrt{\ell_R}$, the similarity condition for the time number gives

$$T_R^* = \frac{\ell_R}{U_{oR}} = \sqrt{\ell_R} \tag{51}$$

The above equation indicates that in a reduced-height model, the time-scale of the events is shortened. This summarizes the base-line scaling laws which will be used in the scaling of the NSTF experiments. A number of the implications of the scaling selections made are discussed in the following section.

1.3.2 Time Number Scaling

Time number, T^*, similarity requires

$$T_R^* = \frac{L_{hR}}{U_{oR}\delta_{i\,R}^2} = 1$$

For $\delta_{iR} = \ell_R$, the above equation gives

$$U_{oR}\ell_R = 1, \text{ or } U_{oR} = \frac{1}{\ell_R} \tag{52}$$

Then, from the Richardson number

$$\frac{\Delta T_{oR}\ell_R}{U_{oR}^2} = 1$$

and

$$\Delta T_{oR} = \frac{U_{oR}^2}{\ell_R} = \frac{1}{\ell_R^3} \tag{53}$$

$$\Delta T_{o,m} = \frac{\Delta T_{o,p}}{\ell_R^3}$$

If $\ell_R = 0.5$, then

$$\Delta T_{oR} = 8, \text{ and } \Delta T_{o,m} = 8\Delta T_{o,p}$$

Similarly, from Eq. (44) and from $A_{oR} = \ell_R^2$

$$\dot{Q}_R = \frac{1}{\ell_R^2} = 4$$

and

$$\dot{Q}_m = 4Q_p$$

The power $\dot{Q}$ transferred from the reactor vessel to the RCCS is

$$\dot{Q} = q^{''}\delta_y L_{Rv} \tag{54}$$

where δ_y is the width of the RCCS cell (section) simulated at NSTF and L_{Rv} is the height of the reactor vessel.

Then,

$$\dot{Q}_R = q_R^{''}\delta y_R \ell_R = q_R^{''}\ell_R^2$$

And from Eq. (54)

$$q_R^{''} = \frac{1}{\ell_R^4} \tag{55}$$

For $\ell_R = 1/2$

$$q_m^{''} = 16 q_p^{''} \tag{56}$$

Equation (56) imposes an excessive requirement on the model (NSTF) heat flux. To overcome this difficulty, the similarity requirements need to be relaxed.

1.3.3 Alternate Time Number Scaling

If $\delta_{iR} = 1$ (similarity requirement for thickness is relaxed), the time ratio T_R^* becomes

$$T_R^* = \frac{L_{hR}}{U_{oR}}$$

For a real time simulation $T_R^* = 1$, and

$$U_{oR} = L_{hR} = \ell_R \tag{57}$$

Then, from $Ri_R = 1$,

$$\frac{\Delta T_{oR}\ell_R}{U_{oR}^2} = \frac{\Delta T_{oR}\ell_R}{\ell_R^2} = \frac{\Delta T_{oR}}{\ell_R} = 1$$

or

$$\Delta T_{oR} = L_{hR} = \ell_R \tag{58}$$

and from the steady state energy balance Eq. (44)

$$\dot{Q}_R = \ell_R^2 A_{oR}$$

The power $\dot{Q}$ transferred from the reactor vessel to the RCCS is

$$\dot{Q} = q'' \delta y L_{Rv}$$

and

$$\ell_R^2 A_{oR} = q_R'' \delta y_R \ell_R$$

For $D_R = \delta y_R$

$$q_R'' = \ell_R D_R \tag{59}$$

1.3.4 <u>Stanton Number Scaling</u>

The similarity requirement imposed by the Stanton number is

$$St_R = \frac{h_R \ell_R}{U_{oR} D_R} = 1.0$$

where h_R is the ratio of the heat transfer coefficient.

For $U_{oR} = \ell_R$ from (Eq. (57) we have

$$St_R = \frac{h_R}{D_R} = 1.0$$

or

$$h_R = D_R$$

If the flow is turbulent and the heat transfer coefficient is given by a relation of the form (Dittus-Boelter correlation)

$$Nu = 0.023\,\mathrm{Re}^{0.8}\,\mathrm{Pr}^{0.4} = \frac{hD}{k}$$

Then

$$h_R = \frac{\left(U_{oR} D_R\right)^{0.8}}{D_R} = \ell_R^{0.8} D_R^{-0.2}$$

For $h_R = D_R$, the above relation gives

$$D_R^{1.2} = \ell_R^{0.8} \tag{60}$$

For $\ell_R = 0.5$, the above relation gives $D_R = 0.630$, or $D_R \approx \ell_R$. For $D_R = \ell_R$,

$$\mathrm{Re}_R = U_R D_R = \ell_R^2$$

and for $\ell_R = 0.5$, the Re ratio becomes $\mathrm{Re}_R = 0.25$. This means that it needs to be assured that the flow in the scaled model remains turbulent.

The cavity radiation number, Nr, gives

$$Nr_R = \frac{\ell_R \delta y_R T_{oR}^4}{\ell_R D_R^2 \ell_R} = \frac{T_{oR}^4}{D_R \ell_R} = 1$$

For $D_R = \ell_R = 1/2$

$$T_{oR}^4 = \ell_R^2$$

or

$$T_{oR} = \sqrt{\ell_R} = 0.707$$

From

$$\Delta T_{oR} = T_{oR}\left(\frac{T_r}{T_o} - 1\right)_R = \ell_R$$

The temperature ratio number gives

$$Nt_R = 0.707$$

versus $Nt_R = 1$ that the similarity condition requires.

The cavity convective number, Nc, gives

$$Nc_R = \frac{\ell_R \delta y_R h_{cavR}}{D_R^2 \ell_R} = \frac{h_{cavR}}{D_R}$$

or

$$h_{cavR} = Nc_R D_R = D_R$$

If the heat transfer coefficient in the cavity is given from [5]

$$Nu = 0.046 R\alpha^{1/3}$$

then

$$h_{cavR} \ell_R = \left[\left(T_h - T_c \right)_R \ell_R^3 \right]^{1/3}$$

and

$$h_{cavR} = \left(T_h - T_c \right)_R^{1/3}$$

Some analysis is needed to evaluate how close the above value is to

$$h_{cavR} = Nc_R D_R = D_R$$

If scaling in the lateral direction is modified and D_R is set equal to one, i.e.,

$$D_R = \delta_{iR} = \delta_{yR} = 1.0$$

then the process described above gives

$$q''_R = \ell_R$$
$$St_R = h_R = 1.0$$

but $h_R = \ell_R^{0.8}$ from the heat transfer correlation (Dittus-Boelter), and for $\ell_R = 0.5$: $h_R = 0.57$, and $\mathrm{Re}_R = 0.5$. From $Nc_R = 1$, we get $T_{oR} = \ell_R^{1/4}$, and $Nt_R = \ell_R^{3/4}$, or $T_{oR} = 0.84$, and $Nt_R = 0.59$ (for $\ell_R = 0.5$) . The similarity condition for the cavity convective number requires $Nc_R = h_{cavR} = 1.0$, but the heat transfer correlation in the cavity gives

$$h_{cavR} = \left(T_h - T_c \right)_R^{1/3}$$

The similarity conditions imposed by the boundary conditions between the solid and the fluid in the pipes requires

$$Bi_R = h_R \delta_{iR} = 1.0$$

or $h_R = 1.0$ for $\delta_{iR} = 1.0$. This is the same condition imposed by $St_R = 1.0$ for $\delta_{iR} = D_R = 1.0$.

1.4 Bottom-Up Scaling

The standard top-down scaling methodology as applied to the scaling of the NSTF air-cooled RCCS experiments is detailed in Section 1.1. It can be seen from the quantitative development in Section 1.1 that the top-down scaling is the standard non-dimensionalization analysis applied to the 1-D conservation equations to obtain the important similarity parameters. It is essentially focused on a one-dimensional loop/circuit incorporating one average hot riser duct where the important variables are the natural convection air velocity in the riser, the corresponding gas mass flow rate and the riser outlet temperature as a function of the imposed heat flux or equivalently the core power. This is the core power, most importantly during the decay heat production accident phase, which is being conducted or radiated to the metal vessel wall boundary.

However it can be seen that the top-down scaling methodology as applied here does encompass 3-D thermofluid phenomena in the plenums, either hot or cold. Furthermore it is not focused on the phenomena involving multiple hot riser ducts such as parallel channel flow stability. In the case of the GA-MHTGR hot plenum, thermal stratification could occur through incomplete mixing of the jet flow from multiple parallel ducts of varying temperature or perhaps less likely from boundary heat losses. The parallel channel flow stability phenomena from the multiple ducts with varying outlet temperature could perhaps lead to recirculation flow patterns between neighboring ducts. The implications of all these phenomena for the heat transfer and heat removal of the core decay heat production to the ultimate heat sink, the atmosphere, may need to be considered. Instead of the heated air flow from the hot risers discharging from the top hot plenum into the hot duct network of the building and exiting from the hot outlet chimney to the atmosphere, it could be that the air flow patterns recirculate and stratify within these volumes and ducts. This would reduce the heat removal by the natural convection flow from the values commensurate with the total natural convection densimetric gravity head. Natural convection phenomena, particularly at low flow rates for air systems with the low gas driving heads are known to be complex to predict. In addition, the viscosities of gases as opposed to those for liquids are noted for increasing with temperature. This leads to the potential for positive feedback and flow stagnation/instability in heated gas systems.

To start the work on the bottoms-up scaling, the focus in this report is on jet behavior in the top hot plenum of the RCCS. The penetration of the hot jet exiting the hot riser ducts into hot plenum should influence the thermal stratification patterns in the hot plenum. It also to a degree determines the conditions for potential recirculation flows between the different hot riser ducts. To this extent then, the initial concentration of the bottom-up scaling is on the maximum ceiling height X_m for jet penetration. Implicit in this are the phenomena of jet entrainment, laminar-to-turbulent transition and ambient

stratification which will be treated at future stages of the scaling analysis. Turner[1.6[conducted experiments on a negative buoyant jet for the axisymmetric case. This is a considerable simplification over a hot riser jet which is initially positive buoyant until it reaches neutral buoyancy and perhaps negative buoyancy. But as a first step it is instructive to note that the Turner data shows

$$\frac{X_m}{D_j} \ \alpha \ F_j^{1/2} \tag{61}$$

so

$$X_m \ \alpha \ D_j^{1/2} U_j \tag{62}$$

So using the notation of Table 2.

$$X_{mR} = D_{jR}^{1/2} \ \ell_R^{1/2} \tag{63}$$

For the selected NSTF RCCS experiment scaling $D_{jR} = 1$ and $\ell_R = 0.5$ giving

$$X_{mR} = 0.707 \tag{64}$$

This should be useful in the scaling of the hot plenum height for the NSTF experiments.

1.5 Study Approach

The RCCS methods experiments and Verification and Validation (V&V) plan has six elements:

1. NSTF large-scale integral testing
   - (a) Facility refurbishment and restart
   - (b) Experiment design
   - (c) Experiment performance
   - (d) Experiment data analysis/reduction and database
2. Scaling study
3. Analysis support for the scaling study and the experiment design
4. Small scale/separate effects tests
5. Instrumentation support for the experiments
6. Code verification and validation with experiment data

From these elements, and in preparation for the integral RCCS experiments in the NSTF, a parallel track effort on two main project tasks is reported here:

1. Analysis support for the scaling study and the experiment design, and
2. Instrumentation support for the experiments.

Analysis support for the scaling study and the experiment design consists of (a) ultimate water heat sink one-dimensional system analyses with the RELAP5 system code and (b) reactor air plenum multi-dimensional CFD analyses with the STARCCM+ CFD code. The reactor/cavity/RCCS is treated as an in-vessel region and an ex-vessel region separated at the primary system boundary interface of the reactor vessel wall. The in-vessel and ex-vessel regions are coupled only through a heat flux boundary condition for the group of events where the integrity of the primary system is maintained and no mass transfer coupling occurs between in-vessel and ex-vessel regions. For reactor cavity phenomena, this is the heat-transfer-only focus. Phenomena that involve blow-down and cavity air/helium distributions, dust/aerosol transport, and blow-down forces (fluid-structure-interaction) loading the mechanical structures of the RCCS will be the focus of the other phases of the project work. The heat-transfer-only focus, as such for these initial scoping analyses, further divides the RCCS and its response to the initiating events into (a) the air transport/heat sink system and (b) the cavity with the air circulation and heat transport. For the STARCCM+ cavity analyses, the air transport/heat sink system is treated as a boundary condition. Cavity analyses will be conducted in the next project stage. For the RELAP5 air transport/heat sink system analyses, the cavity is treated as a natural convection heat transfer correlation.

Instrumentation support for the experiments includes (c) Laser Doppler velocimetry (LDV) instrumentation seeding method studies in a closed natural convection cavity. The LDV is the only measurement technique with the possibility of measuring gas velocities within the cavity. However, LDV requires seeding particles to reflect the laser light that generates signals. Particles are usually kept suspended by forced circulation. The cavity will be a closed natural circulation system. This is a configuration of low velocities and stagnant regions where the potential exists for the seed particles to deposit out off the flow stream, thereby impacting the laser measurement signals of the velocity. The LDV study will determine the feasibility of using LDV for air velocity measurements in the cavity under RCCS conditions.

(a) RELAP5 Air Heat Sink System Analyses

To provide analysis support for these experiments, effort was focused on constructing an input deck for RELAP5, a thermal hydraulics systems code, and modeling the RCCS at full-scale for the GA-MHTGR design. The scenarios assume a loss of forced helium flow in the primary system and natural convection flow only in the RCCS with only heat transfer coupling between the primary system and the cavity. The full-scale RELAP5 model was therefore constructed starting from the vessel wall where a heat flux boundary condition is imposed, a one volume cavity using natural convection correlations and focused on the 1-hot riser model for the air-cooled RCCS all the way from the cold chimney inlet to the hot chimney outlet. The model includes a single down-comer, hot and cold ducting with the bends in the building, the manifolding, hot plenum and both top and bottom cold plenums for one of the two redundant RCCS loops. Riser vessel and cavity heat structure surfaces are included for the in-cavity radiation and natural convection heat transfer. Heat structures and hydrodynamic volumes are further subdivided into axial nodes for greater accuracy. Heat structures also have finely sized

radial nodes. Based on the cavity symmetry, the RCCS design has been modeled in RELAP5 as a one channel grouping of all the hot riser ducts in one half of the reactor cavity. Each half of the cavity is represented by this RELAP5 model together with the top and bottom cold plenum and the hot plenum in that half of the cavity. Also included are the ex-cavity hot and cold duct runs, the manifolds and the cold inlet and hot discharge chimneys, which form that half of the symmetric system, connected to the common atmosphere. It is assumed that the effect on the one RELAP5 group is representative of the effect on both halves and that the heat load is therefore mirror- symmetric. This model was used as a baseline to test the response of the system to varying heat fluxes and confirm the scaling laws. Cases at 10-kW/m^2, 5-kW/m^2, and 2.5-kW/m^2 full-scale heat fluxes were run. The heat flux of 5.0kW/m^2 represents the reference reactor case of medium heat flux. The high heat flux case corresponds to the system model with l0-kW/m^2. The heat flux of 2.5-kW/m^2 is the low heat flux case. It should be emphasized that these are uniform heat fluxes applied at the reactor vessel outer surface over the heated height.

In addition to the full reactor-scale cases, a series of cases were run with a half-scale model at heat fluxes proportionally scaled to the full size. This half-scale deck was used to verify the scaling analysis in the NSTF feasibility study. The system was scaled down to half scale according to the scaling in Section1.2. Essentially the lengths and heights were halved but the widths, depths, diameters and thicknesses in the plane cross-section were kept unaltered. The radial dimensions of the cavity were maintained at full scale. System power was reduced by a factor of the square root of 2, and the scaled heat flux was increased by the same factor to maintain the scaled heat added per unit volume over the standpipes. The half-scale system was converted directly from the full-scale model.

To support the Argonne NSTF heat transfer experiments, a model of the experimental system was prepared as well. The verified scaling allows for comparisons with the experimental system and the full-scale model. The system is 50% height scale, with the same changes made as in the half-scale model per the scaling report in Section 1.2. However the ex-cavity ducting in the half-scale model is replaced by the model of the NSTF chimney. Ambient heat losses from the NSTF test section is included in the baseline cases. Cases were run at three internal power generation levels. These power levels produce the three proportionally scaled heat fluxes previously used. A number of experiment cross section configurations are under discussion but they mainly involve varying the separation distance between the heated surface of the box and the hot risers. The test cavity box depth will be of variable design. There may be experiment configurations where the array of hot riser ducts is offset by a yet-to-be-determined angle to simulate corners of the cavity. This model will be the starting basis for modified RELAP5 models as the experiment matrix is defined.

This work is detailed in Chapter 2.

(b) STARCCM+ RCCS CFD Analyses

At this stage, the CFD analyses are intended to be used to guide the development of an experimental geometry and test plan for experiments related to the air-cooled GA-MHTGR RCCS designs.

Proposed changes in the NSTF test section geometry maintain key scaling parameters provide a need to evaluate multidimensional effects such as turbulent mixing in inlet and outlet plenums of the air-cooled RCCS system. A series of Computational Fluid Dynamics simulations of the GA-MHTGR RCCS system have been completed as a baseline for the development and scaling of the multidimensional aspects of the NSTF experiment. RANS-based simulations of natural convection and radiation heat transport have been carried out using the commercial CFD code STAR-CCM+. Based on the CAD model describing the full GA-MHTGR RCCS air-side geometry an explicit geometry model was developed using the built-in mesh development tools of STAR-CCM+, version 5.02.009. The final mesh represents one symmetric half of the RCCS system, with 114.5 RCCS riser tubes, and uses approximately 9.2 million volumetric cells.

The initial baseline RCCS simulation uses a constant uniform heat flux on the risers rather than a more realistic radiation heat source distribution. The use of the simplified boundary condition enables the initial simulations of the air-cooled RCCS system and its NSTF analog to more easily be used for model development and mesh optimization. Both the upper and lower chimney openings are assumed to be open for flow to maximize the opportunity for re-entrant flow as part of the model development effort. All flow velocities are simulated as result of natural buoyant convection and no flow boundary conditions are specified. A uniform 1·37 k/m2 heat flux is applied to all the risers, which is consistent with a loss of flow accident in which the risers expell all of the heat from the reactor vessel, (10kW/m2), out of the system. An equivalent volumetric heat sink is assumed in the external air volume to allow the natural convection flow to be simulated. A symmetry boundary condition is applied at the symmetry plane so that the model effectively represents the full system. All other boundaries in the model are assumed to be adiabatic no-slip walls.

The development of the flow field was monitored in five selected risers to ensure that the simulation was well converged. The close agreement between the riser temperature and velocity distributions for this fixed heat flux case for the five risers confirms that a converged natural convection solution can be obtained. The temperature distribution in the upper components of the RCCS system with detailed distributions of the hot side components was obtained. Since the heat flux in each riser tube is identical, the temperature distributions in these components are very uniform. However the velocity fields provide some insight into likely regions of thermal stripping or stratification when a more realistic non-uniform heat load distribution is applied. For example, strong recirculation zones form downstream of each of the 90-degree bends in the co-axial ducts. Such flow structures can result in the formation of stagnation points which lead to thermal stresses in adjacent solid materials. However, in this case, these flow features also result in significant turbulence generation, where high turbulent kinetic energies can be observed near the center of each recirculation region.

As with the GA-MHTGR RCCS model, the NSTF experiment-scale STAR-CCM+ CFD model was developed from a CAD representation of the proposed geometry. The mesh settings used in the development of the baseline RCCS mesh were also applied to the NSTF model. The final mesh consists of more than 15 million polyhedral and prismatic polygonal cells. Although based on the experimental geometry currently under discussion, the computational model considers a simplified geometry which neglects the building structure and assumes that adequate ventilation is available to feed coolant to the inlet of the natural convection driven facility. The riser duct heat flux boundary condition and solver settings are the same as those used in the GA-MHTGR model.

The predicted temperature profile in the heated region is quite similar to the profile seen in the GA-MHTGR case. As in that case, uniform heating of the RCCS ducts should be expected and the temperature distribution in the RCCS risers as well as the horizontal and vertical duct segments is very uniform. However the single horizontal inlet configuration results in the formation of a strong recirculation zone in the inlet plenum which may affect the duct flow distribution and stability. Steady state velocity profiles and the good convergence behavior of the simulation suggest that the flow field in the risers is fairly stable, but more detailed unsteady analyses are needed to address stability. Similarly a large recirculation zone forms in the upper plenum as a consequence of the offset position of the risers. This recirculation pattern persists through the horizontal segment of the outlet duct and may interfere with the formation of the recirculation patterns seen downstream of each elbow in the RCCS model.

Building upon this foundational work, the mesh and modeling strategy will be used in future simulations to evaluate the more complex case in which the radiation heat source is applied/and or calculated as part of the simulation.

This work is detailed in Chapter 3.

(c) Cavity LDV Instrumentation

A characterization of local gas velocities within the cavity is desired for comparison with CFD code simulations. An evaluation of instrumentation alternatives identified Laser Doppler Velocimetry (LDV) as the most feasible candidate in view of the facility's high operating temperature and the expectation of rather low flow velocities within the cavity. But LDV cannot function without suspended particles. Maintaining adequate levels of particle "seeding" is difficult in a closed system such as the RCCS and so a feasibility study was conducted to ascertain whether this technique could successfully measure velocity within the cavity.

Candidate seeding materials have been tested in a 1.8 x 0.5 x 0.5 m glass enclosure. The investigation was limited to determining whether a particular material could produce a measurable LDV signal, and if so, how long the signal would last. Signal strength increases with particle size, but larger particles tend to settle more quickly, necessitating more frequent particle injections, which disturbs natural circulation flow patterns. In addition to settling, particles can be lost via electrostatic attraction to enclosure surfaces. The two varieties of incense produced lower count rates than the oils,

but they were quite stable and easy to generate. Despite the low data rates, incense may be preferable to oil as it is less likely to affect the emissivity of cavity surfaces. Further testing of titanium dioxide with alternative dispersion methods may be warranted, but powder dispersion is generally more troublesome than oil atomization and this is recommended only if oils are deemed unacceptable.

It is probable that LDV can be made to function well enough to obtain a number of velocity measurements though not yet clear how much effort will be required to obtain an acceptably extensive cavity velocity map. For steady state tests that run tens of hours, it may be acceptable if, say, ten minutes of data collection are required at each location. One could then map dozens of locations over the course of hours. For transient tests, one may only be able to track velocity at a single location during the course of the test.It is likely that trial and error iterations with the actual facility will be necessary for the final selection of a seeding material and injection mode and to arrive at acceptable data rates and seeding intervals

This work is detailed in Chapter 4.

References

1.1 R. V. Vilim and E. E. Feldman, "Scalability of the Natural Convection Shutdown Heat Removal Test Facility (NSTF) Data to VHTR/NGNP RCCS Designs", ANL-GenIV-049, Argonne National Laboratory Report, June 2005.

1.2 C. Tzanos, "CFD Analysis for the Applicability of the Natural Convection Shutdown Heat Removal test Facility (NSTF) for the simulation of the VHTR RCCS", ANL-GenIV-055, Argonne National Laboratory Report, September 2005.

1.3 M. T. Farmer, et. al., "Natural Convection Shutdown Heat Removal Test Facility (NSTF) Evaluation for Generating Additional Reactor Cavity Cooling System (RCCS) Data", ANL-GenIV-058, Argonne National Laboratory Report, September 2005.

1.4 C. P. Tzanos and M. T. Farmer, "NSTF Feasibility Study for VHTR Water-Cooled RCCS Experiments", ANL-GENIV-079, Argonne National Laboratory Report, September 2006.

1.5 J. G. Collier, "Convective Boiling and Condensation," McGraw-Hill, NY (1972).

1.6 J. S. Turner, "Jets and Plumes with Negative or Reversing Buoyancy", J. Fluid, Mech. 26, 779-792 (1966).

2.0 Air Heat Sink System Analyses

The performance of the Reactor Cavity Coolant System (RCCS) in its assigned functional role either during the plant conditions of normal steady-state operation or off-normal accident transient can be best monitored by the following safety/operational criteria parameters:

i. Temperature of the primary reactor vessel metal boundary
ii. Temperature of the cavity concrete boundary
iii. Temperature of the reactor vessel metal supports in the reactor cavity

The thermo-fluid (T-F) phenomena that affect these safety criteria parameters (i) to (iii) under normal operating or accident conditions can be classified into two categories:

(a) T-F phenomena in the reactor cavity
(b) T-F phenomena in the air duct network of the RCCS connecting to the ultimate heat sink, the ambient atmospheric air environment

The phenomena that are of particular importance are those that affect the passive safety case.

Cavity phenomena determine the passive transfer of the heat produced by the reactor core within the primary vessel from the outer vessel metal wall surface to the air ducts of the RCCS, to the air within the cavity and eventually to the liner/insulation/concrete of the cavity boundary. The experience is that this heat transfer is dominated by radiation heat transfer mechanisms for this air-cooled RCCS design but that some natural convection air heat transfer also occurs driven by the natural convective air flow patterns. While radiant heat transfer phenomena establishes the intra-cavity heat transfer rates and therefore the boundary temperature differences, local hot spots and therefore local peaking factors can be influenced by the patterns of the natural convection air flow. Radiant heat transfer rates are established by the predefined geometry, operating history surface emissivities and the presence or absence of gray gas factors such as graphite dust particles, water vapor and other “impurities”. Natural convection air flow patterns can also be affected by such factors. The geometry of the cavity establishes the radiation view factors between the metal vessel wall and the RCCS hot riser ducts. A non-symmetric/non-uniform reactor cavity geometry leads to non-uniform heating of the riser ducts which could lead to T-F non-uniformities in the T-F phenomena within the air duct network. This could affect the heat transport discharge rates.

Air duct network phenomena determine the wall temperature drop within the hot riser ducts and also whether a significant amount of the heat transferred from the primary vessel wall to the RCCS ducts is passively discharged from the outlet chimneys to the ambient atmosphere or whether it recirculates between various “hot” and “cold” riser ducts or in thermal stratification patterns within the various plena or in the duct network itself. Natural convection phenomena at atmospheric pressure and low flow rates can be complex to predict. In particular, the increasing viscosity of air with temperature leads to the possibility of positive feedback and the potential for local stagnation. These

phenomena are established by the predefined geometry, and the atmospheric flow and pressure boundary conditions at the chimney inlets and outlets. The geometry of the air duct network establishes the flow resistances and velocities between the inlet and outlet ports of the various chimneys in the different flow paths and plena. A non-symmetric /non-uniform network geometry could lead to non-uniform flow patterns which could lead to heat transport patterns which do not directly discharge the core heat transferred from the vessel, to the atmosphere from the outlet hot chimneys in a once-through pathway from the inlet cold chimney. Rather the heat recirculates within the RCCS network.

These are the cavity T-F phenomena and the duct network T-F phenomena which are the subject of the scaling analyses presented in Chapter 1. These are the phenomena which establish the temperatures of importance to the three safety criteria (i) – (iii). With the appropriate scaling laws so determined, the scaled NSTF experiments should provide validation data which can be extrapolated to the full-scale reactor geometry and conditions. This should be carried out for the range of the accident spectrum selected. Different events could envelope different ranges of the parameters. To determine these ranges and also establish the validity of /or distortion caused by the different scaling approximations which had to be made in the discussions of Chapter 1, supporting modeling analyses have been and will continue to be performed. This chapter presents the results obtained by using the 1-D RELAP5 code to simulate the T-F phenomena in the air duct network which passively transports reactor generated heat to the ultimate atmosphere air heat sink. The CFD simulation equivalent results with the STAR-CCM+ code are presented in Chapter 3. Modeling simulations of the multi-D reactor cavity are also to be carried out with the STAR-CCM+ code.

2.1 RCCS Design View Factors

2.1.1 Reactor-Scale Geometry

An evaluation of the variation of the radiation heat transfer view factors in the reactor cavity of the air-cooled RCCS system was performed based on available information on the RCCS design of the GA-MHTGR. In the GA-MHTGR design the cylindrical reactor vessel sits in a reactor cavity which is essentially a square in plane cross section with one curved side. This asymmetrical geometry has the potential for leading to a non-uniform distribution in the azimuthal dependence of the view factor from the outer surface of the metal vessel wall to the outer surface of the hot riser ducts. This could be particularly significant in the corner of the square cavity cross section and in the extremes of the curved side. The non-uniform variation of this view factor from the vessel wall heated surface transferring the reactor core decay heat to the ultimate heat sink cooling of the riser ducts will lead to a non-uniform heating pattern in the air of the risers. Stagnation regions and recirculation flow pattern possibilities between relatively hotter and colder risers may be a consequence of this non–uniform heating. Fig 2.1 shows the plane cross section of the GA-MHTGR cross section with the centrally located reactor vessel. The three reactor vessel supports are also shown. The primary cross-vessel from the reactor vessel to the power conversion unit (PCU) vessel is also shown at the top

edge of the cross-section. The PCU sits in its own silo. The 227 RCCS hot riser ducts (2”x 10”) are also shown in Figure 2.1. There are gaps in the riser duct coverage around the walls of cavity at the location of the reactor vessel supports. The insulation attached to the front of the surface of the down-comer wall serves extra duty at these locations. While not shown in Figure 2.1 the region above the cross-vessel are protected by the air-cooled riser ducts of varying length above the circumference. To scope the variation of the radiation view factors from the vessel wall to the front and side surfaces of the riser ducts, the 227 ducts are grouped into sets of approximately 12 ducts. Starting with Group 1 at the cross-vessel there are 10 groups as the 180^0 azimuthal traverse is made to Group 10 located diametrically opposite on the mid-plane of the curved cavity wall. Since there is a symmetry plane separating the cavity into two identical halves, only half the groups of ducts are shown in the Figure. Further more it should be pointed out in the corners of the cavity, the eight ducts lumped together in Group 3 is significantly smaller in number than the number of riser ducts in the other groups. This should be accounted for when the results for the lumped-group view factors are interpreted.

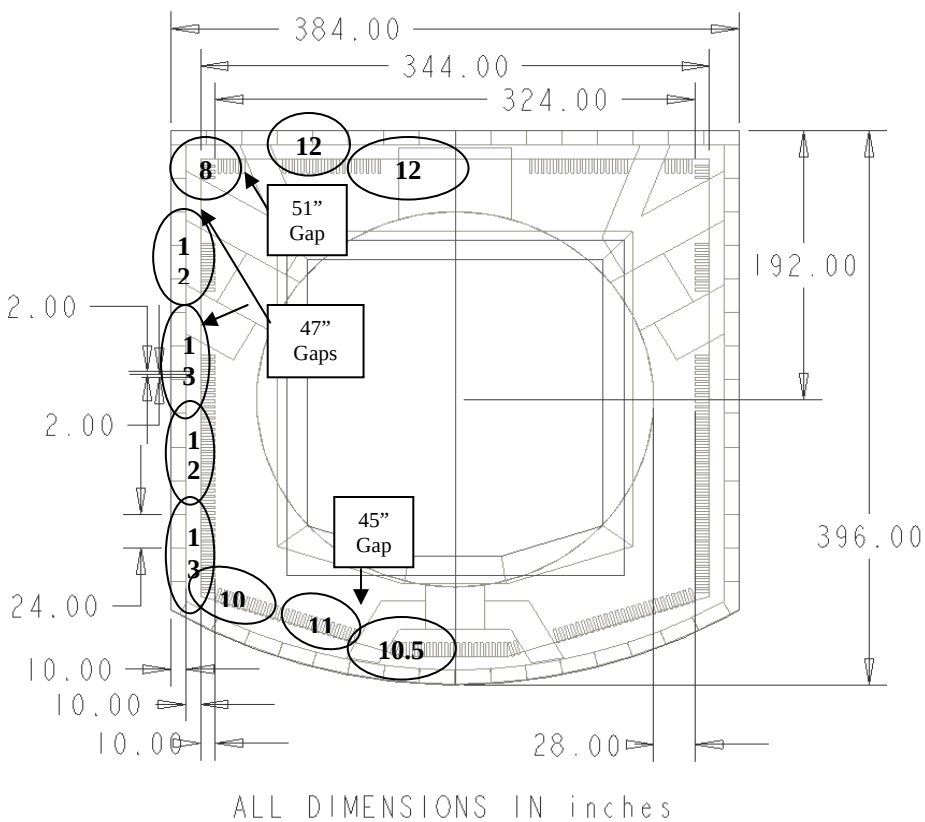

Figure 2.1 Cavity Cross Section- Group of 10 Locations

The radiation heat transfer view factors from the reactor vessel wall for this 10 group lumped configuration of the hot riser ducts in the reactor cavity were evaluated using the NEVADA code.[2.1] All the subsequent view factors presented in this chapter were obtained using this NEVADA methodology. The Net Energy Verification And Determination Analyzer (NEVADA 97) is a thermal radiation analysis software package. The package is equipped with both radiation analysis tools and a special CAD tool for the

radiation analysis. The NEVADA software package consists of several radiation analysis tool, one of which is RENO. The RENO computer code is used for radiation interchange factors calculations using Monte-Carlo Mathematical techniques. It uses statistical ray tracing to compute view factors for complex geometry problems. The number of rays can be changed to improve accuracy level of the program and to account for time constraints. The ten group calculation required that ducts be segregated accordingly. Each duct has a front surface, back surface, and side surfaces (which were lumped together). The ducts were separated into groups shown in Figure 2.1. The same node numbering was kept for the right side of the system as the left side. In order to keep uniformity, the ducts were divided to keep a twelve duct grouping. Due to the geometry problems and number of ducts, the ducts were divided into the groups shown in Fig. 2.1. Group 1 started with the top-middle grouping of Fig. 2.1. The side, front (facing the reactor), and back (facing the cavity wall) surface nodes were numbered 1, 2, and 4, respectively. The group numbering continued in the counter-clockwise direction ending in the bottom –middle group in Fig 2.1. Groups 2-10 were numbered with the first digit being the group number followed by 0 for the Front Surface, 1 for Side Surface, and 2 for the Back Surface. The Reactor Pressure Vessel was input as a perfect cylinder (node 55). The back cavity wall was a single entity (node number 99).

RENO computes complex 3D surface view factors, and it takes into account empty space in the model. The "space" (Up & Down) is the empty space that a surface radiates to. The RELAP5 decks assumed no radiation in the axial direction. Therefore, in order to minimize the view factor towards the top and bottom space, the height of all the surfaces was increased to simulate infinite height: 9999". The height greatly reduced the view factor towards space, giving a more accurate view factor for the RELAP5 input.

Figure 2.2 shows the view factor distribution from the RPV to the front surface and side surface of each group in the counter clockwise direction. On the front wall curve, the view factor for the front surface of group 3 (Node 30) drops dramatically. This is due to the distance of Group 3 from the RPV and that it consists of only 8 ducts. The side surface view factor for Group 3 (Node 31) does not see this dip because the side surfaces of this group can see the RPV surface without any interference from other surfaces. Group 5 see the highest view factors because it is directly facing the RPV, and even though Group 1 is the same distance as Group 5 from the RPV, Group 5 has larger view factors because the group contains more ducts. As it continues around the view factors for both the front and side surface follow the same pattern around as expected with the number of ducts in each group. Table 2.1 shows the view factors from the reactor vessel to the duct surfaces and the view factors from the duct surfaces to the reactor. Table 2.2 shows the surface areas (ft^2) of each component. Since an "infinite" height calculation was made the areas are from the RENO results which were then corrected for the finite height 44' tall cavity in the RELAP5 deck.

The other extreme is to lump all the 227 riser ducts together into one group. The one group calculation required that all ducts be treated together. Each duct has a front surface, back surface, and two side surfaces (which were lumped together as one). The

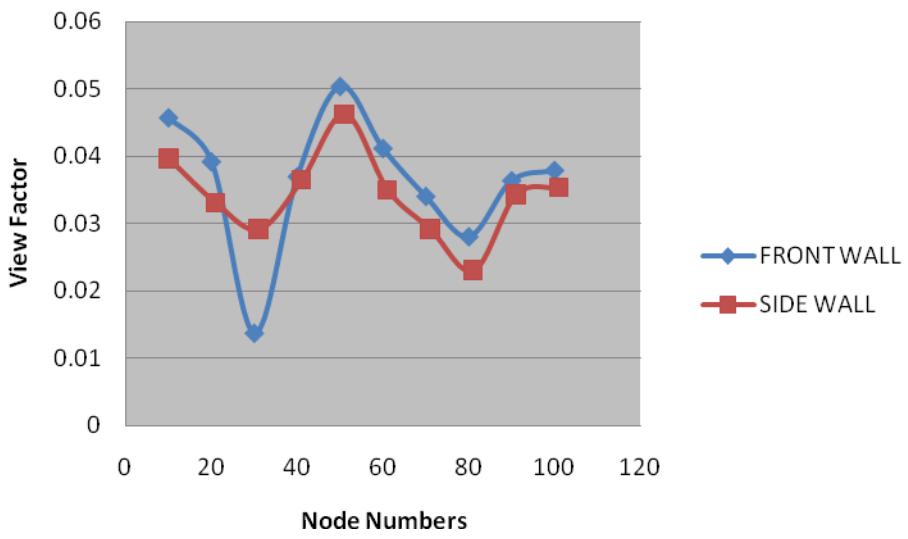

Figure 2.2 View Factors-Group of 10 Azimuthal Distribution

ducts are lumped into the one group shown in Figure 2.3. With the half mirror symmetry of the cavity only half the ducts (113.5) are shown in the group. But the same node numbering was kept for the right side of the system as the left side. The side, front (facing the reactor), and back (facing the cavity wall) surface nodes were numbered 1, 2, and 4, respectively. The Reactor Pressure Vessel was input as a perfect cylinder (node 55). The back cavity wall was a single entity (node number 99).

Table 2.3 shows the view factors from the reactor vessel to the duct surfaces and the cavity back wall for all the surfaces in the 1-Group model configuration. The Table also includes the view factors from the 1-Group duct surfaces to the reactor. Table 2.4 shows the surface areas (ft^2) of each component. Since an "infinite" height calculation was made the area are from the RENO results which were then corrected for the finite 44' tall cavity in the RELAP5 deck. The RENO computation takes into account the "empty space" in the model. This is the top and bottom of the configuration. The "space" (Up & Down) is the empty space that a surface radiates to. The RELAP5 decks assumed no radiation in the axial direction. Therefore, in order to minimize the view factor towards the empty space, the height of all the surfaces was increased to simulate infinite height: 9999". The height greatly reduced the view factor towards space, giving a more accurate view factor for the RELAP5 input.

Table 2.3 shows the view factors from the reactor vessel to the duct surfaces and the cavity back wall for all the surfaces in the 1-Group model configuration. The Table also includes the view factors from the 1-Group duct surfaces to the reactor. Table 2.4 shows the surface areas (ft^2) of each component. Since an "infinite" height calculation was made the area are from the RENO results which were then corrected for the finite 44' tall cavity in the RELAP5 deck. The RENO computation takes into account the "empty space" in the model. This is the top and bottom of the configuration. The "space" (Up &

Table 2.1. View Factors-Group of 10

			Group 1			Group 2			Group 3			Group 4			Group 5		
	Reactor	Cavity Wall	2" Riser Surface Facing Reactor	10 " Side Riser Surface	2" Riser Surface Facing Cavity Wall	2" Riser Surface Facing Reactor	10 " Side Riser Surface	2" Riser Surface Facing Cavity Wall	2" Riser Surface Facing Reactor	10 " Side Riser Surface	2" Riser Surface Facing Cavity Wall	2" Riser Surface Facing Reactor	10 " Side Riser Surface	2" Riser Surface Facing Cavity Wall	2" Riser Surface Facing Reactor	10 " Side Riser Surface	2" Riser Surface Facing Cavity Wall
Node	55	99	2	1	4	20	21	22	30	31	32	40	41	42	50	51	52
Surface	RX	UH3	FW16	SW31	WTB16	FW5	SW9	WTB5	FW	SW1	WTB	F5	s9	B5	F17	s33	B17
From Reactor to surfaces	0.0	0.2912	0.0457	0.0396	0.0	0.0391	0.0331	0.0	0.0137	0.0292	0.0	0.0369	0.0365	0.0	0.0503	0.0462	0.0
From Surfaces to Reactor	0.0	0.1770	0.8028	0.0695	0.0	0.6876	0.0581	0.0	0.3624	0.0769	0.0	0.6489	0.0642	0.0	0.8165	0.0750	0.0

	Group 6			Group 7			Group 8			Group 9			Group 10			
	2" Riser Surface Facing Reactor	10 " Side Riser Surface	2" Riser Surface Facing Cavity Wall	2" Riser Surface Facing Reactor	10 " Side Riser Surface	2" Riser Surface Facing Cavity Wall	2" Riser Surface Facing Reactor	10 " Side Riser Surface	2" Riser Surface Facing Cavity Wall	2" Riser Surface Facing Reactor	10 " Side Riser Surface	2" Riser Surface Facing Cavity Wall	2" Riser Surface Facing Reactor	10 " Side Riser Surface	2" Riser Surface Facing Cavity Wall	Up & Down
Node	60	61	62	70	71	72	80	81	82	90	91	92	100	101	102	
Surface	F26	s51	B26	F38	s75	B38	F1	S1	B1	F11	S21	B11	F19	S37	B19	Space
From Reactor to surfaces;	0.0411	0.0350	0.0	0.0340	0.0292	0.0	0.0280	0.0231	0.0	0.0363	0.0344	0.0	0.0379	0.0354	0.0	0.0041
From Surfaces to Reactor	0.7220	0.0615	0.0	0.5530	0.0471	0.0	0.5919	0.0487	0.0	0.6977	0.0659	0.0	0.7592	0.0442	0.0	

Table 2.2. View Areas-Group of 10

			Group 1			Group 2			Group 3			Group 4			Group 5		
	Reactor	Cavity Wall	2" Riser Surface Facing Reactor	10 " Side Riser Surface	2" Riser Surface Facing Cavity Wall	2" Riser Surface Facing Reactor	10 " Side Riser Surface	2" Riser Surface Facing Cavity Wall	2" Riser Surface Facing Reactor	10 " Side Riser Surface	2" Riser Surface Facing Cavity Wall	2" Riser Surface Facing Reactor	10 " Side Riser Surface	2" Riser Surface Facing Cavity Wall	2" Riser Surface Facing Reactor	10 " Side Riser Surface	2" Riser Surface Facing Cavity Wall
Area ft^2	3092.90	5084.67	176.00	1760.00	1760.00	176.00	1760.00	176.00	117.33	1173.33	117.33	176.00	1760.00	176.00	190.67	1906.67	190.67

	Group 6			Group 7			Group 8			Group 9			Group 10		
	2" Riser Surface Facing Reactor	10 " Side Riser Surface	2" Riser Surface Facing Cavity Wall	2" Riser Surface Facing Reactor	10 " Side Riser Surface	2" Riser Surface Facing Cavity Wall	2" Riser Surface Facing Reactor	10 " Side Riser Surface	2" Riser Surface Facing Cavity Wall	2" Riser Surface Facing Reactor	10 " Side Riser Surface	2" Riser Surface Facing Cavity Wall	2" Riser Surface Facing Reactor	10 " Side Riser Surface	2" Riser Surface Facing Cavity Wall
Area ft^2	176.00	1760.00	176.00	190.67	1906.67	190.67	146.67	1466.67	146.67	161.33	1613.33	161.33	154.00	1540.00	154.00

Down) is the empty space that a surface radiates to. The RELAP5 decks assumed no radiation in the axial direction. Therefore, in order to minimize the view factor towards the empty space, the height of all the surfaces was increased to simulate infinite height: 9999”. The height greatly reduced the view factor towards space, giving a more accurate view factor for the RELAP5 input.

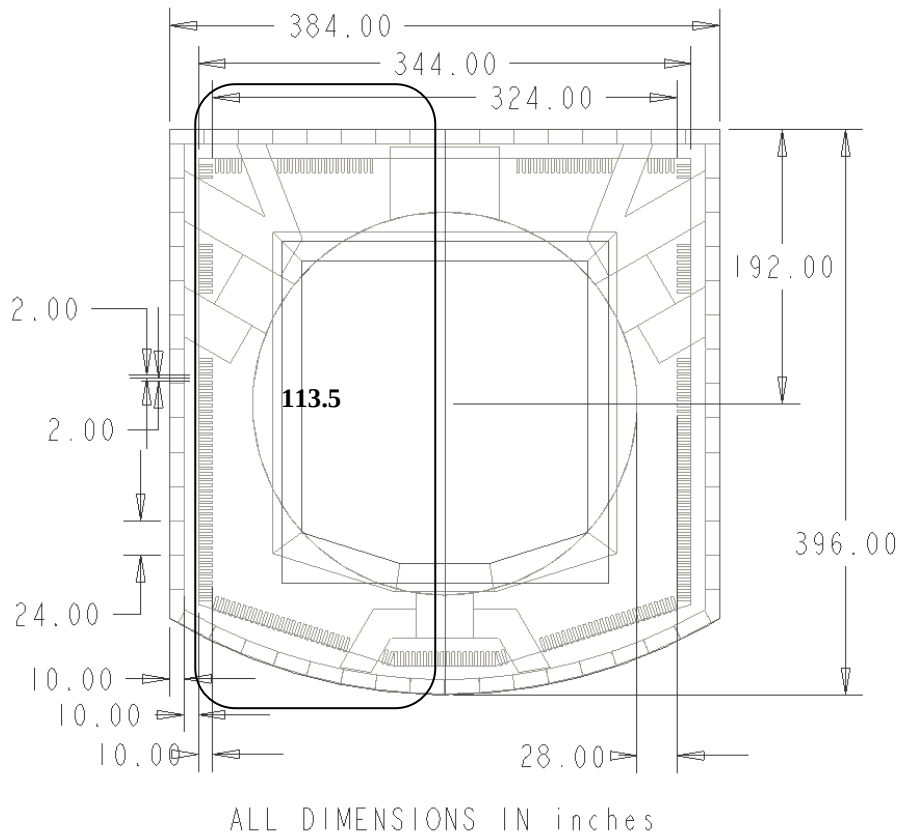

Figure 2.3 Cavity Cross Section-Group of 1 Location

Table 2.3 View Factors-Group of 1

					Group 1			
			Reactor	Cavity Wall	2” Riser Surface Facing Reactor	10” Side Riser Surface	2” Riser Surface Facing Cavity Wall	Up & Down
Node			55	99	2	1	4	
Surface			RX	UH3	FW	SW1	WTB	Space
	55	RX	0.0	0.2912	0.3632	0.3415	0.0	0.0041
	99	UH3	0.1770	0.0734	0.0213	0.3987	0.3271	0.0024
Group 1	2	FW	0.6747	0.0648	0.1077	0.1476	0.0	0.0050
	1	SW1	0.0610	0.1182	0.0177	0.7989	0.003	0.0008
	4	WTB	0.0	0.9992	0.0	0.0	0.0	0.0008

Table 2.4 View Areas-Group of 1

	Reactor	Cavity Wall	2" Riser Surface Facing Reactor	10 " Side Riser Surface	2" Riser Surface Facing Cavity Wall
Area ft^2	3092.90	5084.67	1664.67	16646.67	1664.67

A refinement on the 1-Group configuration would be a 3-Group configuration for the riser ducts. The natural grouping would be by cavity side as the discharge ducts are located at each corner of the cavity. The hot riser ducts are segregated into the three groups shown in Figure 2.4. With the half-mirror symmetry of the cavity only half the ducts (113.5) are shown in the groups. The same node numbering was kept for the right side of the system as the left side. The number of ducts in each group is indicated for the half-configuration shown in Fig 2.4. Group 1 starts with the top-middle grouping of Fig. 2.4. Each duct has a front surface, back surface, and side surfaces (which were lumped together).The side, front (facing the reactor), and back (facing the cavity wall) surface nodes were numbered 1, 2, and 4, respectively. The group numbering continued in the counter-clockwise direction ending in the bottom –middle group in Fig 2.4. Surfaces of Groups 2 and 3 were numbered with the first digit being the group number followed by 0 for the Front Surface, 1 for Side Surface, and 2 for the Back Surface. The Reactor Pressure Vessel was input as a perfect cylinder (node 55). The back cavity wall was a single entity (node number 99).

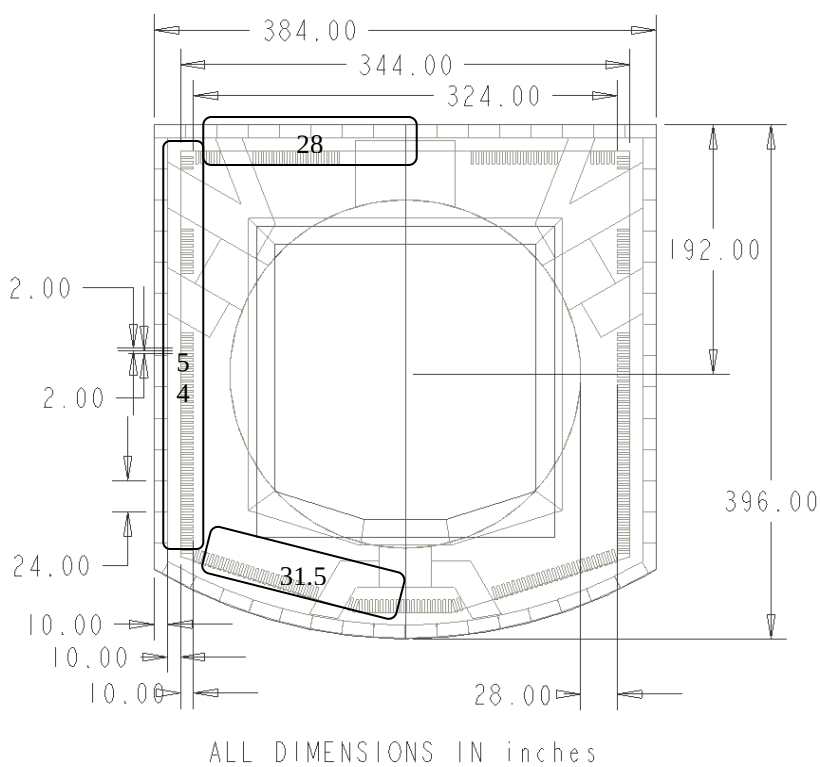

Figure 2.4 Cavity Cross Section-Group of 3 Location

Table 2.5 shows the view factors for all the surfaces in the 3-Group model configuration from the reactor vessel to the duct surfaces and the cavity back wall. This includes the view factors from the reactor to the duct surfaces of each of the three groups. Table 2.6 shows the surface areas (ft^2) of each component. The RELAP5 models which use these view factors as input assumed no radiation in the axial direction. Therefore, in order to minimize the view factor towards the top and bottom, the height of all the surfaces was increased to simulate infinite height: 9999". The height greatly reduced the view factor towards the top and bottom, giving a more accurate view factor for the RELAP5 input. Since this "infinite" height calculation was made, the areas from the RENO results were corrected for the finite 44' tall cavity in the RELAP5 deck. The RENO computation takes into account this "empty space" in the model. This is the top and bottom of the configuration. The Up & Down is this empty space that a surface radiates to.

The 3-Group configuration for the riser ducts can be further decomposed. One possible decomposition scheme is the configuration termed Group 4A. In this configuration the group of hot riser ducts along the cavity wall which has the cross-vessel penetration is subdivided into two sub-groups. Group 1 is now the set of riser ducts around the cross-vessel penetration region while Group 2 is the remaining set of riser ducts along this same wall which are closer to the corner where the discharge ducting that leaves the cavity, connects to the hot plenum. Group 3 and Group 4 remain the same grouping of ducts as in the 3-Group configuration along the other two cavity walls. The number of hot riser ducts in each of the four groups shown in Figure 2.5. With the half-mirror symmetry of the cavity only half the ducts (113.5) are shown in the groups. The same node numbering was kept for the right side of the system as the left side. Group 1 starts with the top-middle grouping of Fig. 2.5. Each duct has a front surface, back surface, and side surfaces (which were lumped together).The side, front (facing the reactor), and back (facing the cavity wall) surface nodes were numbered 1, 2, and 4, respectively. The group numbering continued in the counter-clockwise direction ending in the bottom –middle group in Fig 2.5. Surfaces of Groups 2 to 4 were numbered with the first digit being the group number followed by 0 for the Front Surface, 1 for Side Surface, and 2 for the Back Surface. The Reactor Pressure Vessel was input as a perfect cylinder (node 55). The back cavity wall was a single entity (node number 99).

Table 2.7 shows the view factors from the reactor vessel to the duct surfaces and the cavity back wall for all the surfaces in the 4A-Group model configuration. It also includes the view factors from the reactor to the duct surfaces of each of the three groups. Table 2.8 shows the surface areas (ft^2) of each component. The RELAP5 models which use these view factors as input assumed no radiation in the axial direction. Therefore, in order to minimize the view factor towards the top and bottom, the height of all the surfaces was increased to simulate infinite height: 9999". The height greatly reduced the view factor towards the top and bottom, giving a more accurate view factor for the RELAP5 input. Since this "infinite" height calculation was made, the areas from the RENO results were corrected for the finite 44' tall cavity in the RELAP5 deck. The RENO computation takes into account this "empty space" in the model. This is the top

Table 2.5 View Factors-Group of 3

					Group 1			Group 2			Group 3			
			Reactor	Cavity Wall	2" Riser Surface Facing Reactor	10 " Side Riser Surface	2" Riser Surface Facing Cavity Wall	2" Riser Surface Facing Reactor	10 " Side Riser Surface	2" Riser Surface Facing Cavity Wall	2" Riser Surface Facing Reactor	10 " Side Riser Surface	2" Riser Surface Facing Cavity Wall	Up & Down
Node			55	99	2	1	4	50	51	52	80	81	82	
Surface			Reactor	Cavity Wall	FW	SW1	WTB	F1	s1	B1	F1	S1	B1	Space
	55	Reactor	0	0.29121	0.0931	0.0882	0	0.1679	0.1606	0	0.1022	0.0928	0	0.0041
	99	Cavity Wall	0.1770	0.07343	0.0095	0.0996	0.0807	0.0098	0.1952	0.1556	0.0020	0.1040	0.0908	0.0024
Group 1	2	FW	0.7006	0.11752	0	0.0001	0	0.0711	0.0959	0	0.0048	0.0050	0	0.0049
	1	SW1	0.0663	0.12334	0	0.779	0	0.014	0.016	0	0.0001	0.0001	0	0.0008
	4	WTB	0	0.99931	0	0	0	0	0	0	0	0	0	0.0007
Group 2	50	F1	0.6558	0.06269	0.0369	0.0731	0	0.0002	0.0001	0	0.0706	0.0958	0	0.0048
	51	s1	0.0627	0.12544	0.0049	0.0082	0	0	0.7781	0	0.0077	0.0122	0	0.0008
	52	B1	0	0.99926	0	0	0	0	0	0	0	0	0	0.0007
Group 3	80	F1	0.6847	0.02193	0.0042	0.0009	0	0.1210	0.1326	0	0.0106	0.0186	0	0.0055
	81	S1	0.0532	0.10105	0.0004	0.0001	0	0.0151	0.0195	0	0.0139	0.7839	0.0121	0.0008
	82	B1	0	0.99908	0	0	0	0	0	0	0	0	0	0.0009

Table 2.6 View Areas-Group of 3

			Group 1			Group 2			Group 3		
	Reactor	Cavity Wall	2" Riser Surface Facing Reactor	10 " Side Riser Surface	2" Riser Surface Facing Cavity Wall	2" Riser Surface Facing Reactor	10 " Side Riser Surface	2" Riser Surface Facing Cavity Wall	2" Riser Surface Facing Reactor	10 " Side Riser Surface	2" Riser Surface Facing Cavity Wall
Area ft^2	3092.9	5084.67	410.67	4106.67	410.67	792	7920	792	462	4620	462

Table 2.7. View Factors-Group of 4A

					Group 1			Group 2			Group 3			Group 4			
			Reactor	Cavity Wall	2" Riser Surface Facing Reactor	10 " Side Riser Surface	2" Riser Surface Facing Cavity Wall	2" Riser Surface Facing Reactor	10 " Side Riser Surface	2" Riser Surface Facing Cavity Wall	2" Riser Surface Facing Reactor	10 " Side Riser Surface	2" Riser Surface Facing Cavity Wall	2" Riser Surface Facing Reactor	10 " Side Riser Surface	2" Riser Surface Facing Cavity Wall	Space
Node			55	99	2	1	4	30	31	32	50	51	52	80	81	82	
Surface			RX	UH3	FW16	SW31	WTB16	FW	SW1	WTB	F1	S1	B1	F1	S1	B1	Space
	55	RX	0.0	0.2912	0.0457	0.0396	0	0.0474	0.0485	0	0.1679	0.1606	0	0.1022	0.0928	0	0.0041
	99	UH3	0.1770	0.0734	0.0030	0.0343	0.0346	0.0065	0.0653	0.0461	0.0098	0.1952	0.1556	0.0020	0.1040	0.0908	0.0024
Group 1	2	FW16	0.8028	0.0876	0.0	0.0001	0	0	0	0	0.0498	0.0556	0	0	0	0	0.0042
	1	SW31	0.0695	0.0992	0.0	0.7857	0.0000	0	0.034033	0	0.0051	0.0058	0	0	0	0	0.0006
	4	WTB16	0.0	0.9993	0.0	0	0	0	0	0	0	0	0	0	0	0	0.0007
Group 2	30	FW	0.6244	0.1400	0.0	0	0	0	0.0001	0	0.0868	0.1261	0	0.0084	0.0087	0	0.0055
	31	SW1	0.0639	0.1415	0.0	0.0257	0	0.0000	0.7233	0.0000	0.0208	0.0234	0	0.0002	0.0002	0	0.0009
	32	WTB	0.0	0.9993	0.0	0	0	0	0	0	0	0	0	0	0	0	0.0007
Group 3	50	F1	0.6558	0.0627	0.0111	0.0114	0	0.0257	0.0617	0	0.0002	0.0001	0	0.0706	0.0958		0.0048
	51	S1	0.0627	0.1254	0.0012	0.0013	0	0.0037	0.0069	0	0.0000	0.7781	0.0000	0.0077	0.0122	0	0.0008
	52	B1	0.0	0.9993	0.0	0.0	0.0	0.0	0.0	0.0	0.0	0	0	0	0	0	0.0007
Group 4	80	F1	0.6847	0.0219	0.0	0.0	0.0	0.0042	0.0009	0	0.1210	0.1326	0	0.0106	0.0186	0	0.0055
	81	S1	0.0532	0.1010	0.0	0.0	0.0	0.0004	0.0001	0	0.0151	0.0195	0	0.0139	0.7839	0.0121	0.0008
	82	B1	0.0	0.9991	0.0	0.0	0.0	0	0	0	0	0	0	0	0	0	0.0009

Table 2.8. View Areas-Group of 4A

			Group 1			Group 2			Group 3			Group 4		
	Reactor	Cavity Wall	2" Riser Surface Facing Reactor	10 " Side Riser Surface	2" Riser Surface Facing Cavity Wall	2" Riser Surface Facing Reactor	10 " Side Riser Surface	2" Riser Surface Facing Cavity Wall	2" Riser Surface Facing Reactor	10 " Side Riser Surface	2" Riser Surface Facing Cavity Wall	2" Riser Surface Facing Reactor	10 " Side Riser Surface	2" Riser Surface Facing Cavity Wall
Area ft^2	3092.9	5084.67	176	1760	176	234.67	2346.67	234.67	792	7920	792	462	4620	462

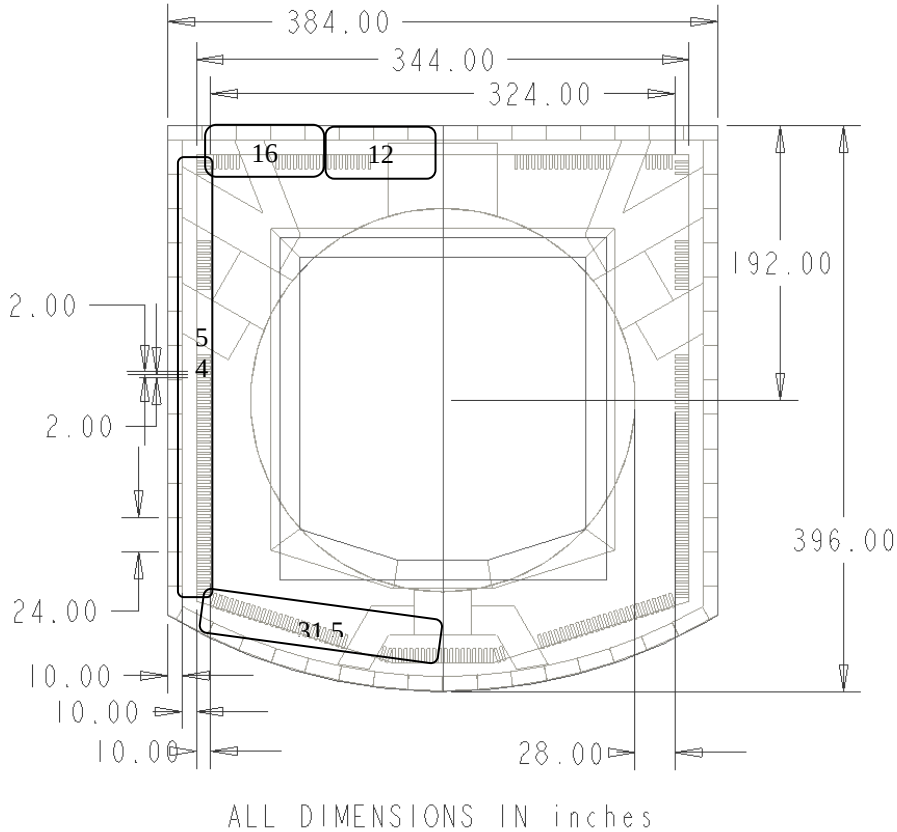

Figure 2.5 Cavity Cross Section-Group of 4A Location

and bottom of the configuration. The Up & Down is this empty space that a surface radiates to.

Another 4-Group configuration for the riser ducts considered in this evaluation is the configuration termed Group 4B. In this configuration the group of hot riser ducts along the curved cavity wall is subdivided into two sub-groups. Group 1 and Group 2 remain the same grouping of ducts as in the 3-Group configuration along the two non-curved cavity walls. Group 3 is now the sub-set of riser ducts along the curved wall which are closer to the corner where the discharge ducting that leaves the cavity, connects to the hot plenum. The remaining sub-set of risers along the curved wall which are closer to the mid-plane of the cavity symmetry now forms Group 4. The number of hot riser ducts in each of the four groups is shown in Figure 2.6. With the half-mirror symmetry of the cavity only half the ducts (113.5) are shown in the groups. The same node numbering was kept for the right side of the system as the left side. Group 1 starts with the top-middle grouping of Fig. 2.4. Each duct has a front surface, back surface, and side surfaces (which were lumped together).The side, front (facing the reactor), and back (facing the cavity wall) surface nodes were numbered 1, 2, and 4, respectively. The group numbering continued in the counter-clockwise direction ending in the bottom –middle group in Fig 2.6. Surfaces of Groups 2 to 4 were numbered with the first digit being the group number

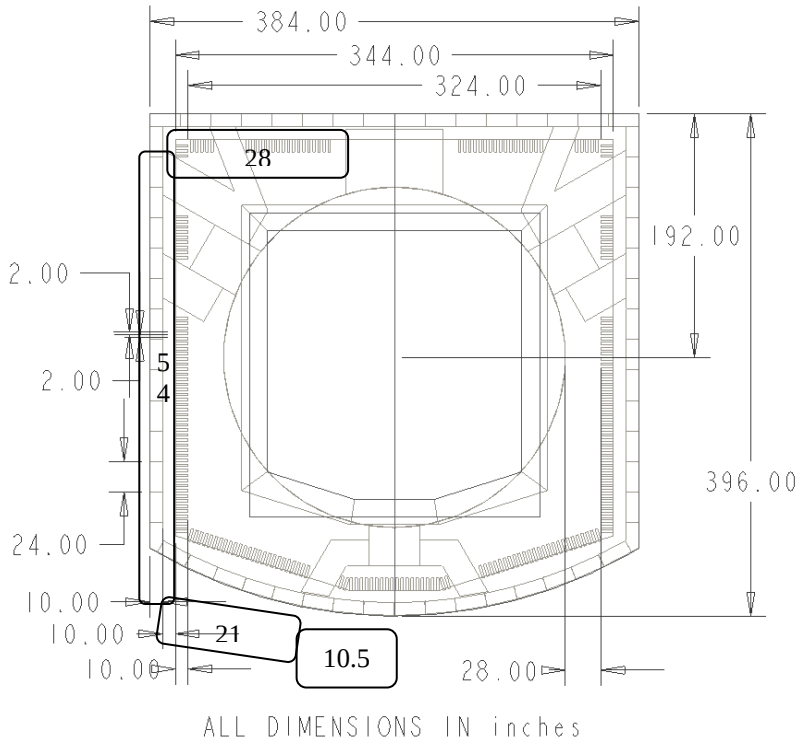

Figure 2.6 Cavity Cross Section-Group of 4B Location

followed by 0 for the Front Surface, 1 for Side Surface, and 2 for the Back Surface. The Reactor Pressure Vessel was input as a perfect cylinder (node 55). The back cavity wall was a single entity (node number 99).

Table 2.9 shows the view factors from the reactor vessel to the duct surfaces and the cavity back wall for all the surfaces in the 4B-Group model configuration. This Table also includes the view factors from the reactor to the duct surfaces of each of the three groups. Table 2.10 shows the surface areas (ft^2) of each component. The RELAP5 models which use these view factors as input assumed no radiation in the axial direction. Therefore, in order to minimize the view factor towards the top and bottom, the height of all the surfaces was increased to simulate infinite height: 9999”. The height greatly reduced the view factor towards the top and bottom, giving a more accurate view factor for the RELAP5 input. Since this “infinite” height calculation was made, the areas from the RENO results were corrected for the finite 44’ tall cavity in the RELAP5 deck. The RENO computation takes into account this “empty space” in the model. This is the top and bottom of the configuration. The Up & Down is this empty space that a surface radiates to.

The final lumped configuration for the riser ducts considered in this evaluation is the configuration termed Group of 5. In this configuration the group of hot riser ducts along the cavity wall which has the cross-vessel penetration remains as Group 1. However, the group of hot riser ducts along the remaining non-curved cavity wall is subdivided into three sub-groups. Group 2 is now the sub-set of riser ducts along the

Table 2.9. View Factors-Group of 4B

					Group 1			Group 2			Group 3			Group 4			
			Reactor	Cavity Wall	2" Riser Surface Facing Reactor	10 " Side Riser Surface	2" Riser Surface Facing Cavity Wall	2" Riser Surface Facing Reactor	10 " Side Riser Surface	2" Riser Surface Facing Cavity Wall	2" Riser Surface Facing Reactor	10 " Side Riser Surface	2" Riser Surface Facing Cavity Wall	2" Riser Surface Facing Reactor	10 " Side Riser Surface	2" Riser Surface Facing Cavity Wall	Space
Node			55	99	2	1	4	50	51	52	80	81	82	100	101	102	
Surface			RX	UH3	FW	SW1	WTB	F1	s1	B1	F1	S1	B1	F19	S37	B19	Space
	55	RX	0	0.2912	0.0931	0.0882	0	0.1679	0.1606	0	0.0644	0.0574	0	0.0379	0.0354	0	0.0041
	99	UH3	0.1770	0.0734	0.0095	0.0996	0.0807	0.0098	0.1952	0.1556	0.0020	0.0674	0.0605	0.0000	0.0366	0.0302	0.0024
Group 1	2	FW	0.7006	0.1175	0	0.0001	0	0.0711	0.0959	0	0.0048	0.0050	0	0	0	0	0.0049
	1	SW1	0.0663	0.1233	0.0000	0.7793	0.0000	0.0141	0.0158	0	0.0001	0.0001	0	0	0	0	0.0008
	4	WTB	0	0.9993	0	0	0	0	0	0	0	0	0	0	0	0	0.0007
Group 2	50	F1	0.6558	0.0627	0.0369	0.0731	0	0.0002	0.0001	0	0.0513	0.0655	0	0.0193	0.0303	0	0.0048
	51	s1	0.0627	0.1254	0.0049	0.0082	0	0.0000	0.7781	0.0000	0.0058	0.0091	0	0.0019	0.0030	0	0.0008
	52	B1	0	0.9993	0	0	0	0	0.0001	0	0	0	0	0	0	0	0.0007
Group 3	80	F1	0.6471	0.0323	0.0064	0.0013	0	0.1321	0.1487	0	0.0077	0.0126	0	0.0031	0.0030	0	0.0057
	81	S1	0.0577	0.1113	0.0007	0.0001	0	0.0168	0.0234	0	0.0013	0.7831	0.0000	0.0010	0.0037	0	0.0009
	82	B1	0	0.9990	0	0	0	0	0	0	0	0	0	0	0	0	0.0010
Group 4	100	F19	0.7592	0.0011	0	0	0	0.0992	0.1004	0	0.0063	0.0208	0	0.0040	0.0038	0	0.0050
	101	S37	0.0442	0.0806	0	0	0	0.0113	0.0114	0	0.0003	0.0066	0	0.0367	0.7717	0.0365	0.0007
	102	B19	0	0.9993	0	0	0	0	0	0	0	0	0	0	0	0	0.0007

Table 2.10. View Areas-Group of 4B

			Group 1			Group 2			Group 3			Group 4		
	Reactor	Cavity Wall	2" Riser Surface Facing Reactor	10 " Side Riser Surface	2" Riser Surface Facing Cavity Wall	2" Riser Surface Facing Reactor	10 " Side Riser Surface	2" Riser Surface Facing Cavity Wall	2" Riser Surface Facing Reactor	10 " Side Riser Surface	2" Riser Surface Facing Cavity Wall	2" Riser Surface Facing Reactor	10 " Side Riser Surface	2" Riser Surface Facing Cavity Wall
Area ft^2	3092.90	5084.67	410.67	4106.67	410.67	792.00	7920.00	792.00	308.00	3080.00	308.00	154.00	1540.00	154.00

remaining non-curved wall which are closer to the corner with Group 1 where the discharge ducting that leaves the cavity, connects to the hot plenum. The sub-set of centrally located riser ducts along this non–curved wall form Group 3. Group 4 is the remaining sub-set of risers along this non-curved wall which are closer to the other corner with the curved wall where the other discharge ducting that leaves the cavity, connects to the hot plenum. Group 5 is the same grouping of ducts as in the 3-Group configuration along the curved cavity wall. The number of hot riser ducts in each of the five groups is shown in Figure 2.7. With the half-mirror symmetry of the cavity only half the ducts (113.5) are shown in the groups. The same node numbering was kept for the right side of the system as the left side. Group 1 starts with the top-middle grouping of Fig. 2.7 Each duct has a front surface, back surface, and side surfaces (which were lumped together).The side, front (facing the reactor), and back (facing the cavity wall) surface nodes were numbered 1, 2, and 4, respectively. The group numbering continued in the counter-clockwise direction ending in the bottom –middle group in Fig 2.7. Surfaces of Groups 2 to 5 were numbered with the first digit being the group number followed by 0 for the Front Surface, 1 for Side Surface, and 2 for the Back Surface. The Reactor Pressure Vessel was input as a perfect cylinder (node 55). The back cavity wall was a single entity (node number 99).

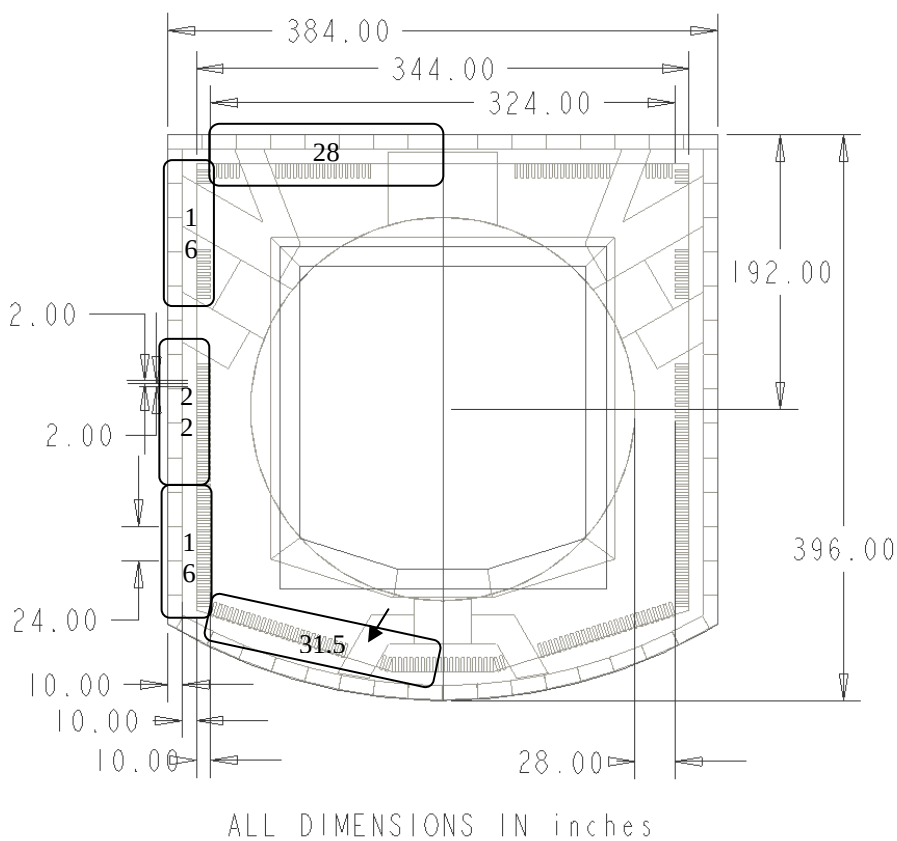

Figure 2.7 Cavity Cross Section-Group of 5Location

Table 2.11 shows the view factors from the reactor vessel to the duct surfaces and the cavity back wall for all the surfaces in the 4B-Group model configuration. It also

Table 2.11. View Factors-Group of 5

					Group 1			Group 2			Group 3			Group 4			Group 5			
			Reactor	Cavity Wall	2" Riser Surface Facing Reactor	10 " Side Riser Surface	2" Riser Surface Facing Cavity Wall	2" Riser Surface Facing Reactor	10 " Side Riser Surface	2" Riser Surface Facing Cavity Wall	2" Riser Surface Facing Reactor	10 " Side Riser Surface	2" Riser Surface Facing Cavity Wall	2" Riser Surface Facing Reactor	10 " Side Riser Surface	2" Riser Surface Facing Cavity Wall	2" Riser Surface Facing Reactor	10 " Side Riser Surface	2" Riser Surface Facing Cavity Wall	Space
Node			55	99	2	1	4	40	41	42	50	51	52	70	71	72	80	81	82	
Surface			RX	UH3	FW	SW1	WTB	F1	S1	B1	F17	s33	B17	F35	s67	B35	F1	S1	B1	Space
	50	RX	0.0000	0.2912	0.0931	0.0882	0.0000	0.0212	0.2510	0.0000	0.1031	0.0955	0.0000	0.0436	0.0400	0.0000	0.1022	0.0928	0.0000	0.0041
	99	UH3	0.1770	0.0734	0.0095	0.0996	0.0807	0.0021	0.0375	0.0230	0.0055	0.1025	0.0865	0.0022	0.0552	0.0461	0.0020	0.1040	0.0908	0.0024
Group 1	2	FW	0.7006	0.1175	0.0000	0.0001	0.0000	0.0300	0.0366	0.0000	0.0408	0.0589	0.0000	0.0004	0.0005	0.0000	0.0048	0.0050	0.0000	0.0049
	1	SW1	0.0663	0.1233	0.0000	0.7793	0.0000	0.0065	0.0067	0.0000	0.0076	0.0091	0.0000	0.0000	0.0000	0.0000	0.0001	0.0001	0.0000	0.0008
	4	WTB	0.0000	0.9993	0.0000	0.0000	0.0000	0.0000	0.0000	0.0000	0.0000	0.0000	0.0000	0.0000	0.0000	0.0000	0.0000	0.0000	0.0000	0.0007
Group 2	40	F1	0.5591	0.0893	0.1047	0.2262	0.0000	0.0000	0.0000	0.0000	0.0000	0.0000	0.0000	0.0000	0.0000	0.0000	0.0074	0.0075	0.0000	0.0050
	41	S1	0.0663	0.1628	0.0128	0.0235	0.0000	0.0000	0.7237	0.0000	0.0000	0.0033	0.0000	0.0000	0.0000	0.0000	0.0032	0.0032	0.0000	0.0010
	42	B1	0.0000	0.9992	0.0000	0.0000	0.0000	0.0000	0.0001	0.0000	0.0000	0.0000	0.0000	0.0000	0.0000	0.0000	0.0000	0.0000	0.0000	0.0007
Group 3	50	F17	0.7248	0.0633	0.0380	0.0712	0.0000	0.0002	0.0000	0.0000	0.0000	0.0001	0.0000	0.0000	0.0000	0.0000	0.0448	0.0531	0.0000	0.0045
	51	s33	0.0696	0.1224	0.0057	0.0088	0.0000	0.0000	0.0009	0.0000	0.0000	0.7667	0.0000	0.0000	0.0141	0.0000	0.0051	0.0059	0.0000	0.0008
	52	B17	0.0000	0.9993	0.0000	0.0000	0.0000	0.0000	0.0000	0.0000	0.0000	0.0000	0.0000	0.0000	0.0000	0.0000	0.0000	0.0000	0.0000	0.0007
Group 4	70	F35	0.5744	0.0483	0.0005	0.0004	0.0000	0.0000	0.0000	0.0000	0.0000	0.0000	0.0000	0.0000	0.0001	0.0000	0.1504	0.2203	0.0000	0.0055
	71	s67	0.0494	0.1126	0.0001	0.0001	0.0000	0.0000	0.0000	0.0000	0.0000	0.0241	0.0000	0.0000	0.7713	0.0000	0.0144	0.0272	0.0000	0.0007
	72	B35	0.0000	0.9993	0.0000	0.0000	0.0000	0.0000	0.0000	0.0000	0.0000	0.0000	0.0000	0.0000	0.0001	0.0000	0.0000	0.0000	0.0000	0.0007
Group 5	80	F1	0.6847	0.0219	0.0042	0.0009	0.0000	0.0019	0.0083	0.0000	0.0428	0.0469	0.0000	0.0763	0.0775	0.0000	0.0106	0.0186	0.0000	0.0055
	81	S1	0.0532	0.1010	0.0004	0.0001	0.0000	0.0002	0.0008	0.0000	0.0045	0.0049	0.0000	0.0104	0.0138	0.0000	0.0139	0.7839	0.0121	0.0008
	82	B1	0.0000	0.9991	0.0000	0.0000	0.0000	0.0000	0.0000	0.0000	0.0000	0.0000	0.0000	0.0000	0.0000	0.0000	0.0000	0.0000	0.0000	0.0009

Table 2.12. View Areas-Group of 5

			Group 1			Group 2			Group 3			Group 4			Group 5		
	Reactor	Cavity Wall	2" Riser Surface Facing Reactor	10 " Side Riser Surface	2" Riser Surface Facing Cavity Wall	2" Riser Surface Facing Reactor	10 " Side Riser Surface	2" Riser Surface Facing Cavity Wall	2" Riser Surface Facing Reactor	10 " Side Riser Surface	2" Riser Surface Facing Cavity Wall	2" Riser Surface Facing Reactor	10 " Side Riser Surface	2" Riser Surface Facing Cavity Wall	2" Riser Surface Facing Reactor	10 " Side Riser Surface	2" Riser Surface Facing Cavity Wall
Area ft^2	3092.90	5084.67	410.67	4106.67	410.67	234.67	2346.67	234.67	322.67	3153.33	322.67	234.67	2420.00	234.67	462.00	4620.00	462.00

includes the view factors from the reactor to the duct surfaces of each of the three groups. Table 2.12 shows the surface areas (ft^2) of each component. The RELAP5 models which use these view factors as input assumed no radiation in the axial direction. Therefore, in order to minimize the view factor towards the top and bottom, the height of all the surfaces was increased to simulate infinite height: 9999". The height greatly reduced the view factor towards the top and bottom, giving a more accurate view factor for the RELAP5 input. Since this "infinite" height calculation was made, the areas from the RENO results were corrected for the finite 44' tall cavity in the RELAP5 deck. The RENO computation takes into account this "empty space" in the model. This is the top and bottom of the configuration. The Up & Down is this empty space that a surface radiates to.

2.1.2 Experiment Geometry

The experimental geometry is based on the planned experiment at the Argonne NSTF [2.3]. The NSTF was originally designed to simulate a Reactor Vessel Auxiliary Cooling System (RVACS) for the Advanced Liquid Metal Reactor Program. The NSTF test section essentially consists of a metal box, 7.7 m in height and 1.32 m x 1.46 m in cross section, surrounded on the outside by insulation. One side of the box contains a ceramic heater to simulate heating from the active core height (6.7 m maximum) in a reactor. There is a small air gap between this heater and a steel plate simulating the RPV. The opposite unheated side of the box is meant to represent the metal shield and concrete structure around the reactor. The other two sides consist of two steel brackets each, to support the structure, with insulation between and behind the brackets, as shown in Figure 2.8.

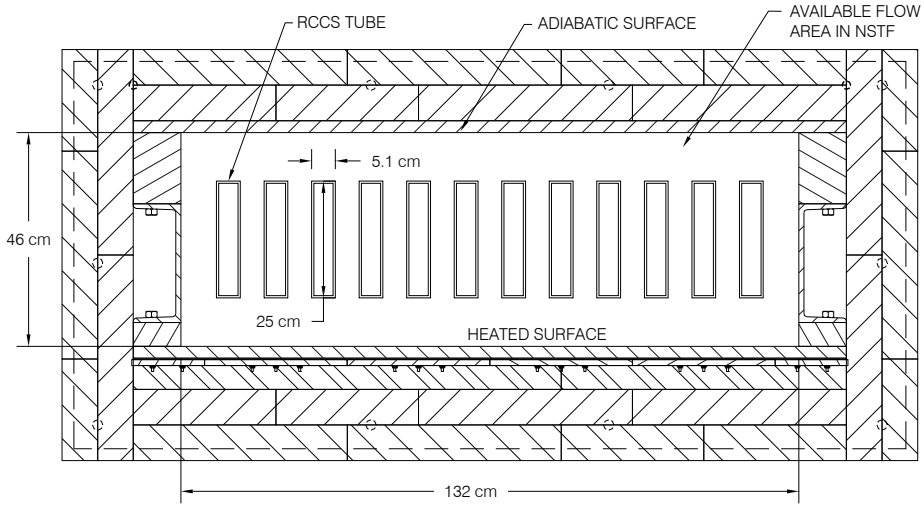

Figure 2.8. Experiment Cross Section – Group of 2 Location

Twelve riser ducts are located near the back wall, with the same shape and radial dimensions as the full-scale model. The bottom ends are located above the bottom of the box, to provide flow area for the natural circulation of air in the cavity. The riser ducts have a total length of 22', which means that they occupy the entire heated length of the box, and are flush with the top cover of the box. This configuration exists because the

cover is necessary to support the riser. Furthermore this cover forms the bottom of the hot plenum into which the hot risers discharge the heated natural convection air which is removing the core residual heat. As was discussed in section 2.1.1 and displayed in Figure 2.2 there is considerable azimuthal variation in the radiation view factors from the reactor vessel wall to the surfaces of the hot riser ducts. To simulate this variation in the experiments one approach is to vary the depth of the box. This thereby changes the distance between the heated box surface simulating the reactor vessel wall and the riser ducts. The effect of this variation on the view factors from the heated box wall to the other surfaces in the test cross section is displayed Figures 2.9 and 2.10. There is a 2-Group lumping of the riser ducts incorporated in these results. The Inner Group ducts are the eight central ducts and the Outer Group is the subset of the two outer ducts on each side of the Inner Group flanking the two side walls of the box. In this fashion the temperature gradient induced by the heat loss through the side wall insulation can be modeled by the corresponding RELAP5 calculations. Figure 2.9 show the results for the actual heated wall test height of 22ft. The top Figure is for the raw data while the bottom Figure normalizes the raw view factors to the values of 1 at a separation distance between the heated surface and the front wall of the riser ducts of 4”. It appears that a variation of a factor of 2 can be produced by this approach in both the front duct wall and side duct wall view factors. While the view factor for the box side wall can dominate at the largest separation it appears that at the minimum separation distance the view factor for the vessel to the front duct wall of the twelve test ducts can approach the larger values for the reactor cavity configuration. As for the reactor cavity the corresponding view factors for the side duct wall are close to the front duct wall. The potential radiation heat losses to the box sides require attention to the insulation of these sides and reflectivity of the surfaces. The potential losses to the top and bottom are very small at the minimum separation but are more significant for the maximum separation. Figure 2.10 is the equivalent of Figure 2.9 but for an “infinite” heater test height. This shows the effect on the top and bottom losses. It essentially redistributes those view factors to the other surfaces. Table 2.13 and Table 2.15 presents the details of the raw view factor data displayed in Figure 2.10 at the minimum and maximum separation points of 4” and 45” respectively. These are the view factor numbers which are used in the RELAP5 calculations presented later in Section 2.4 since the RELAP5 models do not treat the axial radiation heat transfer. The corresponding surface areas for those calculations are tabulated in Tables 2.14 and 2.16 respectively.

To arrive at this modeling approach a series of radiation heat transfer parametrics on the view factors were performed with NEVADA/RENO. The basic configuration is the NSTF test section box enclosing a varying number of riser ducts. The riser duct plane cross section dimensions (2” front wall x 10” side wall) remains that of the GA-MHTGR values for the whole set of parameterics. However the duct height varies from the node size of 2.2’ used in the RELAP5 analyses discussed in the next section, to 22’ which is the half scale height and finally to 44’ which is the full height of the heated vessel wall in the corresponding RELAP5 models. Figs 2.11 to 2.13 show the results for the view factors form the heated surface of the box. This heated surface of the box is intended to simulate the hot reactor vessel wall during the experiment. The Back Wall in the Figures is the box wall directly opposite the heated surface while the Insulated Side Wall is the

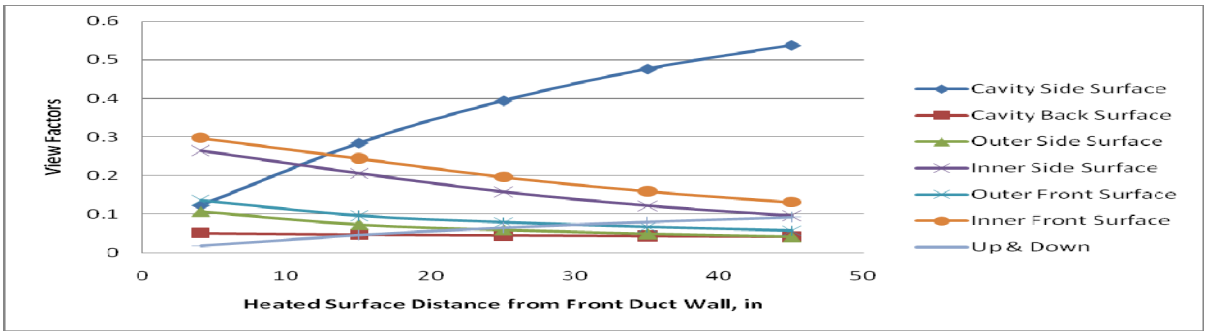

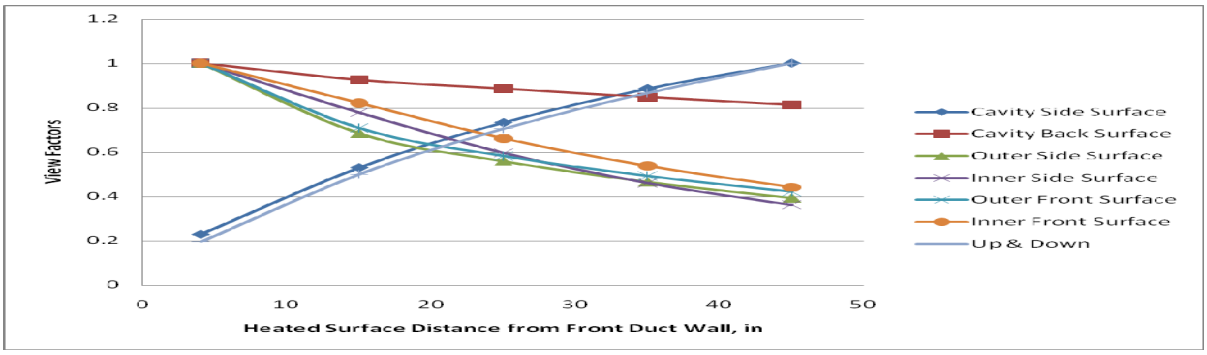

Figure 2.9 Two Group Raw and Normalized View Factors with Experiment Cavity Depth 22' Height)

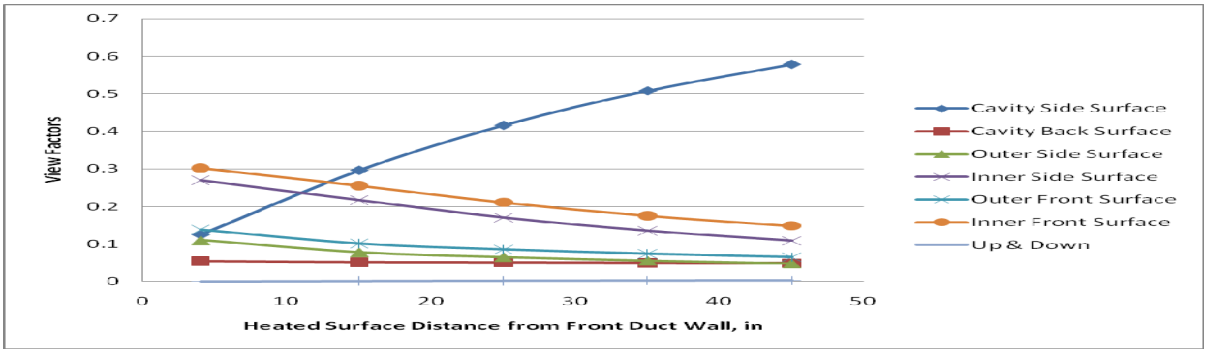

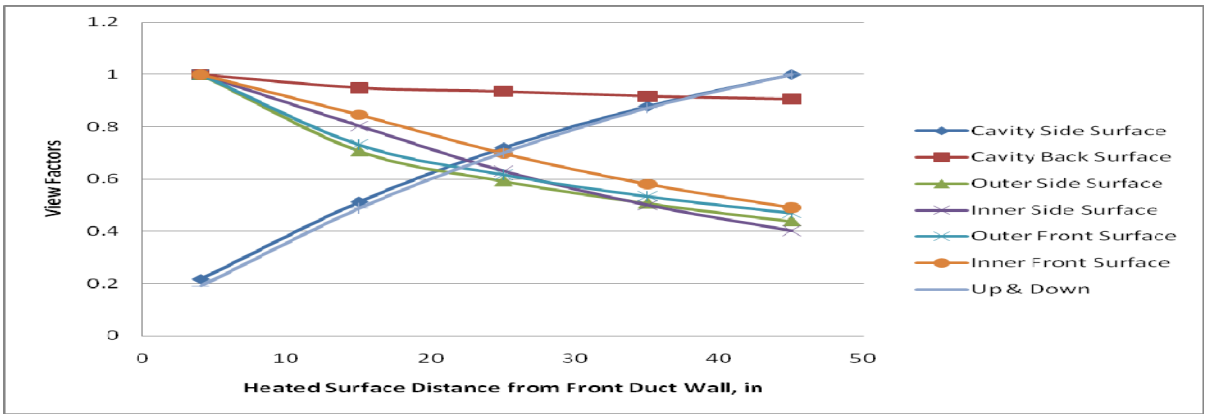

Figure 2.10 Two Group Raw and Normalized View Factors with Experiment Cavity Depth (9999' Height)

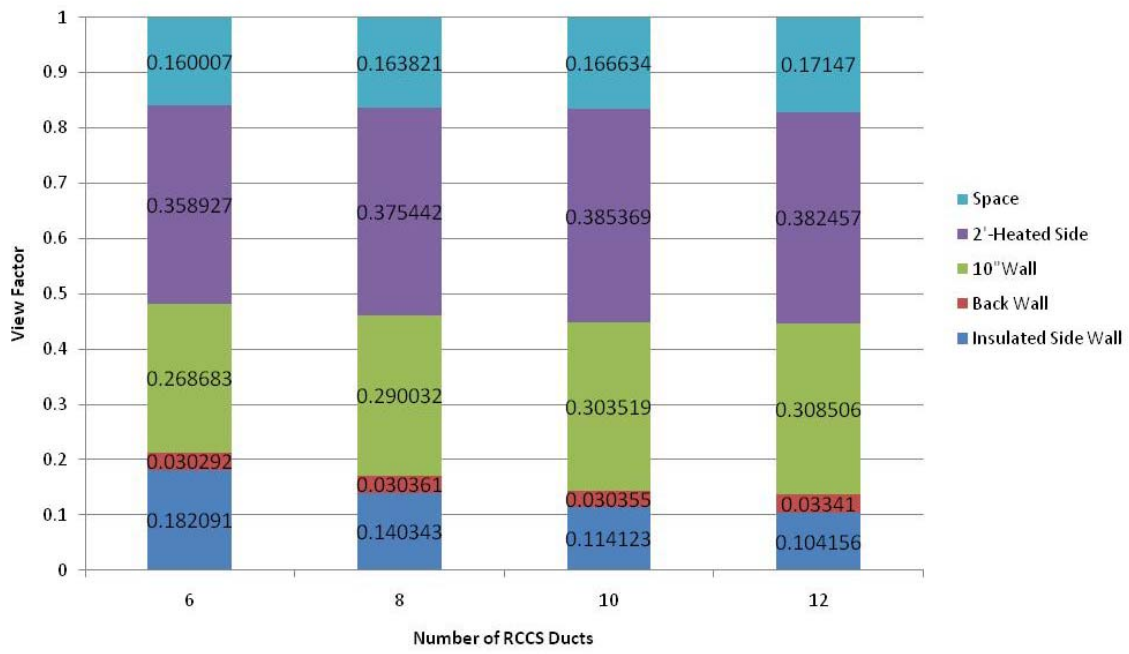

Figure 2.11 Experiment View Factors with Riser Ducts (2.2' Height)

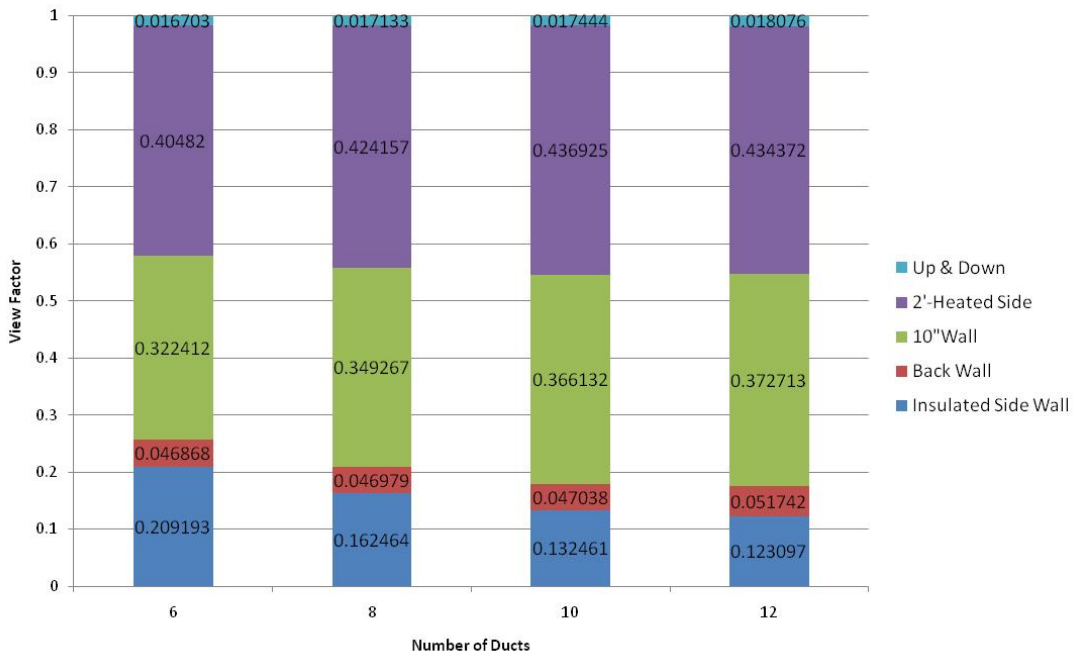

Figure 2.12 Experiment View Factors with Riser Ducts (22' Height)

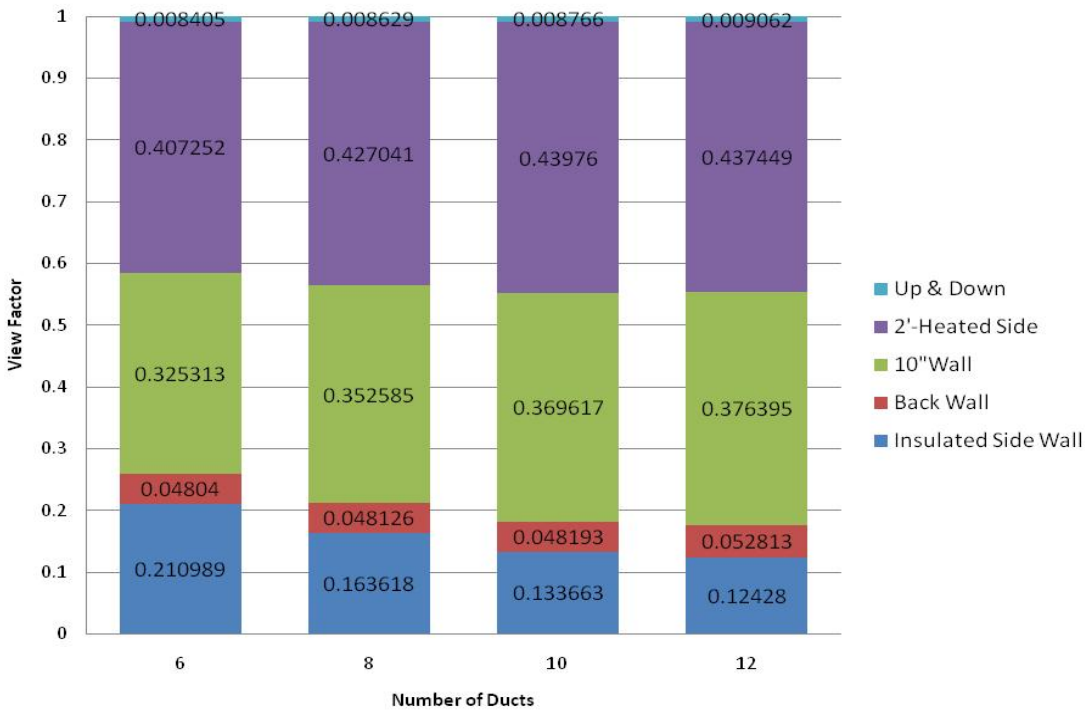

Figure 2.13 Experiment View Factors with Riser Ducts (44' Height)

two box side walls grouped together. These non-heated walls of the box are backed by insulation to minimize the parasitic heat losses during the experiments. It is evident that the axial radiant heat transfer to the top and bottom of the box as represented by the Space view factor is important at the RELAP5 nodal level but once the height is increased to 22' the top and bottom losses out off NSTF are insignificant and can be neglected in the analytical evaluation. For the full height reactor scale configuration this is even more evident. The dependence on the number of ducts provides guidance for the selection of the grouping of ducts and number of riser channels in the RELAP5 modeling. This is to account for the heat losses to the side walls of the box and the transverse temperature gradients.

Table 2.13.Two Group Experiment View Factors-4" Separation

				Inner Group				Outer Group				
			Reactor	2" Riser Surface Facing Reactor	10 " Side Riser Surface	2" Riser Surface Facing Cavity Wall	Cavity Back Surface	2" Riser Surface Facing Reactor	10 " Side Riser Surface	2" Riser Surface Facing Cavity Wall	Cavity Side Surface	Up & Down
			Heated	FW2	SW3	WTB3	UH3	FW1	SW1	WTB	UH1	Space
			1	2	3	4	5	6	7	8	9	
	Heated	1	0.0	0.3020	0.2700	0.0	0.0541	0.1380	0.1102	0.0	0.1253	0.0004
Inner Group	FW2	2	0.9816	0.0	0.0	0.0	0.0	0.0	0.0	0.0	0.0179	0.0005
	SW3	3	0.0878	0.0	0.717212	0.0	0.0877	0.0	0.1025	0.0	0.0046	0.0003
	WTB3	4	0.0	0.0	0.0	0.0	0.9817	0.0	0.0	0.0	0.0180	0.0004
	UH3	5	0.0541	0.0	0.2700	0.3020	0.0	0.0	0.1102	0.1379	0.1253	0.0005
Outer Group	FW1	6	0.8964	0.0	0.0	0.0	0.0	0.0	0.0	0.0	0.1031	0.0005
	SW1	7	0.0716	0.0	0.2049	0.0	0.0716	0.0	0.4098	0.0	0.2418	0.0003
	WTB	8	0.0	0.0	0.0	0.0	0.8964	0.0	0.0	0.0	0.1032	0.0004
	UH1	9	0.1810	0.0079	0.0204	0.0080	0.1809	0.0229	0.5374	0.0229	0.0180	0.0005

Table 2.14.Two Group Experiment View Areas-4” Separation

		Inner Group				Outer Group			
	Reactor	2" Riser Surface Facing Reactor	10 " Side Riser Surface	2" Riser Surface Facing Cavity Wall	Cavity Back Surface	2" Riser Surface Facing Reactor	10 " Side Riser Surface	2" Riser Surface Facing Cavity Wall	Cavity Side Surface
Area ft^2	95.333	29.3333	293.333	29.3333	95.333	14.66667	146.6667	14.66667	66.000

Table 2.15.Two Group Experiment View Factors-45” Separation

				Inner Group				Outer Group				
			Reactor	2" Riser Surface Facing Reactor	10 " Side Riser Surface	2" Riser Surface Facing Cavity Wall	Cavity Back Surface	2" Riser Surface Facing Reactor	10 " Side Riser Surface	2" Riser Surface Facing Cavity Wall	Cavity Side Surface	Up & Down
Node			Heated	FW2	SW3	WTB3	UH3	FW1	SW1	WTB	UH1	Space
Surface			1	2	3	4	5	6	7	8	9	
Reactor	Heated	1	0.0000	0.1490	0.1085	0.0000	0.0489	0.0649	0.0482	0.0000	0.5787	0.0025
Inner Group	FW2	2	0.4844	0.0000	0.0000	0.0000	0.0000	0.0000	0.0000	0.0000	0.5155	0.0026
	SW3	3	0.0354	0.0000	0.7174	0.0000	0.0879	0.0000	0.1021	0.0000	0.0568	0.0004
	WTB3	4	0.0000	0.0000	0.0000	0.0000	0.9817	0.0000	0.0000	0.0000	0.0179	0.0004
Cavity Back Surface	UH3	5	0.0488	0.0000	0.2700	0.3022	0.0000	0.0000	0.1102	0.1378	0.1305	0.0006
Outer Group	FW1	6	0.4216	0.0000	0.0000	0.0000	0.0000	0.0000	0.0000	0.0000	0.5761	0.0022
	SW1	7	0.0313	0.0000	0.2049	0.0000	0.0717	0.0000	0.4097	0.0000	0.2820	0.0004
	WTB	8	0.0000	0.0000	0.0000	0.0000	0.8965	0.0000	0.0000	0.0000	0.1032	0.0004
Cavity Side Surface	UH1	9	0.2550	0.0699	0.0772	0.0024	0.0576	0.0389	0.1912	0.0070	0.2986	0.0020

Table 2.16.Two Group Experiment View Areas-45” Separation

		Inner Group				Outer Group			
	Reactor	2" Riser Surface Facing Reactor	10 " Side Riser Surface	2" Riser Surface Facing Cavity Wall	Cavity Back Surface	2" Riser Surface Facing Reactor	10 " Side Riser Surface	2" Riser Surface Facing Cavity Wall	Cavity Side Surface
Area ft^2	95.333	29.3333	293.333	29.3333	95.333	14.66667	146.6667	14.66667	216.3333

2.2. RELAP5 Modeling

RELAP5-3D is a one-dimensional thermal hydraulics code developed by Idaho National Laboratory [2.2], initially designed for the analysis of transients in LWR systems. The code is generalized to handle a complex fluid system of liquid, vapor, and non-condensable substances, as well as heat transfer in the fluid and piping system. Systems are modeled as a series of hydrodynamic volumes containing flowing fluids, junctions that connect these volumes, heat structures to represent the piping and other physical objects, and radiation/conduction enclosures to facilitate non-convective heat transfer between heat structures. This section presents the results obtained by using the RELAP5 systems code to simulate the T-F phenomena in the air duct network which passively transports reactor generated heat to the ultimate atmosphere air heat sink. The

equivalent CFD simulation results with the STAR-CCM+ code are presented in Chapter 3. Modeling simulations of the multi-D reactor cavity are also to be carried out with the STAR-CCM+ code.

To address the effects of the non-symmetry/non-uniformity of the system geometry advantage is first taken of the half symmetry in the reactor cavity and the air duct network designs. Figure 2.7 shows this symmetry plane which cuts across the cavity walls A and C. The air duct network has in essence a two loop redundancy with the two loops (I and II) joined at the common manifold to the two sets of chimneys. A single failure should not block the discharge of the heated RCCS air to the atmosphere. Focusing on half of the RCCS, Loop I, it can be seen that the two hot-side connectors to the hot plenum at the two corners leading to the ex-cavity hot manifold in the building forces a certain non-symmetry in the hot-side of the air duct network. Approximately half of the hot air ducts along wall A feed to one of the two corners while approximately half of the hot riser ducts along wall C feed to the other corner. The flow split of the hot riser ducts along wall B between the two corners depend upon the flow resistance distribution in this non-symmetrical arrangement. The resistance in the ex-cavity hot manifold is one contributing factor. If thermal stratification and multi-dimensional flow patterns occur in this hot manifold or in the hot plenum then the concept of a 1-D flow resistance model requires modification. This multi-dimensional evaluation is carried out in the STAR-CCM CFD analysis summarized in Chapter 3.

Assuming that multi-dimensional effects do not occur then to establish the consequences for 1-D recirculation within the air duct network by using the 1-D RELAP5 system code, reference should be made to Figure 2.14. In this 1-D approach, a series of connected sequential RELAP5 calculations are carried out with the sequence of fluid flow nodalization/modeling shown in the series of figures. Each RELAP5 calculation in this scheme provides forcing boundary conditions for the subsequent RELAP5 calculation in the staggered steps. After the 1-channel RELAP5 analysis has been completed,

a. A 3-channel RELAP5 analyses is first performed where channel #1 represents the lumped average hot riser ducts along the half of wall C which feeds to the far corner of hot plenum discharging to the far side of the ex-cavity hot manifold. Channel #2 represents the average hot riser duct along wall B located equidistant from the two corners of the hot plenum which it feeds. Channel #3 is the equivalent of channel #1 but for wall A instead of wall C.
b. The results from (a) are used to provide the flows for the two forcing boundary conditions for walls A and C at the respective corners. The hot riser ducts along wall B are now separated into 3 different channels. Channel #1 now represents a lumped sub-group of hot riser ducts (16) closest to the near corner while channel #3 is the equivalent representation for a sub-group closest to the far corner. Channel #2 represents the lumped average central hot riser ducts along wall B
c. This is a combination of (a) and (b). Channel #3 is the lumped average hot riser duct along wall B. The wall A hot riser ducts are still represented

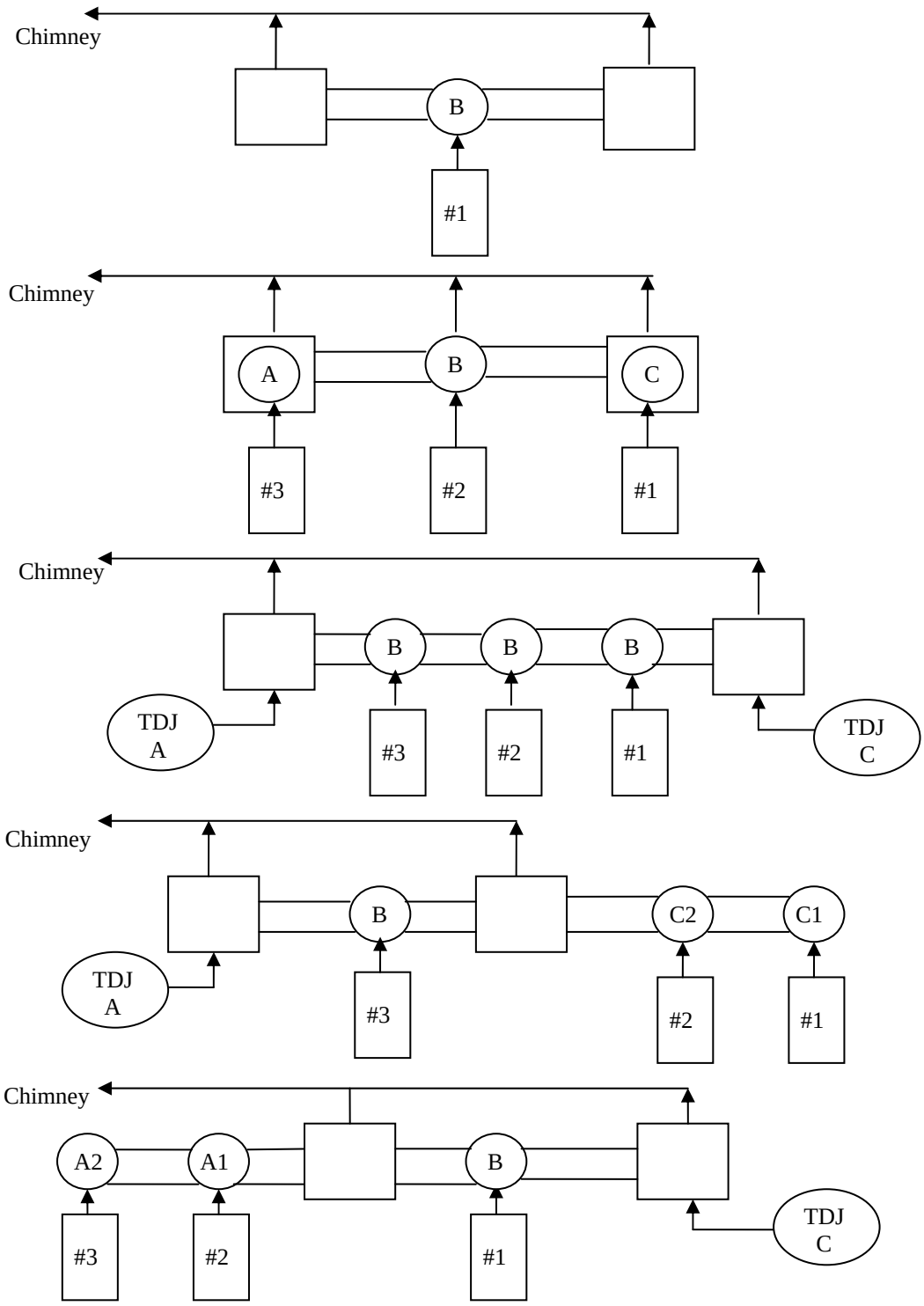

Figure 2.14 Flow Channel Modeling Groups

by a forcing boundary conditions using the flow results from (a). However the hot riser ducts along wall C are now represented by two channels #1 and #2. Channel #2 is the lumped average riser duct for the subgroup closest to the far corner, while channel #1 represents the centrally located riser ducts along wall C.

d. This is the equivalent of (c) but for the curved wall A instead of wall C.

In this modeling approach, the staggered sequence of RELAP5 analyses will (i) first evaluate the potential for gross recirculation of the air flow pattern and heat transport between the riser ducts along the four walls of the cavity as a whole and (ii) then evaluate the potential for recirculation of the air flow between the hot riser ducts at different locations along each wall. As a first step in implementing this approach one channel RELAP models have been constructed to first confirm the validity of the scaling approach defined in Chapter 1 before effort is focused on (a) to (d). To verify the scaling approach, the results are presented in Section 2.2.1 to 2.2.3 for a full-scale model of the GA-MHTGR RCCS, a half-scale model as dictated by the scaling approach and a model of the proposed NSTF experiments for the GA-MHTGR RCCS.

2.2.1 Full-Scale Model

The full-scale and half-scale standpipe system is shown, not to scale, in Figure 2.15. Heat structures are indicated in red and hydrodynamic volumes in blue. Heat structures and hydrodynamic volumes are further subdivided into axial nodes for greater accuracy. Heat structures also have finely sized radial nodes, which are not shown for clarity. The dimensions of the system are strictly those from the geometry. The GA-MHTGR air-cooled RCCS design has been modeled in RELAP5 as a one channel grouping of all the hot riser ducts in one half of the reactor cavity. Each half of the cavity is represented by this RELAP5 model together with the top and bottom cold plenum and the hot plenum in that half of the cavity. Also included are the ex-cavity hot and cold duct runs, the manifolds and the cold inlet and hot discharge chimneys, which form that half of the symmetric system, connected to the common atmosphere. It is assumed that the effect on the one RELAP5 group is representative of the effect on both halves and that the heat load is therefore mirror- symmetric. Dimensions are based on version V4 of the project CAD drawings and converted into the necessary RELAP5 input.

The RELAP5 modeling effort focused on the 1-hot riser model for the air-cooled RCCS of the GA-MHTGR all the way from the cold chimney inlet to the hot chimney outlet. The model includes a single down-comer, hot and cold ducting with the bends in the building, the manifolding, hot plenum and both top and bottom cold plenums for one of the two redundant RCCS loops. The simple cavity model is the branch B900 connected to an arbitrary large surge volume TDV905. TDV905 smooths out temperature-induced volumetric expansion. Heat structure HS9000 represents the heated vessel metal wall while HS9001 simulates the adiabatic back cavity wall. With the exception of these two heat structures there are no other metal heat sinks except for the hot riser duct wall. Additional metal heat capacity will be added later. Pipe 970 represents the heated portion of the hot riser with nodes numbered from 1 to 20. The unheated upper

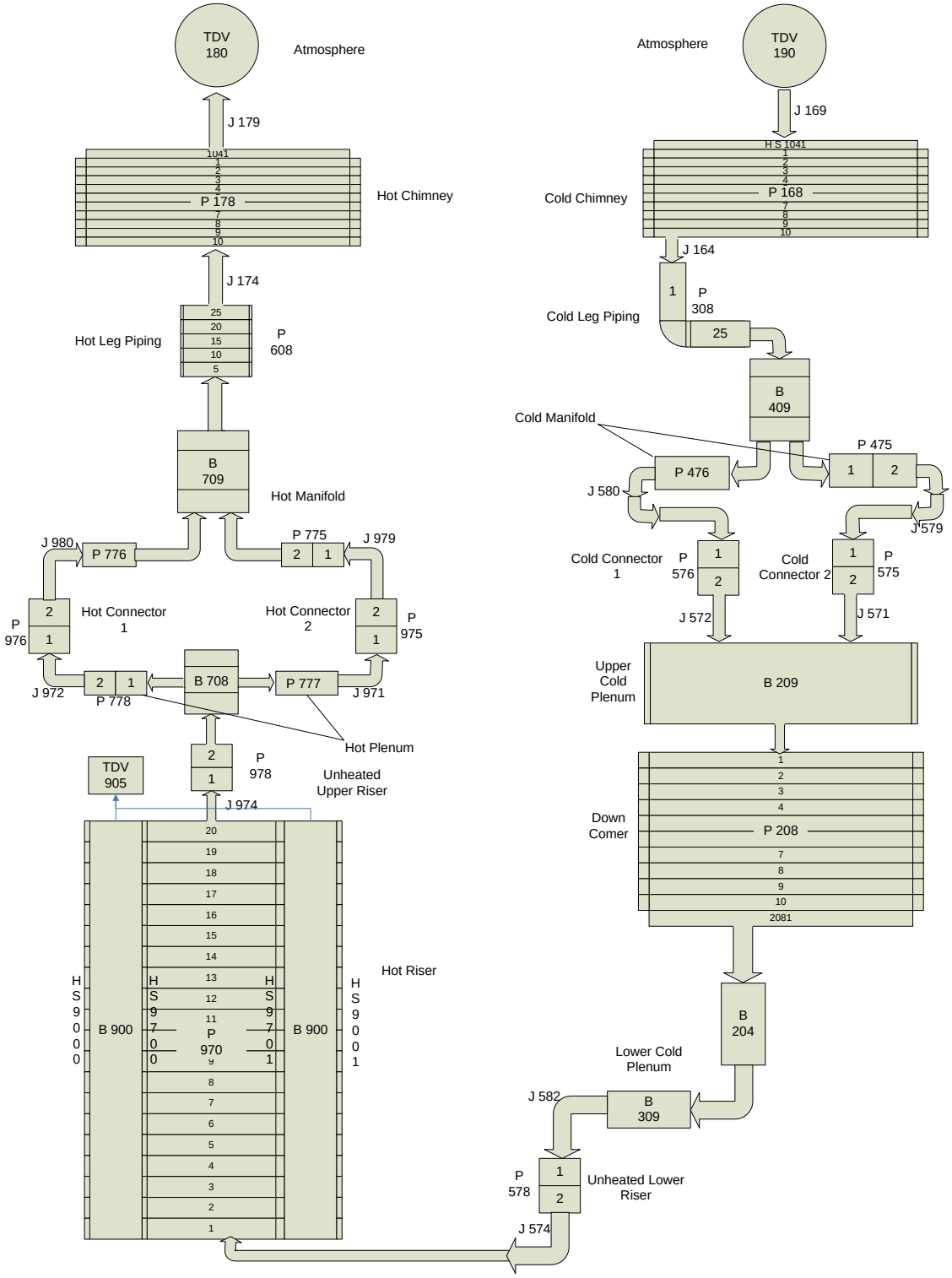

Figure 2.15. Full- Scale Model Cavity and Duct Network

part of the riser is represented by junction 974 and pipe 978. Junction 982 connects this upper riser section to the hot plenum. The hot plenum has two pipes 777 and 778 connected by branch 708. The connection with the hot riser is between the two pipes so this represents the flow splitting in the hot plenum to the four corners where the hot ducting exiting the reactor cavity is located. Since this is a half-system representation for the RCCS, only one of the two loops, Loop A is simulated. There are therefore only two vertical hot connectors, pipe 976 and pipe 975 to the horizontal hot duct manifold. Junctions 972 and 971 are the two junctions associated with these two connectors respectively which exit upward from the hot plenum. The horizontal manifold is represented by two sections pipe 775 and pipe 776 joined by branch 709. Pipe 775 represents the section between the two vertical connectors which are joined to the horizontal manifolding through junctions 979 and 980. Branch 709 connects the horizontal manifold to the ducting through the building which leads to the hot discharge chimneys. It allows the branching and flow merging effects to be simulated. The hot building ducting is represented by pipe 608 while pipe 178 is the volume for the hot chimney. There is a similar nodalization structure on the cold side. Pipe 168 represents the volume of the cold inlet suction chimneys while branch 309 represents part of the lower cold plenum. It allows the branching and flow splitting effects into the multiple hot risers from the multiple down-comers to be simulated. Pipe 475 is the analog of pipe 775 on the cold side. It is the cold manifold section between the two cold connectors, pipe 575 and pipe 576, leading to the upper cold plenum. Branch 209 is the upper cold plenum which is connected to the downcomer represented by pipe 208.

It should be reemphasized that for flexibility the height/length of pipe 970 which represents the heated portion of the hot riser has been selected to be 44’. So heat fluxes applied at the reactor vessel outer surface can give a maximum heated height of 44’. The unheated top riser height P978 has been chosen to be 7’ while the bottom unheated riser P578 has been selected to be 6’. The riser total height is therefore 57’. During actual transient scenarios the vessel wall heat flux is not spatially uniform particularly in the axial direction. The reactor power shape and the in-vessel natural convection lead to flux peaking and produce flux skews. Furthermore the active core height is only 26’ while the graphite stack height is ~ 37.7’. The first top reflector block-to- first bottom-reflector block height is ~32’. Finally it should be noted that the cylindrical part of the vessel is ~ 43’(bottom of head flange) to 45.57’ tall (top of head flange). It can be seen that this range of heights could possibly lead to a wide range of heated lengths of the vessel which could be radiating significant heat load to the RCCS ducts driven by the core residual heat. The chosen nodalization allows flexibility.

Since RELAP5 is essentially a 1-D code approximations have to be developed for representing the various plenums which are part of the RCCS. The ex-cavity duct runs and connectors are essentially one dimensional flow so it is simple to pick that flow direction in the RELAP5 volumes and the flow geometrical data associated with those flow components. In the case of the lower cold plenum the main flow direction is across the width of the plenum from the set of multiple down-comers to the set of multiple hot risers. The flow areas and the hydraulic diameters are evaluated using that 1-D flow assumption. In the case of the hot plenum the main flow direction is along the length of

the plenum towards the four corners of the plenum where the discharge ducting is located. The flow area and hydraulic diameter is therefore given by the axial cross section through the hot plenum. The final in-cavity plenum is the upper cold plenum. Similar to the hot plenum the main flow direction is long the length of the plenum as cold inlet air flow is pulled into the plenum at the entrances at the corners, turned and distributed across the plenum to the multiple cold down-comer channels. The flow areas, hydraulic diameters and other required flow geometry data are therefore computed by the same method as the hot plenum flow geometry data. The two cold air inlet chimneys and the two hot air discharge chimneys which are part of this half of the RCCS are lumped into a single cold chimney pipe P168 and a single hot chimney pipe P178. While the GA-MHTGR RCCS design for redundant capability has both a top port and a bottom side port for all of the chimneys, P178 and P168 approximates the respective chimney flows as vertical one dimensional with a single port at the top of the chimney. But the junction flow areas at these ports include all the design port areas. A final note here regarding the approximation of multi-dimensionality is that the interfacing between the ex-cavity ducting and the plenums in some regions reflects a combination of duct geometry and plenum geometry. Certainly alternative modeling approximations could be made.

The model demonstrates successful heat removal capabilities, even under conservatively high heat flux. However, in the single riser group flow mode there can be no evaluation of the potential flow recirculation between riser ducts. Since in a recirculation mode the residual heat may not be totally discharged to the ultimate heat sink the atmosphere, this model may need to be reevaluated. Removing this issue would appear to require multiple RELAP5 channels to represent different groups of hot riser ducts. This will be considered in the future. Heat losses from the system to the building environment are probably not significant but the heat transfer between the cold and hot sides of the RCCS could be more important. In particular in the long duct runs. This will be included in future models. Also slated for inclusion in the next iteration on RELAP5 modeling is the effect of intra-riser duct radiation between the four internal surfaces. With these changes, axially varying flux profiles or time-dependent fluxes should also be examined with the next set of RELAP5 models.

2.2.2 Half-Scale Model

The half-scale system was converted directly from the full-scale model. The design and nodalization is identical, and all assumptions made in the full scale were carried forward to the half scale. The system was scaled down to half scale according to the scaling reported in Section 1.3. Essentially, the lengths and heights were halved but the widths, depths, diameters and thicknesses in the plane cross-section were kept unaltered. The half-scale RELAP5 model has a number of different modifications which will be carried out in the next iteration. Since the half-scale deck was built by converting the full-scale deck it is the same set of modeling issues discussed above.

2.2.3 Experimental Model

The experimental system model was the starting point for the full-scale model. Figure 2.16 shows the experimental system RELAP5 model. This is based on the NSTF experiment cross section shown in Fig 2.8. A number of experiment cross section configurations are under discussion but they mainly involve varying the separation distance between the heated surface of the box and the hot risers. The test cavity box depth will be of variable design. There may be experiment configurations where the array of hot riser ducts is offset by a yet-to-be-determined angle to simulate corners of the cavity. Figure 2.16 will be the starting basis for modifying RELAP5 models as the experiment matrix is defined.

The twelve hot risers in the test cavity box section are grouped into two separate RELAP5 channels. These two channels are pipes P970 and 971. This is a two group lumping of the riser ducts incorporated in this model. The inner group consists of the eight inner central ducts and the outer group is the subset of the two outer ducts on each side of the inner group flanking the two side walls of the test section box. In this fashion the temperature gradient induced by the heat loss through the side wall insulation can be modeled by the corresponding RELAP5 calculations. The riser lengths are selected to be 22'. This is the heated surface height /length of heat structure HS9000 which simulates the heated wall of the box. This heated wall represents the hot vessel wall. Heat structure HS8000 and branch B800 are the NSTF ceramic heaters and the 1/8" air gap between these heaters and the heated box wall. The cavity box back wall is given by HS9712. The side wall is HS9002. All the box walls are externally insulated. Heat losses to the surrounding air from the insulation are also accounted for by the inclusion of the branches B300 and B400 on the outside to represent the surrounding air. Volumes TD405 and TD305 are arbitrary large volumes of air which form isothermal heat sinks to absorb the parasitic heat losses and to smooth out any volume expansion caused by temperature changes in the branches. A similar arrangement of branch and connected volume B900/TD905 is used to represent the box cavity air. HS9700, HS9701 and HS9702 simulate the front wall, two lumped side walls and back wall of the inner group of riser ducts. HS9710, HS9711 and HS9712 are the walls for the other group of riser ducts. The external ducting and hot manifold for the heated air from the test box hot risers is represented by pipe P978. It also includes the chimney discharging to the atmosphere. HS9780 is the metal structure around this flow path. The bottom suction inlet to the test box cavity is represented by branch B960 which takes its suction from the atmospheric air in volume TD950. TD980 is the corresponding air volume on the discharge side.

Both natural convection heat transfer and radiation heat transfer are simulated in the model. However the radiant heat transfer is only in the plane cross section as specified by the view factors. Axial radiation heat transfer, in particular to the top and bottom of the test cavity box, is not simulated. Slated for inclusion in the next iteration on RELAP5 modeling is the effect of intra-riser duct radiation between the four internal surfaces of the hot riser ducts. Currently the circumferential conduction around the duct walls of the hot riser ducts are simulated but this will be replaced by the simulation of the intra-duct

radiant heat transfer. Ambient heat losses from the insulated duct/chimney system to the building environment will also be included in the next iteration.

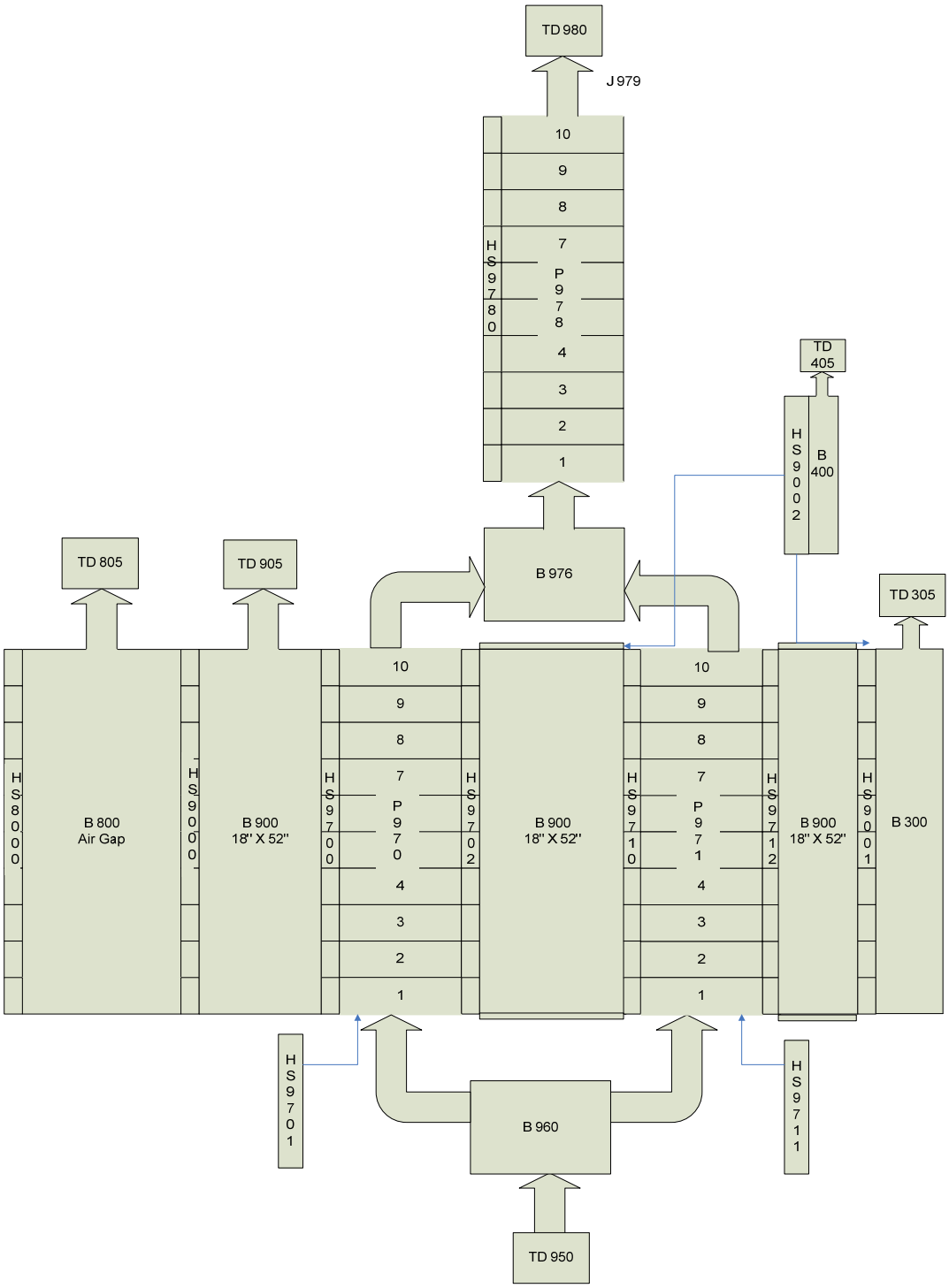

Figure 2.16. Experiment System Model Cavity and Duct Network

2.3. GA Results

This page left intentionally blank.

Figure 2.17. GA Results for RCCS Heat Load [2.3]

This page left intentionally blank.

Figure 2.18. GA Results for Vessel Temperature [2.3]

Table 2.17 GA Results for Depressurized Conduction Cooldown[2.3]

2.4 RELAP5 Results

The one-hot riser model deck was the baseline for the full-scale reactor air heat sink system analyses. Modifications will be made in the next iteration to better model heat losses such as between cold and hot ducting. The model was used as a baseline to test the response of the system to varying heat fluxes and confirm the scaling laws. Cases at 10-kW/m^2, 5-kW/m^2, and 2.5-kW/m^2 full-scale heat fluxes were run. The heat flux of 5.0kW/m^2 represents the reference reactor case of medium heat flux. The high heat flux case corresponds to the system model with l0-kW/m$^{2.}$. The heat flux of 2.5-kW/m^2 is the low heat flux case. It should be reemphasized that these are uniform heat fluxes applied at the reactor vessel outer surface with a heated height of 44'. During actual transient scenarios the vessel wall heat flux is not spatially uniform particularly in the axial direction. The reactor power shape and the natural convection in-vessel lead to flux peaking and produces flux skews. Furthermore the active core height is only 26' while the graphite stack height is ~ 37.7'. The First top-reflector block -to- First bottom-reflector block height is ~32'. Finally it should be noted that the cylindrical part of the vessel is ~ 43' (bottom of head flange) to 45.57' tall (top of head flange). It can be seen that this range of heights could possibly lead to a wide range of heated lengths of the vessel which could be radiating significant heat load to the RCCS ducts driven by the core residual heat. The reactor core power transferred during the decay heat accidents at peak RCCS heat load could vary from 1.75 MW for pressurized scenarios to 1.5 MW for depressurized scenarios. The steady state load at normal operating condition is ~ 0.7 MW. The envelope of uniform heat flux cases selected for this set of RELAP5 evaluations should cover this range of possible heat fluxes.

In addition to the full reactor scale cases, a series of cases were run with a half-scale model at heat fluxes proportionally scaled to the full size. This half-scale deck is used to verify the scaling analysis in Chapter 1. The duct flow areas and the radial dimensions of the cavity are maintained at full scale. Duct lengths, height and the cavity height are halved. The system power is reduced by a factor of the square root of 2, and scaled heat flux is increased by the same factor to maintain the scaled heat added per unit volume over the riser ducts. There are therefore also three corresponding heat flux cases; high, medium and low but different numerical values from the full-scale cases. The pressure loss over the system as represented by the friction drop dimensionless number will have to be preserved in the next iteration. Discussions are ongoing with the experimenters about calibration procedures for the system pressure flow drop at selected forced flow rates. Heat losses between the hot and cold sides will also be added.

To support the Argonne NSTF heat transfer experiments, cases with the experimental system was run as well. The baseline model of the experimental system is a two-hot riser model. This grouping of two risers is to allow transverse temperature gradients driven by the parasitic heat losses to be evaluated. The scaling allows for comparisons between the experimental system and the full-scale model. The system is currently assumed to be 50% scale, with the same changes made as in the half-scale model. As to be expected the major difference with the half-scale model is in the external duct runs, manifolds, connectors and the chimneys. Atmospheric parasitic heat loss from the NSTF box is included in the baseline cases. Cases were run at three internal power

generation levels. These power levels produce the three proportionally scaled heat fluxes equivalent to the full scale cases. Cases modeling no heat losses to the atmosphere, various separation distances between the box heated surface and the riser ducts and a one–hot riser approach were also evaluated.

A summary of the results for all the RELAP5 cases is presented in Table 2.18

Table 2.18. Summary of Cases

Full-Scale Values in Parenthesis	Full-Scale Reactor	Half-Scale Reactor	NSTF Experiment
High Flux ($9.95\ kW/m^2$).	Baseline (6.66 hours)	Baseline	Baseline Atmospheric Heat Loss RELAP5 Channels
Medium Flux ($4.97\ kW/m^2$)	Baseline (6.66 hours)	Baseline	Baseline
Low Flux ($2.50\ kW/m^2$)	Baseline (6.66 hours)	Baseline	Baseline

2.4.1 Full-Scale Model Result

Table 2.19 gives a summary of the full-scale results.

Case (1): Medium Heat Flux/No Modifications

This model is considered the baseline for all comparisons. The heat flux incident on the pressure vessel was $4.97\ kW/m^2$, representing a total heat load on half the pressure vessel of 0.715 MW. This was fortuitously close to the peak RCCS heat load as reported in [2.2] during a depressurization decay heat driven scenario Driven by this incident heat flux, the heat transferred from the outer surface of the pressure vessel wall is partitioned into a radiation heat flux of $4.0\ kW/m^2$ and a convective heat flux of $0.95\ kW/m^2$ off the vessel wall. This leads to a heat flux incident upon the front wall of the hot riser duct of $2.20\ kW/m^2$ .The case was run from cold shutdown conditions with a step-up to the driving power level. The transient duration was 24,000 seconds.

The model performed as expected as the T-F conditions monotonically increase to reach a stable steady condition in the asymptote. Table 2.19 shows that the peak air mass flow rate is 6.62 kg/s and the peak air velocity in the duct is 6.28 m/s. The peak pressure vessel wall temperature is 602ºK while the peak cavity wall surface temperature is 389ºK. The corresponding air temperature at the duct outlet is 393ºK. Focusing on the riser duct the peak front wall temperature is 467ºK; the peak side wall temperature is 411ºK and the peak duct back wall temperature is 420ºK. The time history of the riser duct air mass flow rate is shown in Figure 2.19. The variation in the air mass flow rate at various locations through the flow paths of the ex-cavity ducting network to the chimney is show in Figure 2.20. The axial locations included in the Figure start from the bottom of the riser and

proceed to the top. Figures 2.21 and 2.22 display the corresponding air flow velocities. The transient history of the pressure vessel outer wall temperature is given at the surface nodes starting from the bottom and proceeding to the top of the heated segment in Figure 2.23. The corresponding liner (insulation) temperature at the corresponding axial locations on the back wall of the cavity is displayed in Figure 2.24. More details on the temperatures of the hot riser duct can be found in Figure 2.25. The transient behavior of the temperatures of the hot riser duct front wall, side wall, back wall and air coolant can be observed. The metal temperatures in these Figures are axial profiles starting with the bottom node and proceed to the outlet end. In the case of the air temperature, temperatures ex-hot riser duct can also be found in Figure 2.25d. The locations start with the cold chimney inlet and transport through the cold suction ducting and manifolds down through the top and bottom cold plenums by way of the down-comer. Hot side locations can also be found in Figure 2.25d where the air heated by the transferred core residual heat rises out off the outlet of the hot riser into the hot plenum and thereon to the hot discharge ducting and manifolds into the hot chimney for ultimate discharge into the atmosphere.

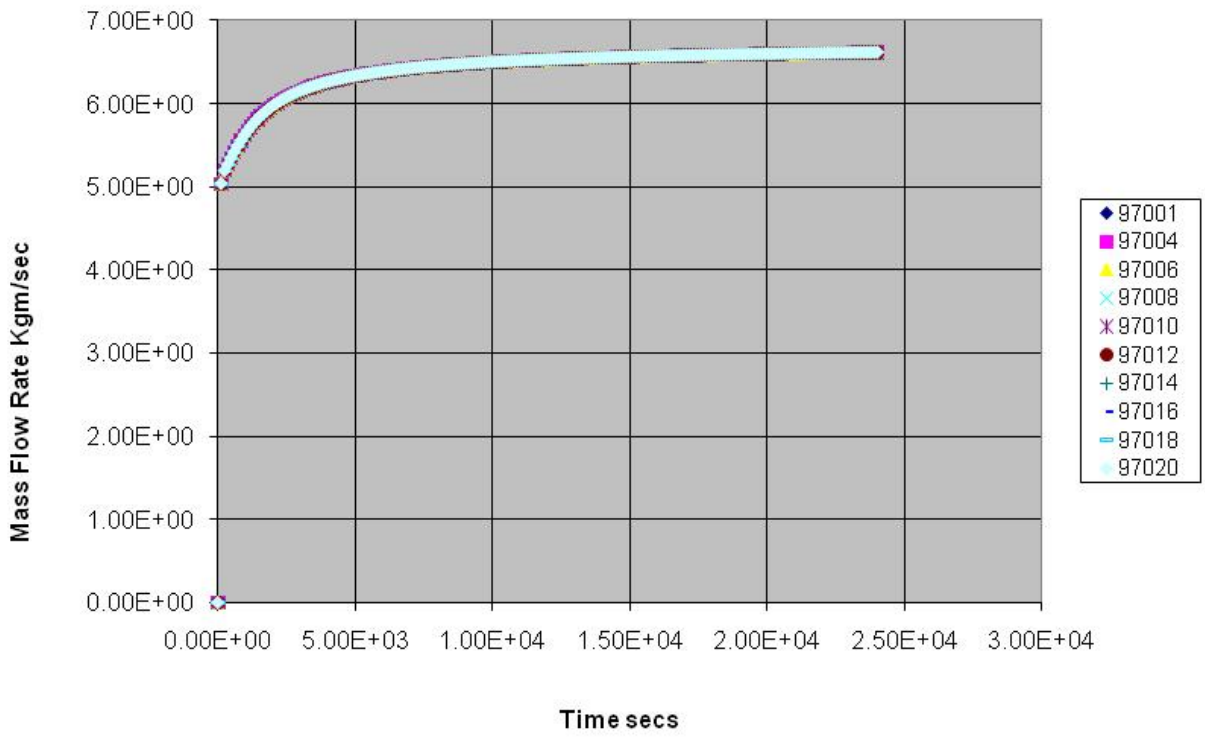

Figure 2.19. Full Scale/Medium Flux Riser Duct Air Total Mass Flow

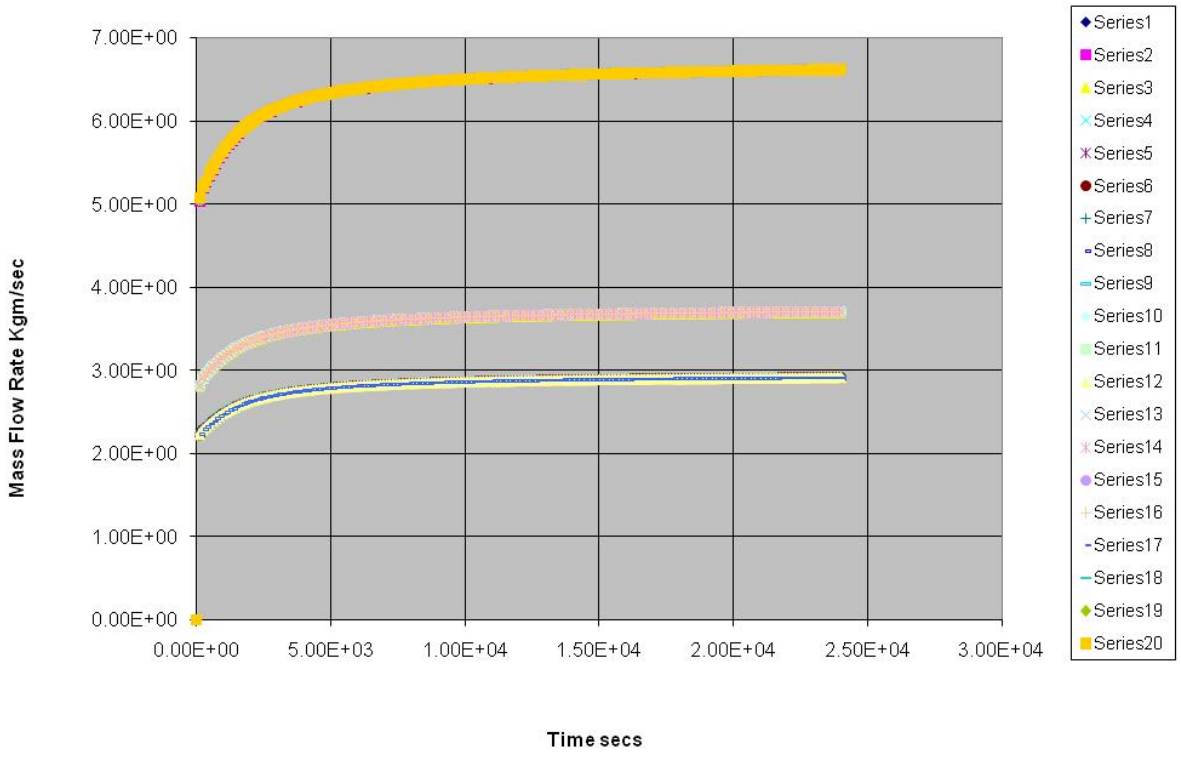

Figure 2.20. Full Scale/Medium Flux Hot Network Air Mass Flow

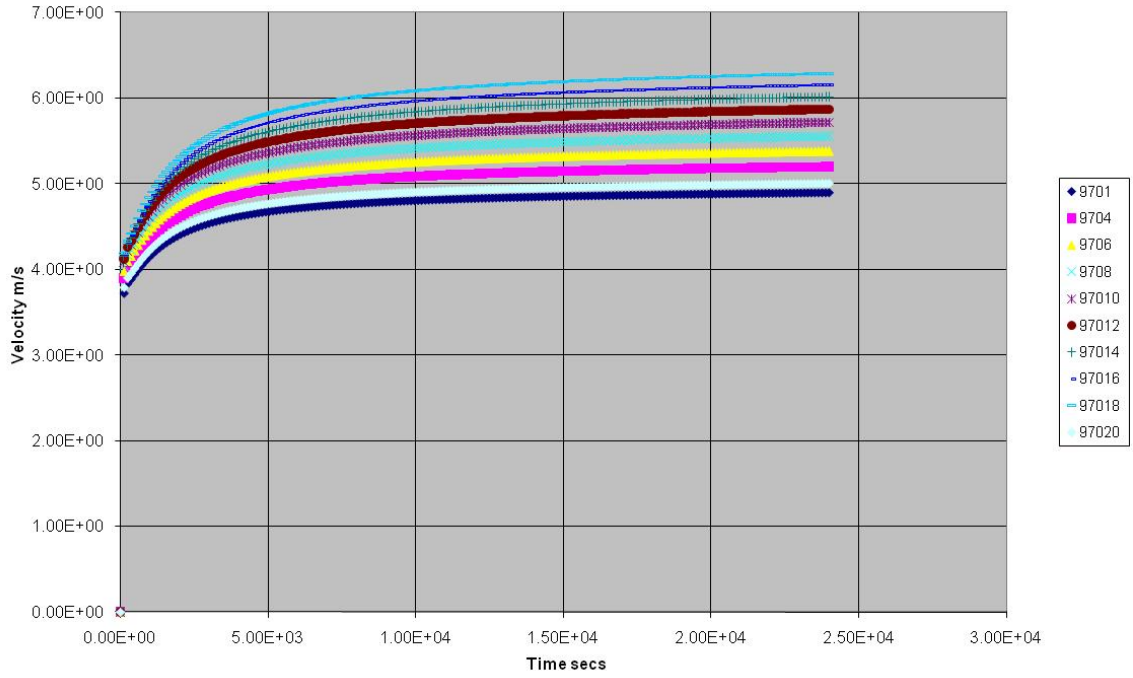

Figure 2.21. Full Scale/Medium Flux Riser Duct Air Velocity

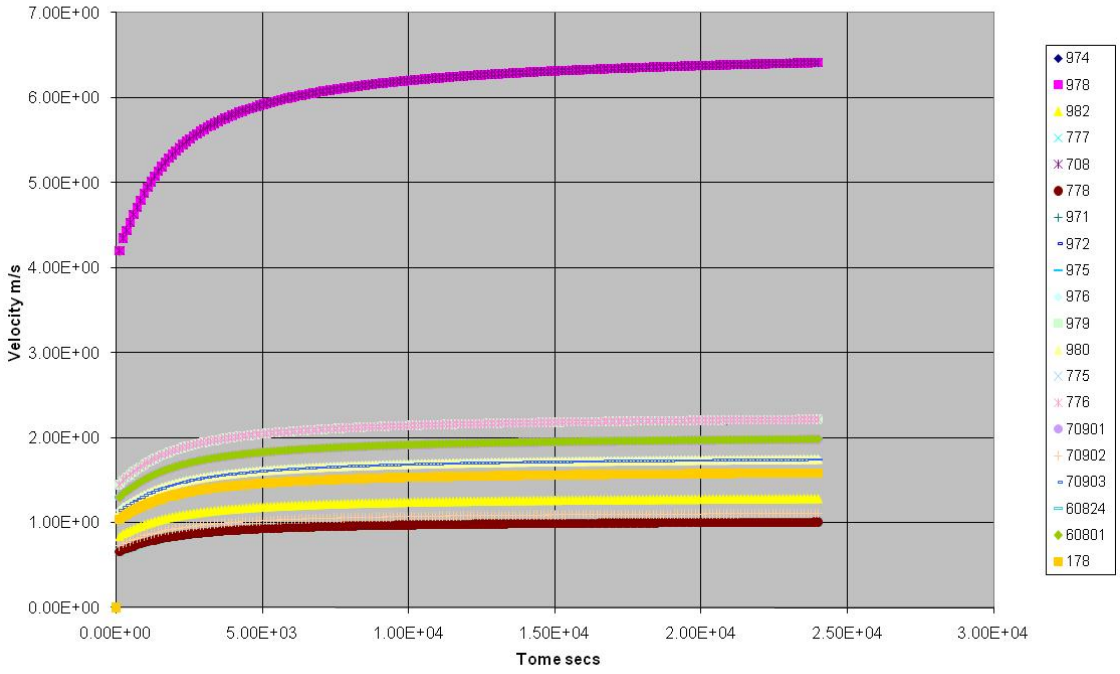

Figure 2.22. Full Scale/Medium Hot Network Air Velocity

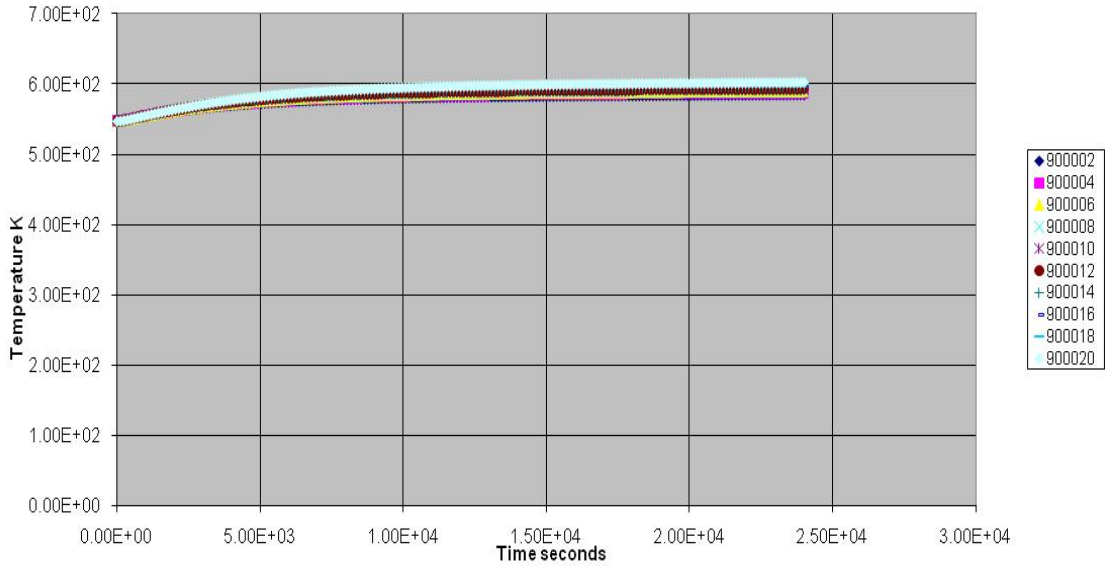

Figure 2.23. Full Scale/Medium Flux RPV Temperature

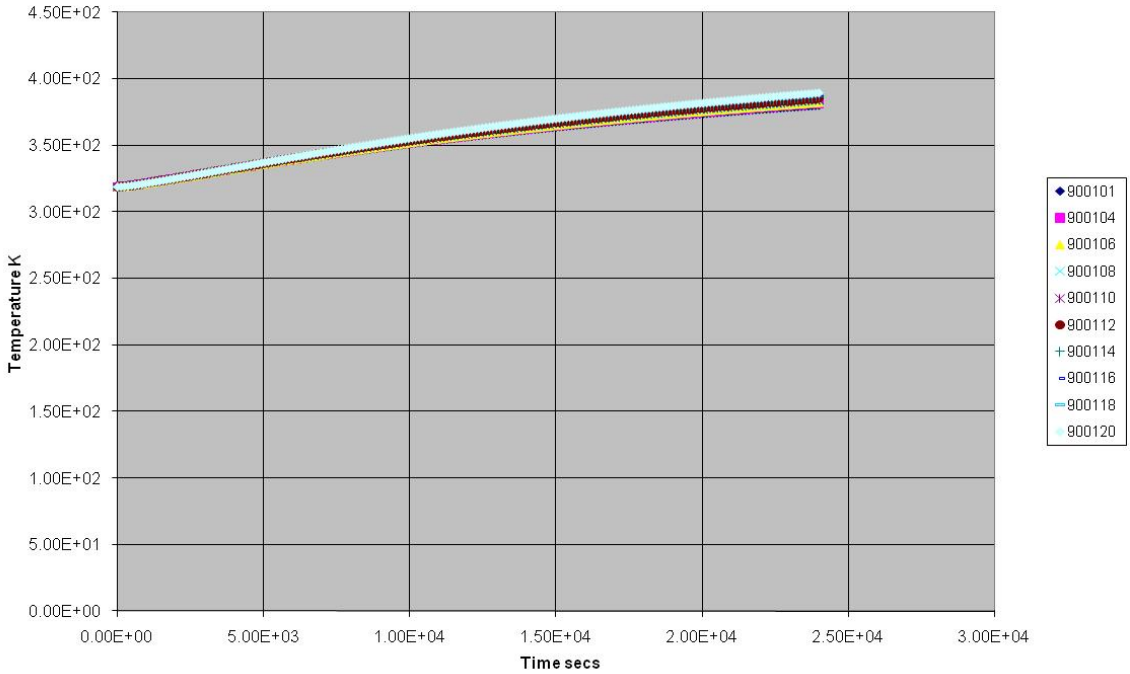

Figure 2.24. Full Scale/Medium Flux Cavity Back Liner Temperature

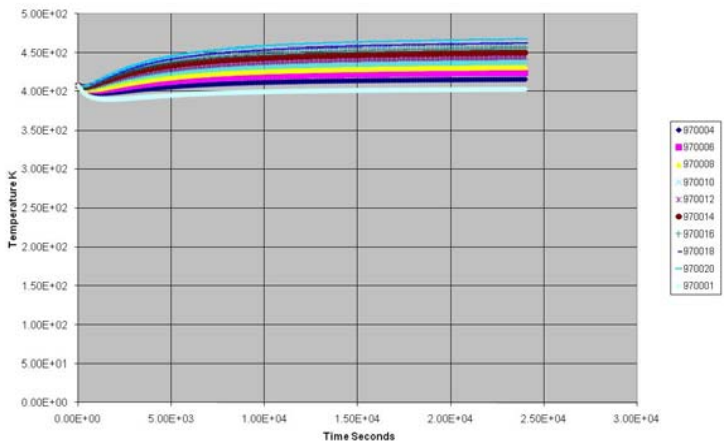

Figure 2.25a. Front Wall Temperatures

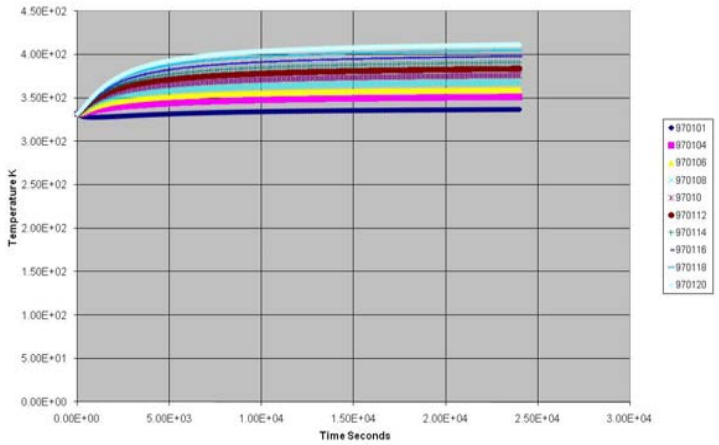

Figure 2. 25b. Side Wall Temperatures

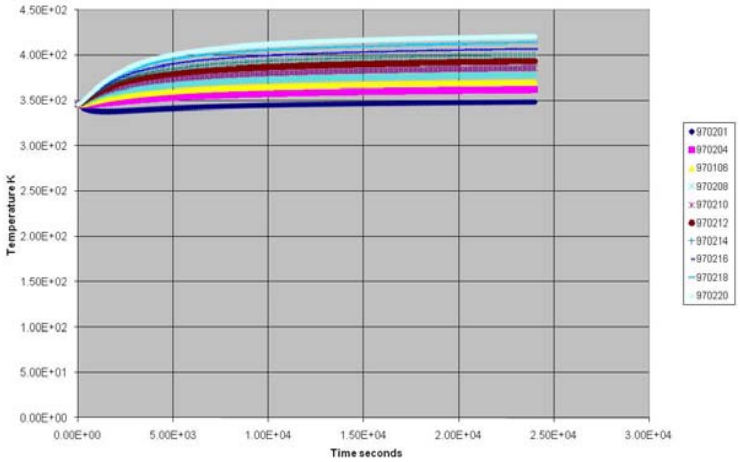

Figure 2. 25c. Back Wall Temperatures

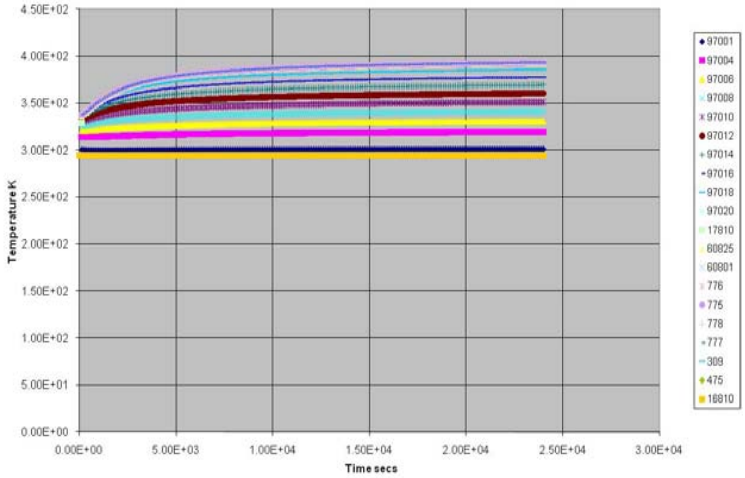

Figure 2. 25d. Air System Temperature Profile

Figure 2.25. Full Scale/Medium Flux Riser Duct Temperatures

Table 2.19 Summary of Full Scale/Half Scale Case Results

Model	Heat Flux	Modifications	Transient Length[s]	Peak Front Duct Wall Heat Flux [kW/m^2]	Peak Air Mass Flow Rate [kg/s]	Peak Duct Air Flow Velocity [m/s]	Peak Temperatures [K]			Peak Duct Temperatures [K]		
							RPV	Cavity Wall	Air Duct Outlet	Front Wall	Side Wall	Back Wall
Full Scale	High	None	24000	4.5146	7.5	8.43	739	471	471	593	505	519
Full Scale	Med	None	24000	2.2030	6.62	6.28	602	389	393	467	411	420
Full Scale	Low	None	24000	1.0308	5.61	4.8	500	347	352	394	362	367
Half Scale	High	None	24000	5.8443	6.6	6.93	801	504	438	633	501	527
Half Scale	Med	None	24000	2.991	5.81	5.28	653	409	376	495	410	424
Half Scale	Low	None	24000	1.423	4.96	4.13	539	358	341	409	360	368

Case (2): High Heat Flux/No Modification

This model was used to determine the effects of differing heat flux on the system, as well as provide a conservative estimate for concrete temperatures. The heat flux on the pressure vessel wall was 9.95 kW/m^2, which is equivalent to 1.43 MW of total heat from half the system.

Driven by this incident heat flux, the heat transferred from the outer surface of the pressure vessel wall is partitioned into a radiation heat flux of 8.76 kW/m^2 and a convective heat flux of 1.18 kW/m^2 off the vessel wall. This leads to a heat flux incident upon the front wall of the hot riser duct of 4.51 kW/m^2 .The case was run from cold shutdown conditions with a step-up to the driving power level. The transient duration was 24,000 seconds.

The model performed as in the medium heat flux baseline case with the T-F conditions monotonically increasing to reach a stable steady condition in the asymptote. Table 2.19 shows that the peak air mass flow rate is 7.5 kg/s and the peak air velocity in the duct is 8.4 m/s. The peak pressure vessel wall temperature is 739ºK while the peak cavity wall surface temperature is 471ºK. The corresponding air temperature at the duct outlet is 471ºK. Focusing on the riser duct the peak front wall temperature is 593ºK; the peak side wall temperature is 505ºK and the peak duct back wall temperature is 519ºK. The time histories of all these parameters are similar to those for the medium heat flux base line case and are therefore not included in this report.

Case (3): Low Heat Flux/No Modification

This model was used to determine the effects of differing heat flux on the system, as well as provide a conservative estimate for concrete temperatures. The heat flux on the pressure vessel wall was 2.5 kW/m^2, which is equivalent to 0.36 MW of total heat from half the system. This was fortuitously close to the peak RCCS heat load as reported in [2.2] for 100% normal steady state power conditions. Driven by this incident heat flux, the heat transferred from the outer surface of the pressure vessel wall is partitioned into a radiation heat flux of 1.83 kW/m^2 and a convective heat flux of 0.66 kW/m^2 off the vessel wall. This leads to a heat flux incident upon the front wall of the hot riser duct of 1.03 kW/m^2 .The case was run from cold shutdown conditions with a step-up to the driving power level. The transient duration was 24,000 seconds.

The model performed as in the medium heat flux baseline case with the T-F conditions monotonically increasing to reach a stable steady condition in the asymptote. Table 2.19 shows that the peak air mass flow rate is 5.61 kg/s and the peak air velocity in the duct is 4.8 m/s. The peak pressure vessel wall temperature is 500ºK while the peak cavity wall surface temperature is 347ºK. The corresponding air temperature at the duct outlet is 352K. Focusing on the riser duct the peak front wall temperature is 394ºK; the peak side wall temperature is 362ºK and the peak duct back wall temperature is 367ºK. The time histories of all these parameters are similar to those for the medium heat flux base line case and are therefore not included in this report.

2.4.2 Half-Scale Model Results

Table 2.19 gives a summary of the half-scale results.

Case (1): Medium Heat Flux/No Modifications

This model was run to verify the scaling analysis of the full-scale system with medium heat flux, as well as to provide a baseline to compare with the experimental setup. The heat flux, in accordance with the scaling study, was increased from the medium flux used in the full-scale model by a factor of $\sqrt{2}$, to a value of 7.0 kW/m^2. This is heat flux incident on the pressure vessel. It represents a total heat load on half the pressure vessel of 0.506 MW. Driven by this incident heat flux, the heat transferred from the outer surface of the pressure vessel wall is partitioned into a radiation heat flux of 5.80 kW/m^2 and a convective heat flux of 1.23 kW/m^2 off the vessel wall. This leads to a heat flux incident upon the front wall of the hot riser duct of 2.99 kW/m^2 .The case was run from cold shutdown conditions with a step-up to the driving power level. The transient duration was 24,000 seconds.

The model performed as expected as the T-F conditions monotonically increase to reach a stable steady condition in the asymptote. Table 2.19 shows that the peak air mass flow rate is 5.81 kg/s and the peak air velocity in the duct is 5.28 m/s. The peak pressure vessel wall temperature is 653ºK while the peak cavity wall surface temperature is 409ºK. The corresponding air temperature at the duct outlet is 376ºK. Focusing on the riser duct the peak front wall temperature is 495ºK; the peak side wall temperature is 410ºK and the peak duct back wall temperature is 424ºK. The time history of the riser duct air mass flow rate is shown in Figure 2.26.The axial locations included in the Figure start from the bottom of the riser and proceed to the top. Figure 2.27 displays the corresponding air flow velocities. The transient history of the pressure vessel outer wall temperature is given at the surface nodes starting from the bottom and proceeding to the top of the heated segment in Figure 2.28. The corresponding liner (insulation) temperature at the corresponding axial locations on the back wall of the cavity is displayed in Figure 2.29. The transient behavior of the temperatures of the hot riser duct air coolant can be observed in Fig 2.30. Nodes 97001 to 97020 start from the bottom of the riser duct and proceed to riser top outlet. Temperatures outside the hot riser duct can also be found in Figure 2.30. The locations start with the cold chimney inlet and transport through the cold suction ducting and manifolds down through the top and bottom cold plenums by way of the down-comer. Hot side locations can also be found in Figure 2.30 where the air heated by the transferred core residual heat rises out off the outlet of the hot riser into the hot plenum and thereon to the hot discharge ducting and manifolds into the hot chimney for ultimate discharge into the atmosphere.

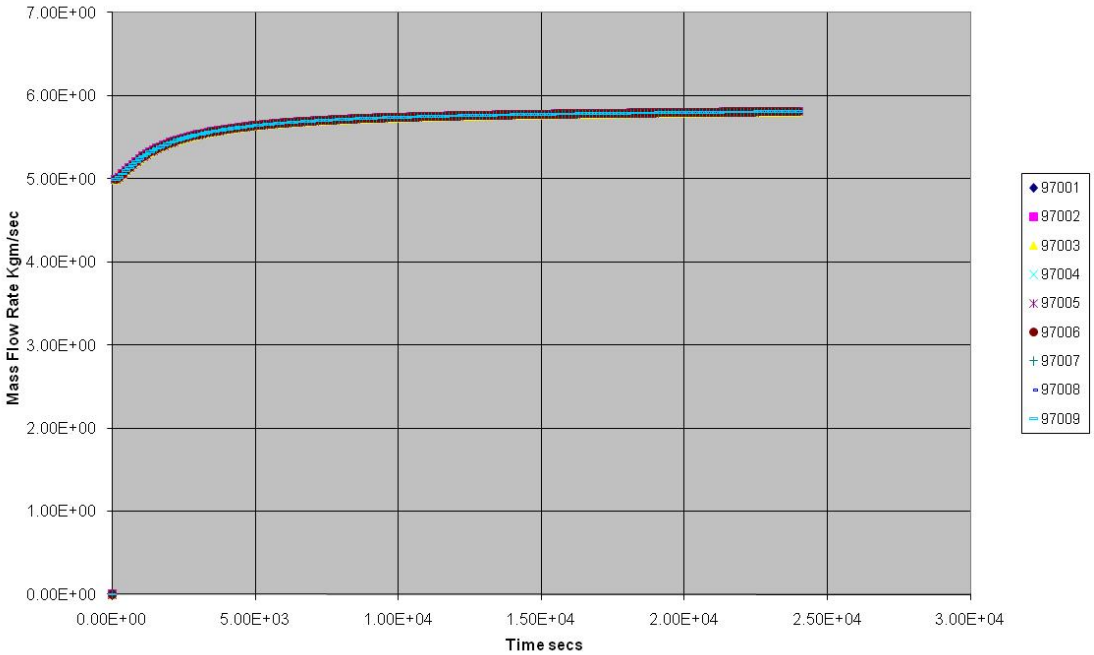

Figure 2.26. Half Scale/Medium Flux Riser Duct Air Total Mass Flow

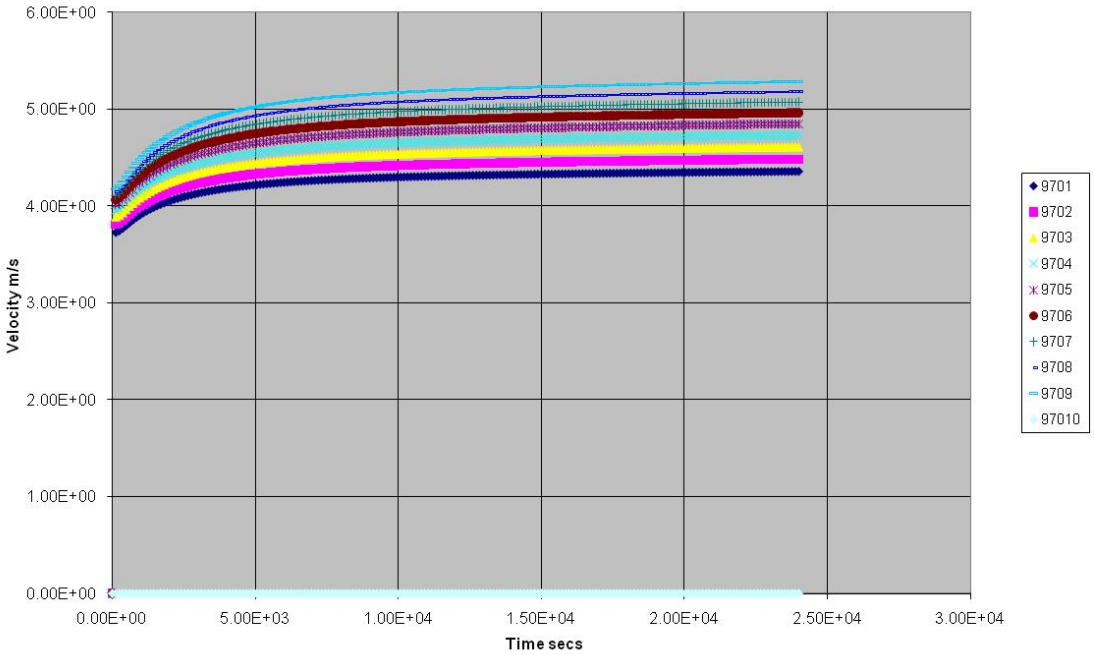

Figure 2.27. Half Scale/Medium Flux Riser Duct Air Velocity

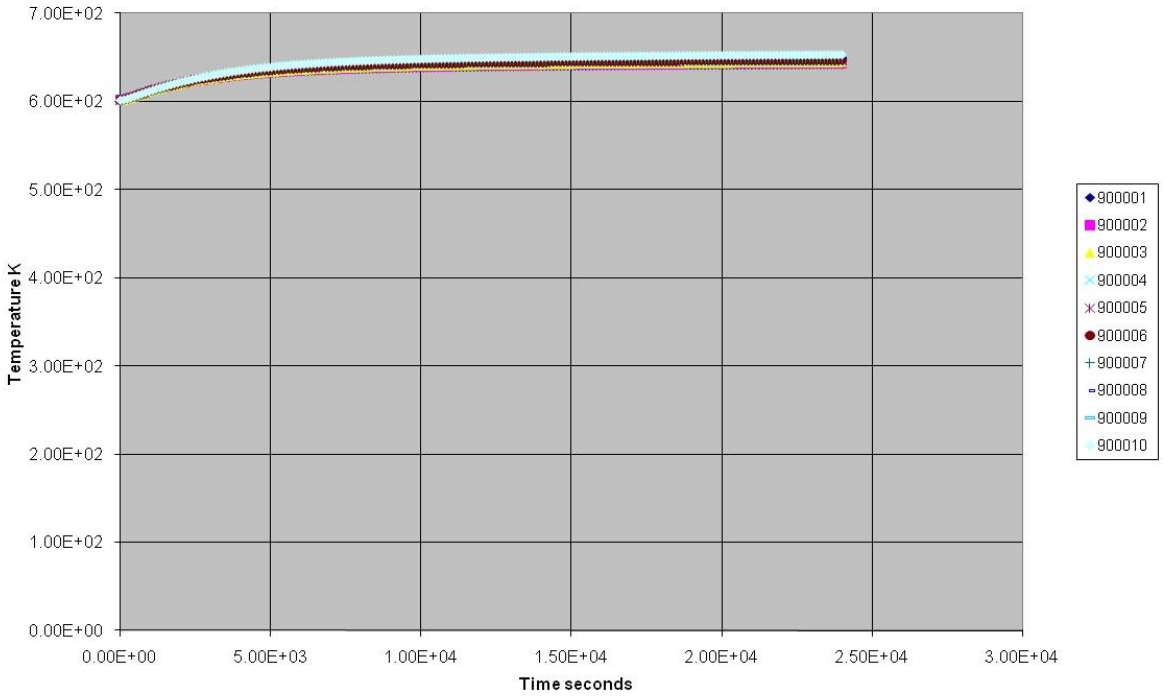

Figure 2.28. Half Scale/Medium Flux RPV Temperature

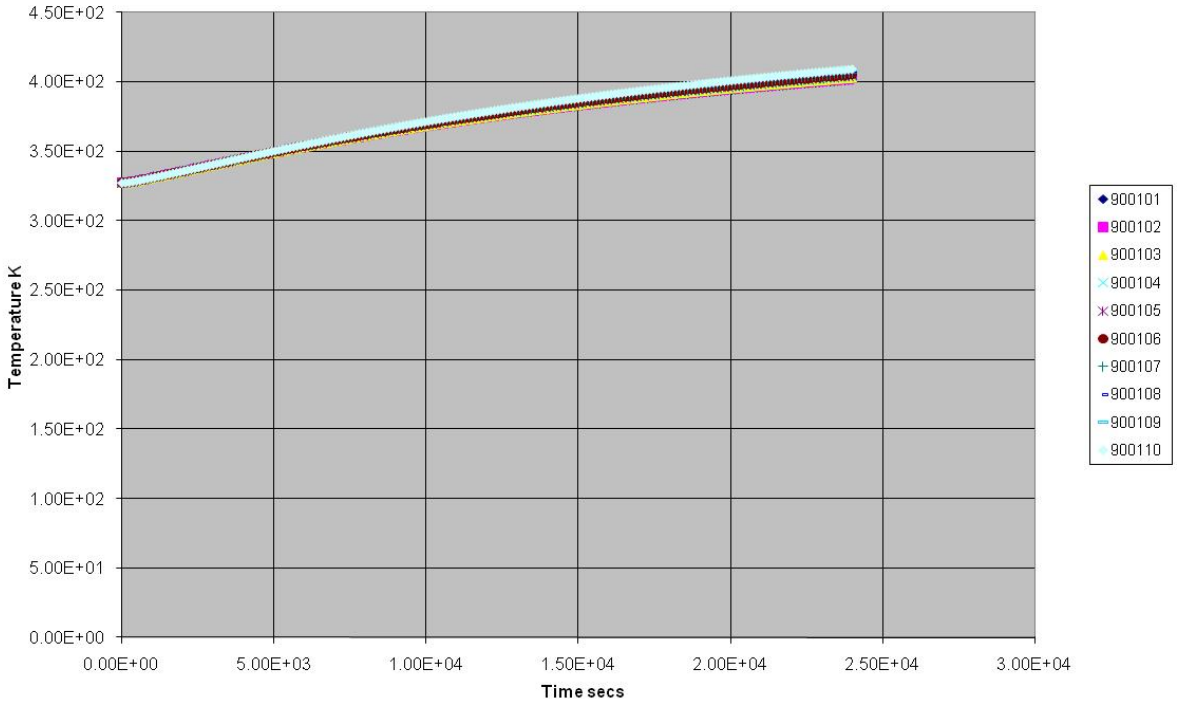

Figure 2.29. Half Scale/Medium Flux Cavity Back Liner Temperature

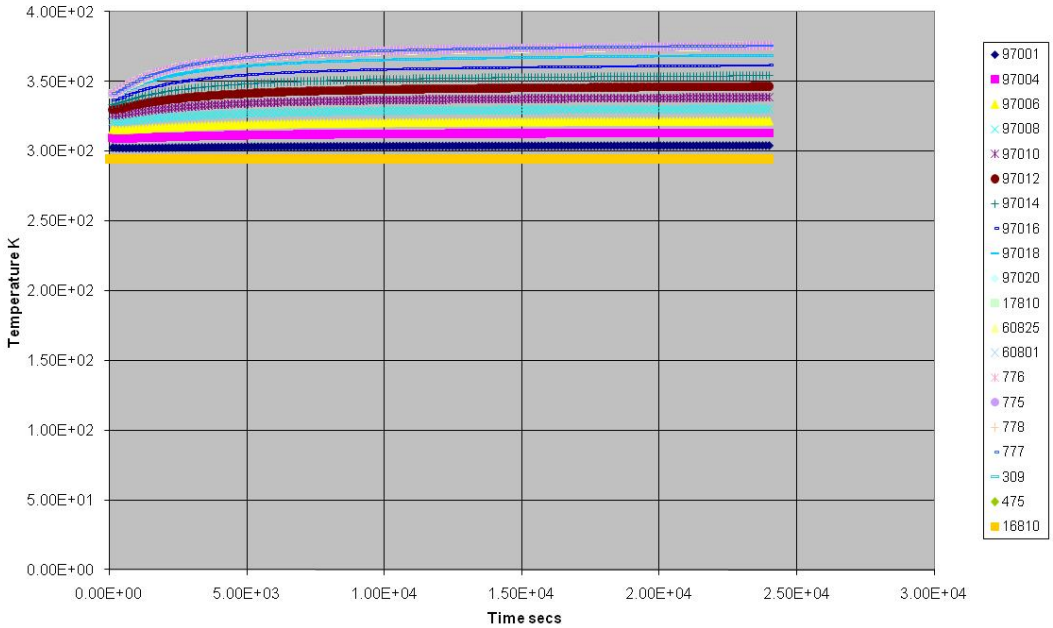

Figure 2.30. Half Scale/Medium Flux Air System Temperature Profile

Case (2): High Heat Flux/No Modifications

This model was run to verify the scaling analysis with a conservatively high estimate of the heat flux. The heat flux was scaled from the full-scale case to14.0 kW/m^2. This is equivalent to 1.01 MW of total heat from half the system. Driven by this incident heat flux, the heat transferred from the outer surface of the pressure vessel wall is partitioned into a radiation heat flux of 12.58 kW/m^2 and a convective heat flux of 1.46 kW/m^2 off the vessel wall. This leads to a heat flux incident upon the front wall of the hot riser duct of 5.84 kW/m^2 .The case was run from cold shutdown conditions with a step-up to the driving power level. The transient duration was 24,000 seconds.

The model performed as in the medium heat flux baseline case with the T-F conditions monotonically increasing to reach a stable steady condition in the asymptote. Table 2.19 shows that the peak air mass flow rate is 6.6 kg/s and the peak air velocity in the duct is 6.9 m/s. The peak pressure vessel wall temperature is 801ºK while the peak cavity wall surface temperature is 504ºK. The corresponding air temperature at the duct outlet is 438ºK. Focusing on the riser duct the peak front wall temperature is 633ºK; the peak side wall temperature is 501ºK and the peak duct back wall temperature is 527ºK. The time histories of all these parameters are similar to those for the medium heat flux base line case and are therefore not included in this report.

.

Case (3): Low Flux/No Modifications

This model was run to determine the effects of low heat flux on the half-scale system with respect to the scaling analysis. The heat flux was scaled in accordance with

the scaling study to 3.52 kW/m^2. This is equivalent to 0.253 MW of total heat from half the system. Driven by this incident heat flux, the heat transferred from the outer surface of the pressure vessel wall is partitioned into a radiation heat flux of 2.63 kW/m^2 and a convective heat flux of 0.88 kW/m^2 off the vessel wall. This leads to a heat flux incident upon the front wall of the hot riser duct of 1.42 kW/m^2 .The case was run from cold shutdown conditions with a step-up to the driving power level. The transient duration was 24,000 seconds.

The model performed as in the medium heat flux baseline case with the T-F conditions monotonically increasing to reach a stable steady condition in the asymptote. Table 2.19 shows that the peak air mass flow rate is 4.96 kg/s and the peak air velocity in the duct is 4.13 m/s. The peak pressure vessel wall temperature is 539ºK while the peak cavity wall surface temperature is 358ºK. The corresponding air temperature at the duct outlet is 341ºK. Focusing on the riser duct the peak front wall temperature is 409ºK; the peak side wall temperature is 360ºK and the peak duct back wall temperature is 368ºK. The time histories of all these parameters are similar to those for the medium heat flux base line case and are therefore not included in this report.

2.4.3 Experimental Model Results

Table 2.20 gives a summary of the experimental model results.

Case (1): Medium Power/No Modifications

This model was run to predict the behavior of the NSTF experiment configuration. This *No Modifications* case has a separation distance of 4” between the front of the hot riser ducts and the heated surface of the NSTF box. This model is considered the baseline for all the comparisons between the Experimental Model cases. The total internal power generation in the heater was 54.0 kW. This corresponds to the same total heat load per riser duct as in the half-scale case. Since the half-scale case has the same number of hot riser ducts (227) as the full-scale case, the power ratio is 113.5:12. The RELAP5 models simulate only half the full reactor cavity and the NSTF experiment has 12 ducts. This model ratio is considered the baseline for all the comparisons with the half-scale cases. An alternative is to ratio the curved reactor surface area to the rectilinear NSTF box area. The heat flux incident on the heated surface of the NSTF box was 6.1 kW/m^2, representing a total heat load of 54 kW. Driven by this incident heat flux, the heat transferred from the outer surface of the heated box wall is partitioned into a radiation heat flux of 4.88 kW/m^2 and a convective heat flux of 1.1 kW/m^2 off the vessel wall. This leads to a heat flux incident upon the front wall of the inner central group of hot riser ducts of 3.48 kW/m^2. The corresponding heat flux incident upon the front wall of the outer boundary group of hot riser ducts of 3.28 kW/m^2 .The case was run from cold shutdown conditions with a step-up to the driving power level. The transient duration was 24,000 seconds.

The model performed as expected as the T-F conditions monotonically increase to reach a stable steady condition in the asymptote. Table 2.20 shows that in the chimney

Table 2.20. Summary of Experiment Scale Results

Model	Heat Flux	Modifications	Transient Length[s]	Peak Inner Duct Front Wall Heat Flux [kW/m^2]	Peak Outer Duct Front Wall Heat Flux [kW/m^2]	Peak Chimney Mass Flow [kg/s]	Inner Duct			Outer Duct		
							Peak Air Temperature [K]	Peak Air Mass Flow Rate [kg/s]	Peak Air Flow Velocity [m/s]	Peak Air Temperature [K]	Peak Air Mass Flow Rate [kg/s]	Peak Air Flow Velocity [m/s]
Experiment Scale	High	4” Separation	24000	6.9662	6.6202	0.797	425	0.531	7.29	432	0.252	7.42
Experiment Scale	Med	4” Separation	24000	3.4394	3.2368	0.638	368	0.428	5.39	364	0.213	5.43
Experiment Scale	Low	4” Separation	24000	1.5839	1.483	0.506	338	0.337	3.95	335	0.169	3.96
Experiment Scale	High	45” Separation	24000	5.450	5.2109	0.741	411	0.494	6.92	433	0.248	7.32
Experiment Scale	Med	45” Separation	24000	2.440	2.309	0.607	360	0.403	4.98	367	0.204	5.15
Experiment Scale	Low	45” Separation	24000	1.0039	0.93915	0.465	331	0.309	3.54	334	0.156	3.61
Experiment Scale	High	4” No Heat Loss	24000	9.242	8.819	0.797	469	0.531	8.44	479	0.266	8.62
Experiment Scale	High	4” No Heat Loss 1 Channel	24000	9.3418		0.796	473	0.796	8.49			

Model	Heat Flux	Modifications	Transient Length[s]	Peak Temperature RPV [K]	Peak Temperature Cavity Wall [K]	Peak Temperature Chimney Outlet [K]	Peak Temperatures Inner Duct [K]			Peak Temperatures Outer Duct [K]		
							Front Wall	Side Wall	Back Wall	Front Wall	Side Wall	Back Wall
Experiment Scale	High	4” Separation	24000	783	516	420	645	483	472	637	494	478
Experiment Scale	Med	4” Separation	24000	633	414	364	502	399	391	496	403	393
Experiment Scale	Low	4” Separation	24000	518	358	334	413	355	349	409	356	350
Experiment Scale	High	45” Separation	24000	783	513	410	592	462	465	592	496	482
Experiment Scale	Med	45” Separation	24000	628	407	355	458	384	382	457	398	390
Experiment Scale	Low	45” Separation	24000	512	351	328	383	344	342	381	350	345
Experiment Scale		4” No Heat Loss	24000	871	589	463	736	548	538	728	563	546
Experiment Scale		4” No Heat Loss 1 Channel	24000	872	610	463	741	553	553			

the peak air mass flow rate is 0.64 kg/s. For the group of eight inner central riser ducts Table 2.20 shows that the peak air mass flow rate is 0.43 kg/s and the peak air velocity in the duct is 5.39 m/s. Table 2.20 also shows that for the four outer boundary riser ducts the peak air mass flow rate is 0.21 kg/s and the peak air velocity in the duct is 5.43 m/s. The corresponding values for the peak air riser outlet temperatures are 368ºK and 364ºK. The peak heated box wall temperature is 633ºK while the peak box back wall surface temperature is 414ºK. The corresponding air temperature at the chimney outlet is 364ºK. Focusing on the central inner riser ducts the peak front wall temperature is 502ºK; the peak side wall temperature is 399ºK and the peak duct back wall temperature is 391ºK. In the case of the outer boundary riser ducts the peak front wall temperature is 496ºK; the peak side wall temperature is 403ºK and the peak duct back wall temperature is 393ºK The time history of the chimney air mass flow rate is shown in Figure 2.31 for nodes at the top and bottom of the chimney. Additional details regarding the time history of the various hot riser ducts air mass flow rates and velocities is shown in Figure 2.32.The variation in the air mass flow rates and velocities at various locations start from the bottom of the riser and proceed to the top outlet end. More details on the temperatures of the central inner hot riser ducts can be found in Figure 2.33. The transient behavior of the temperatures of the hot riser duct front wall, side wall, back wall and air coolant can be observed. The metal temperatures in these Figures are axial profiles starting with the bottom node and proceed to the outlet end. In the case of the air temperature, temperatures inside the hot riser duct at these locations can also be found in Figure 2.33d. Figure 2.34 displays the corresponding temperatures for the outer boundary riser ducts. The transient history of the box heated wall temperature is given at the surface nodes starting from the bottom and proceeding to the top of the heated segment in Figure 2.35. The corresponding liner temperature at the corresponding axial locations on the back wall of the box is displayed in Figure 2.36. The temperatures at locations from the chimney inlet to the chimney outlet are displayed in Figure 2.37.

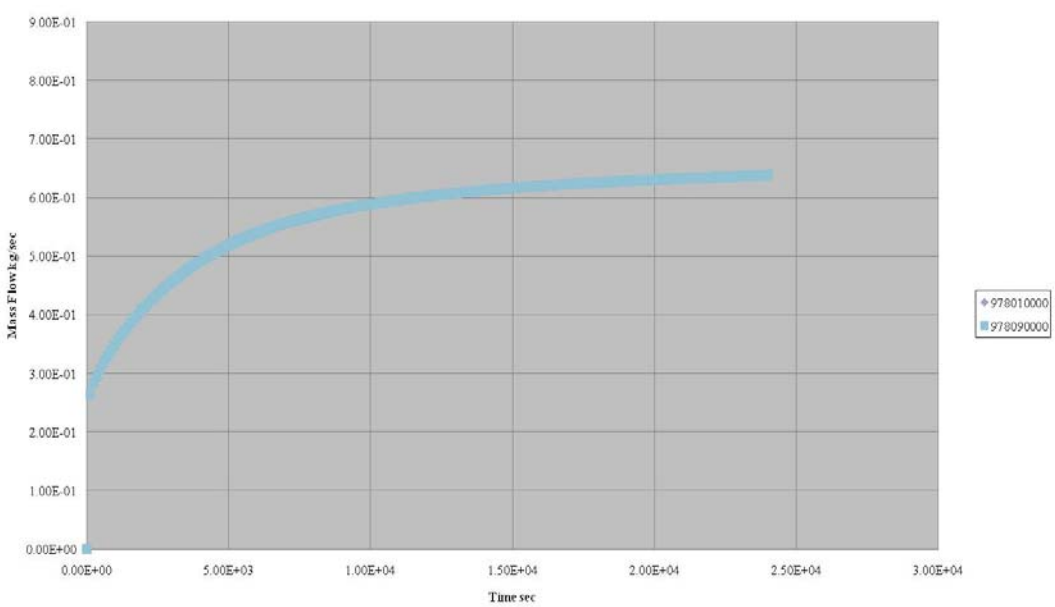

Figure 2.31 Experiment/Medium Flux (4”) Chimney Air Total Mass Flow

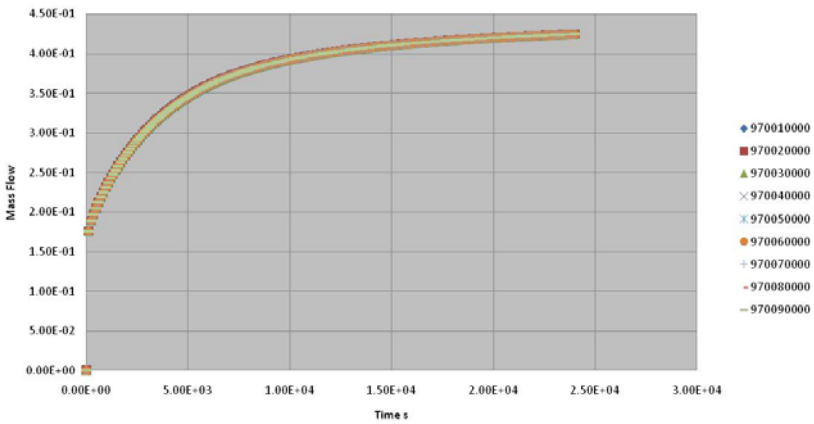

Figure 2.32a Inner Ducts Air Mass Flow [kg/s]

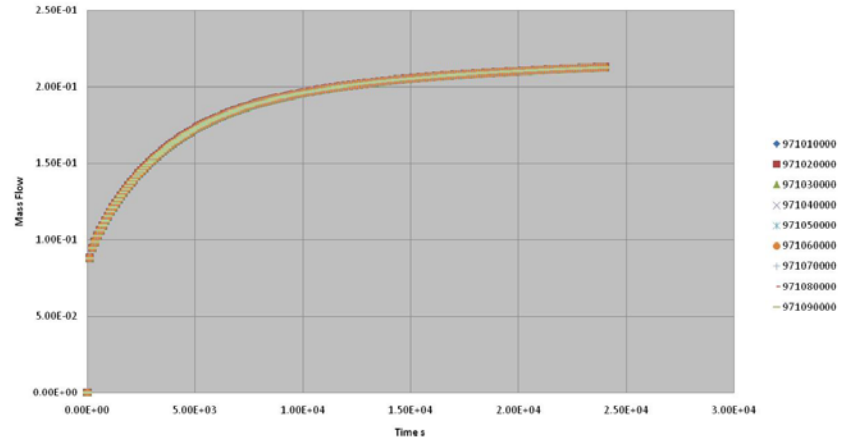

Figure 2.32b Outer Ducts Air Mass Flow [kg/s]

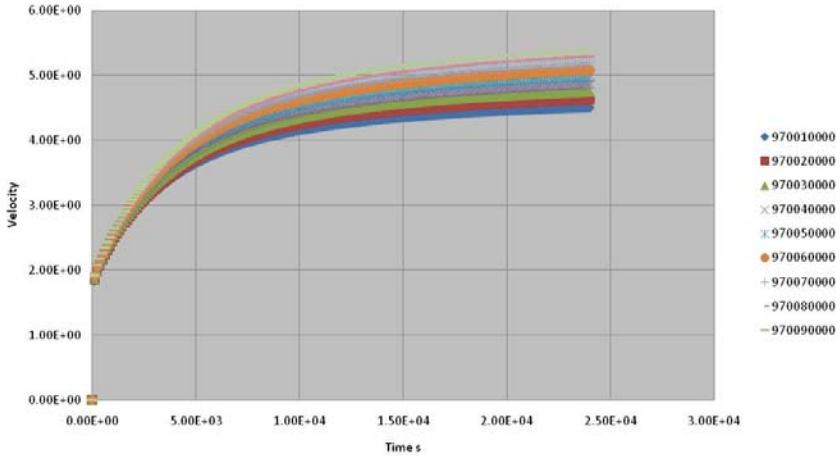

Figure 2.32c Inner Ducts Air Velocity [kg/s]

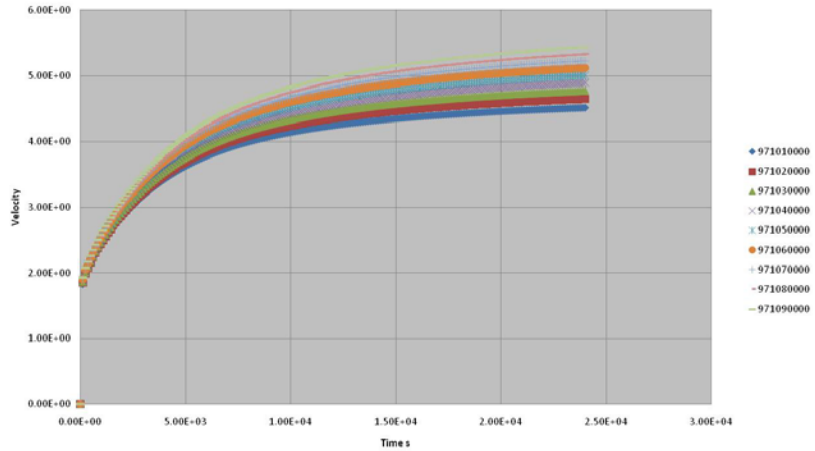

Figure 2.32d Outer Ducts Air Velocity[m/s]

Figure 2.32 Experiment /Medium Flux (4”) Riser Duct Air Flow

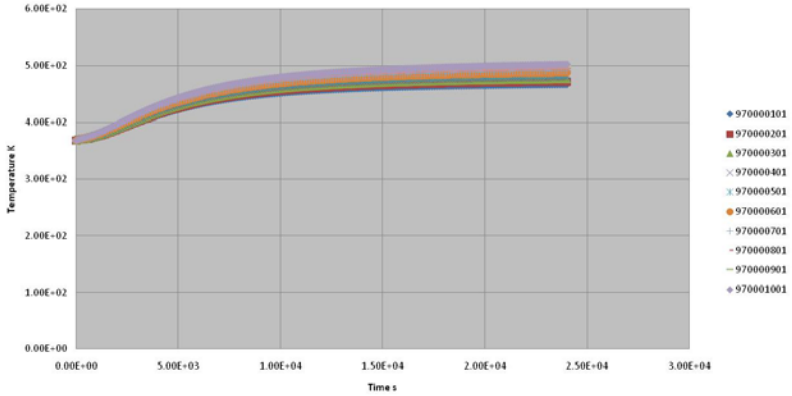

Figure 2.33a. Inner Ducts Front Wall Temperatures

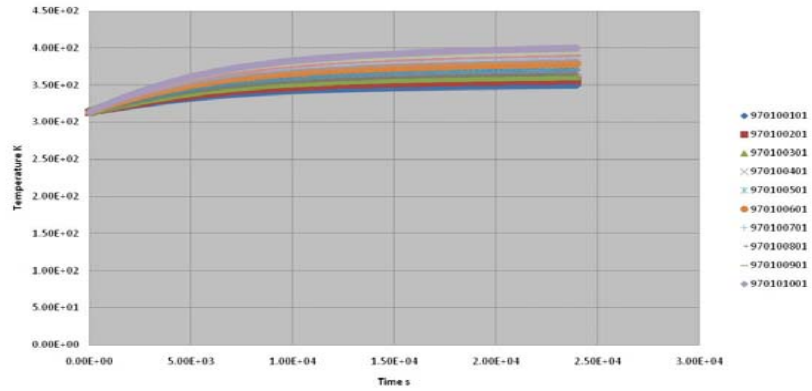

Figure 2.33b. Inner Ducts Side Wall Temperatures

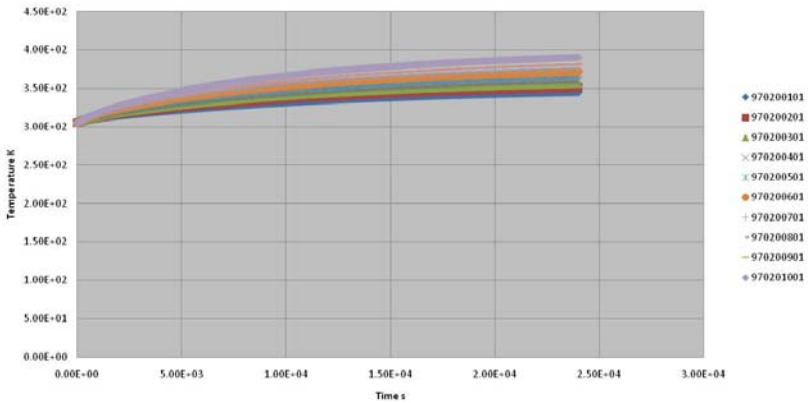

Figure 2.33c Inner Ducts Back Wall Temperatures

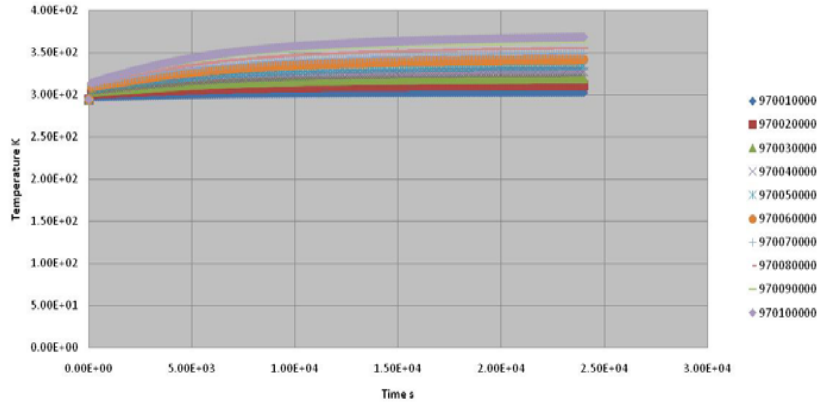

Figure 2.33d. Inner Ducts Air Temperatures

Figure 2.33. Experiment /Medium Flux(4”) Inner Riser Duct Temperatures

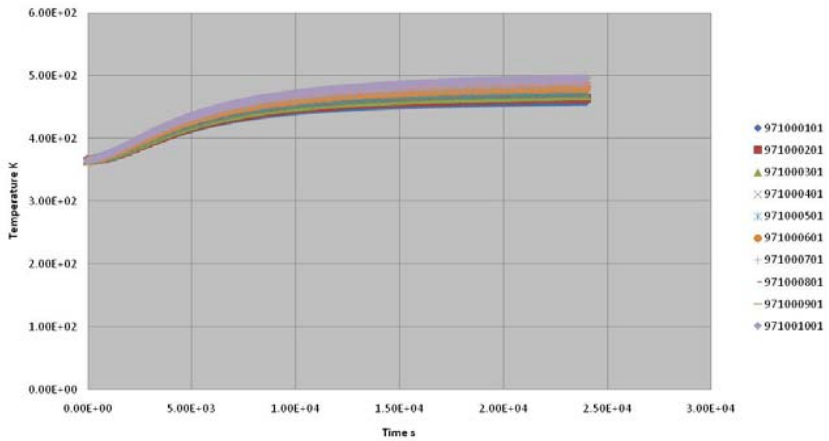

Figure 2.34a. Outer Ducts Front Wall Temperatures

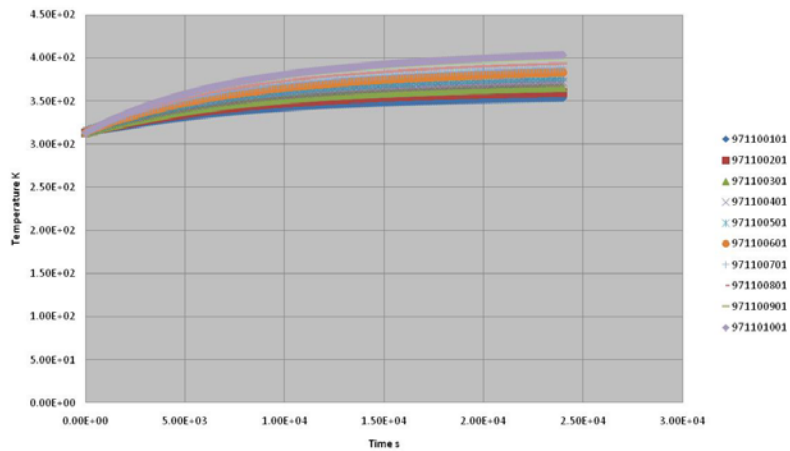

Figure 2.34b. Outer Ducts Side Wall Temperatures

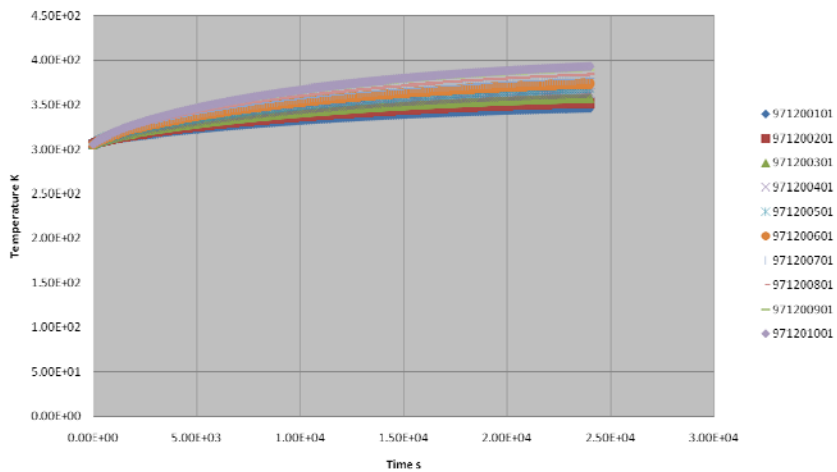

Figure 2.34c Outer Ducts Back Wall Temperatures

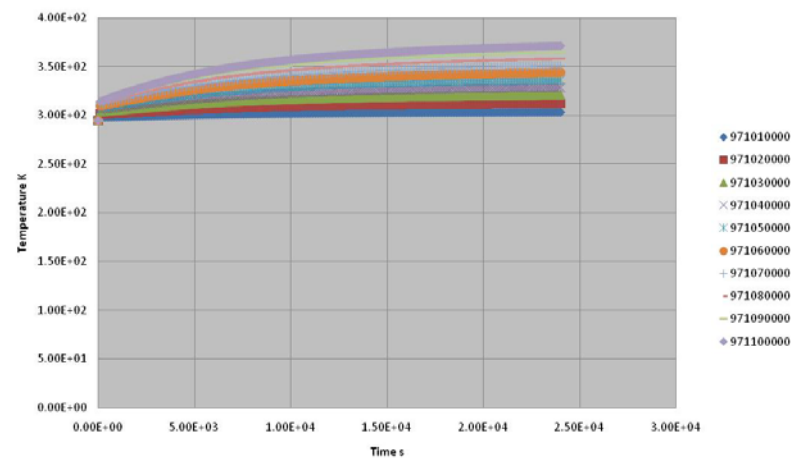

Figure 2.34d. Outer Ducts Air Temperatures

Figure 2.34 Experiment /Medium Flux(4”) Outer Riser Duct Temperatures

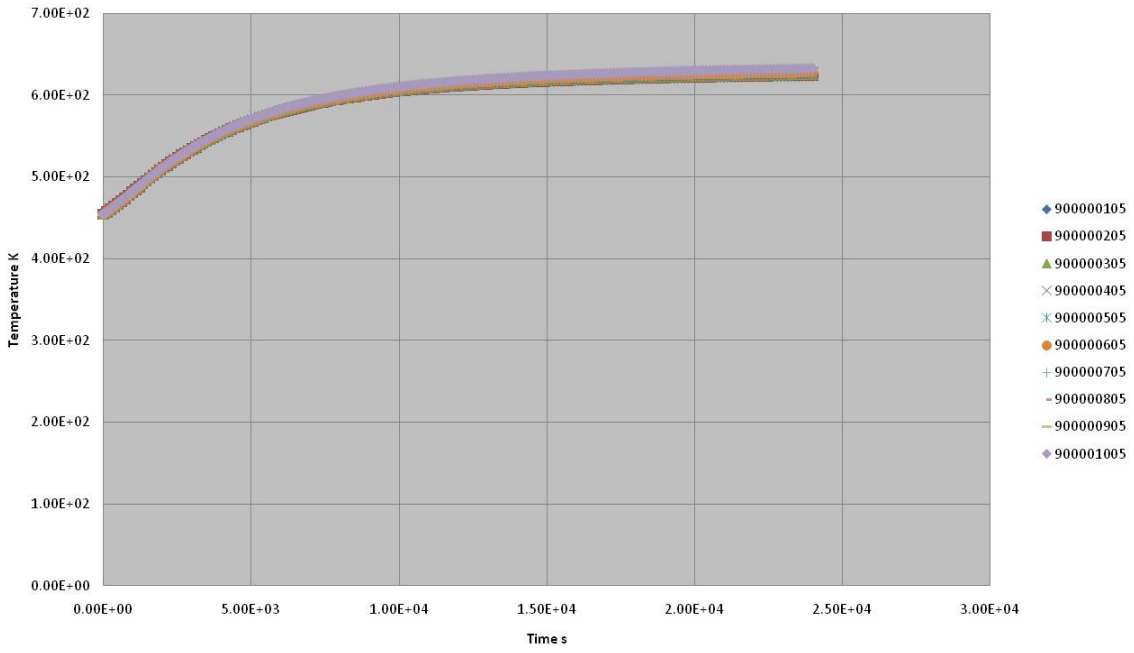

Figure 2.35 Experiment /Medium Flux (4”) RPV Temperature

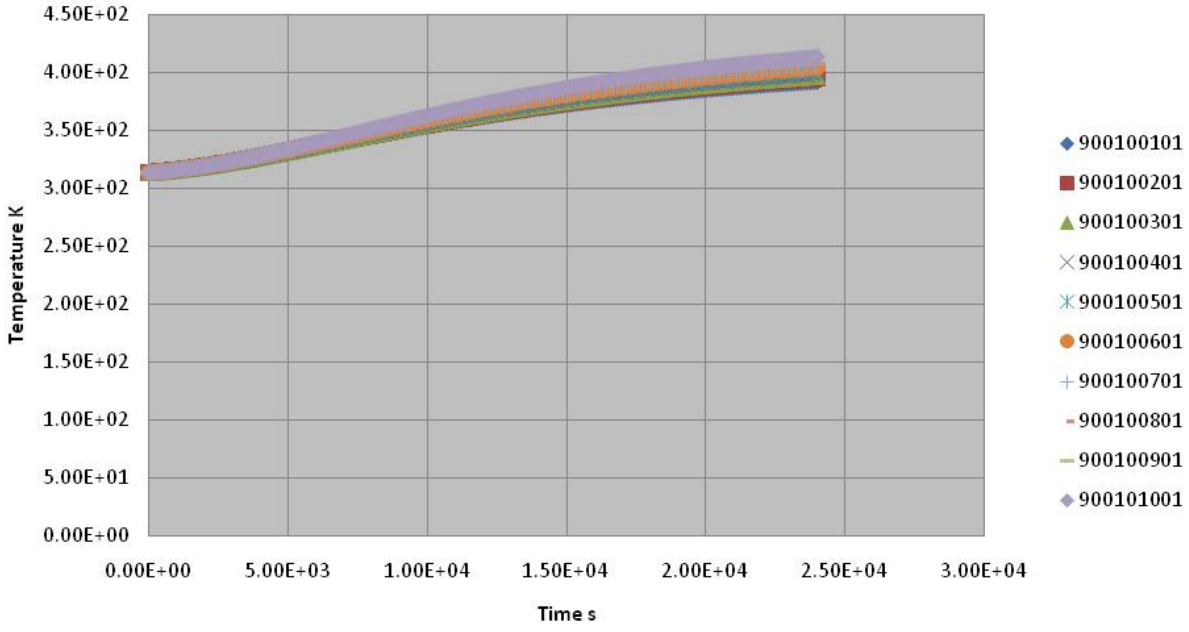

Figure 2.36 Experiment/Medium Flux (4”) Back Liner Temperature

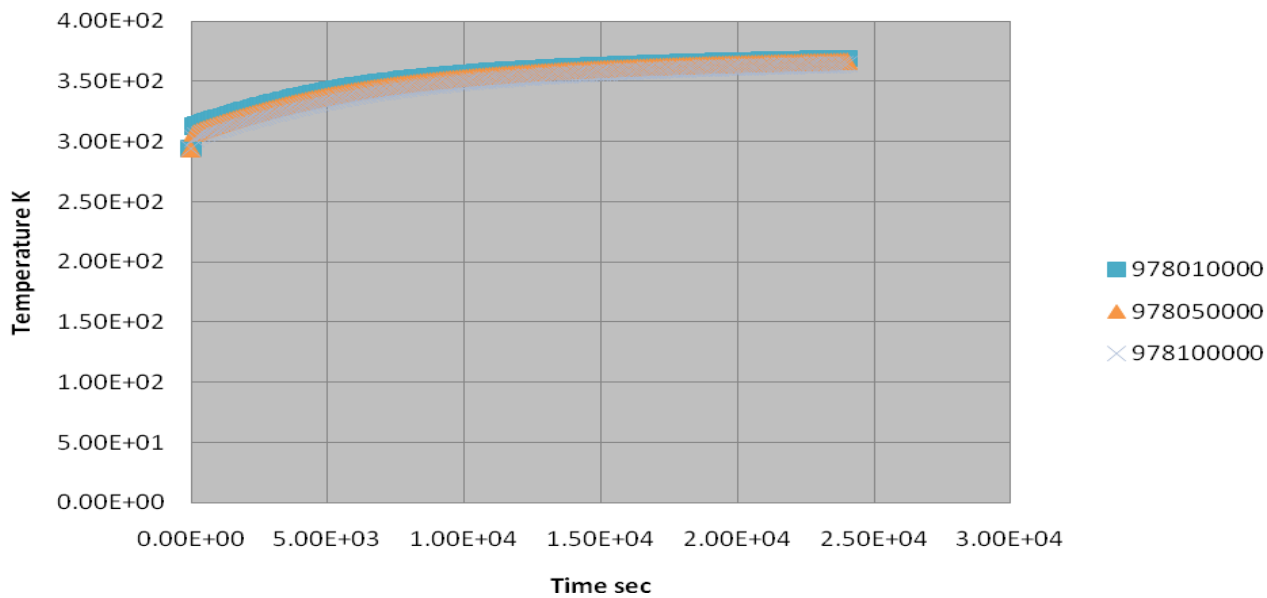

Figure 2.37 Experiment/Medium Flux (4") Chimney Air Temperatures

Case (2): High Power/No Modifications

This model was run to predict the behavior of the NSTF experiment configuration. The total internal power generation in the heater was 108.3 kW, corresponding to the power reduction ratio from the half-scale case. The heat flux incident on the heated surface of the NSTF box was 12.2kW/m^2. Driven by this incident heat flux, the heat transferred from the outer surface of the heated box wall is partitioned into a radiation heat flux of 10.78kW/m^2 and a convective heat flux of 1.19kW/m^2 off the vessel wall. This leads to a heat flux incident upon the front wall of the inner central group of hot riser ducts of 6.97kW/m^2. The corresponding heat flux incident upon the front wall of the outer boundary group of hot riser ducts of 6.62 kW/m^2 .The case was run from cold shutdown conditions with a step-up to the driving power level. The transient duration was 24,000 seconds.

The model performed as expected as the T-F conditions monotonically increase to reach a stable steady condition in the asymptote. Table 2.20 shows that in the chimney the peak air mass flow rate is 0.79 kg/s. For the group of eight inner central riser ducts Table 2.20 shows that the peak air mass flow rate is 0.53 kg/s and the peak air velocity in the duct is 7.29 m/s. Table 2.20 also shows that for the four outer boundary riser ducts the peak air mass flow rate is 0.25 kg/s and the peak air velocity in the duct is 7.42 m/s. The corresponding values for the peak air riser outlet temperatures are 425ºK and 432ºK. The peak heated box wall temperature is 783ºK while the peak box back wall surface temperature is 516ºK. The corresponding air temperature at the chimney outlet is 420ºK. Focusing on the central inner riser ducts the peak front wall temperature is 645ºK; the peak side wall temperature is 483ºK and the peak duct back wall temperature is 472ºK. In the case of the outer boundary riser ducts the peak front wall temperature is 637ºK; the

peak side wall temperature is 494ºK and the peak duct back wall temperature is 478ºK. The time histories of all these parameters are similar to those for the medium heat flux base line case and are therefore not included in this report.

Case (3): Low Power/No Modifications

The total internal power generation in the heater was 27.0 kW, corresponding to the power reduction ratio from the half-scale case. The heat flux incident on the heated surface of the NSTF box was 3.0kW/m^2. Driven by this incident heat flux, the heat transferred from the outer surface of the heated box wall is partitioned into a radiation heat flux of 2.15kW/m^2 and a convective heat flux of 0.76kW/m^2 off the vessel wall. This leads to a heat flux incident upon the front wall of the inner central group of hot riser ducts of 1.58kW/m^2. The corresponding heat flux incident upon the front wall of the outer boundary group of hot riser ducts of 1.48kW/m^2 .The case was run from cold shutdown conditions with a step-up to the driving power level. The transient duration was 24,000 seconds.

The model performed as expected as the T-F conditions monotonically increase to reach a stable steady condition in the asymptote. Table 2.20 shows that in the chimney the peak air mass flow rate is 0.50 kg/s. For the group of eight inner central riser ducts Table 2.20 shows that the peak air mass flow rate is 0.34 kg/s and the peak air velocity in the duct is 3.95m/s. Table 2.20 also shows that for the four outer boundary riser ducts the peak air mass flow rate is 0.17 kg/s and the peak air velocity in the duct is 3.96 m/s. The corresponding values for the peak air riser outlet temperatures are 338K ºand 335ºK. The peak heated box wall temperature is 518ºK while the peak box back wall surface temperature is 358ºK. The corresponding air temperature at the chimney outlet is 334ºK. Focusing on the central inner riser ducts the peak front wall temperature is 413ºK; the peak side wall temperature is 355ºK and the peak duct back wall temperature is 349ºK. In the case of the outer boundary riser ducts the peak front wall temperature is 409ºK; the peak side wall temperature is 356ºK and the peak duct back wall temperature is 350ºK. The time histories of all these parameters are similar to those for the medium heat flux base line case and are therefore not included in this report.

Case (4): Riser Grouping

These models were run to determine the effect of varying the grouping of the hot risers. It also modifies the non-adiabatic boundary conditions on the box exterior for the experiment configuration to have a basis for comparison with the similar full-scale and half-scale cases. The first 2-Group case with no heat losses to ambient was run at a power of 150kW which results in a heat flux of 9.24kW/m^2 incident on the front wall of the inner central group of hot riser ducts. The corresponding heat flux incident upon the front wall of the outer boundary group of hot riser ducts is 8.82kW/m^2. As with the other cases, the system was run from cold shutdown conditions with a step-up to the driving power level. The transient duration was 24,000 seconds.

In the RELAP5 baseline model, the air heat sink volume was deleted and the box outer boundary conditions were changed to adiabatic from convective. This means that the back wall and side walls of the box no longer lose heat to the surrounding air atmosphere. As in this case's full-scale and half-scale counterparts there are no parasitic heat loss terms to the external environment. In the baseline case the box back wall heat loss flux was 2.1W/m^2 and the box side wall heat loss flux was 0.31W/m^2.With the modification to adiabatic boundary conditions these terms will now both be zero.

The model performed as expected as the T-F conditions monotonically increase to reach a stable steady condition in the asymptote. Table 2.20 shows that in the chimney the peak air mass flow rate is 0.79 kg/s. For the group of eight inner central riser ducts Table 2.20 shows that the peak air mass flow rate is 0.53 kg/s and the peak air velocity in the duct is 8.44m/s. Table 2.20 also shows that for the four outer boundary riser ducts the peak air mass flow rate is 0.26 kg/s and the peak air velocity in the duct is 8.62 m/s. The corresponding values for the peak air riser outlet temperatures are 469ºK and 479ºK. The peak heated box wall temperature is 871ºK while the peak box back wall surface temperature is 589ºK. The corresponding air temperature at the chimney outlet is 463ºK. Focusing on the central inner riser ducts the peak front wall temperature is 736ºK; the peak side wall temperature is 548ºK and the peak duct back wall temperature is 538ºK. In the case of the outer boundary riser ducts the peak front wall temperature is 728ºK; the peak side wall temperature is 563ºK and the peak duct back wall temperature is 546ºK. The time histories of all these parameters are similar to those for the medium heat flux base line case and are therefore not included in this report.

This RELAP5 model was then modified further. All the hot riser ducts are now lumped into a single RELAP5 channel. This is to determine the effect of varying the grouping of the hot risers. The adiabatic boundary conditions on the box exterior for the experiment configuration are maintained. As previously, this case was run at a power of 150kW which results in a heat flux of 9.34kW/m^2 incident on the front wall of single group of hot riser ducts. The model performed as expected as the T-F conditions monotonically increase to reach a stable steady condition in the asymptote. Table 2.20 shows that in the chimney the peak air mass flow rate is 0.79 kg/s. For the group of riser ducts Table 2.20 shows that the peak air mass flow rate is 0.79 kg/s and the peak air velocity in the duct is 8.49m/s. The corresponding value for the peak air riser outlet temperatures is 473ºK. The peak heated box wall temperature is 872ºK while the peak box back wall surface temperature is 610ºK. The corresponding air temperature at the chimney outlet is 463ºK. Focusing on the riser ducts the peak front wall temperature is 741ºK; the peak side wall temperature is 553ºK and the peak duct back wall temperature is 553ºK. The time histories of all these parameters are similar to those for the medium heat flux base line case and are therefore not included in this report.

Case (5): Medium Power/45" Separation

This model was run to predict the effect of varying the view factors in the NSTF experiment configuration. The *No Modifications* case has a separation distance of 4" between the front of the hot riser ducts and the heated surface of the NSTF box. For this

case that distance is increased to 45”. The total internal power generation in the heater remains at 54.0 kW. The heat flux incident on the heated surface of the NSTF box therefore remains 6.1kW/m^2. The heat transferred from the outer surface of the heated box wall is still partitioned into a radiation heat flux of 5.80kW/m^2 and a convective heat flux of 1.23 kW/m^2 off the vessel wall. However this now leads to a heat flux incident upon the front wall of the inner central group of hot riser ducts of 2.44kW/m^2. The corresponding heat flux incident upon the front wall of the outer boundary group of hot riser ducts of 2.31kW/m^2. This is due to the change in view factors with the change in the separation distance. The case was run from cold shutdown conditions with a step-up to the driving power level. The transient duration was 24,000 seconds.

The model performed as expected as the T-F conditions monotonically increase to reach a stable steady condition in the asymptote. Table 2.20 shows that in the chimney the peak air mass flow rate is 0.61kg/s. For the group of eight inner central riser ducts Table 2.20 shows that the peak air mass flow rate is 0.4 kg/s and the peak air velocity in the duct is 4.98 m/s. Table 2.20 also shows that for the four outer boundary riser ducts the peak air mass flow rate is 0.2 kg/s and the peak air velocity in the duct is 5.15 m/s. The corresponding values for the peak air riser outlet temperatures are 360ºK and 367ºK. The peak heated box wall temperature is 628ºK while the peak box back wall surface temperature is 407ºK. The corresponding air temperature at the chimney outlet is 355ºK. Focusing on the central inner riser ducts the peak front wall temperature is 458ºK; the peak side wall temperature is 384ºK and the peak duct back wall temperature is 382ºK. In the case of the outer boundary riser ducts the peak front wall temperature is 457ºK; the peak side wall temperature is 398ºK and the peak duct back wall temperature is 390ºK The time history of the chimney air mass flow rate is shown in Figure 2.38 for nodes at the top and bottom of the chimney. Additional details regarding the time history of the various hot riser ducts air mass flow rates and velocities is shown in Figure 2.39.The variation in the air mass flow rates and velocities at various locations start from the bottom of the riser and proceed to the top outlet end. More details on the temperatures of the central inner hot riser ducts can be found in Figure 2.40. The transient behavior of the temperatures of the hot riser duct front wall, side wall, back wall and air coolant can be observed. The metal temperatures in these Figures are axial profiles starting with the bottom node and proceed to the outlet end. In the case of the air temperature, temperatures inside the hot riser duct at these locations can also be found in Figure 2.40d. Figure 2.41 displays the corresponding temperatures for the outer boundary riser ducts. The transient history of the box heated wall temperature is given at the surface nodes starting from the bottom and proceeding to the top of the heated segment in Figure 2.42. The corresponding liner temperature at the corresponding axial locations on the back wall of the box is displayed in Figure 2.43. The temperatures at locations from the chimney inlet to the chimney outlet are displayed in Figure 2.44.

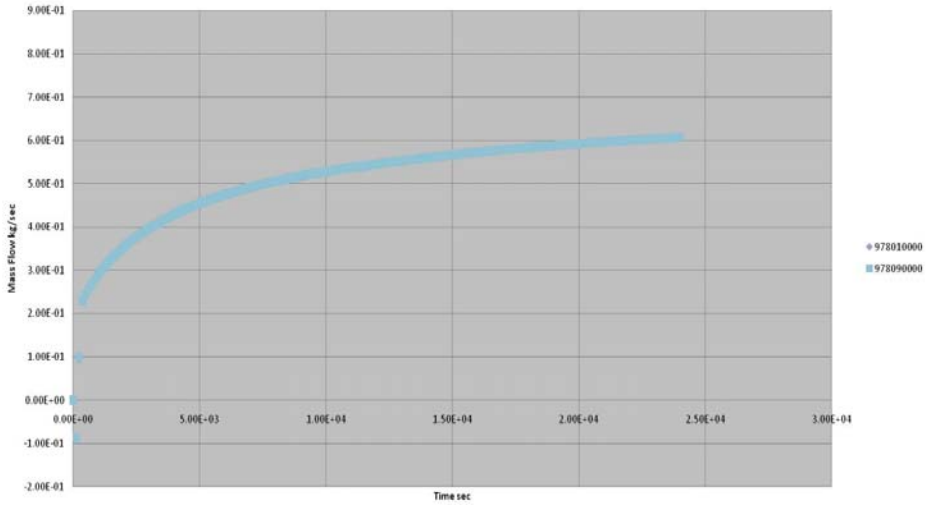

Figure 2.38 Experiment/Medium Flux (45”) Chimney Air Total Mass Flow

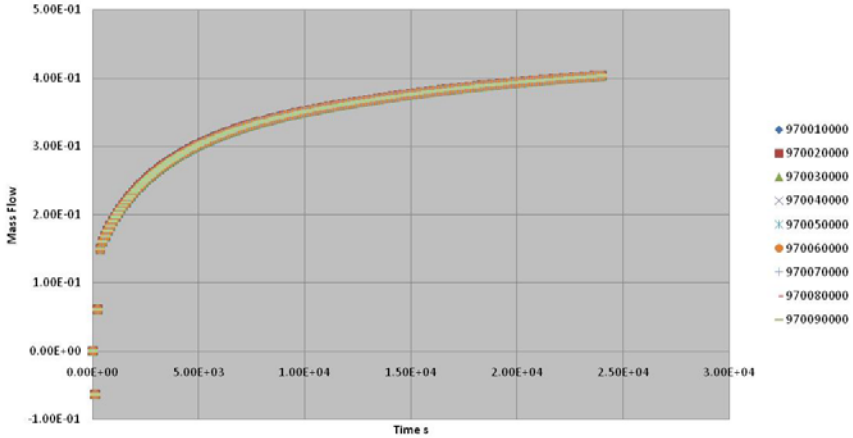

Figure 2.39a Inner Ducts Air Mass Flow [m/s]

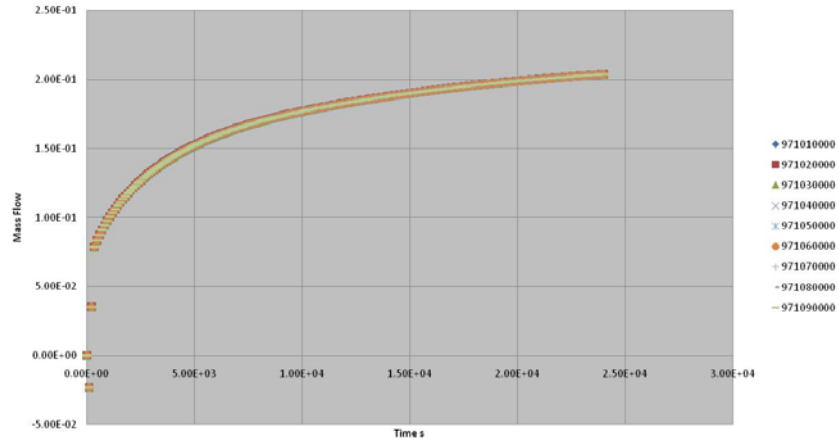

Figure 2.39b. Outer Ducts Air Mass Flow[m/s]

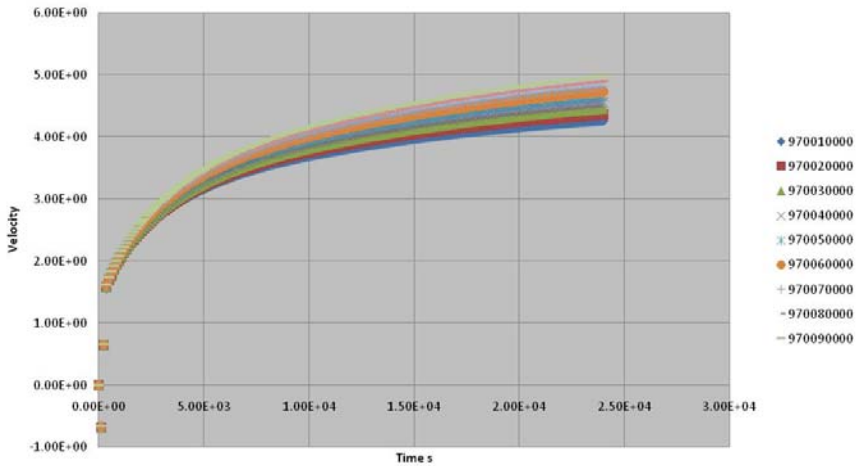

Figure 2.39 Inner Ducts Air Velocity [m/s]

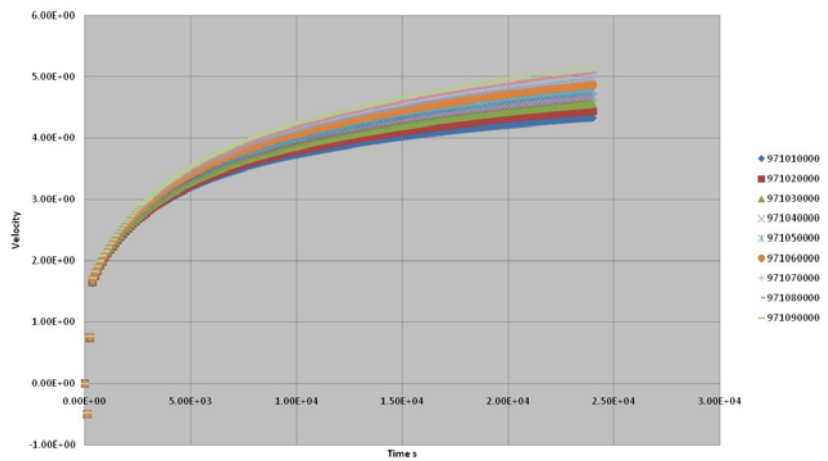

Figure 2.39b. Outer Ducts Air Velocity m/s]

Figure 2.39 Experiment /Medium Flux (45”) Riser Duct Air Flow

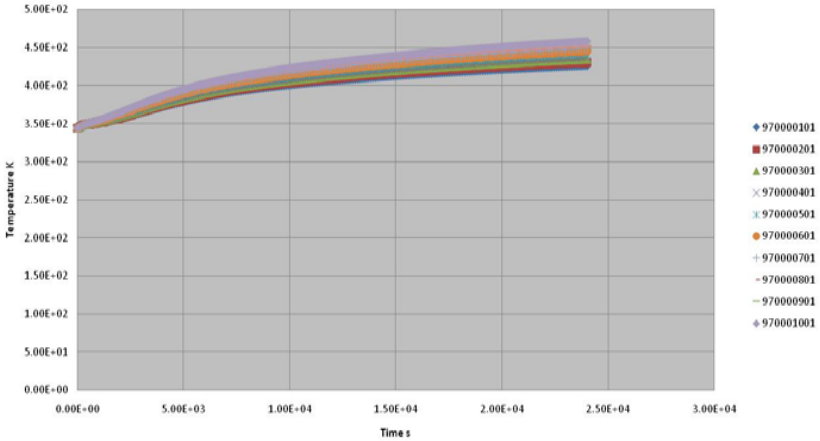

Figure 2.40a. Inner Ducts Front Wall Temperatures

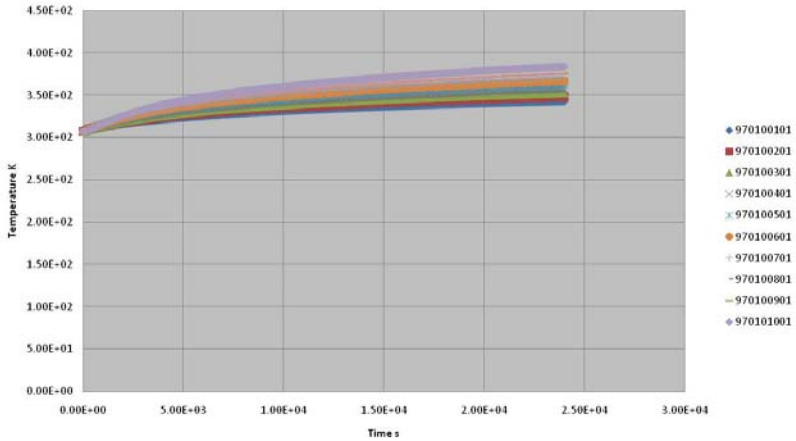

Figure 2.40b Inner Ducts Side Wall Temperature

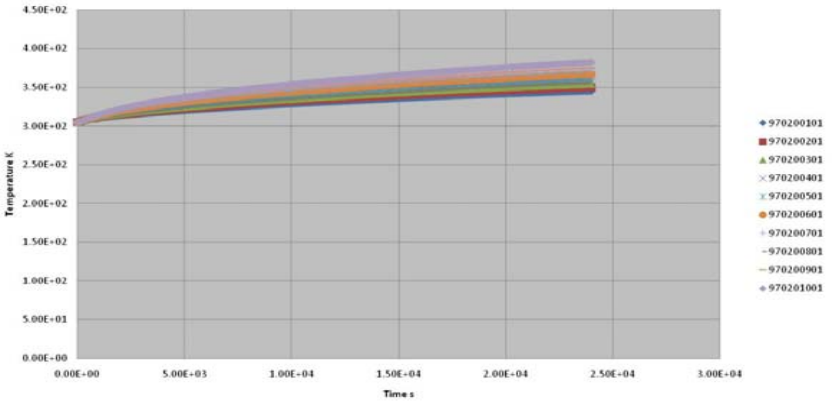

Figure 2.40c. Inner Ducts Back Wall Temperatures

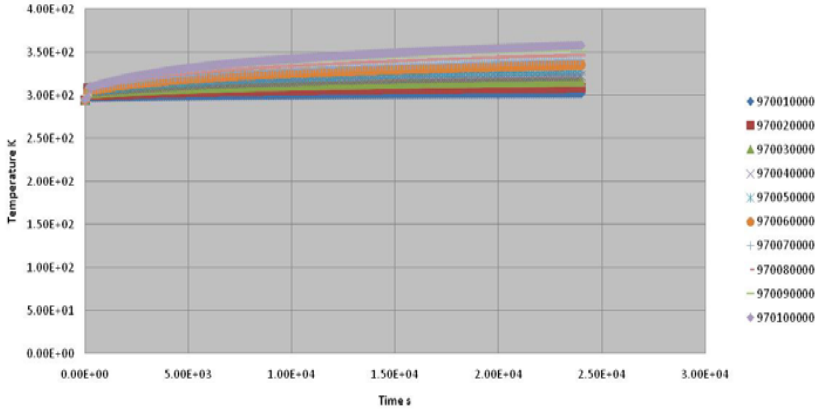

Figure 2.40d. Inner Ducts Air Temperatures

Figure 2.40 Experiment /Medium Flux (45”) Inner Riser Duct Temperatures

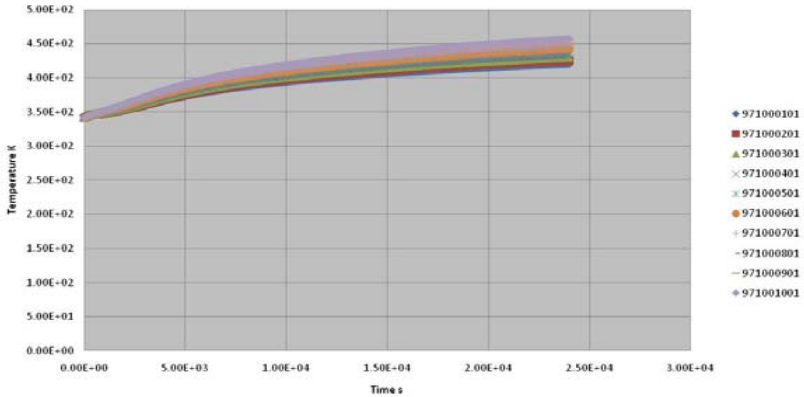

Figure 2.41a. Outer Ducts Front Wall Temperatures

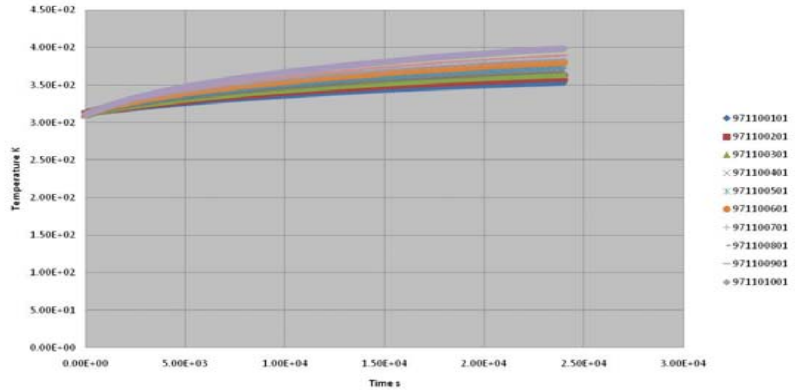

Figure 2.41b. Outer Ducts Side Wall Temperatures

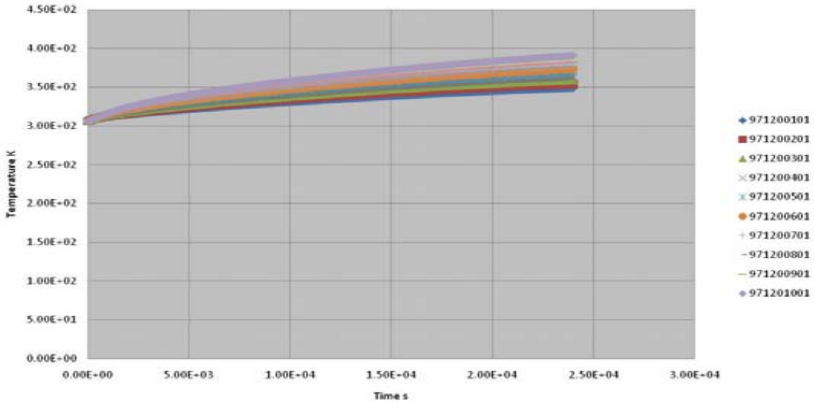

Figure 2.41c. Outer Ducts Back Wall Temperatures

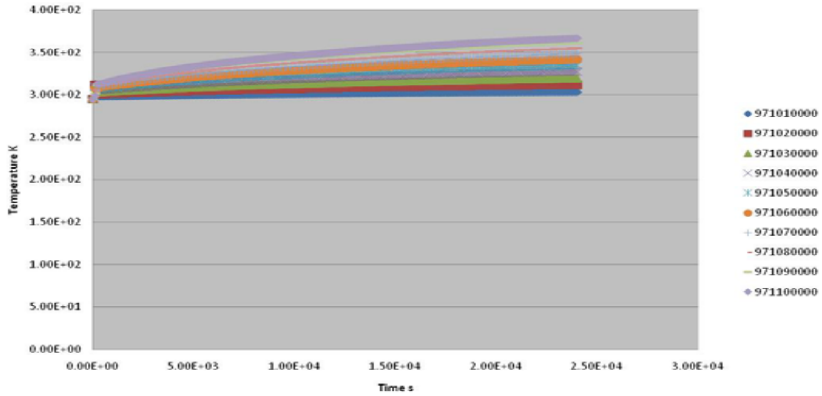

Figure 2.41d. Outer Ducts Air Temperatures

Figure 2.41 Experiment /Medium Flux (45”) Outer Riser Duct Temperatures

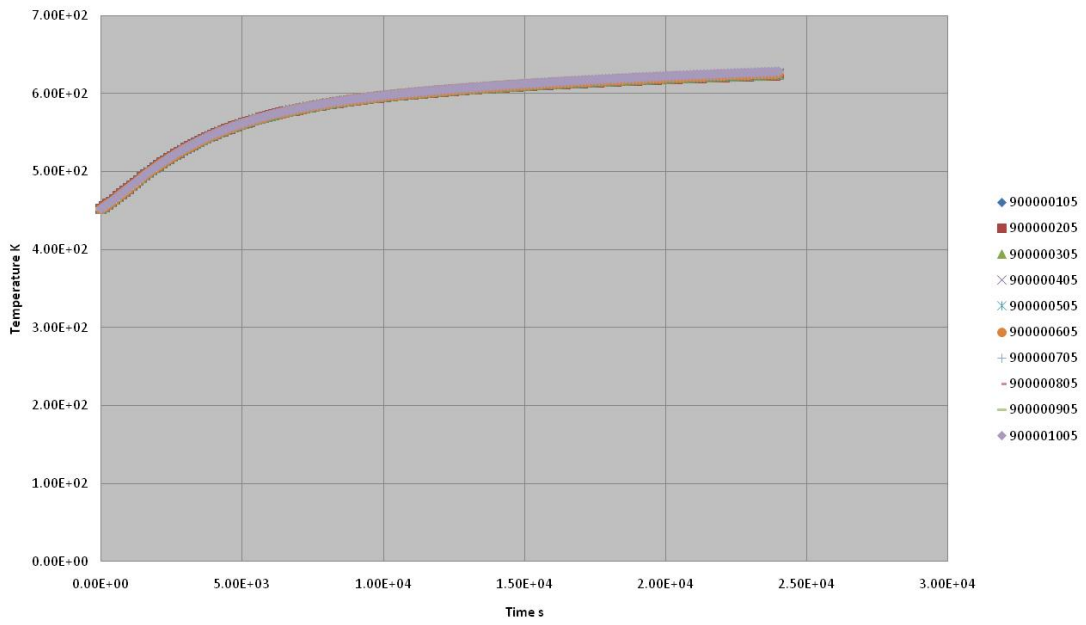

Figure 2.42 Experiment/Medium Flux (45”) RPV Temperature

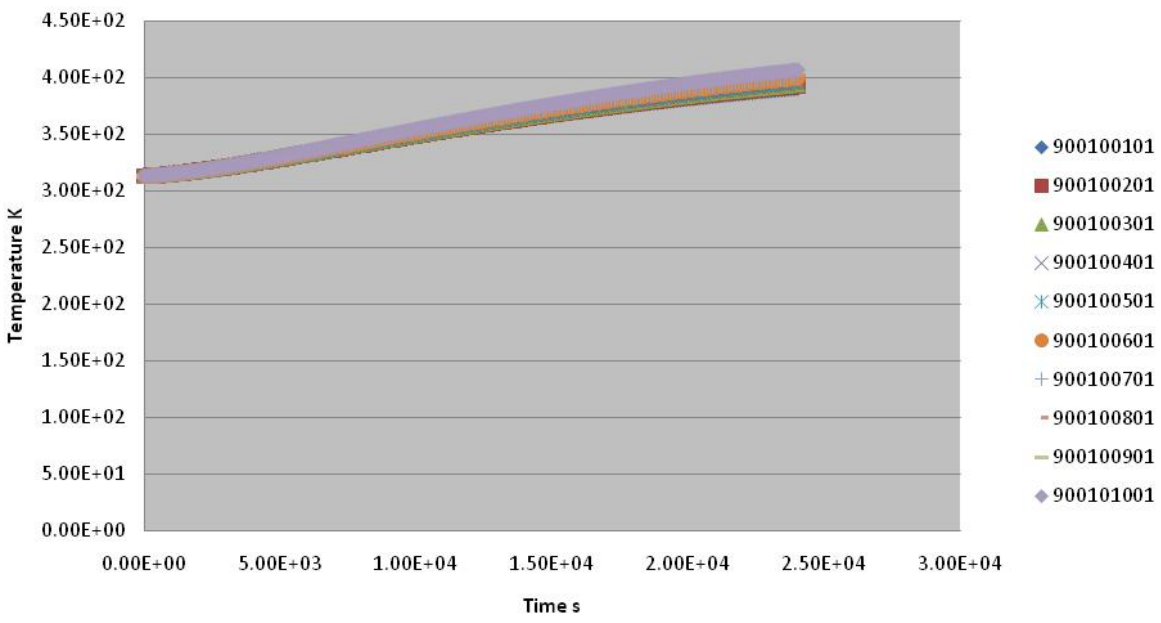

Figure 2.43. Experiment/Medium Flux (45”) Back Liner Temperature

.

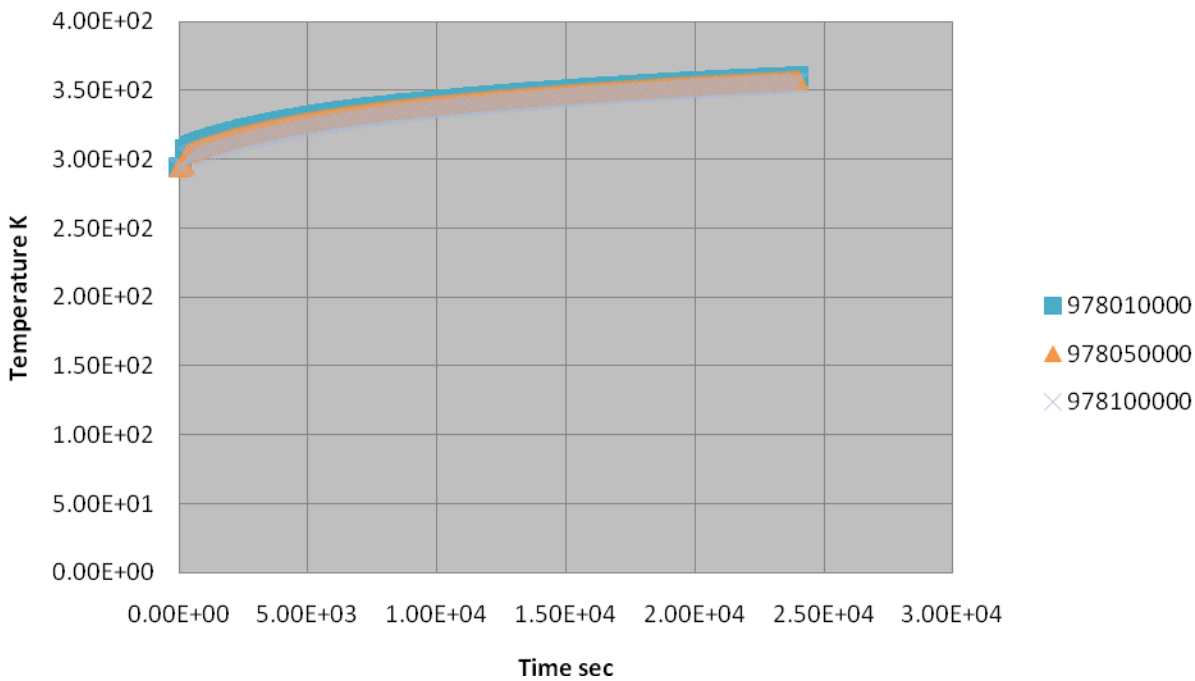

Figure 2.44. Experiment/Medium Flux (45”) Chimney Air Temperatures

Case (6): High Power/45” Separation

This model was run to predict the effect of varying the view factors in the NSTF experiment configuration. The *No Modifications* case has a separation distance of 4” between the front of the hot riser ducts and the heated surface of the NSTF box. For this case that distance is increased to 45”. The total internal power generation in the heater remains at 108.3 kW. The heat flux incident on the heated surface of the NSTF box therefore remains 12.2kW/m^2. The heat transferred from the outer surface of the heated box wall is still partitioned into a radiation heat flux of 10.78kW/m^2 and a convective heat flux of 1.19 kW/m^2 off the vessel wall. However this now leads to a heat flux incident upon the front wall of the inner central group of hot riser ducts of 5.45kW/m^2. The corresponding heat flux incident upon the front wall of the outer boundary group of hot riser ducts of 5.21kW/m^2. This is due to the change in view factors with the change in the separation distance. The case was run from cold shutdown conditions with a step-up to the driving power level. The transient duration was 24,000 seconds.

The model performed as expected as the T-F conditions monotonically increase to reach a stable steady condition in the asymptote. Table 2.20 shows that in the chimney the peak air mass flow rate is 0.74 kg/s. For the group of eight inner central riser ducts Table 2.20 shows that the peak air mass flow rate is 0.49 kg/s and the peak air velocity in the duct is 6.92 m/s. Table 2.20 also shows that for the four outer boundary riser ducts the peak air mass flow rate is 0.25 kg/s and the peak air velocity in the duct is 7.32 m/s. The corresponding values for the peak air riser outlet temperatures are 411ºK and 433ºK. The peak heated box wall temperature is 783ºK while the peak box back wall surface

temperature is 513ºK. The corresponding air temperature at the chimney outlet is 410ºK. Focusing on the central inner riser ducts the peak front wall temperature is 592ºK; the peak side wall temperature is 462ºK and the peak duct back wall temperature is 465ºK. In the case of the outer boundary riser ducts the peak front wall temperature is 592ºK; the peak side wall temperature is 496ºK and the peak duct back wall temperature is 4828ºK. The time histories of all these parameters are similar to those for the medium heat flux base line case and are therefore not included in this report.

Case (3): Low Power/45" Separation

This model was run to predict the effect of varying the view factors in the NSTF experiment configuration. The *No Modifications* case has a separation distance of 4" between the front of the hot riser ducts and the heated surface of the NSTF box. For this case that distance is increased to 45". The total internal power generation in the heater remains at 27.0 kW. The heat flux incident on the heated surface of the NSTF box therefore remains 3.0kW/m^2. The heat transferred from the outer surface of the heated box wall is still partitioned into a radiation heat flux of 2.15kW/m^2 and a convective heat flux of 0.76 kW/m^2 off the vessel wall. However this now leads to a heat flux incident upon the front wall of the inner central group of hot riser ducts of 1.0kW/m^2. The corresponding heat flux incident upon the front wall of the outer boundary group of hot riser ducts of 0.94kW/m^2. This is due to the change in view factors with the change in the separation distance. The case was run from cold shutdown conditions with a step-up to the driving power level. The transient duration was 24,000 seconds.

The model performed as expected as the T-F conditions monotonically increase to reach a stable steady condition in the asymptote. Table 2.20 shows that in the chimney the peak air mass flow rate is 0.46 kg/s. For the group of eight inner central riser ducts Table 2.20 shows that the peak air mass flow rate is 0.31 kg/s and the peak air velocity in the duct is 3.54m/s. Table 2.20 also shows that for the four outer boundary riser ducts the peak air mass flow rate is 0.15 kg/s and the peak air velocity in the duct is 3.61m/s. The corresponding values for the peak air riser outlet temperatures are 331ºK and 334ºK. The peak heated box wall temperature is 512ºK while the peak box back wall surface temperature is 351Kº. The corresponding air temperature at the chimney outlet is 328ºK. Focusing on the central inner riser ducts the peak front wall temperature is 383ºK; the peak side wall temperature is 344ºK and the peak duct back wall temperature is 342ºK. In the case of the outer boundary riser ducts the peak front wall temperature is 381ºK; the peak side wall temperature is 350ºK and the peak duct back wall temperature is 345ºK. The time histories of all these parameters are similar to those for the medium heat flux base line case and are therefore not included in this report.

2.5. Conclusions

The GA-MHTGR air-cooled RCCS design has been modeled in RELAP5 as a one channel grouping of all the hot riser ducts in one half of the reactor cavity. Each half of the cavity is represented by this RELAP5 model together with the top and bottom cold plenum and the hot plenum in that half of the cavity. Also included are the ex-cavity hot

and cold duct runs, the manifolds and the cold inlet and hot discharge chimneys, which form that half of the symmetric system, connected to the common atmosphere. It is assumed that the effect on the one RELAP5 group is representative of the effect on both halves and that the heat load is therefore mirror- symmetric.

The model demonstrates successful heat removal capabilities, even under conservatively high heat flux. However, in the single riser group flow mode there can be no evaluation of the potential flow recirculation between two riser ducts. Since in a recirculation mode the residual heat may not be totally discharged to the ultimate heat sink the atmosphere, this may need to be reevaluated. Removing this issue would appear to require a redesign of the RELAP5 model, as variations in the view factors and differences in flow path resistances will have an effect. Thermal stratification in the various plenums, particularly in the hot plenum and the resulting effect on internal circulation flow patterns within these flow volumes also contribute to the uncertainties in the ultimate residual heat removal to the atmosphere. This issue will be addressed by the STRA-CCM+ CFD assessment provided in Chapter 4. This is a multidimensional effect which is difficult to address with a system level code such as RELAP5. Heat losses from the system to the building environment are probably not significant but the heat transfer between the cold and hot sides of the RCCS could be more important; in particular in the long duct runs. This will be included in future models. Also slated for inclusion in the next iteration on RELAP5 modeling is the effect of intra-riser duct radiation between the four internal surfaces. With these changes, axially varying flux profiles or time-dependent fluxes should also be examined with the RELAP5 models.

The system was scaled down to half scale according to the Argonne scaling report [2.1]. Essentially the lengths and heights were halved but the widths, depths, diameters and thicknesses in the plane cross-section were kept unaltered. The half-scale RELAP5 model has a number of different modifications which will be carried out in the next iteration. Since the half-scale deck was built by converting the full-scale deck it is the same set of modeling issues discussed above. While the results at a high level appear in the right range, the results still need to be non-dimensionalized and compared with the full-scale cases to confirm the scaling analysis. Additional cases will be needed for calibrating and preserving the Friction Drop number as required by the selected scaling laws. Orifices may need to be added and discussions are ongoing with the experiment designers about the preferred forced flow range for the calibration.

The model of the NSTF experiment configuration was also prepared and run successfully. The behavior of the system is similar to the half-scale results but differences can be observed. This is likely due to the configuration of the ex-vessel ducting and manifolds. More assessment of the results is needed, especially relating the full- to half-scale systems. Several design parameters and modeling assumptions require clarification for a final model of the system — primarily box design and radiation view factors. More accurate view factors can be applied to allow axial radiation to the top and bottom. Axial conduction in the major cavity heat structures should also be examined. With these changes, axially varying flux profiles or time-dependent fluxes can be examined with the

RELAP5 models. Other experimental changes need to be incorporated in the model as they are decided upon.

References

2.1 NEVADA Software Package Reference Manual, TAC Technologies, 1999.
2.2 INEEL, RELAP5-3D, Code Manual, INEEL-EXT-98-00834, Revision 2.4, 2005.
2.3 J. Sauerwein, private communication, General Atomics, December 17, 2009.

3.0 Air-Cooled RCCS CFD Analysis

3.1 Motivation and Objective

As part of the on-going facility upgrade, the Natural Shutdown Test Facility is being modified to enable experiments evaluating the performance of an air-cooled Reactor Cavity Cooling System. Proposed changes in the NSTF test section geometry maintain key scaling parameters such as total system height and riser dimensions but also provide a need to evaluate multidimensional effects such as turbulent mixing in inlet and outlet plena of the air-cooled RCCS system. A series of Computational Fluid Dynamics simulations of the proposed RCCS system have been completed as a baseline for the development and scaling of the multidimensional aspects of the NSTF experiment.

3.2 RCCS System Model Geometry

The air-cooled Reactor Cavity Cooling System uses a natural convection driven flow of air from outside the power plant to remove residual heat during operational and emergency transients. Air enters the system through an external vent, travels through the outer annulus of a coaxial duct to the upper region of the reactor cavity where it fills a cold upper plenum. Cold outside air from the plenum flows down through insulated downcomers lining the cavity walls to a lower cold plenum and then rises through the heated RCCS ducts. The heated air is collected in an upper hot plenum and then exits through the central region of the coaxial duct to an external chimney. An illustration of the full system is shown in Figs. 3.1 and 3.2. Elevations of RCCS components are shown in Fig. 3.3 and 3.4. Dimensions of individual components are shown in Figs. 3.4 through 3.7.

3.3 Methodology

RANS-based simulations of natural convection and radiation heat transport have been completed using the commercial CFD code STAR-CCM+. The general-purpose commercial CFD code STAR-CCM+ is a finite volume formulation code for the analysis of compressible and incompressible flows and heat transfer. STAR-CCM+ supports the use of generic polyhedral mesh elements, greatly simplifying the generation of computational meshes for complex geometries.

The SIMPLE algorithm is used with Rhie-Chow interpolation for pressure-velocity coupling and algebraic multi-grid preconditioning. A 2nd-order central differencing scheme and the realizable k-epsilon turbulence model with a two-layer all y+ wall treatment (Norris & Reynolds) were applied. The convergence criteria was defined as the reduction of all equation residuals by 4 orders of magnitude, or, in other words, reducing the normalized residuals below 10^{-4}.

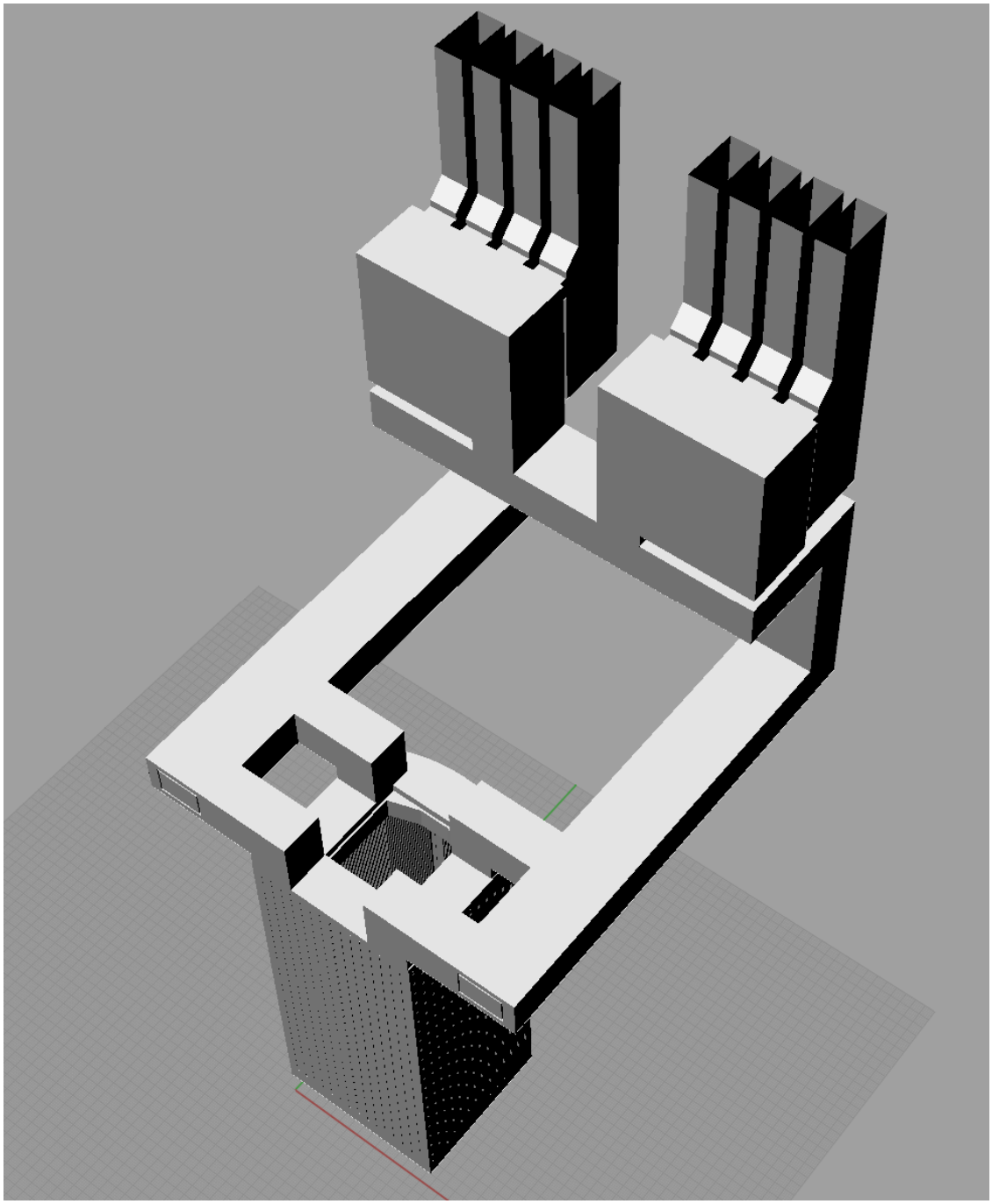

Figure 3.1. Complete RCCS Model

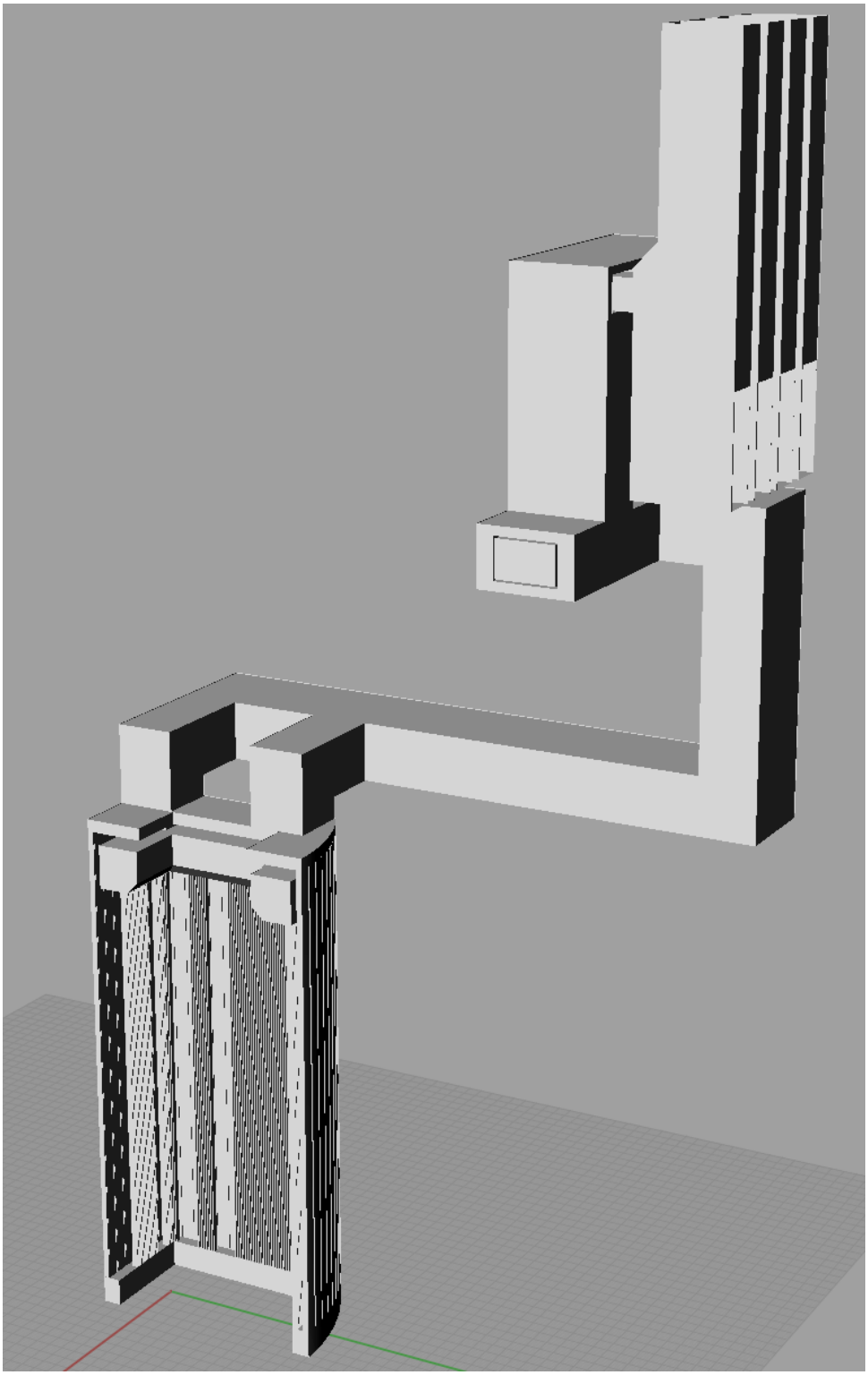

Figure 3.2. Full RCCS Side Cut Away View

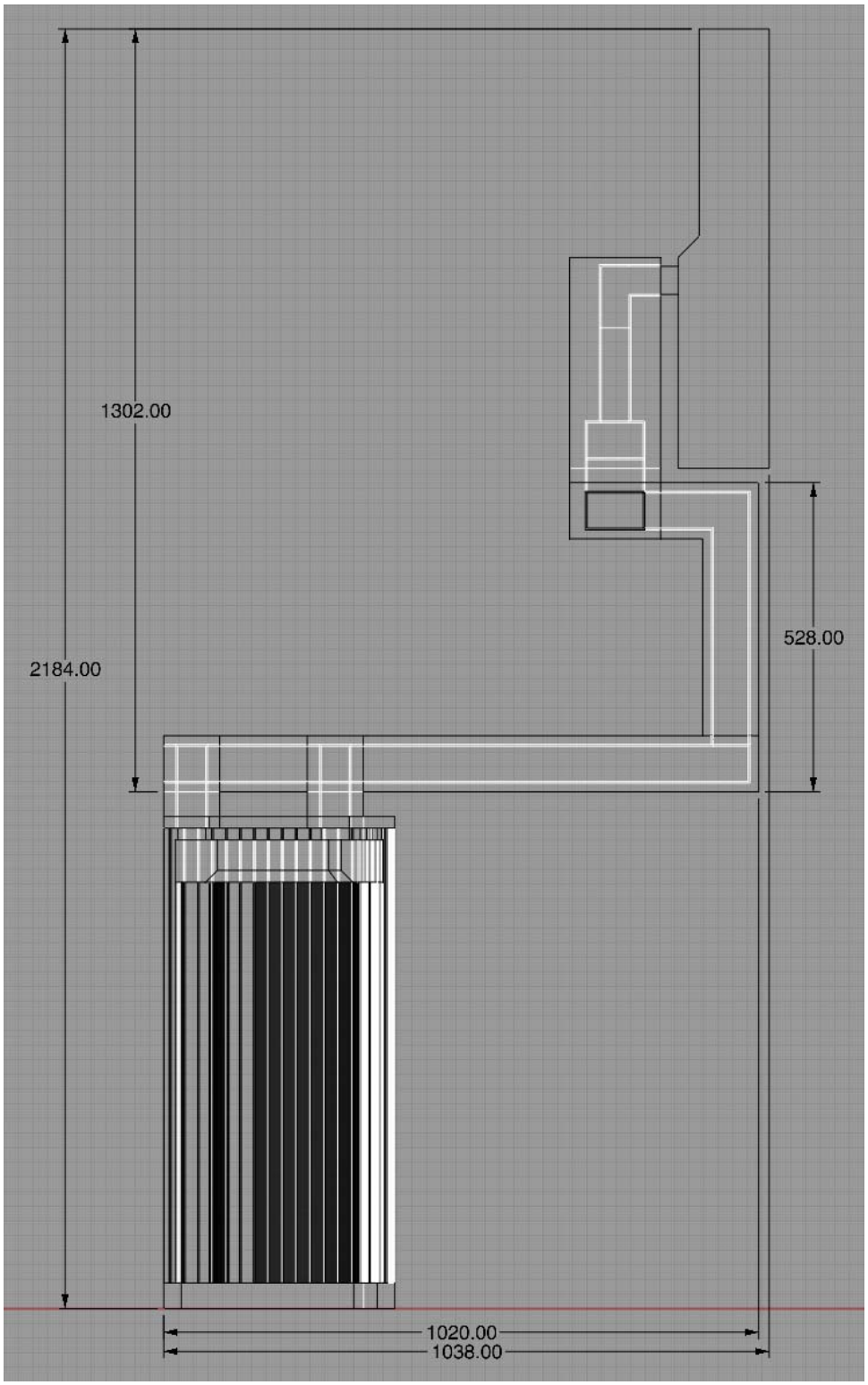

Figure 3.3. Vertical Dimensions Cross-Cut Symmetric Half of RCCS (inches)

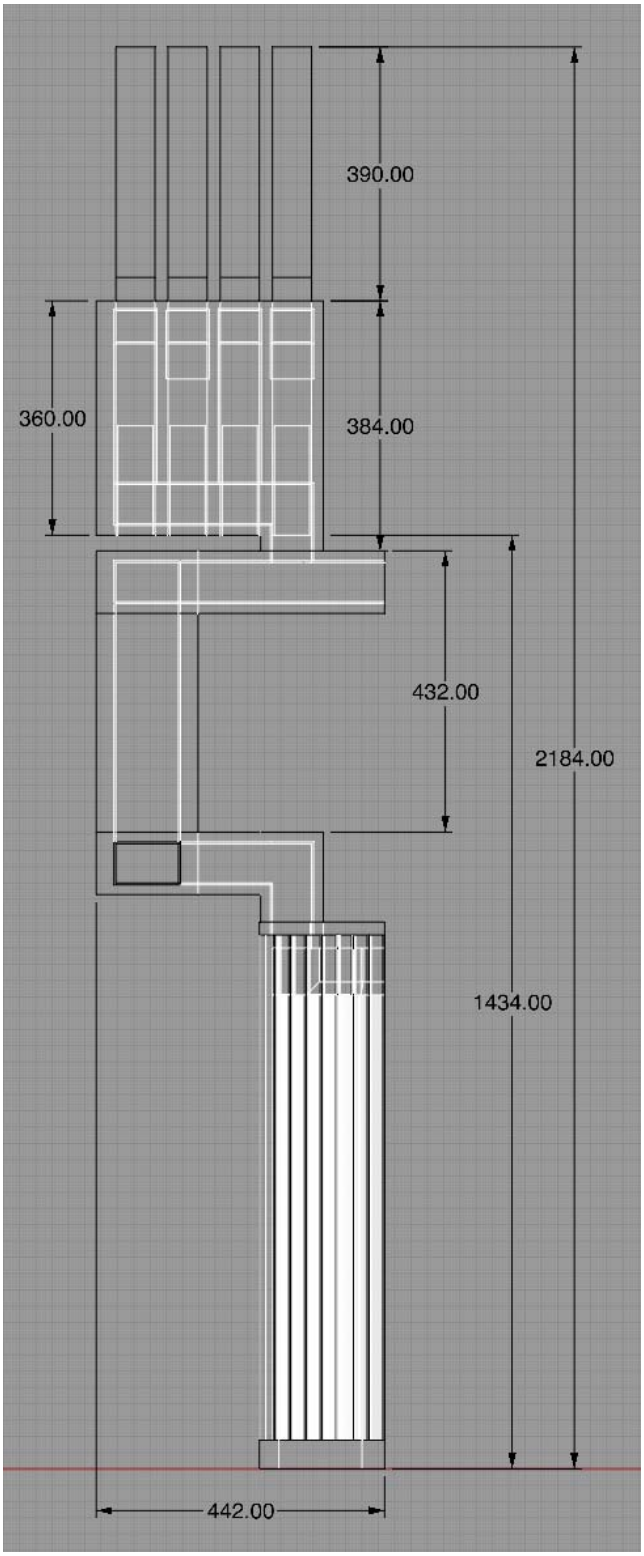

Figure 3.4. Vertical Dimensions Face-On Symmetric Half of RCCS (inches)

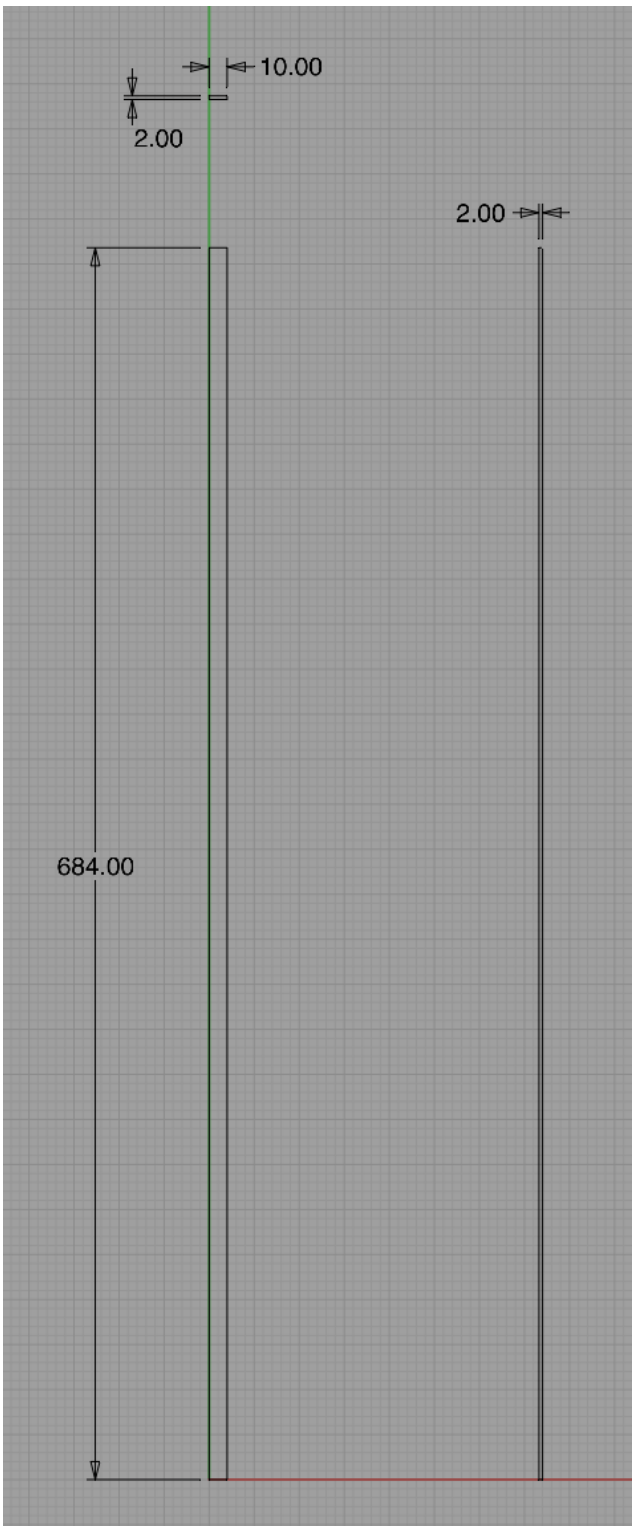

Figure 3.5. Riser Dimensions (inches)

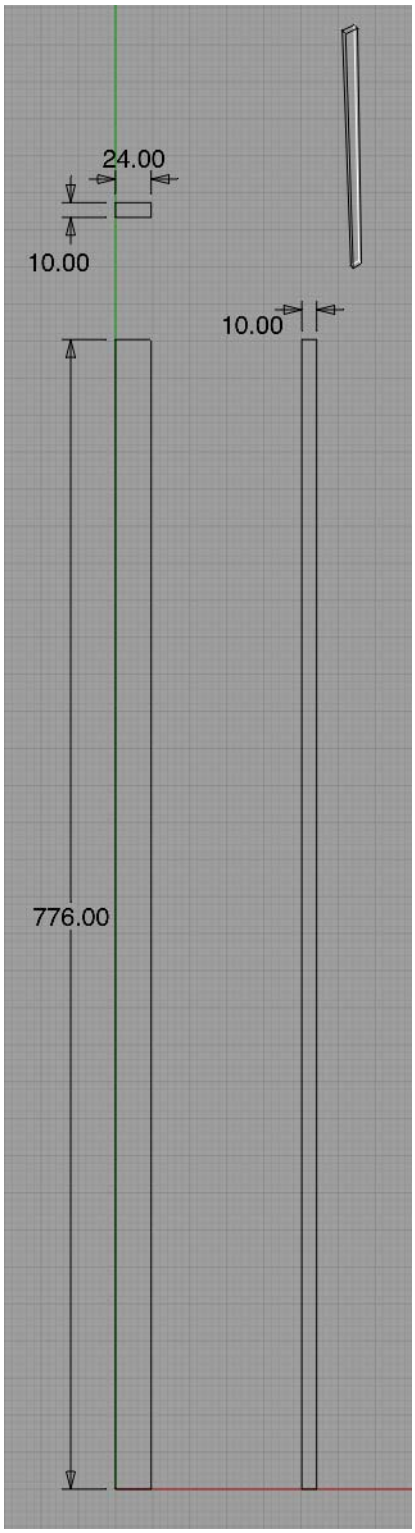

Figure 3.6. Downcomer Dimensions (inches)

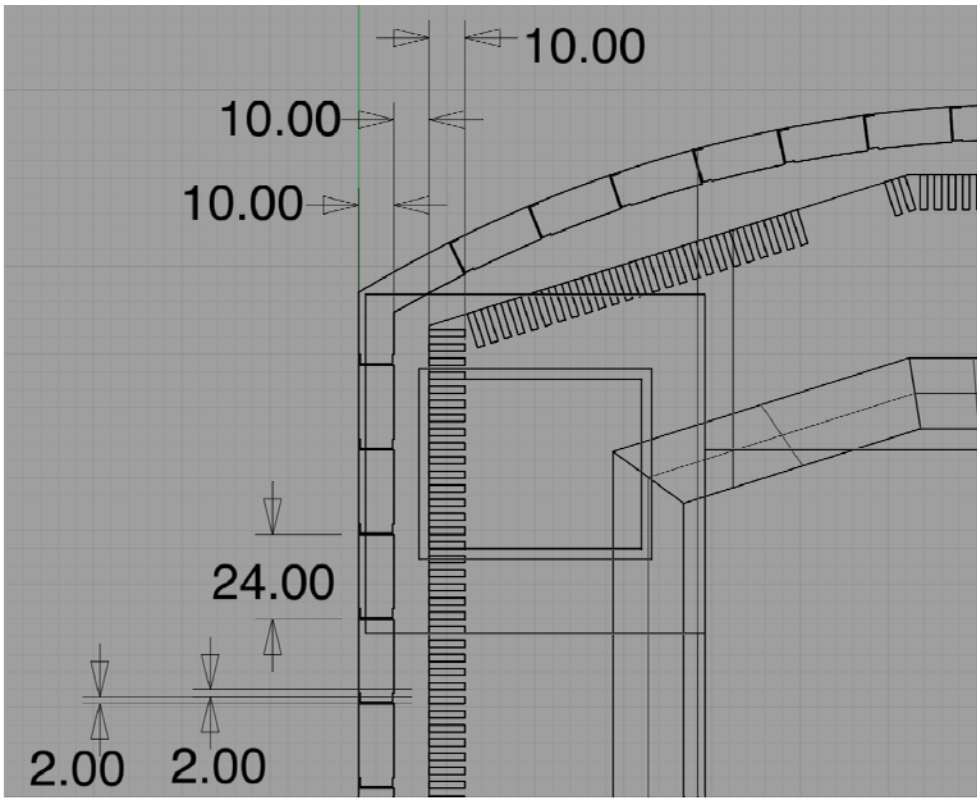

Figure 3.7. Riser and Downcomer Cross-Section Drawing Showing Plenum and Co-axial Duct Location

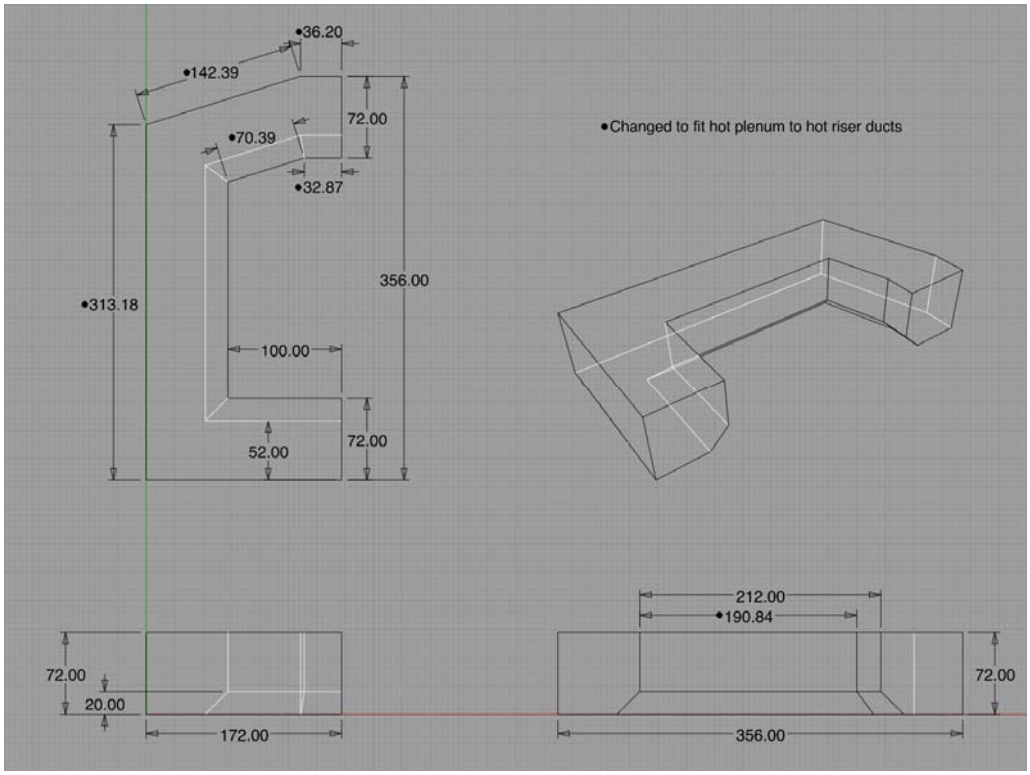

Figure 3.8. Upper Hot Plenum Dimensions (inches). One Symmetric Half is Shown.

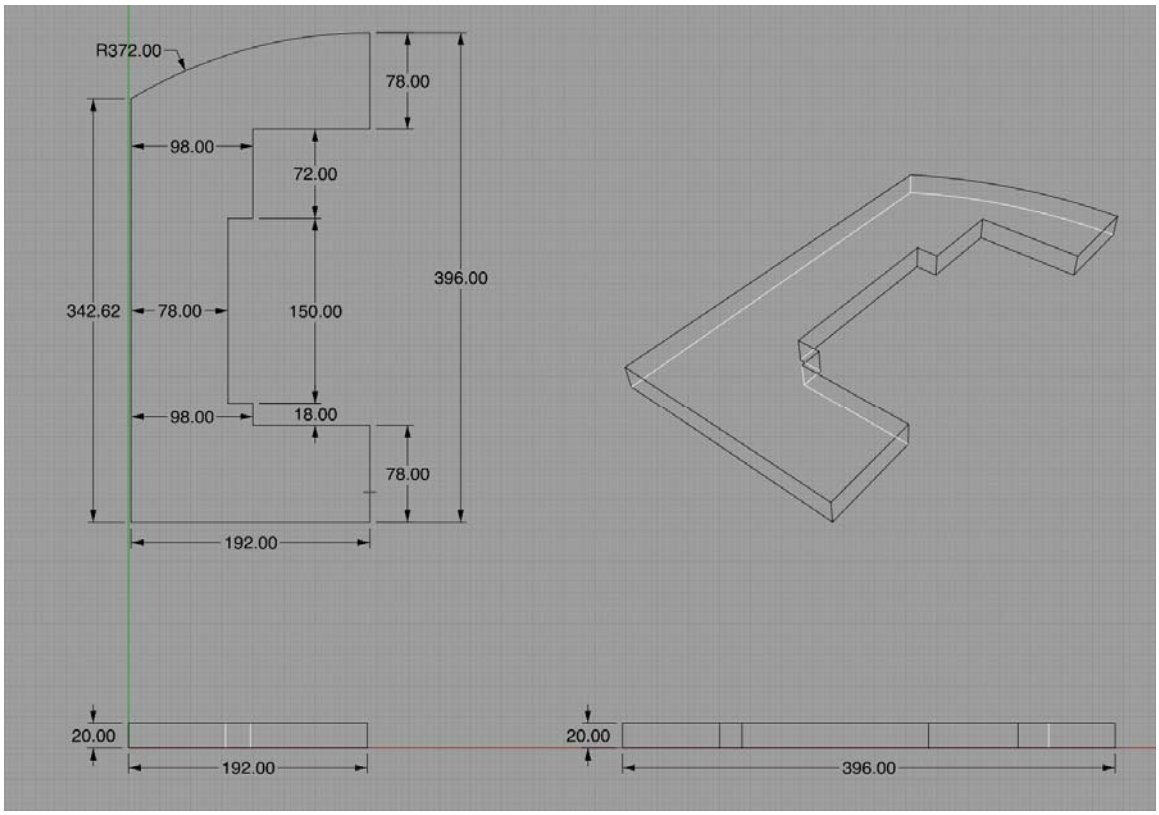

Figure 3.9. Upper Cold Plenum Dimensions (inches). One Symmetric Half is Shown.

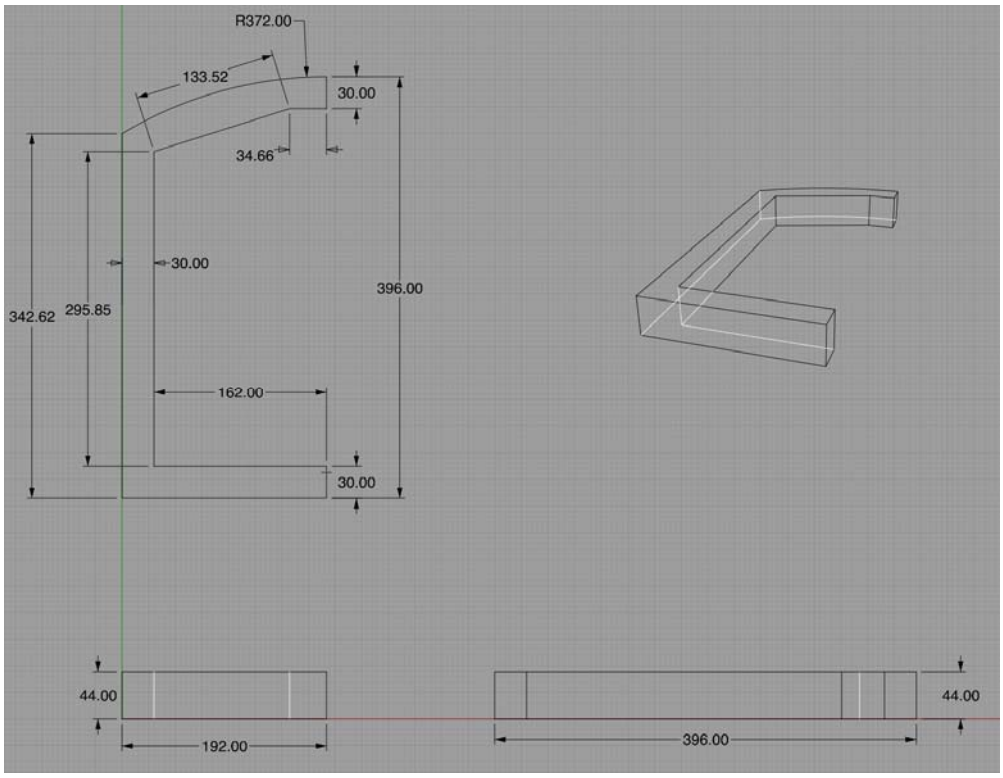

Figure 3.10. Lower Cold Plenum Dimensions (inches). One Symmetric Half is Shown.

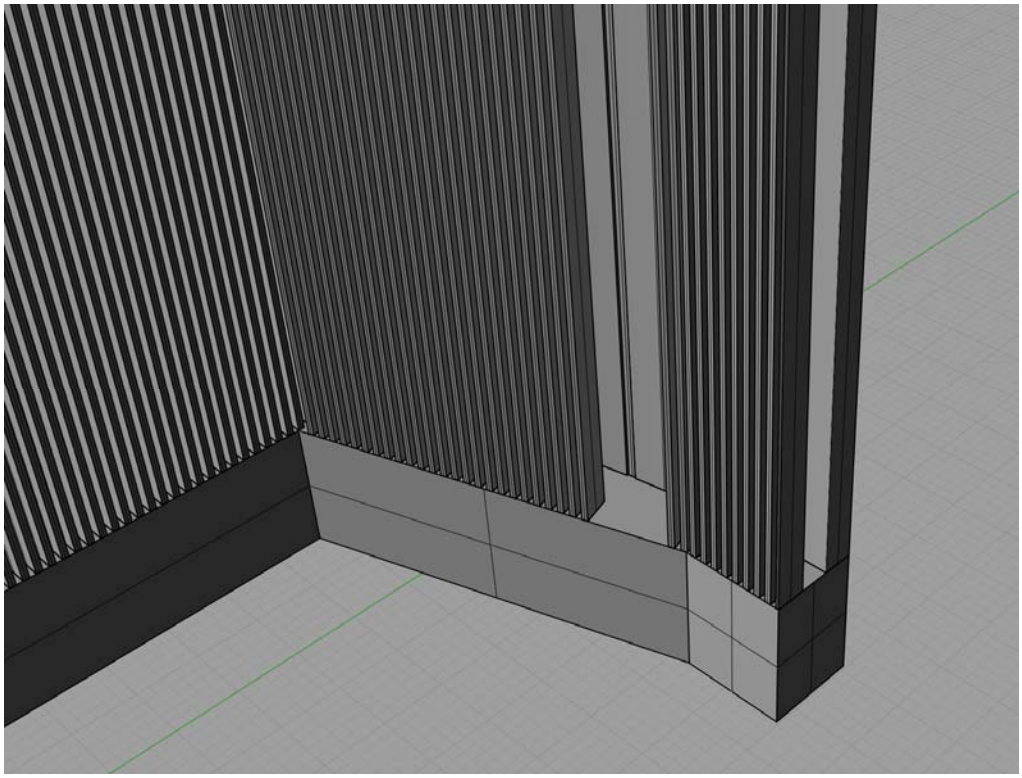

Figure 3.11. Detail View Showing Intersection of Lower Cold Plenum with Downcomer and Riser

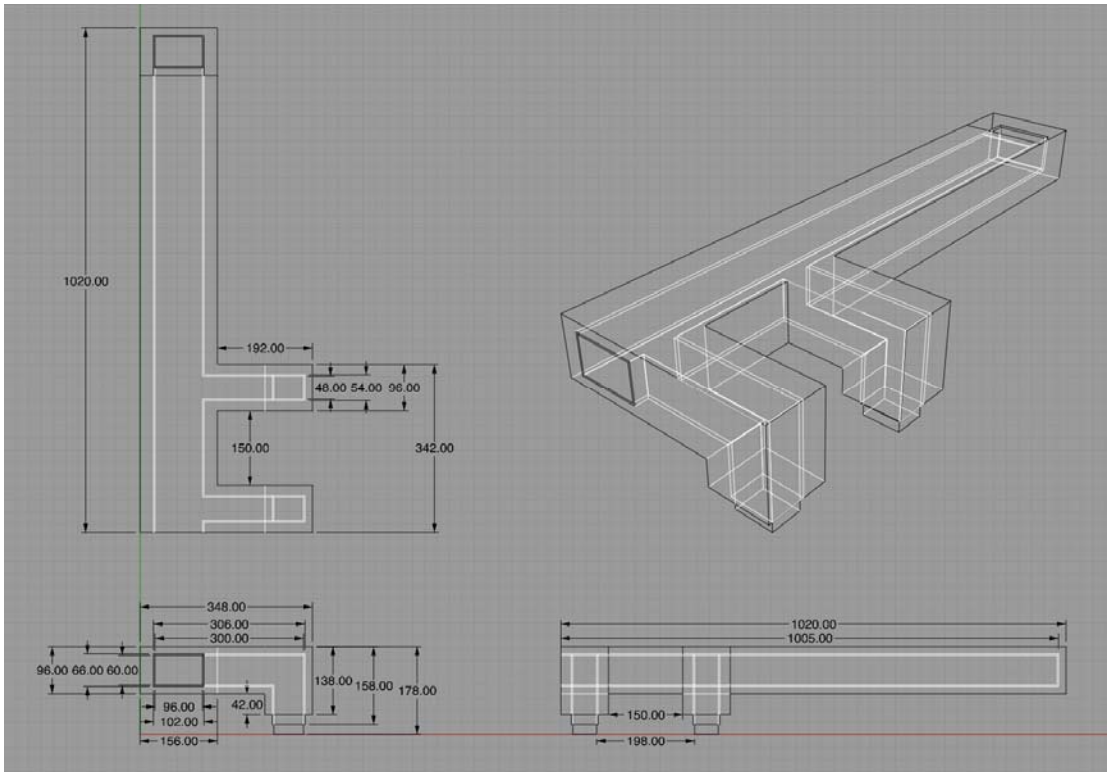

Figure 3.12. Co-axial Duct Dimensions (inches). Connects Upper Plena to Header.

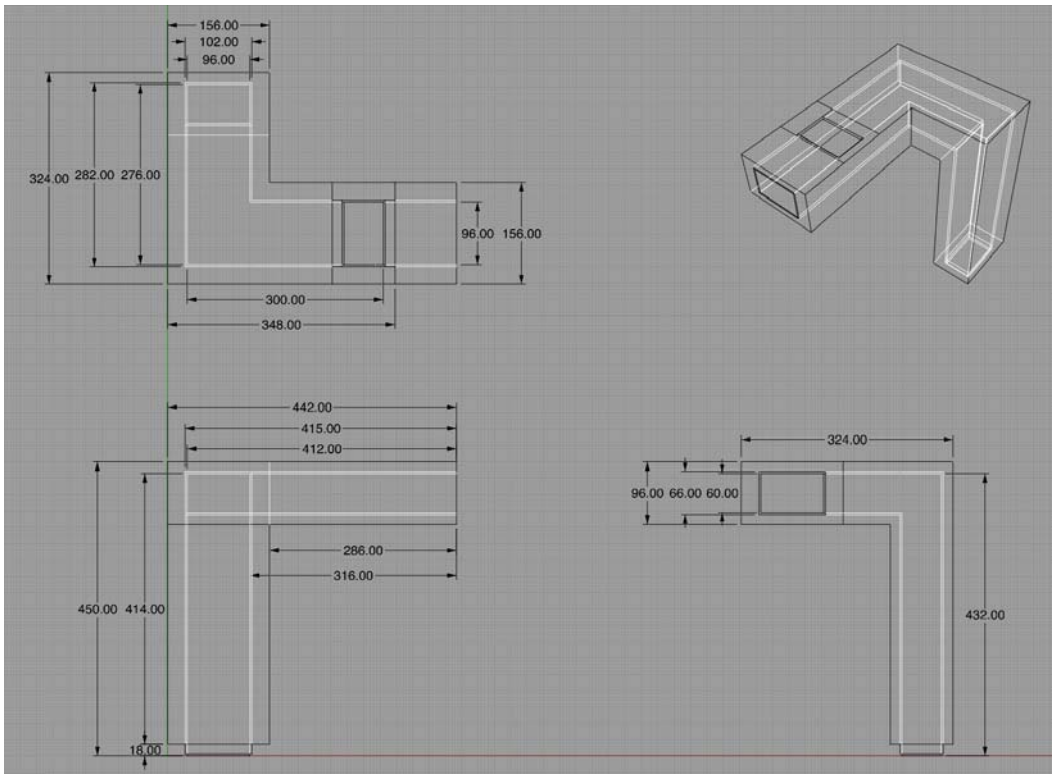

Figure 3.13. Co-axial Header Dimensions (inches). Connects Duct and to Inlet and Outlet Manifold.

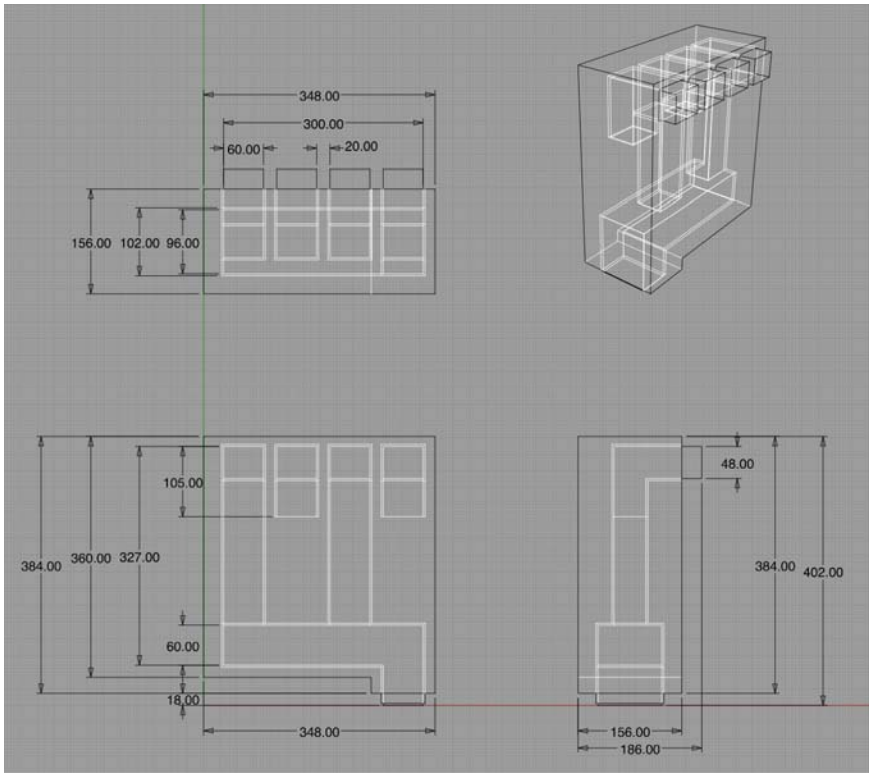

Figure 3.14. Inlet and Outlet Manifold Dimensions (inches)

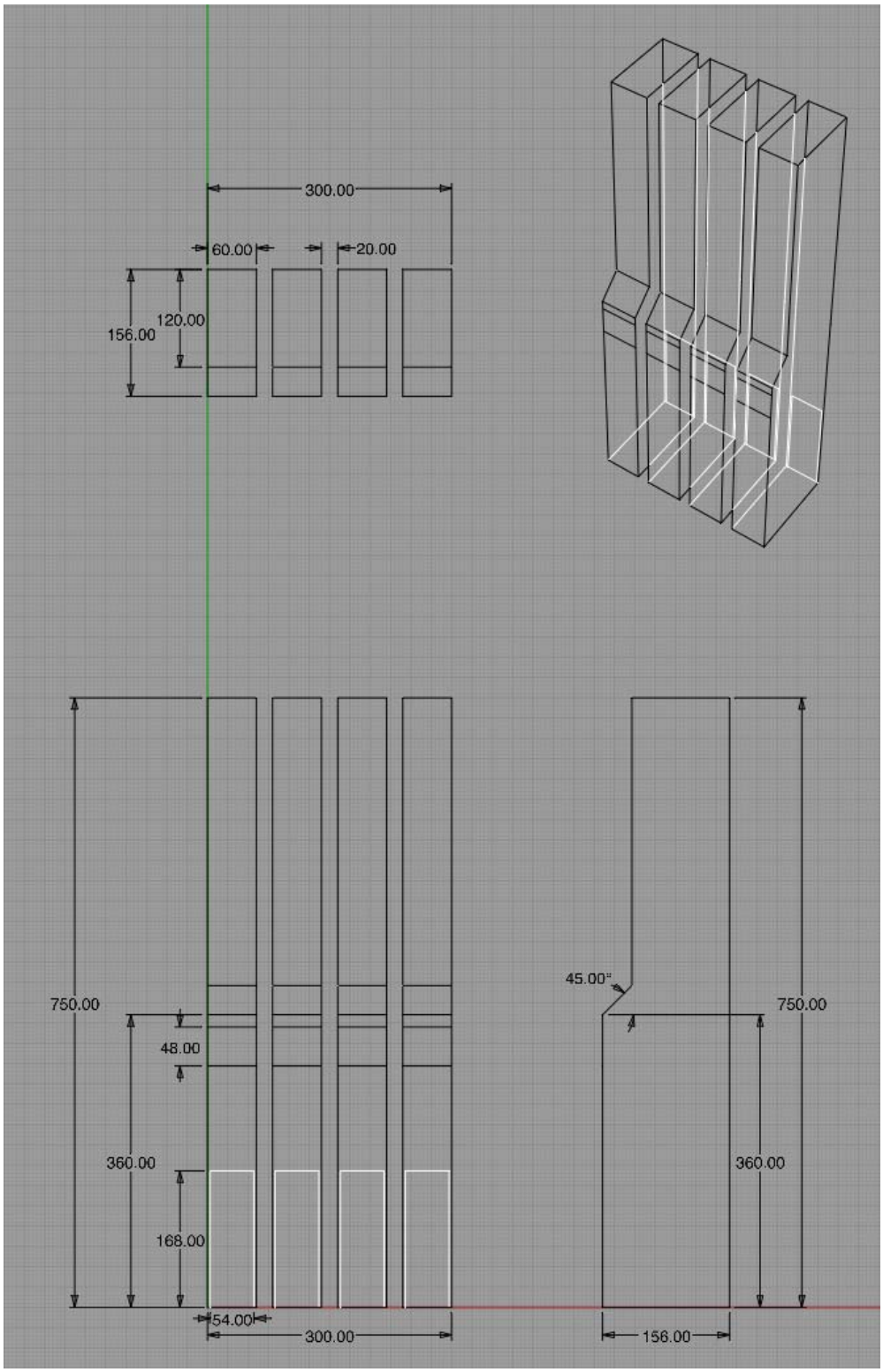

Figure 3.15. Chimney Dimensions (inches)

3.4 Fixed Heat Flux RCCS Model and Simulation Results

The initial baseline RCCS simulation uses a constant uniform heat flux on the risers rather than a more realistic radiation heat source distribution. The use of the simplified boundary condition enables the initial simulations of the air-cooled RCCS system and its NSTF analog to more easily be used for model development and mesh optimization. These simulations are also critical for the development of convergence criteria which truly ensure that that fully converged natural convection solutions have been obtained, since conventional residual based convergence criteria can be misleading in natural convection cases.

Based on the CAD model describing the full GA-MHTGR RCCS air-side geometry an explicit geometry model was developed using the built-in mesh development tools of STAR-CCM+, version 5.02.009. Using the CAD surfaces, a well-defined triangulated surface mesh was generated using the default STAR-CCM+ meshing tools. Based on this triangulated surface, a polyhedral volumetric mesh was generated. A polygonal prismatic wall extrusion layer is used to improve the applicability of the wall treatment employed in these simulations. The final mesh represents one symmetric half of the RCCS system, with 114.5 RCCS riser tubes, and uses approximately 9.2 million volumetric cells. Figure 3.16 shows a cross-sectional view of the mesh through the risers, upper plena and inlet/outlet ducts.

A volume of air was placed around the inlets and outlets of the chimney to close the loop of the system and allow natural convection flow. Both the upper and lower chimney openings are assumed to be open for flow to maximize the opportunity for re-entrant flow as part of the model development effort. All flow velocities are simulated as result of natural buoyant convection and no-flow boundary conditions are specified. A uniform 1·237 kW/m2 heat flux applied to all the risers, which is consistent with a loss of flow accident in which the risers expelling all of the heat from the reactor vessel, 10kW/m2, out of the system. An equivalent volumetric heat sink is assumed in the external air volume to allow the natural convection flow to be simulated. A symmetry boundary condition is applied at the symmetry plane so that the model effectively represents the full system. All other boundaries in the model are assumed to be adiabatic no-slip walls.

The baseline simulation, which was completed using 32 cores on a commercial-grade Linux computing cluster, required more than 18000 iterations to reach a well-converged steady state. While standard residual based convergence criteria are satisfied within a few thousand iterations, the uniform constant heat flux assumption allows a more rigorous convergence test to be applied – the flow fields in each of the 114.5 vertical risers should be nearly identical. The development of the flow field was monitored in 5 selected risers to ensure that the simulation was well converged. Figure 3.17 and Figure 3.18 display the axial temperature and velocity profiles of 5 risers as the air travels up the ducts. The close agreement between the riser temperature and velocity distributions for this fixed heat flux case confirms that a converged natural

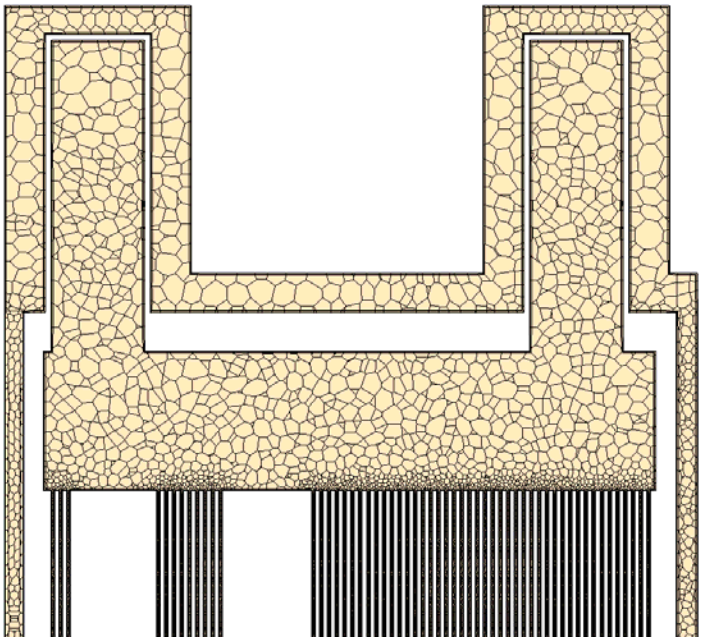

Figure 3.16. Mesh Representation of Plane at Center of Risers

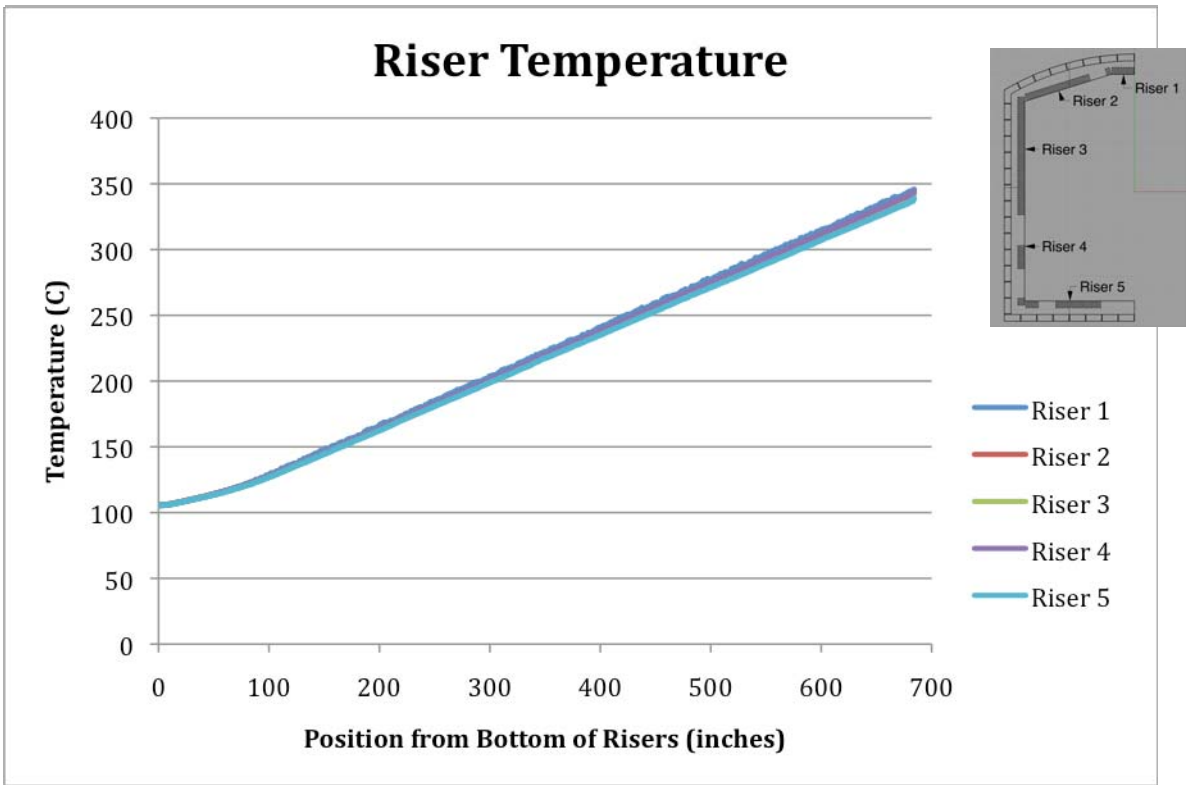

Figure 3.17. Temperature Profile in Risers

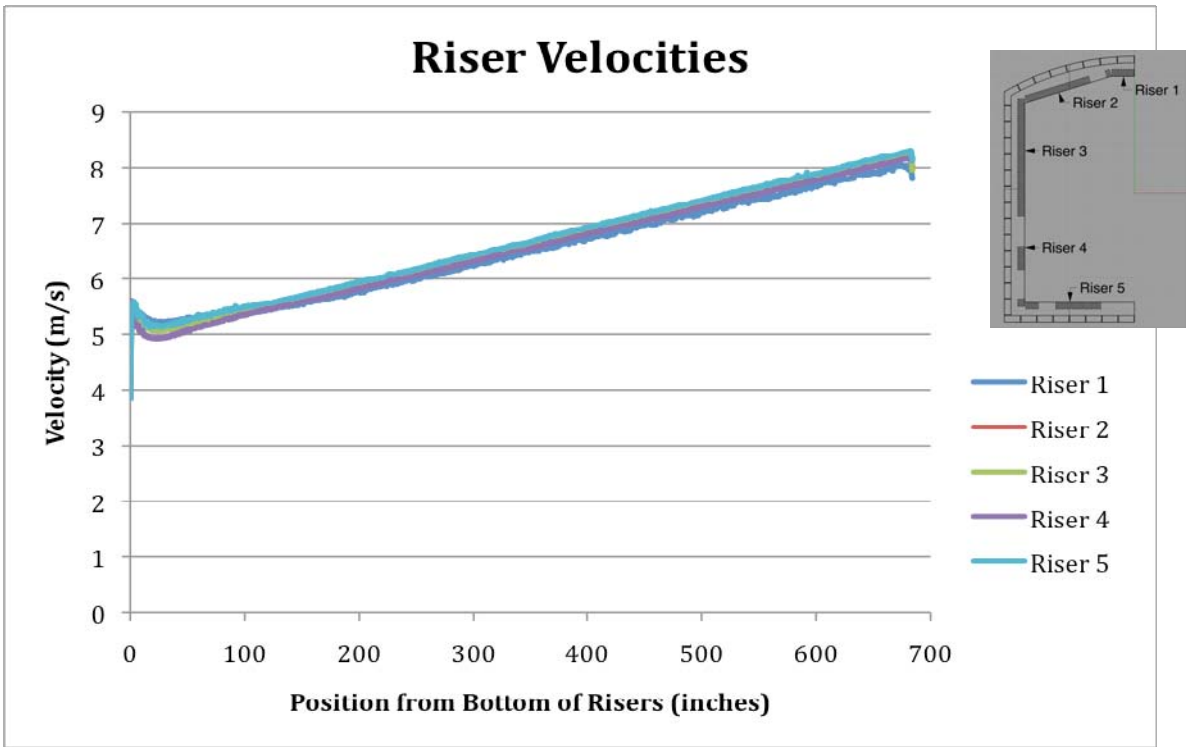

Figure 3.18. Velocity Profile in Risers

convection solution can be obtained using the optimized mesh and the solver options selected. Figure 3.19 shows a predicted temperature distribution within the risers.

The temperature distribution in the upper components of the RCCS system is shown in Figure 3.20, with detailed distributions of the hot side components shown in Figures 3.21 through 3.23. Since the heat flux in each riser tube is identical, the temperature distributions in these components are very uniform. However, the velocity fields, shown in Figures 3.24 through 3.28 provide some insight into likely regions of thermal stripping or stratification when a more realistic non-uniform heat load distribution is applied. For example, strong recirculation zones form downstream of each of the 90-degree bends in the co-axial ducts. Such flow structures can result in the formation of stagnation points which lead to thermal stresses in adjacent solid materials. However, in this case, these flow features also result in significant turbulence generation, as shown in Figures 3.29 through 3.32 where high turbulent kinetic energies are observed near the center of each recirculation region.

One significant model development concern is the sizing of the large air volume which serves as heat sink and air source for the natural convection driven RCCS coolant flow. In Figure 3.33, streamlines were generated beginning from a seed point at the mid-plane of 5 selected RCCS tubes. Of those 5 streamlines, two – blue and yellow – actually exit the RCCS system into the cold volume, recirculate briefly and then re-enter the RCCS. The temperature profile along the blue streamline, shown in Figure 3.34, confirms that the coolant entering the RCCS is adequately cooled by the heat sink to the desired ambient temperature.

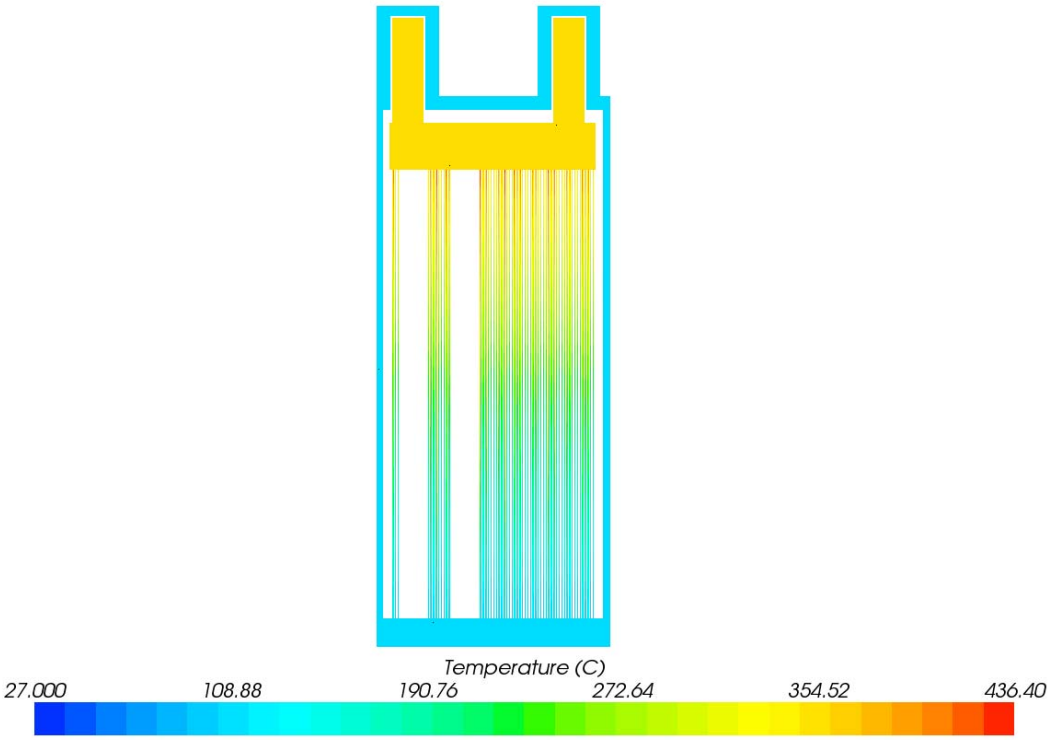

Figure 3.19. Temperature Distribution in RCCS Risers

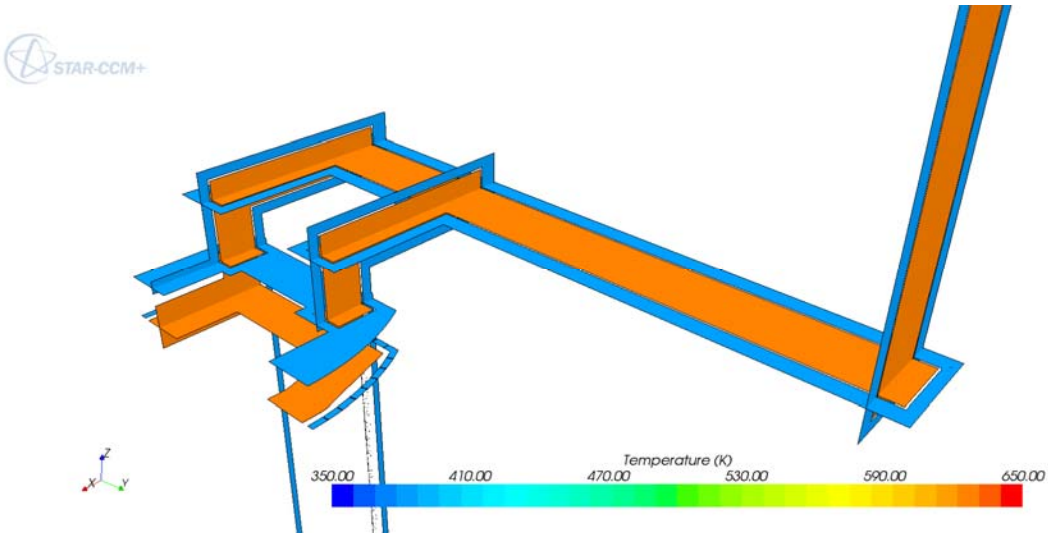

Figure 3.20. Temperature Distribution in RCCS Upper System Components

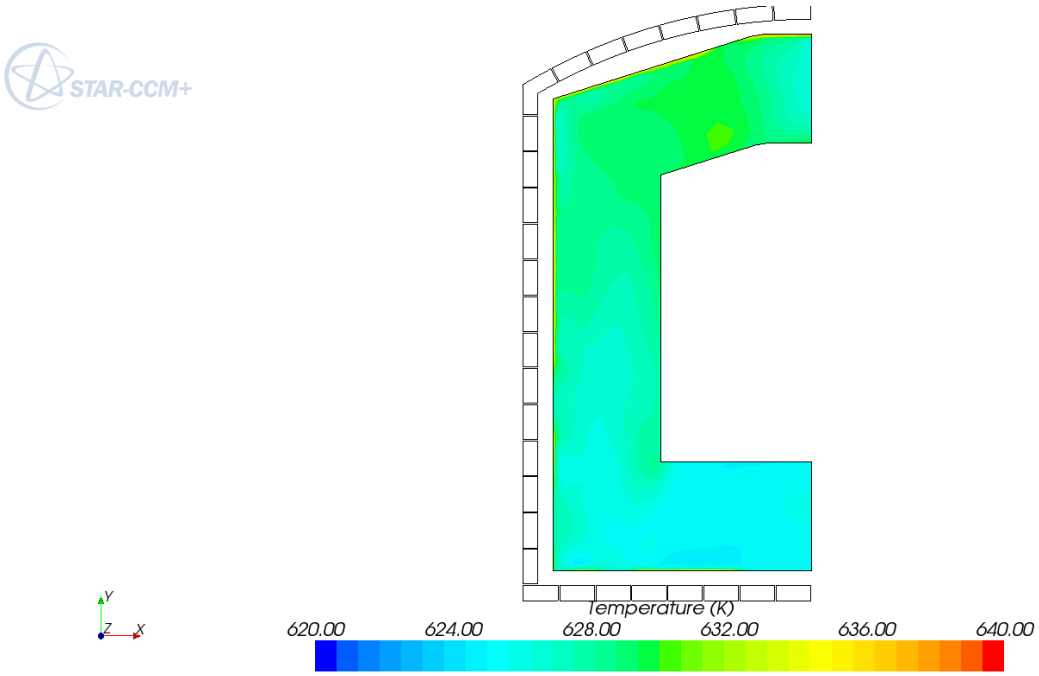

s

Figure 3.21. Temperature Distribution in Hot Plenum

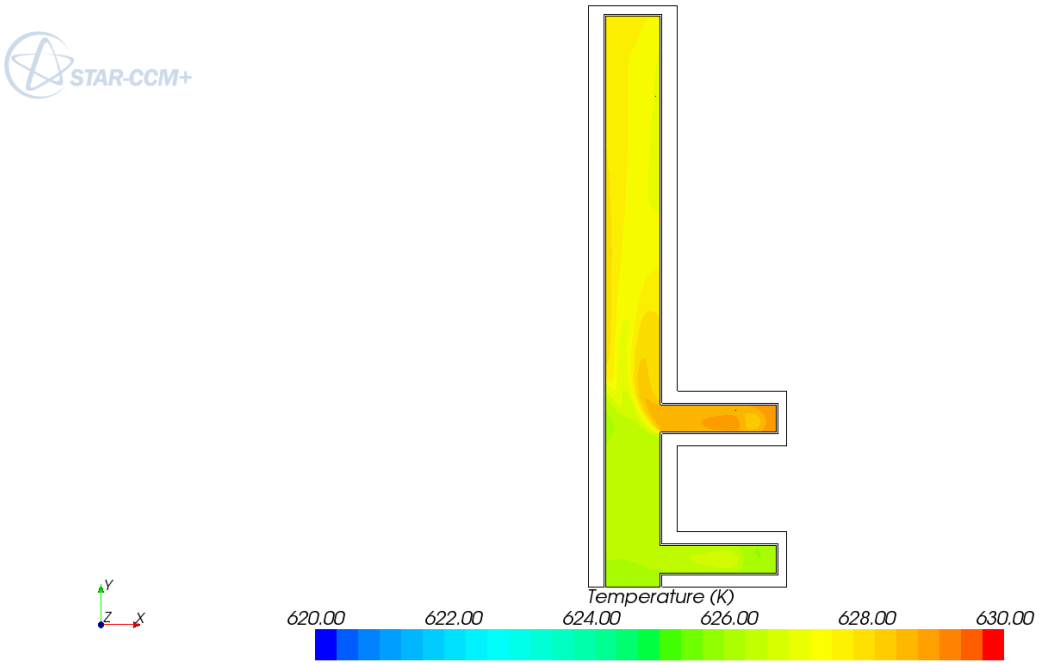

Figure 3.22. Temperature Distribution in Hot Duct from Hot Plenum to Hot Header

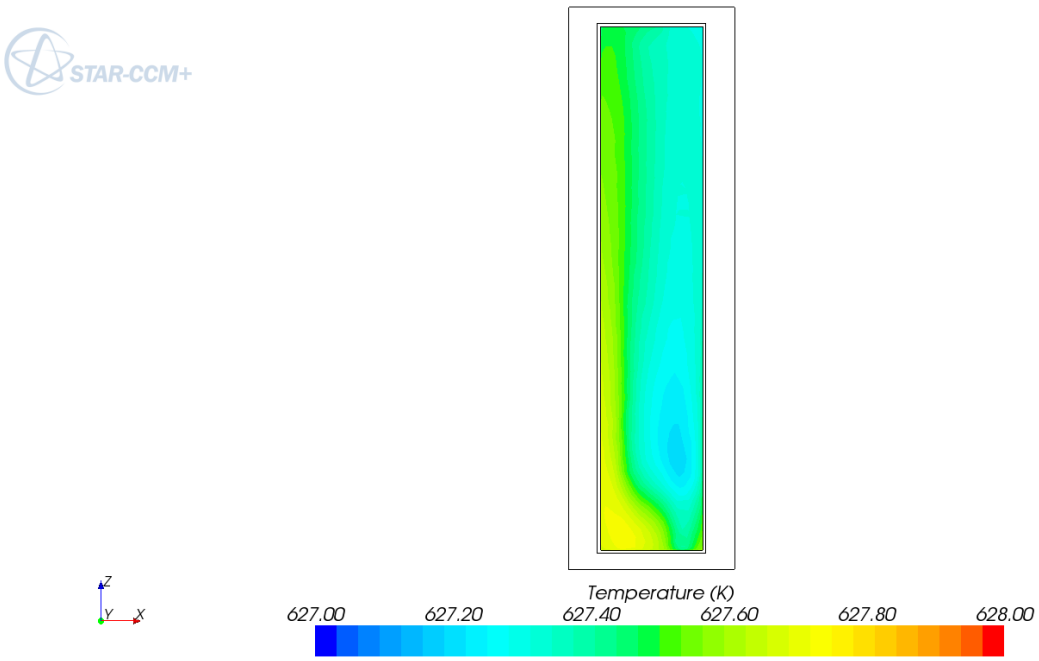

Figure 3.23. Temperature Distribution in Vertical Hot Header from Hot Duct to Outlet Manifold

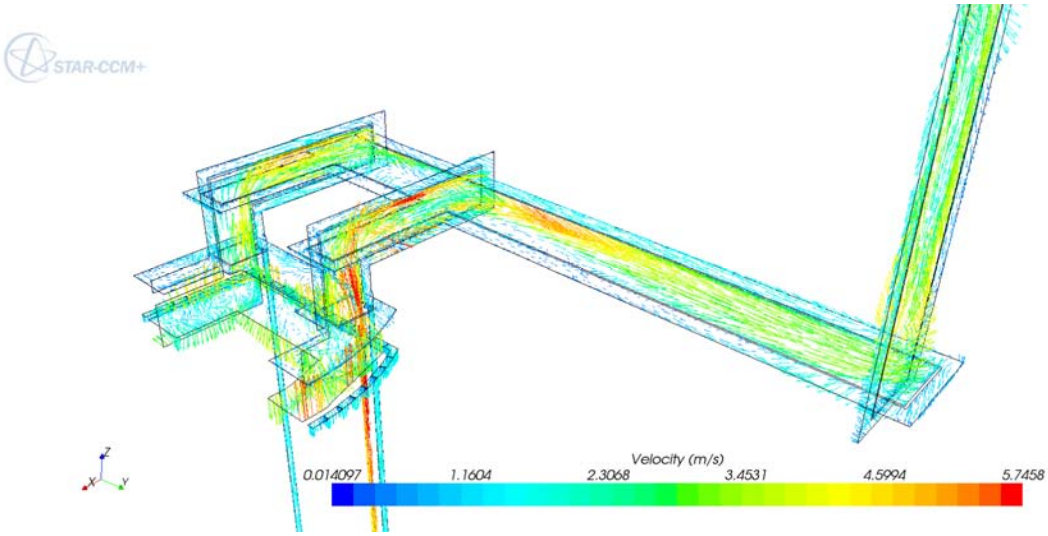

Figure 3.24. Velocity Vector Field in RCCS Upper System Components, including Hot and Cold Plena and Co-axial Ducts and Headers

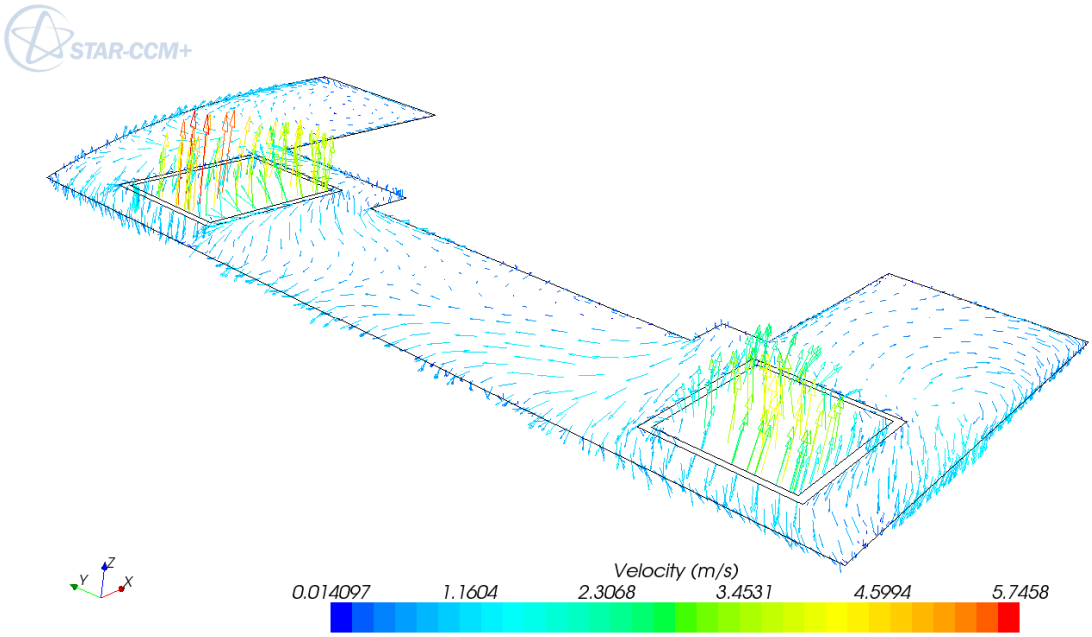

Figure 3.25. Velocity Vector Field at Mid-plane of Cold Plenum, including Flow from Hot Plenum through Hot Ducts

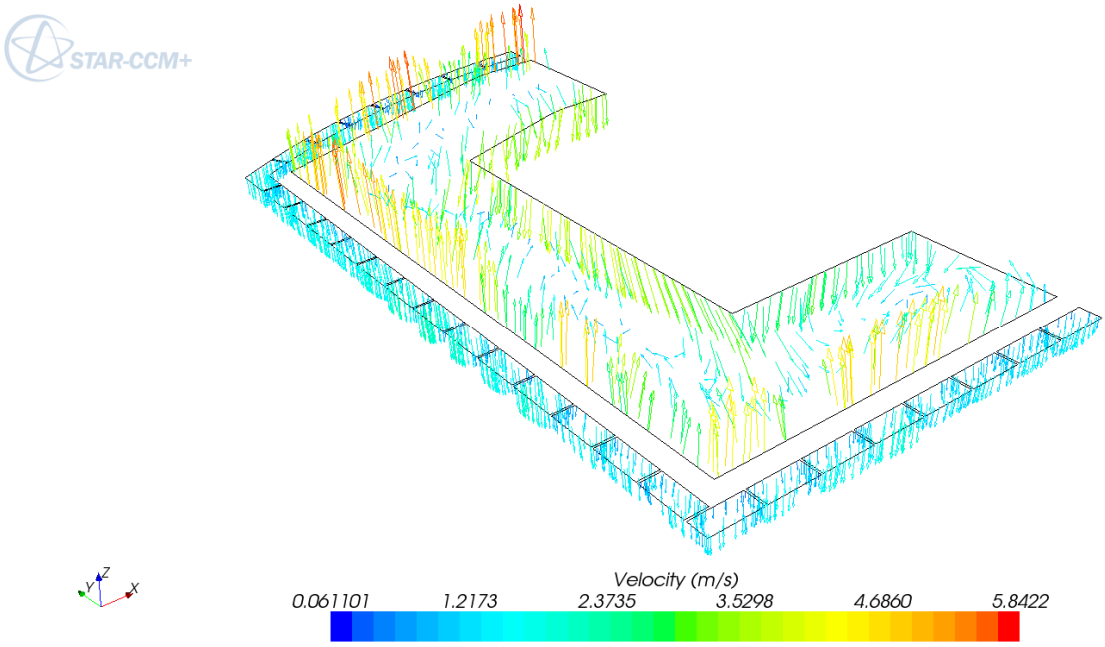

Figure 3.26. Velocity Vector Field at Mid-plane of Hot Plenum, including Downflow in Downcomers

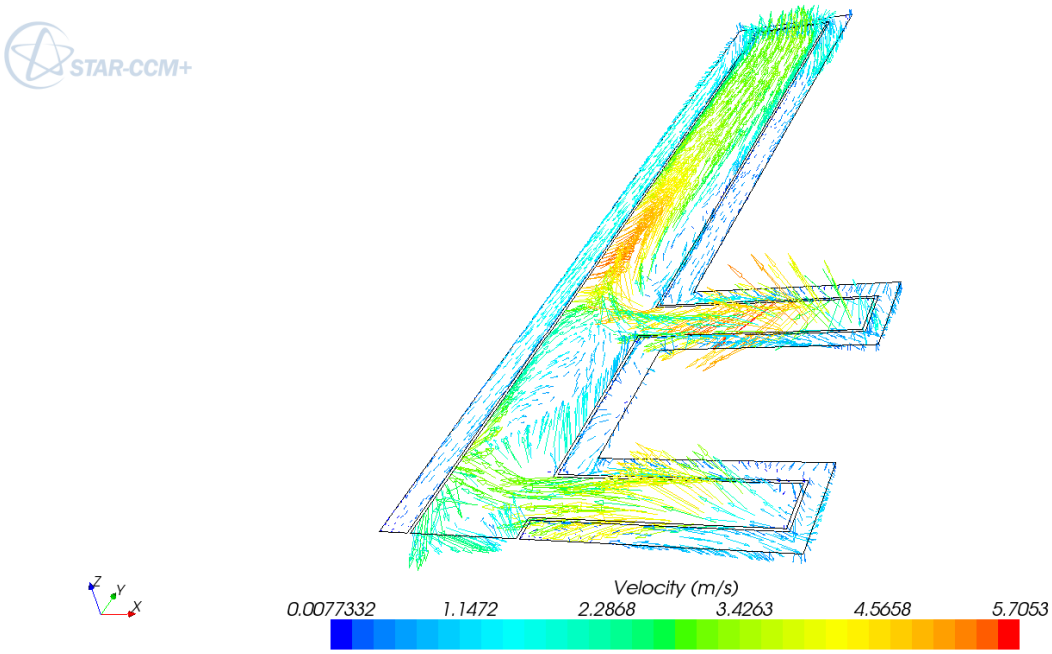

Figure 3.27. Velocity Vector Field in the Co-axial Duct from the Upper Plena to the Vertical Header

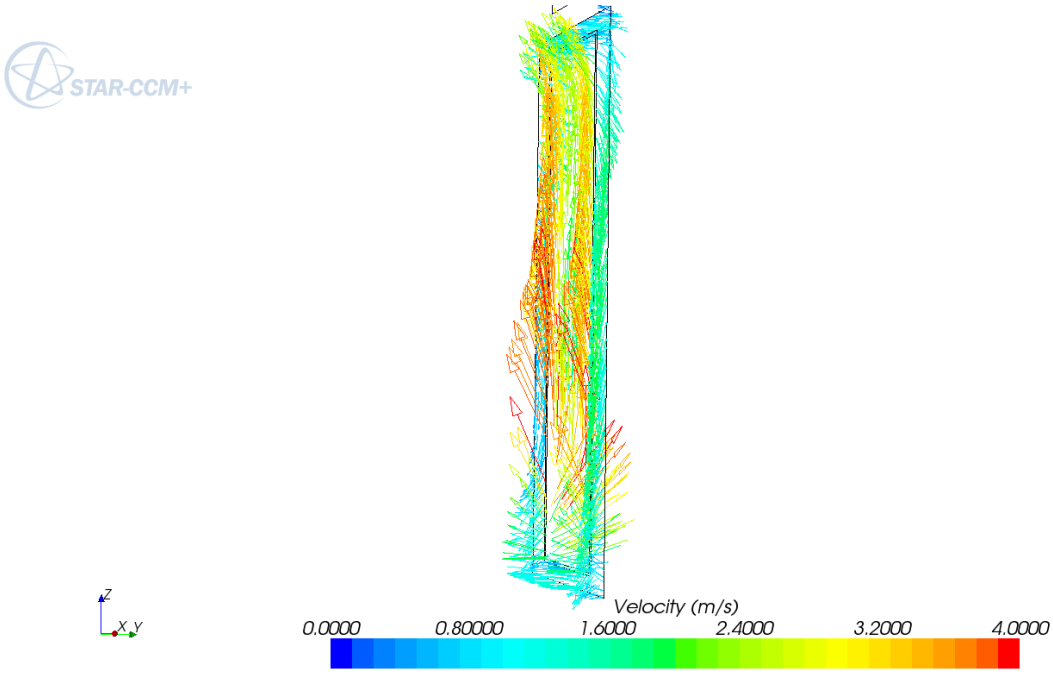

Figure 3.28. Velocity Vector Field in the Vertical Co-axial Header between the Co-axial Duct and the Outlet Manifold

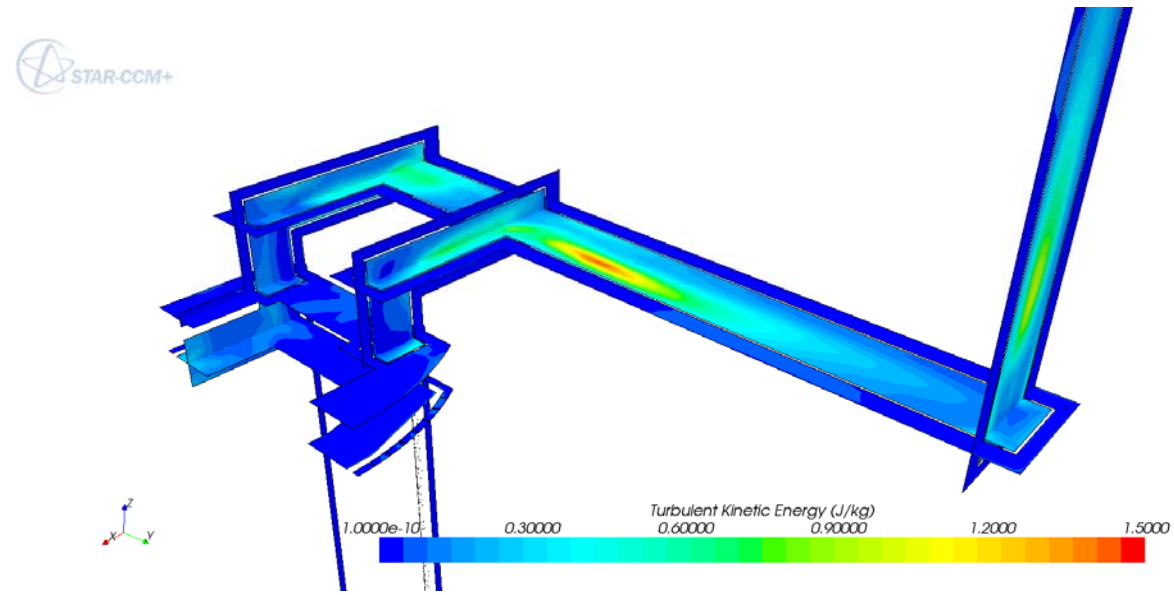

Figure 3.29. Turbulent Kinetic Energy Distribution in the RCCS Upper System Components.

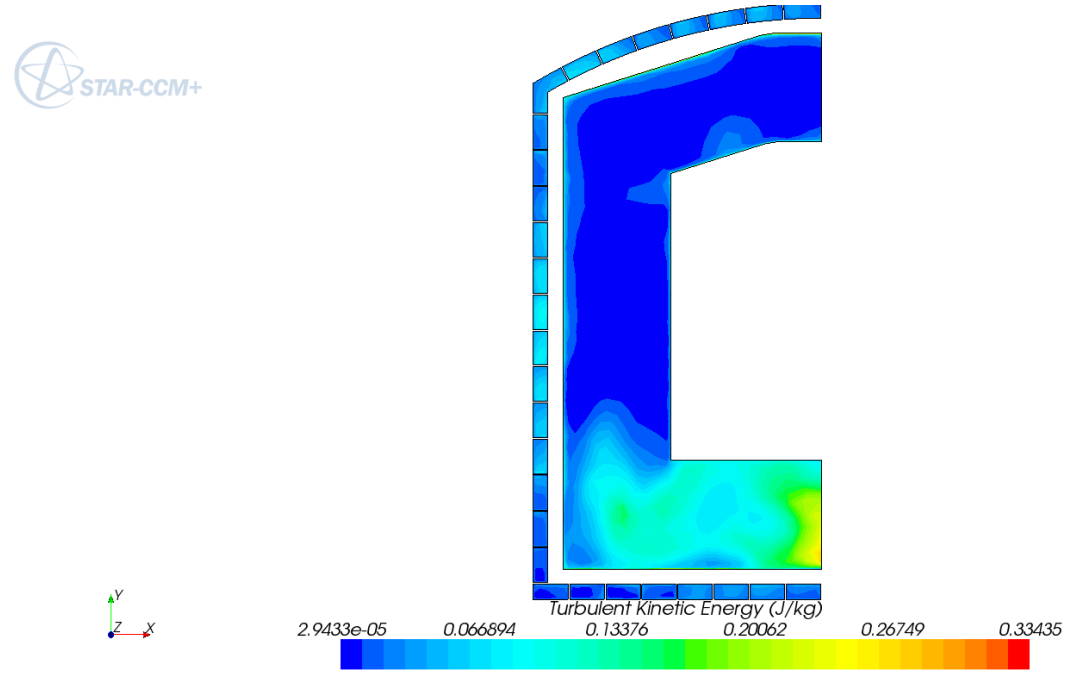

Figure 3.30. Turbulent Kinetic Energy Distribution at the Mid-plane of the Hot Plenum.

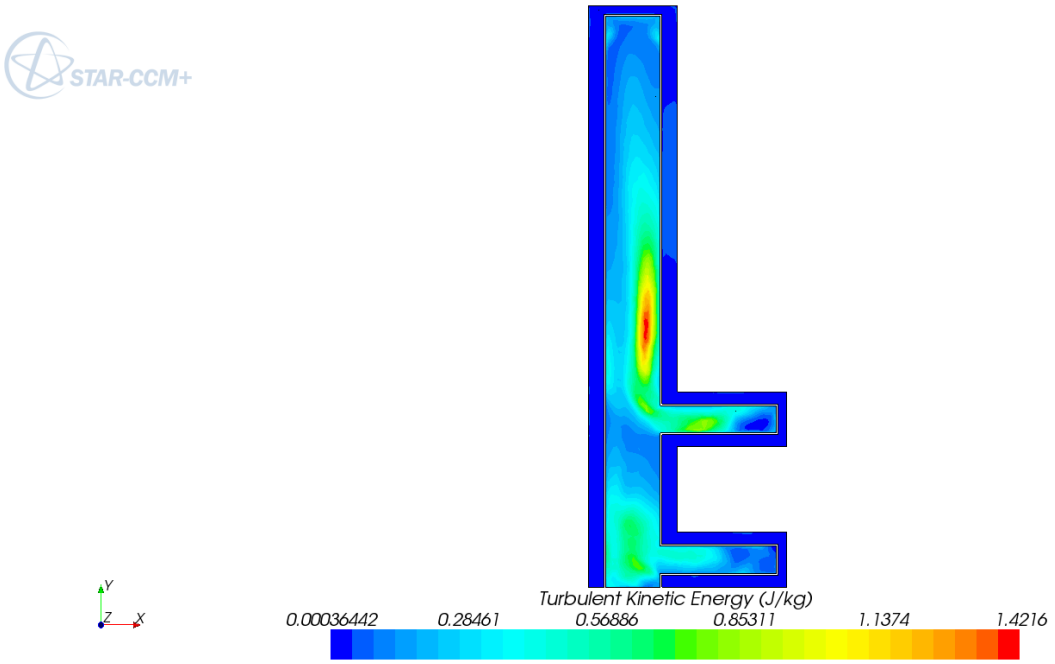

Figure 3.31. Turbulent Kinetic Energy Distribution at Mid-plane of Co-axial Duct from Upper Plena toVertical Header

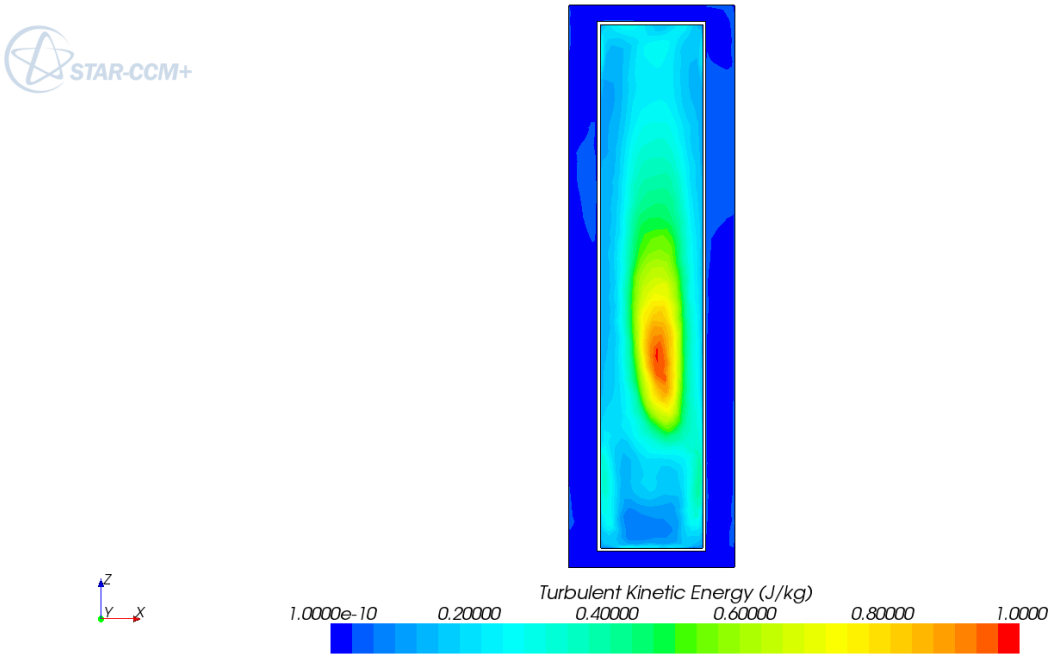

Figure 3.32. Turbulent Kinetic Energy Distribution in Vertical Co-axial Header between Co-axial Duct and Outlet Manifold

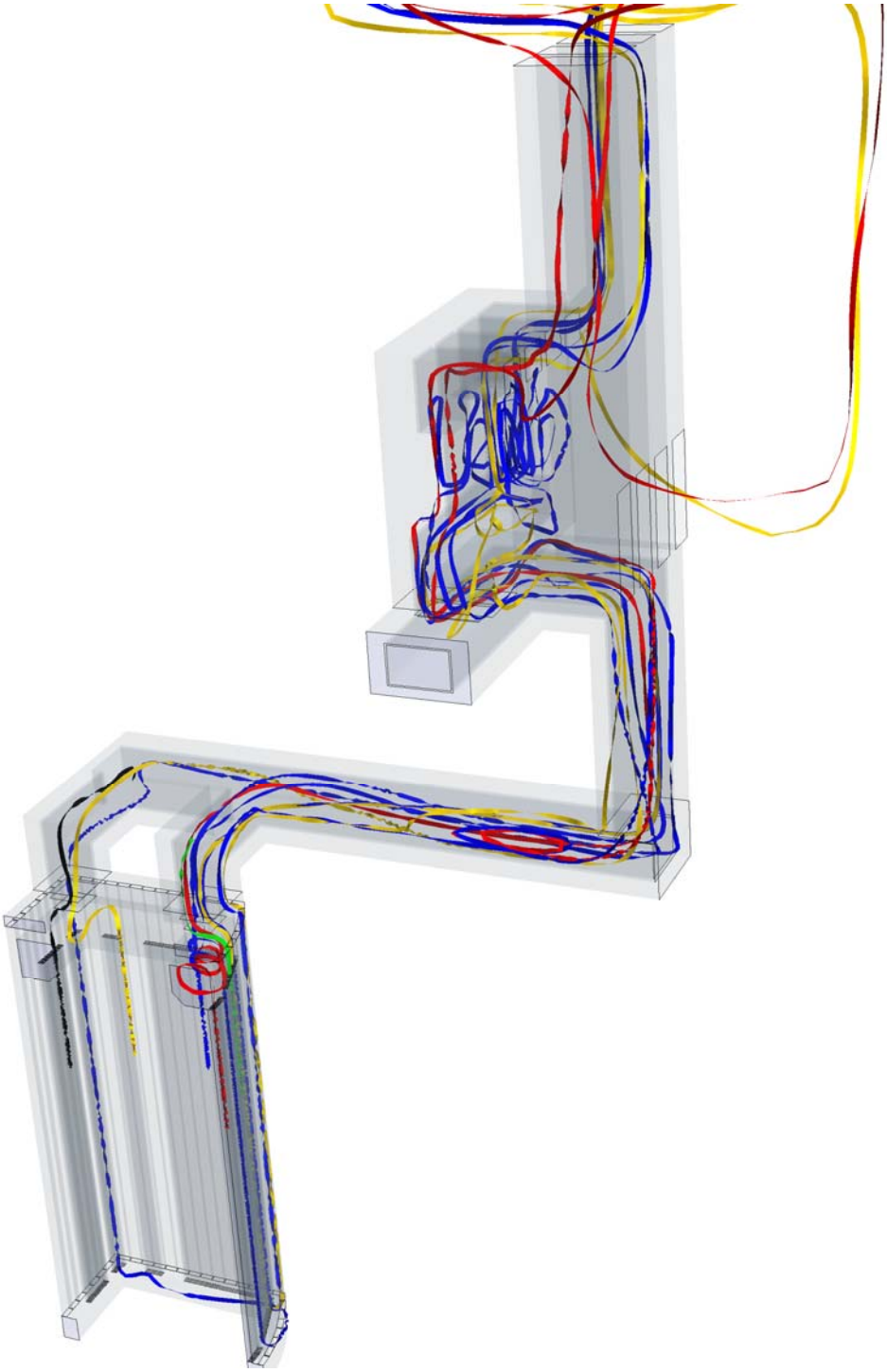

Figure 3.33. Streamlines Showing the Path of Air from 5 Different RCCS Riser Tubes

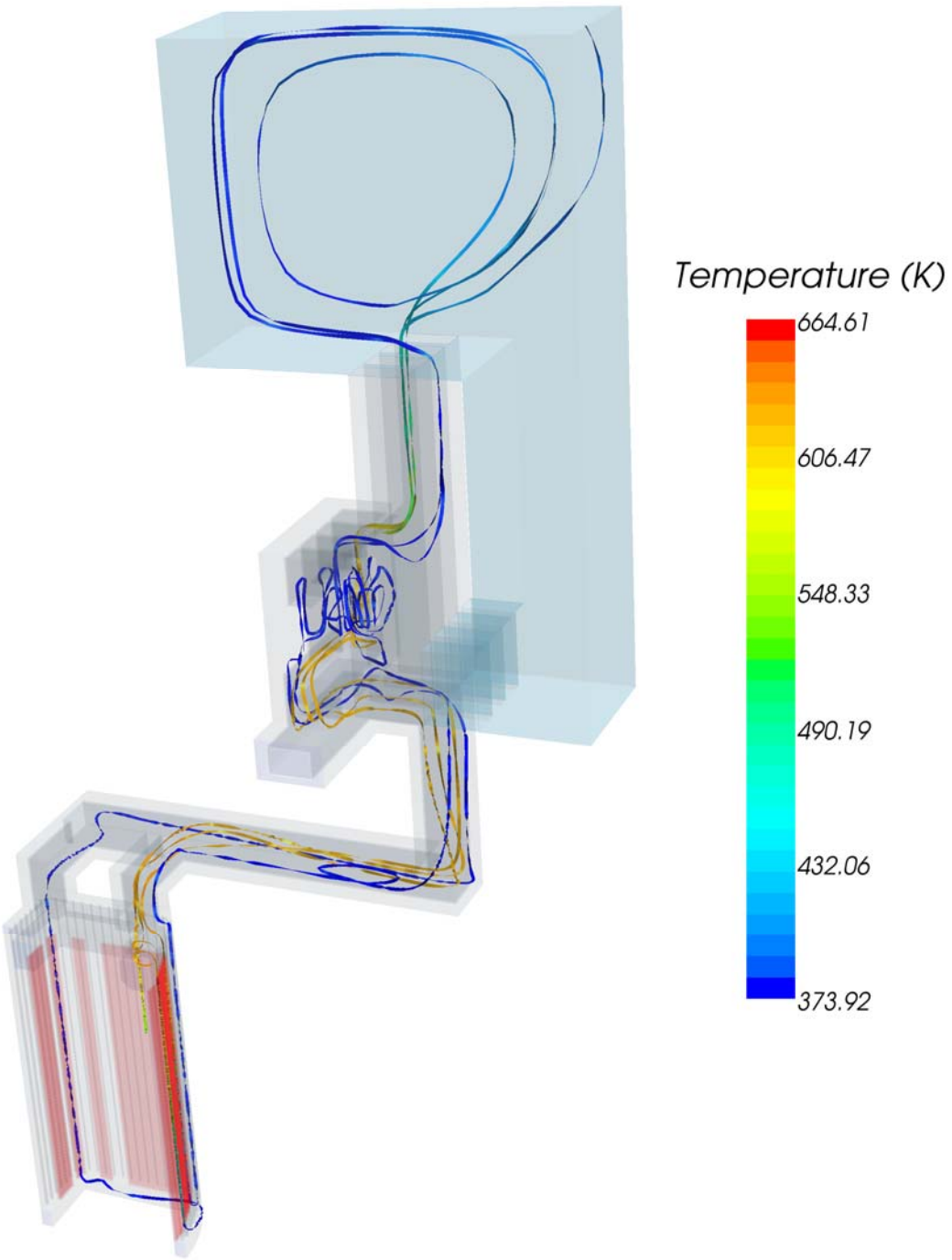

Figure 3.34. Temperature Along Selected Streamline, which Travels through the RCCS Three Times

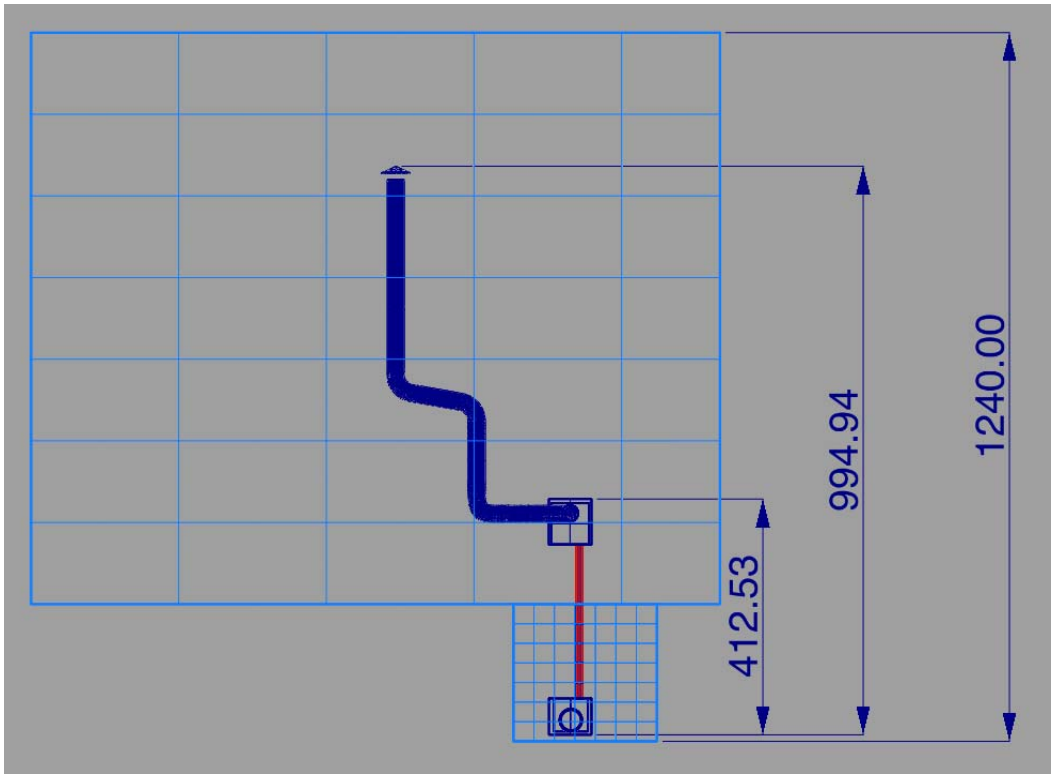

Figure 3.35. Vertical Dimension of the NSTF Air-cooled RCCS Experiment Model

3.5 NSTF Experiment Model

The proposed air-cooled RCCS experiments in the NSTF are designed to provide a well-scaled representation of the operation of RCCS system. Although based on the experimental geometry currently being discussed. The computational model considers a simplified geometry which neglects the building structure and assumes that adequate ventilation is available to feed coolant to the inlet of the natural convection driven facility. The geometry and axial dimensions of the model are shown in Figure 3.35. In the model, air enters the test section from a large common air volume, accelerates through the risers, and passes into an outlet plenum before emptying into the common air volume through a tall circular chimney. Since the common air volume used in the model is very large in comparison to the heated region of the experiment, a constant temperature surface condition is used rather than the more complicated volumetric sink condition used in the GA-MHTGR RCCS analysis. The riser duct heat flux boundary condition and solver settings are the same as those used in that full-scale model.

The computational mesh was constructed based on CAD data describing the NSTF geometry. The mesh settings used in the development of the baseline RCCS mesh were also applied to the NSTF model. The final mesh consists of more than 15 million polyhedral and prismatic polygonal cells. The NSTF mesh uses more cells than the GA-MHTGR RCCS mesh as a consequence of the curved contours of the RCCS outlet ducts and chimney. The baseline simulation was completed using 32 cores of a commercial grade Linux cluster and required 8360 iterations to reach a converged steady state. As in

the full scale reactor RCCS simulations, convergence is determined through a combination of printed residual values and variation in monitoring point values.

The predicted temperature profile in the heated region is quite similar to the profile seen in the full-scale GA-MHTGR RCCS case, as shown in Figure 3.36. As in the full-scale case, uniform heating of the RCCS ducts should be expected and the temperature distribution in the RCCS risers as well as the horizontal and vertical duct segments are very uniform, as shown in Figures 3.37 through 3.39. However, as seen in Figure 3.40 and 3.41, the single horizontal inlet configuration results in the formation of a strong recirculation zone in the inlet plenum which may affect the duct flow distribution and stability. Steady state velocity profiles and the good convergence behavior of the simulation suggest that the flow field in the risers, shown in Figure 3.42, is fairly stable, but more detailed unsteady analyses are needed to address stability.

Similarly, as seen in Figures 3.43 and 3.44, a large recirculation zone forms in the upper plenum as a consequence of the offset position of the risers. This recirculation pattern persists through the horizontal segment of the outlet duct and may interfere with the formation of the recirculation patterns seen downstream of each elbow in the RCCS model. For completeness, the vertical duct velocity field is shown in Figure 3.45.

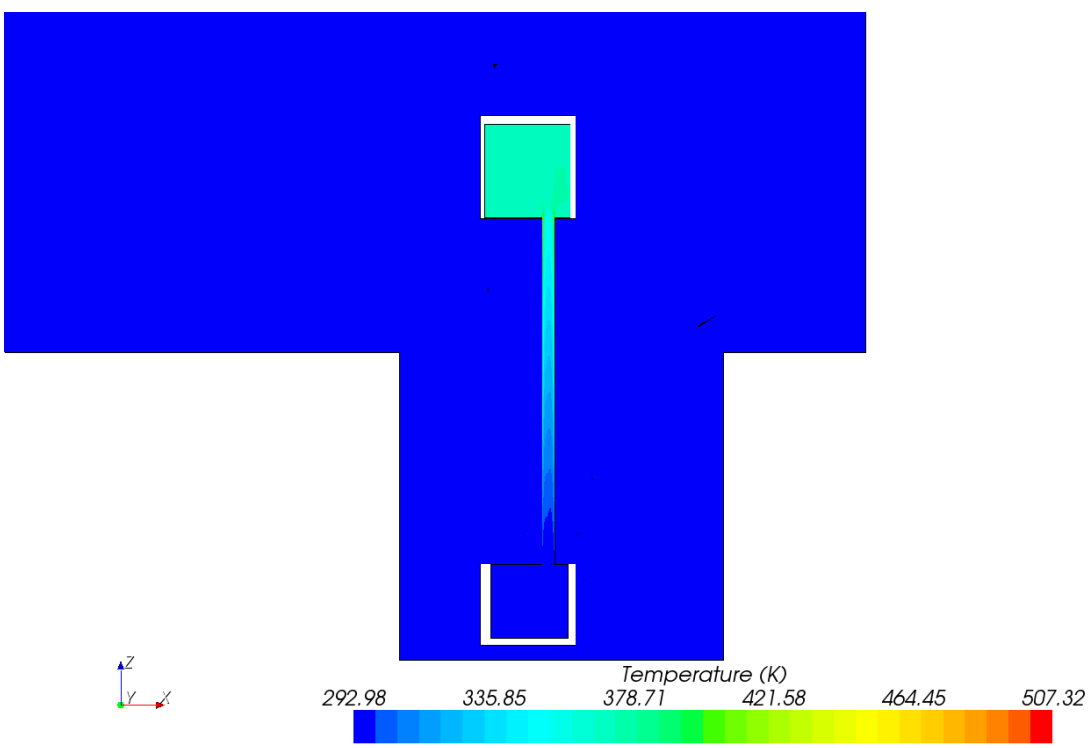

Figure 3.36. Temperature Distribution Showing Temperature Increase in Riser Section

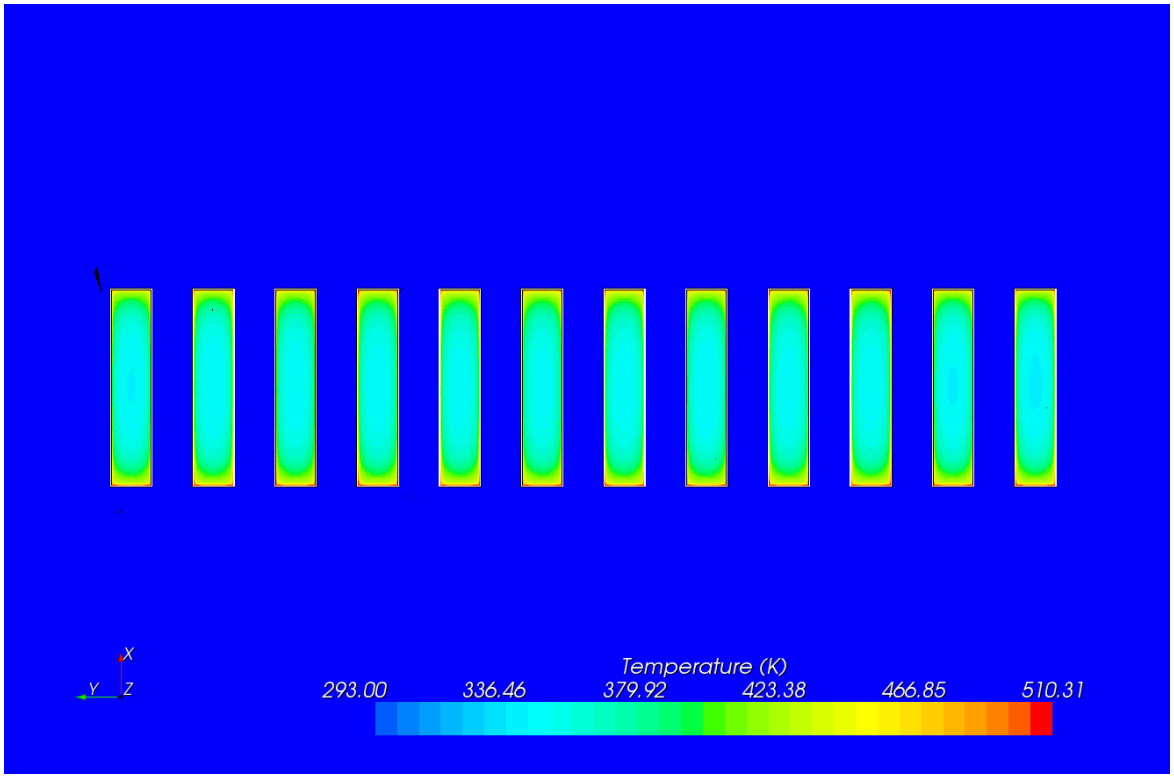

Figure 3.37. Temperature Distribution at the Top of the Risers

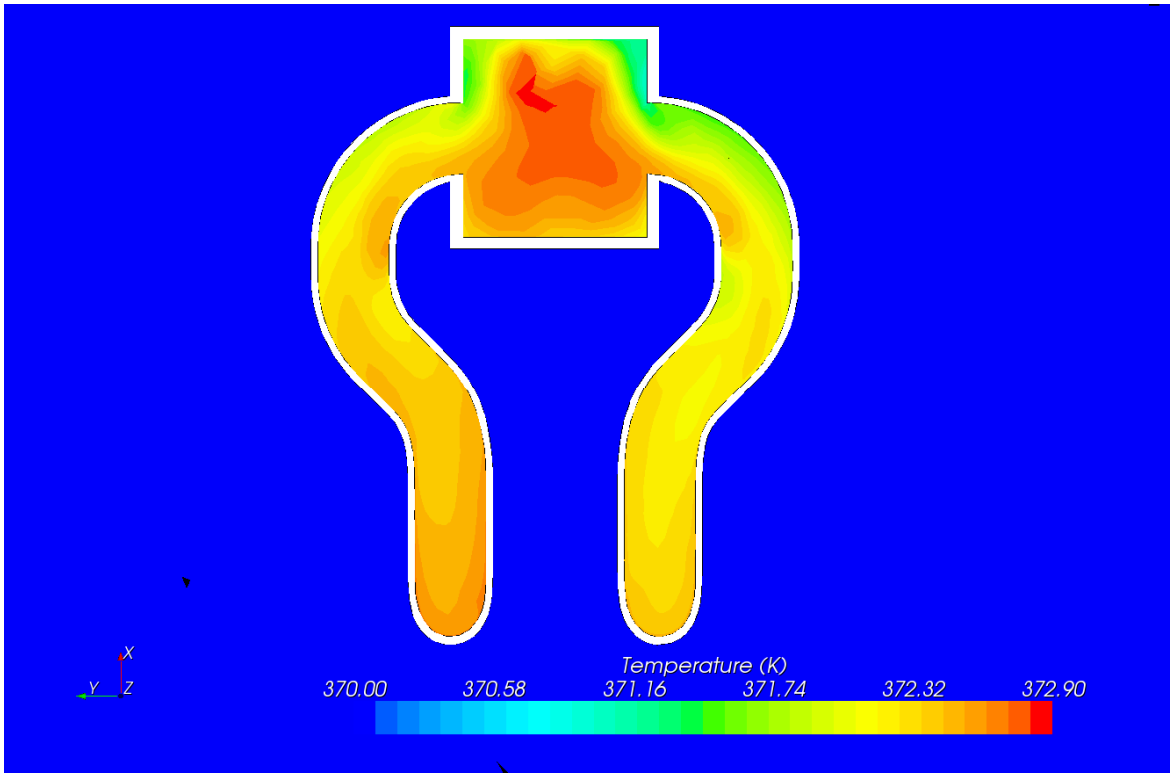

Figure 3.38. Temperature Distribution at the Mid Plane of the Horizontal Outlet Ducts

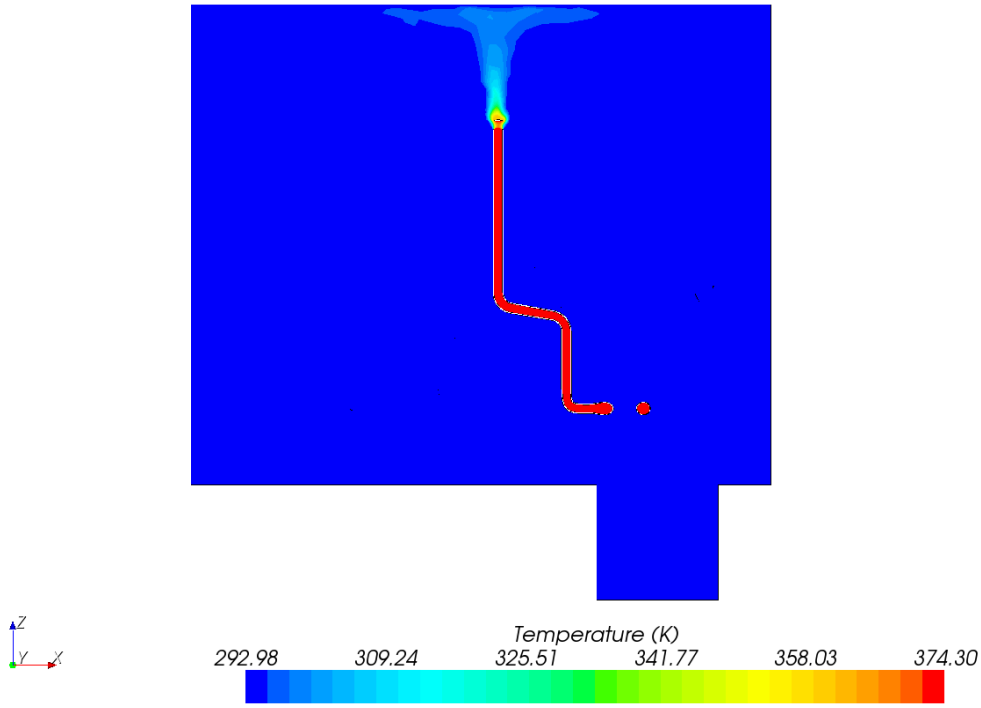

Figure 3.39. Temperature Distribution at the Mid-plane of the Vertical Ducts Showing the Plume exiting the Test Section

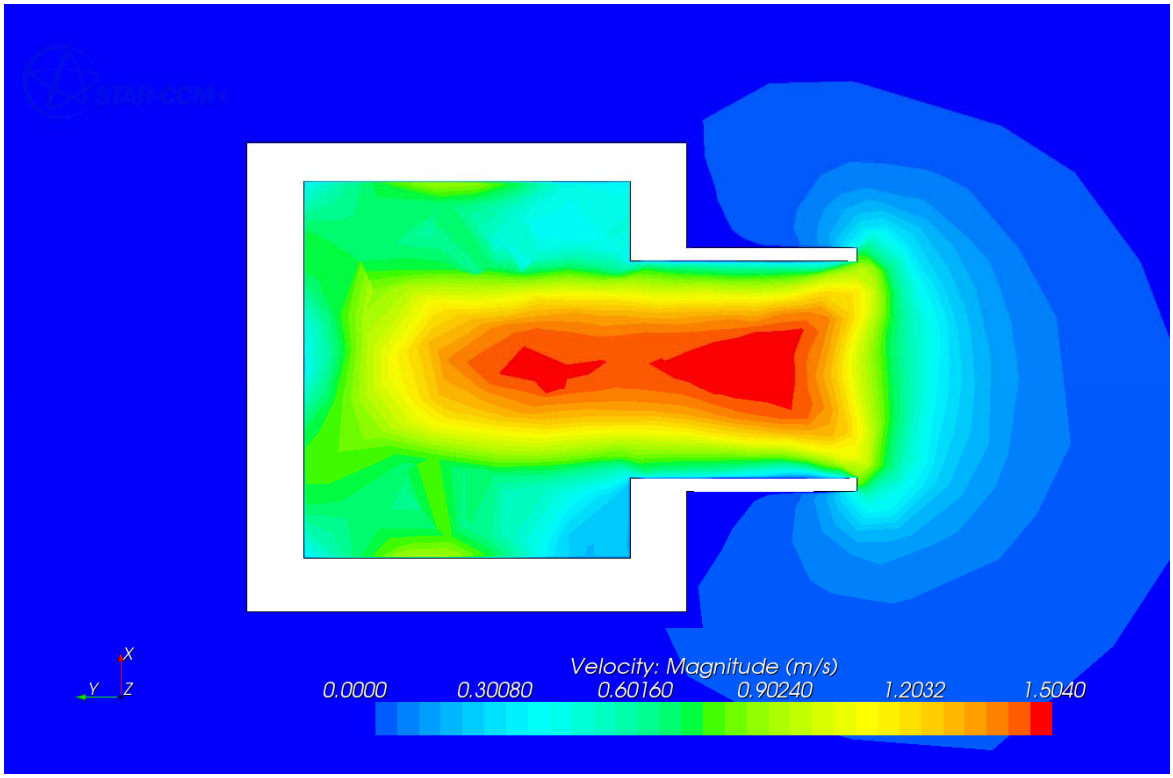

Figure 3.40. Velocity Magnitude at the Mid-plane of the Lower Plenum and Inlet Nozzle.

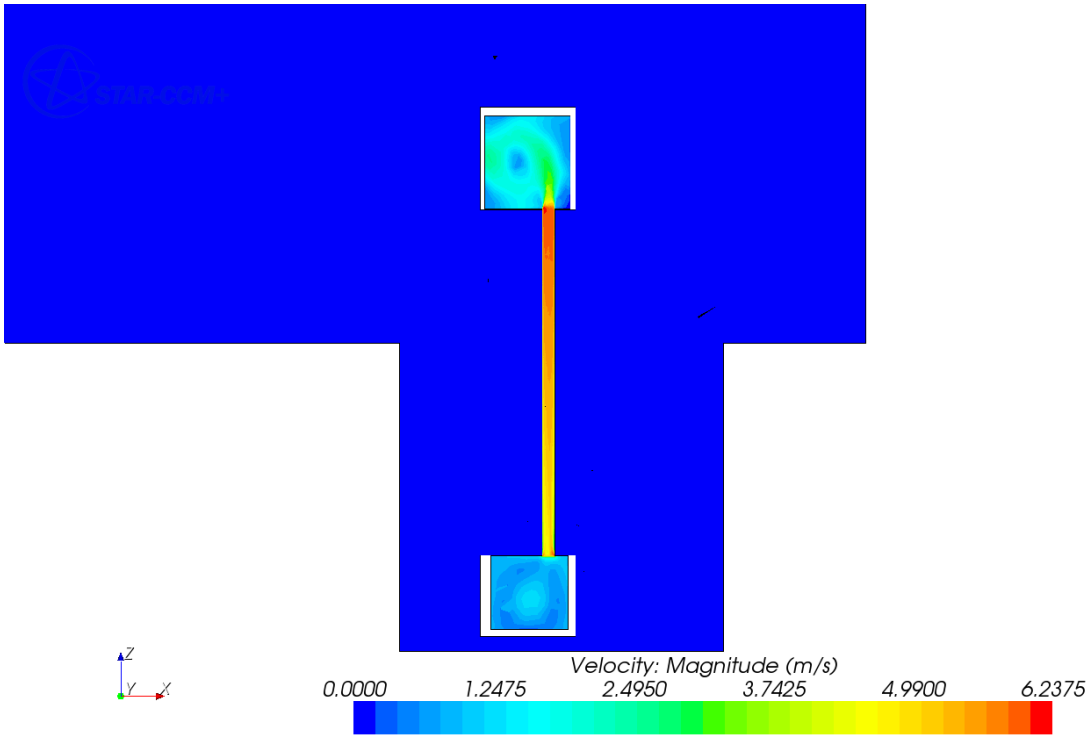

Figure 3.41. Velocity Magnitude in the Riser Section of the NSTF Test Section

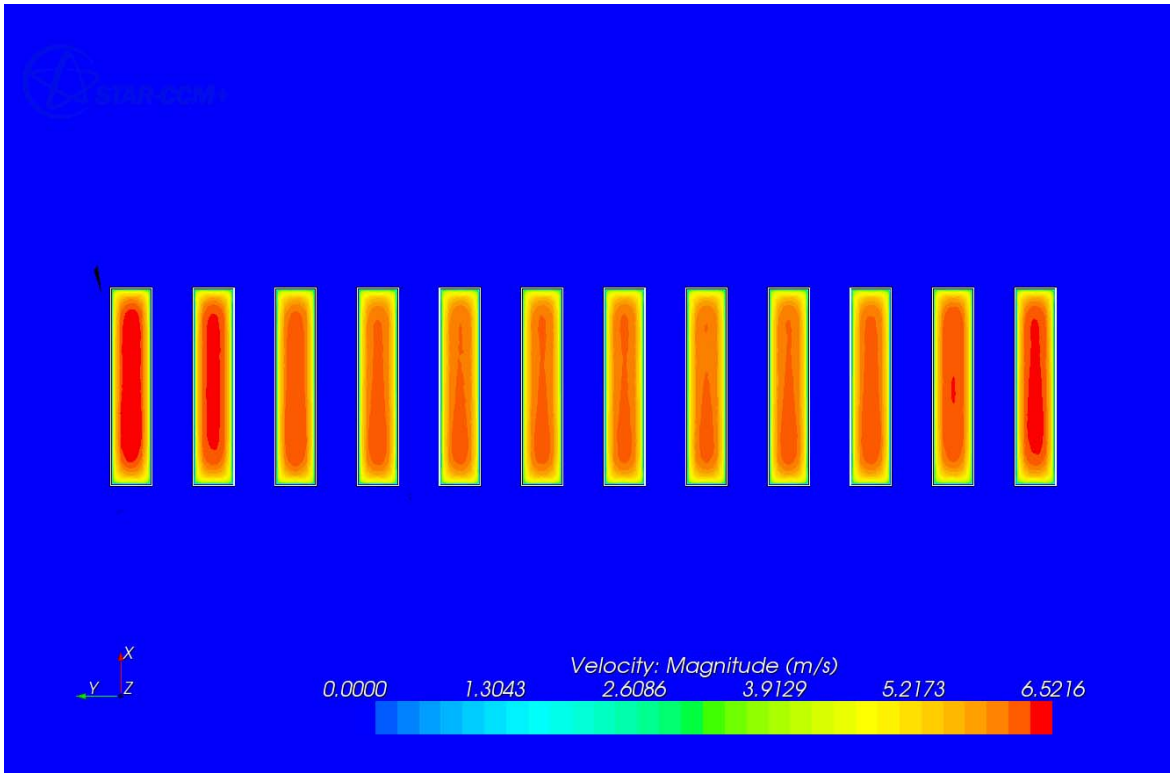

Figure 3.42. Velocity Magnitude at the Top of the Heated Riser Region

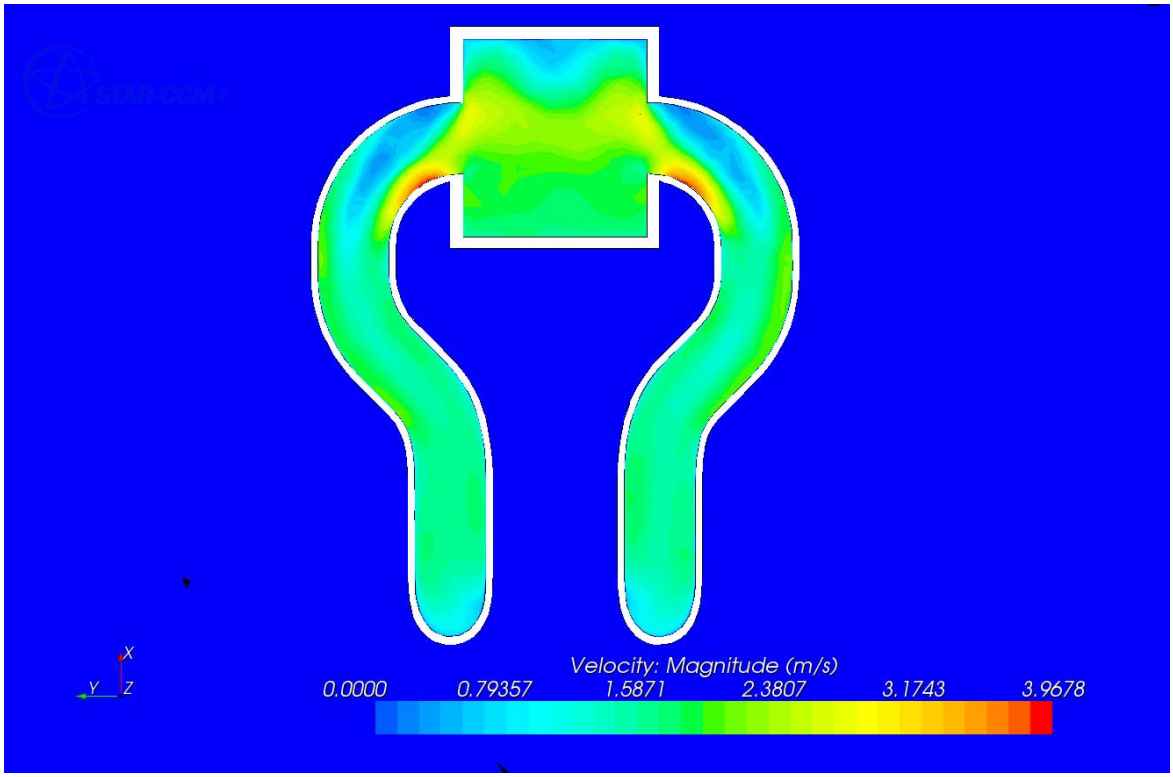

Figure 3.43. Velocity Magnitude at the Mid-plane of the Horizontal Ducts

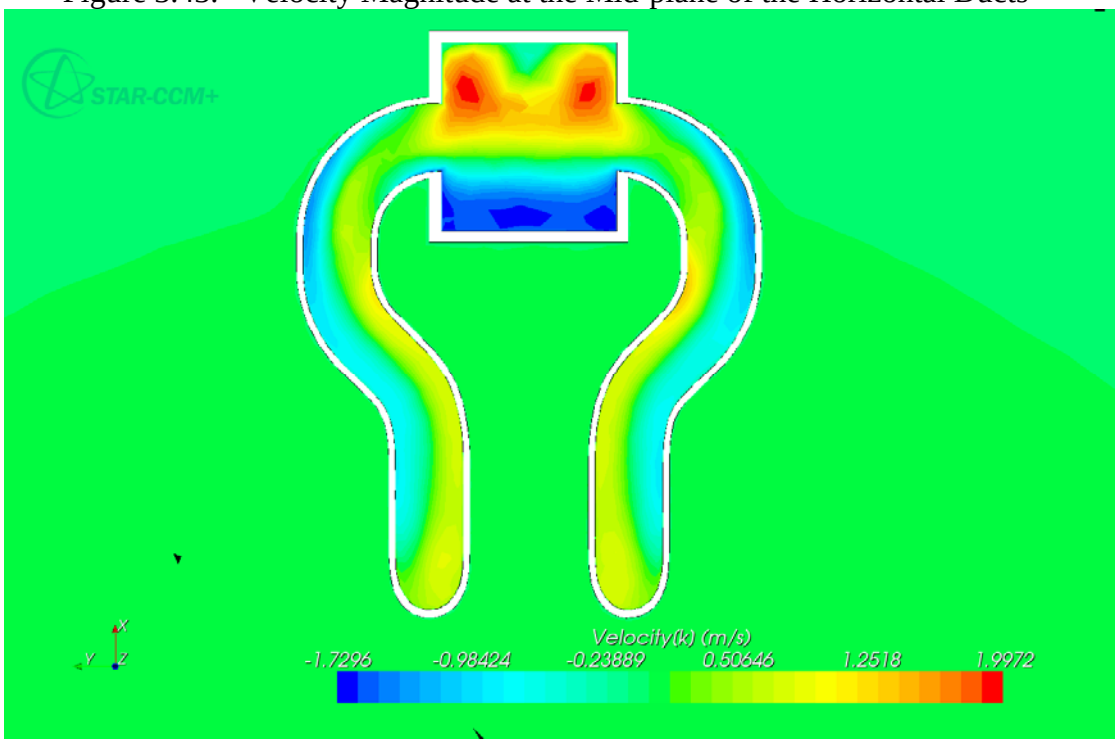

Figure 3.44. Vertical Velocity Vector Component at the Mid-plane of the Horizontal Ducts

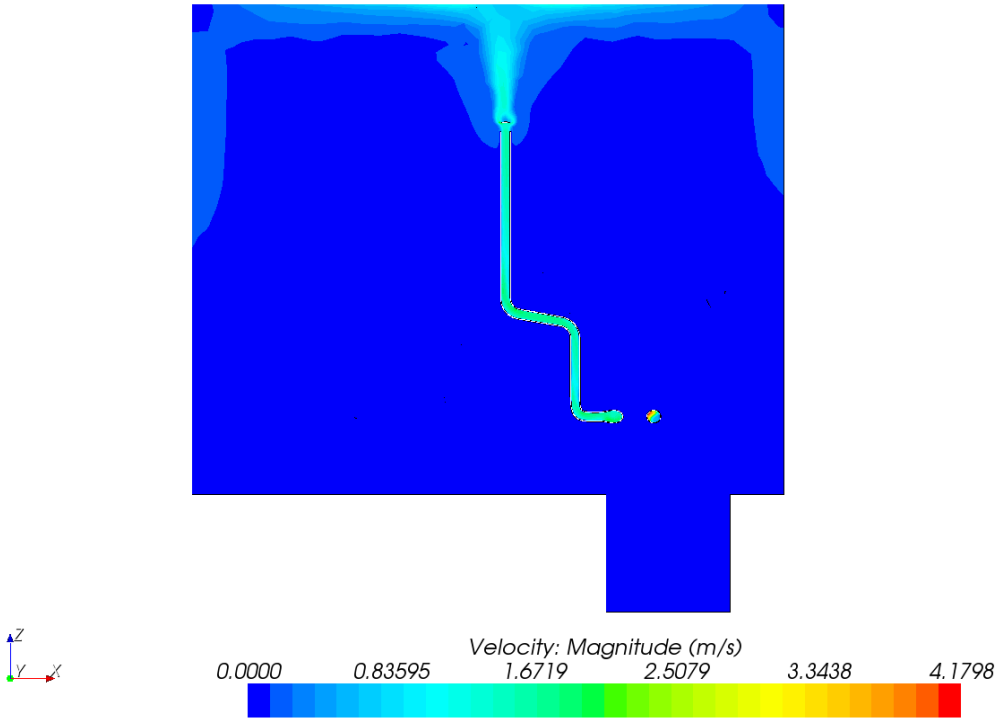

Figure 3.45. Velocity Magnitude at the Mid-plane of the Vertical Ducts

3.6 Summary and Planned Future Work

The initial baseline simulations for the air-cooled GA-MHTGR RCCS and the related NSTF experiment confirm that converged steady state natural convection solutions can be obtained for the detailed full-scale and NSTF system geometries. A convergence monitoring strategy based on the comparison of distributions in geometrically similar risers has been developed to address the shortcomings of conventional convergence monitoring approaches for such cases. Furthermore the baseline simulations have been used to identify key flow features for both geometries and may be used to improve mesh density and grading in those regions if desired. Building upon this foundational work, the mesh and modeling strategy will be used in future simulations to evaluate the more complex case in which the radiation heat source is applied/and or calculated as part of the simulation.

4.0 Cavity Velocity Measurement Feasibility Tests

4.1 Background

A characterization of local gas velocities within the cavity is desired for comparison with CFD code simulations. An evaluation of instrumentation alternatives identified Laser Doppler Velocimetry (LDV) as the most feasible candidate in view of the facility's high operating temperature and the expectation of rather low flow velocities within the cavity. LDV is a well-established optical measurement technique that functions through the detection of laser light scattered from particles suspended within the flow. This has the great advantage of allowing one to measure without inserting a probe into the flow, but it cannot function without the suspended particles. Maintaining adequate levels of particle "seeding" is difficult in a closed system such as the RCCS and so a feasibility study was conducted to ascertain whether this technique could successfully measure velocity within the cavity.

4.2 Laser Doppler Velocimetery

LDV involves crossing a pair of laser beams at the desired measurement point. Because the laser generates coherent light, an interference pattern is created in the region where the beams cross (Fig. 4.1). The pattern consists of a series of light and dark fringes with a spacing defined by the light wavelength and the angle between the beams. The beam diameter is typically a couple of millimeters and the length of the measurement volume from tens of microns to hundreds of microns. Particles passing through the measurement volume reflect light that is subsequently collected through lenses and fiber optics and registered by detectors. As particles travel across the fringes of the measurement volume, the amount of light they reflect rises and falls so that the detector registers an oscillating signal. Since the fringe spacing is known, the component of velocity perpendicular to the fringes can be determined by the frequency of the oscillations. Additional velocity components can be measured with other, typically orthogonal, paired beams.

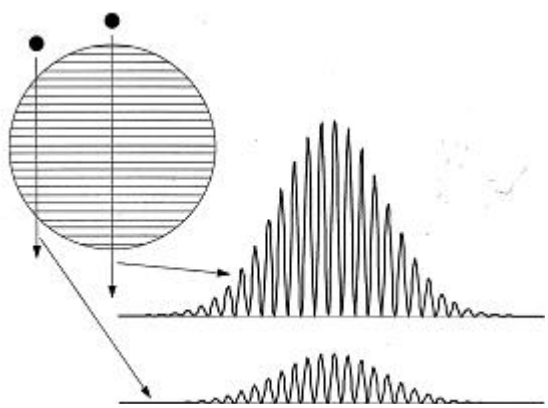

Figure 4.1. Particles Moving Across an Interference Pattern of Light and Dark Fringes (top left) Generate Oscillating Levels of Reflected Light, "Doppler bursts", that are Captured by a Detector

The LDV system we are using consists of a laser, an optical module to split the main beam into 3 beam pairs and fiber optics to carry the beam to a set of lenses for focusing and positioning (Fig. 4.2). The lenses are built into a "transceiver", which, as the name suggests, both sends the incident beams and collects the reflected light. The reflected light is sent back through the fiber optic cable and distributed among detectors within a module containing filters and amplifiers. Signals are then routed to a processor for data reduction and finally transferred to a PC for display and further analysis.

LDV is typically used with open flow systems and forced circulation loops. The working fluid may have naturally suspended particles or, more commonly, seeding is introduced upstream of the region where velocity is to be measured. Without such particles to reflect light, there is no signal for the LDV to process. For liquid flows, particles can remain suspended indefinitely if they are neutrally buoyant, while for gases, the tendency for settling under the influence of gravity must be counteracted by the flow or repeated/continuous seeding. The difficulty posed by the RCCS application is that the cavity is closed, the working fluid is air, and the expected velocities are rather low. These three factors together make it particularly difficult to use LDV, though it remains the best candidate technique for this application.

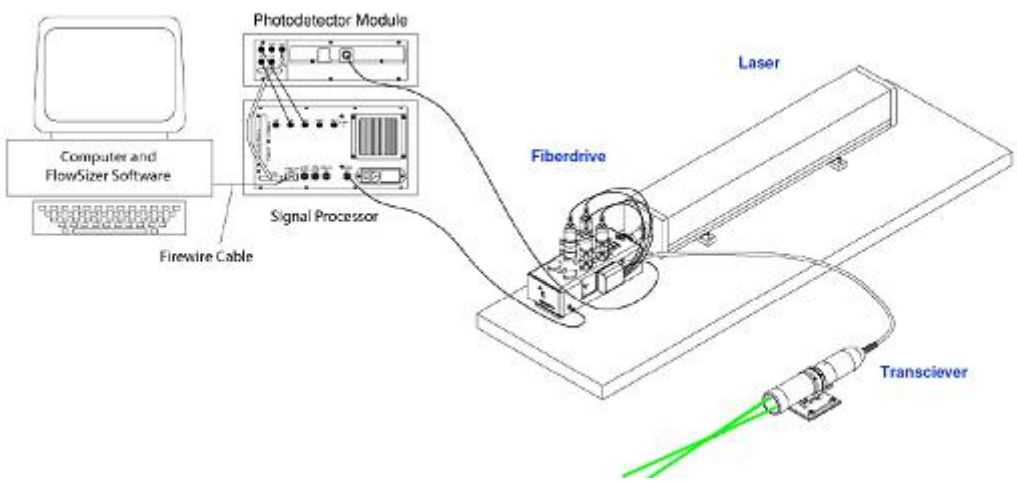

Figure 4.2. The Major Components of the TSI Laser Doppler Velocimetry System. On of the Two Transceivers is Shown

4.3 LDV in Similar Applications

LDV has been used successfully in natural circulation experiments involving closed systems at low temperature and also open systems at high temperature, though such applications are uncommon. We have been unable to find reports of any combination high-temperature/closed system applications like the RCCS. There have been studies of buoyancy-induced flows within glass enclosures in which heat sources and sinks generate circulation. Enclosures have been seeded with Al_2O_3 [4.1] and incense smoke [4.2], with particles reportedly remaining suspended for hours. Insect repellant was used to seed an enclosure for a particle image velocimetry system (PIV)

[4.3], a technique employing a laser light sheet to illuminate suspended particles, which are then imaged and analyzed to produce a two-dimensional map of fluid velocity. PIV and LDV share many of the same types of seeding issues. PIV measurements were made with an oil mist in a large-scale, high-temperature, open flow natural circulation facility akin to the open flow NSTF. [4.4] Wall temperatures in the 11 m-high duct ranged up to 300°C. These examples suggest that there may be suitable seeding particles for LDV measurements within the RCCS.

4.4 Experiment Configuration

Candidate seeding materials have been tested in a 1.8 x 0.5 x 0.5 m glass enclosure. The investigation was limited to determining whether a particular material could produce a measurable LDV signal, and if so, how long the signal would last. Signal strength increases with particle size, but larger particles tend to settle more quickly, necessitating more frequent particle injections, which disturbs natural circulation flow patterns. In addition to settling, particles can be lost via electrostatic attraction to enclosure surfaces. The variety of seeding particles reportedly used in enclosure studies suggests that the optimal seeding technique, i.e. material type, size, and injection method, may vary with the fluid flow physics, the type of LDV system, and the materials used for the enclosure itself.

Six different seeding candidates were tested: 1) propylene glycol mist generated by a compressed-air atomizer, 2) mineral oil atomized by a gas propellant (theatrical smoke, brand name Haze-in-a-can), 3) incense in stick form, 4) incense in coil form, 5) a citronella candle (insect repellent), and 6) titanium dioxide powder (3 μm). The method of introducing seeding particles into the enclosure varied with the type of seeding particle. The oil mists were added by opening slightly a hinged sidewall/door. The enclosure is filled with mist over the course of a few seconds until a fog is visible to the eye and the door is closed. For the incense and candle, the material is allowed to burn for some minutes with the door closed until a stable LDV signal is observed. The door is then opened slightly to extinguish the material and subsequently closed to initiate measurements. The titanium dioxide was dispersed using a jet of compressed air.

Figure 4.3 shows the test setup in operation with the transceivers mounted on the traverse, the beams crossing within the smoke-filled enclosure, and beam termination on a laser curtain. Figure 4.4 provides a close-up view of the beams and the measurement volume where the beams cross. All measurements were made in the lower end of the tank as shown in the photos.

4.5 Test Results

One of the figure of merit for these scoping tests is the rate which particles generate discernible signals for the photodetectors and signal processing unit. This “count rate” determines in part how long one must collect data before the measurement statistics are acceptable. High count rates generally provide better statistics and allow one to more quickly begin a new measurement. Low count rates require longer collection

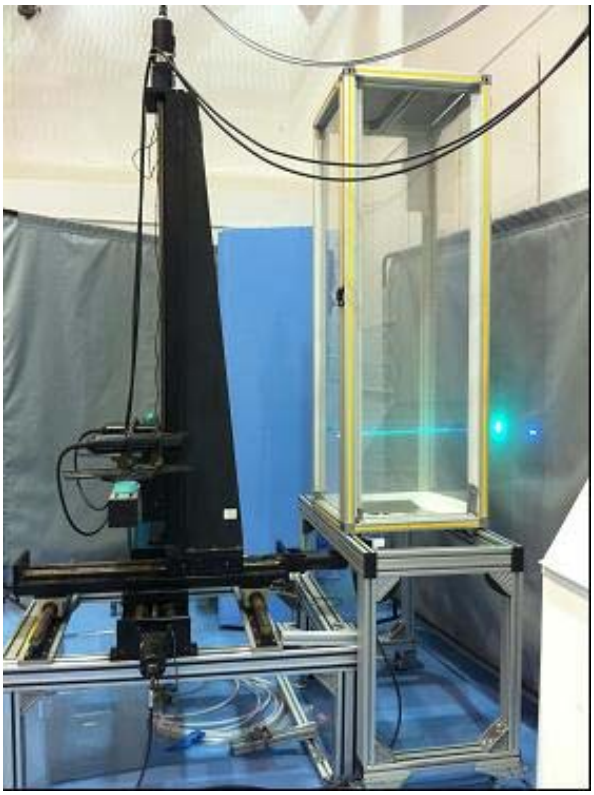

Figure 4.3. Active LDV Transceivers Oriented for Measurements in Lower Region of Glass Enclosure

Figure 4.4. Laser Beams Crossing to form Measurement Volume

times, which can cause difficulties if test conditions cannot be held steady or adequate seeding levels cannot be maintained. Measured peak count rates for the six candidate materials are shown in Fig. 4.5. The peak rate occurs immediately after the enclosure is seeded. It can be seen that count rates for the oils are much higher than for any of the smoke-based seeding materials while titanium particles generated the best data rate of all the candidates. The observed data rates are rather low for LDV measurements in general (one could expect kHz data rates for forced convection), but these levels are not unusual for this type of flow.[4.2, 4.5] It is typical to collect at least several thousand counts to produce a single velocity measurement, and so a measurement would take several minutes at the lower count rates. Based on these peak count rates, any of the tested materials has the potential for use in the RCCS. It should be recognized that peak count rates can be expected to vary with the mode of particle dispersion, injection time, flow velocity, laser power at the transceiver, and cavity size. Therefore these measurements are useful primarily for comparing signal strength among seeding candidates and providing an order of magnitude indication of the count rate one could expect in a natural circulation environment.

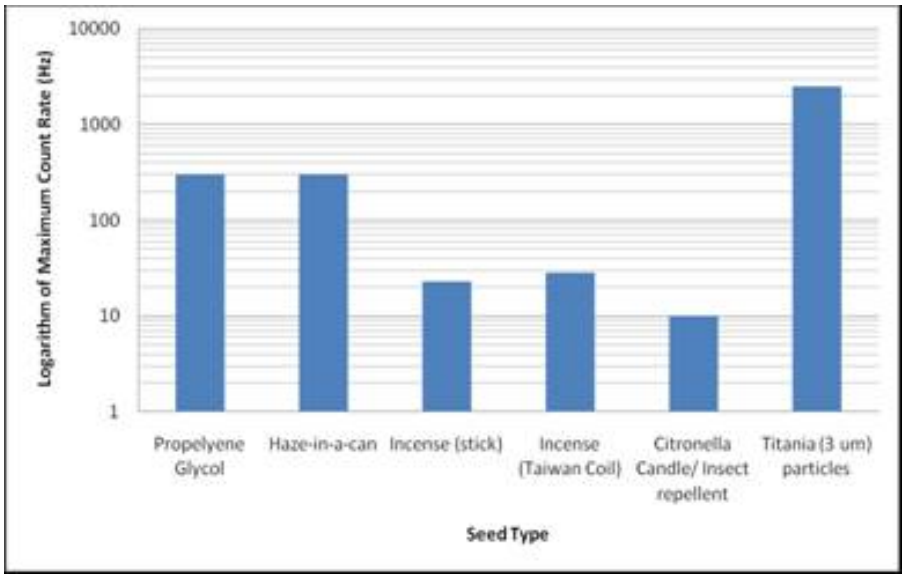

Figure 4.5. Maximum Data Rate for Candidate Seeding Materials

Our second figure of merit is signal duration, which provides a rough indication of the particle injection frequency that might be required to maintain adequate count rates. The signal strength is determined by measuring the count rate at intervals after the enclosure has been seeded. The results are plotted in Fig. 4.6 for each of the candidate materials, except the citronella candle, which did not consistently produce a detectable signal. Signal strength is presented as a normalized count rate so plots can be read as the fraction of initial count rate versus time. We are using a 3-component system and so count rates were recorded on three different channels. For an idealized LDV measurement the count rate would be the same for each channel, but they differ in practice for a number of reasons. The main reason for the difference here is unbalanced beam power, which was much higher for channel one, causing the initial count rate to be much higher than the other channels. The relative count rate was then observed to drop the most for channel one, as shown in the plots. Normally one would balance beam power to optimize the quality of the velocity measurement, but we are concerned only with count rates and so we have maximized power on all channels as the fiber optic cables are old and power output is somewhat low. In summary, the observed count rate divergence among channels evident in the plots is not an issue here.

The plots show a difference in the behavior of the high and low count rate materials. Count rates for the incense, which are low at the outset, drop ~20% and subsequently stabilize. In contrast, the oils and titanium dioxide, which initially produce high count rates, fall precipitously in the first 5-10 minutes. The mineral oil stabilizes at rates similar to that of the incense while the propylene glycol and titanium dioxide rates drop to zero within ten minutes. This was surprising since the settling velocity of the particles used here is small, in the range of 1-3 μm, and they are all expected to stay suspended for hours. The difference between propylene glycol and the mineral oil might be attributed to the delivery mechanism, which was an air-driven Laskin-type aerosol

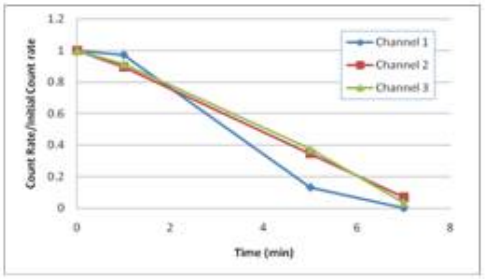

(a)

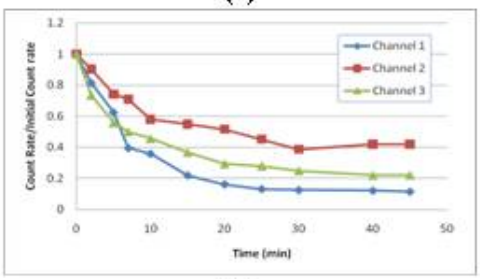

(b)

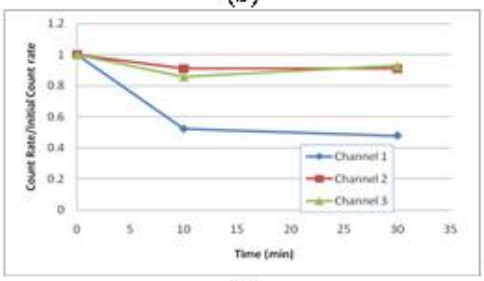

(c)

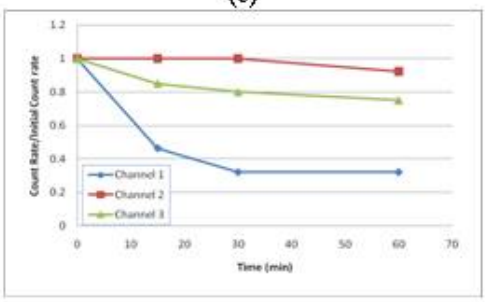

(d)

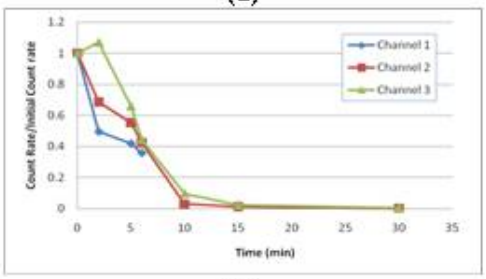

(e)

Figure 4.6. Normalized Count Rate for a) Propylene glycol, b) Mineral Oil, c) Stick Incense, and d) Coil Incense, and e) Titanium Dioxide.

generator for the former and a pressurized spray can for the latter. It is possible that the Laskin generator adds some charge to the particles causing them to attach to the tank walls. Static charge may also be the culprit in the loss of titanium dioxide particles, but it is also possible that the dispersal method was unsuccessful in breaking up the powder into single particles and so they settled much more quickly than expected. No particle sizing device was available to measure size distribution immediately after dispersal.

4.6 Discussion

All of the tested materials generated acceptable count rates in the minutes immediately after seeding except the insect repellant, which had extremely low or zero count rates even during some of the time the candle was burning. Maximum count rates for the oils were more than ten times higher than rates for the incense, which in turn were twice that of the insect repellent. The titanium dioxide count rates were an order of magnitude higher than that of the oils. The high initial count rates would seem to recommend the titanium dioxide and oils since measurements could be completed more quickly and with superior statistics. In addition, the Hattori study showed that oil could be used in a high temperature natural circulation configuration similar to that of the RCCS. However, the titanium dioxide and propylene glycol signals virtually disappeared in less than ten minutes, a period likely to be too short to permit many measurements between seeding injections. In contrast, the mineral oil signal stabilized after 10-20 minutes and generated an acceptable signal for nearly an hour. As both these aerosols consist of oil droplets of similar size, we speculate that the atomization mode influenced the affinity of the droplets for the walls. This suggests that seeding longevity in the RCCS could depend upon how the material is atomized and introduced into the cavity. Temperature may also influence the degree to which the oil tends to attach to the walls.

The two varieties of incense produced lower count rates than the oils, but they were quite stable and easy to generate. Despite the low data rates, incense may be preferable to oil as it is less likely to affect the emissivity of cavity surfaces. Further testing of titanium dioxide with alternative dispersion methods may be warranted, but powder dispersion is generally more troublesome than oil atomization and this is recommended only if oils are deemed unacceptable.

Measurements at high temperature were beyond the scope of this study and so we have only the Hattori work to indicate that LDV should be feasible for a natural circulation system with high temperature surfaces. With the notion that LDV is indeed feasible for velocity measurements within the RCCS, several operational issues should be considered:

1) Though oils provide the best data rates, are they acceptable despite their potential to alter cavity surfaces? Could oil vaporize near the hot cavity surface and alter the gas composition and flow pattern?
2) After cavity seeding, how much time must elapse before natural circulation patterns are reestablished and measurements can begin? The length of the

seed/wait/measure cycle must be considered since the facility run time can become lengthy when measuring at many locations.

3) Will particle losses through the open ports be significant over the course of a measurement campaign? Must seeding frequencies be substantially increased to compensate?
4) Will the low data rates and potentially high ratio of noisy signals make obtaining the desired turbulence data statistics difficult?

It is probable that LDV can be made to function well enough to obtain a number of velocity measurements though not yet clear how much effort will be required to obtain an acceptably extensive cavity velocity map. For steady state tests that run tens of hours, it may be acceptable if, say, ten minutes of data collection are required at each location. One could then map dozens of locations over the course of hours. For transient tests, one may only be able to track velocity at a single location during the course of the test.
It is likely that trial and error iterations with the actual facility will be necessary for the final selection of a seeding material and injection mode and to arrive at acceptable data rates and seeding intervals. A final upgrade of the LDV system is recommended for this particular application (the signal processor and photodetectors were replaced while the original laser and transceivers were retained). The laser is a large water cooled unit that will be difficult to move for measurements on different levels. New systems use small air cooled solid state units that are much more portable and durable. The transceivers will also pose difficulties if 3D measurements are to be made since beams from each transceiver must cross in precisely the same spot. Alignment can be performed outside the test section and the probes then moved for the measurement, but it will be difficult to confirm that correct alignment is maintained (other than good coincidence measurements among the three channels). Alternatively, it is now possible to incorporate all three velocity component measurements into a single probe, ensuring alignment as it is moved and directed to different measurement locations.

References

4.1 Lankhorst A., Angirasa D., Hoogendoorn C., (1993) LDV Measurements of Buoyancy-induced Flows in an Enclosure at High Rayleigh Numbers, Experimental Thermal and Fluid Science 6 74-79.

4.2 Tian, Y.S., and Karayiannis (2000) Low Turbulent Natural Convection in an Air Filled Square Cavity, Part I, The Thermal and Fluid flow Fields., Int. j. Heat Mass Transfer 3 6 849-866.

4.3 Manum M., Johnson D., Hollands K., Leong W., (2008) PIV Measurements of the Flow Field Inside an Enclosed Cubical Cavity in Natural Convection, Experiments in Fluids 44 4 647-659.

4.4 Hattori Y., Tsuji T., Nagano Y., and Tanaka N. (2006) Turbulence Characteristics of Natural-Convection Boundary Layer in Air Along a Vertical Plate Heated at High Temperatures, Int. J. Heat and Fluid Flow 27 445-455.

4.5 Marakami S., Kato S., and Yoshie R., (1995) Measurement of Turbulence Statistics in a Model Fire Room by LDV. ASHRAE Transactions 101:3905.

Nuclear Engineering Division
Argonne National Laboratory
9700 South Cass Avenue, Bldg. 208
Argonne, IL 60439

www.anl.gov

Argonne National Laboratory is a U.S. Department of Energy
laboratory managed by UChicago Argonne, LLC